UNIVERSITY OF LIVERPOOL

Porous Liquids based on the Porous Organic Cage and Ionic Liquid

Aiting Kai

Thesis submitted in accordance with the requirements of the University of Liverpool for the degree of Doctor of Philosophy

September 2022

Supervisor: Professor Andy Cooper

Table of Contents

Table of Contents 2
Acknowledgement I
Abstract II
Overview III
Abbreviations V
Chemical Abbreviations V
Chapter 1 1
1.1 General types of porous liquids and a brief history introduction 3
1.2 Porosity characterisation method 5
1.3 Progress of porous liquids 6
1.3.1 Type I porous liquids 6
1.3.1.1 Pore generators and general construction methods 6
1.3.1.1.1 Hollow materials 7
1.3.1.1.2 Metal organic framework 9
1.3.1.1.3 Porous organic molecules 11
1.3.1.1.4 Coordination cages and metal organic cages 13
1.3.1.2 Progress 15
1.3.1.2.1 Type I porous liquids based upon porous organic cages 15
1.3.1.2.2 Type I porous liquids based upon hollow inorganic materials 19
1.3.1.2.3 Type I porous liquids based upon MOFs 24
1.3.1.2.4 Type I porous liquids based upon a coordination cage 27
1.3.1.3 Summary 28
1.3.2 Type II porous liquids 29
1.3.2.1 Pore generators 29
1.3.2.2 Solvent selection 29
1.3.2.3 Progress 30
1.3.2.4 Summary 34
1.3.3 Type III porous liquids 34
1.3.3.1 Pore generators and preparation methods 34
1.3.3.2 Solvent selection 34
1.3.3.3 Phase stability 35
1.3.3.4 Progress 36

1.3.3.4.1 ZIF-8 36
1.3.3.4.2 Other MOFs 38
1.3.3.4.3 Other porous materials 40
1.3.3.5 Summary 42
1.4 Applications of porous liquids 42
1.5 Summary of porous liquids 42
Chapter 2 44
2.1 Gas laws and gas solubility in liquids 45
2.2 Gas sorption and methodology of gas uptake measurement of porous liquids in the thesis 47
2.3 CD 49
2.4 PXRD 50
2.5 DLS 51
2.6 LUMiSizer® 52
2.7 TGA 53
2.8 Wettability 53
2.9 Rheology 54
Chapter 3 57
3.1 Author contributions 58
3.2 Introduction 59
3.3 Synthesis and characterisation of POC microparticles 63
3.4 Screening for type III porous liquids using POC microparticles 68
3.5 Properties and stability study of type III CC3-*R*/CC3-*S* microparticle porous liquids 77
3.5.1 Concentration 77
3.5.2 Viscosity 82
3.5.3 Rheology 83
3.5.4 Phase stability 87
3.5.5 Pore carrier stability 92
3.5.6 Recyclability and aging 95
3.5.7 Gas release of the dispersions of CC3-*R*/CC3-*S* microparticles in [BPy][NTf_2] by temperature and pressure 96
3.6 Conclusion 100
Chapter 4 102

4.1 Author contributions 103
4.2 Introduction 104
4.3 Solubility screening 104
4.4 Porosity screening 108
4.5 Conclusion 114
Chapter 5 116
5.1 Author contributions 117
5.2 Introduction 118
5.3 Study of tying RCC1 with ILSA-S3 120
5.4 Melting behaviour study 129
5.4.1 Thermal study 129
5.4.2 Rheology description 132
5.4.3 Further melting point decrease strategy 133
5.5 Porosity study by CO_2 sorption of RCC1-ILSA-S3 136
5.6 Stability study 141
5.7 Trials to improve porosity 144
5.7.1 RCC3-5FT-IL 144
5.7.2 RCC5-IL 147
5.8 Conclusion 148
Chapter 6 150
Chapter 7 155
7. 1 General synthetic and analytical methods 156
7.2 Chapter 3 experimental data 160
7.2.1 Synthesis and characterisation 160
7.2.2 Sorption data 164
7. 3 Chapter 4 experimental data 167
7. 4 Chapter 5 experimental data 176
7.5 Reference 187

Acknowledgement

I would like to thank Prof Andy Cooper and Dr Xiaofeng Wu, who made my dream of a PhD journey here realised in the first place, and many thanks to Dr Marc Little and Dr Becky Greenaway for their academic support during this journey. Thank you to Dr Peng Cui, Dr Ben Egleston, Dr Rachel Kearsey and Dr Mike Brand for their kind help to me in adjusting to the lab in the first year, Dr Qiang Zhu for the discussions, Ms Xiaoqi for the circular dichroism spectroscopy help and the delicious desserts, Dr Xiang Zhou for the high-performance liquid chromatography measurement and the coffee time, and Mr Bin Lin for the rheology book. And a special thanks to Dr Xiaoyan Wang, Dr Zhiwei Fu, Dr Zhongfu Pang, and Dr Xue Wang, for their tolerance of my confusing talks while I felt down. At last, big thanks to all the AIC group members and it has been a great honour to work with all of you.

Abstract

Porous liquids, coined in 2007, are a novel kind of flowing porous materials which have gained rapid advances since the first experimental example was achieved in 2015. Porous liquids include three categories, where type I porous liquids are neat porous materials flowing at room temperature, type II and type III are two-component porous solutions and dispersions with size-excluded solvents respectively. The established construction strategies to achieve porosity in the liquid involve various precursors ranging from inorganic to organic-inorganic hybrid and pure organic materials, among which the porous organic cage, with its molecular structure, discrete cavities, and good solubility, has the potential in being made into all three types of porous liquids.

This thesis describes the formation of three types of porous liquids prepared using porous molecular cages and ionic liquids to explore new methods of constructing porous liquids. In Chapter 3, porous cage cocrystals **CC3**-*R*/**CC3**-*S* were studied as the porogen in a type III system. To form porous liquids, several commercial and synthesised ionic liquids (imidazolium, pyridinium, ammonium, phosphonium cations paired with fluorine-containing anions) were studied in Chapters 3 and 4 as size-excluded solvents in type II and III systems containing porous organic molecules (Noria, cyclodextrin, **CC19**, scrambled cage). In Chapter 5, a novel cage-tying method that involves an aminal ring-forming reaction between aldehydes and secondary amines was studied as a post-functionalisation method to construct type I porous liquid with reduced cage molecules (**RCC1** and **RCC3**). The results from Chapter 3 demonstrated the formation of type III porous liquid systems in ionic liquids using cages as pore carriers; initial solubility screening data of selected porous organic molecules in ionic liquids were determined in Chapter 4; and in Chapter 5 a potential type I porous liquid system containing a cage salt was successfully synthesised, which showed a melting behaviour below 90 °C and a three-fold CO_2 uptake compared with that of the monomer. The work presented in this thesis not only enriches the library of porous liquids based upon porous organic imine cages, but also provides initial data on using ionic liquids as size-excluded solvents for cage-based porous liquid systems, and, more importantly, creates new porous liquid construction methods.

Overview

An emerging increase of porous liquids examples have been realised in recent years (especially after 2018), with construction compositions varied from hollow silica/carbon and metal organic frameworks to porous organic cages, coordination cages, covalent organic frameworks and so on. However, challenges for porous liquids still exist, such as low uptakes and high viscosity, which would pose disadvantages for practical application. Thus, the main aim of this thesis was to overcome some of the issues and put forward new routes to construct porous liquids.

The thesis is composed of seven chapters:

Chapter 1 introduced the basic conception and types of porous liquids, related characterisation techniques, some investigated applications, and summarised the realised porous liquid systems according to the porous liquid types and corresponding construction precursors.

Chapter 2 displayed some key topics and characterisation techniques covered in the thesis.

Chapter 3 studied constructing type III porous liquid systems using a [4+6] porous organic imine cage cocrystal **CC3**-*R*/**CC3**-*S* as pore carriers and ionic liquids as size-excluded solvents.

Screened ionic liquids included imidazolium, pyridinium, ammonium, and phosphonium cations pared with the bis(trifluoromethanesulfonyl)imide anion. The size-exclusion requirement for ionic liquids to be excluded from an [4+6] imine porous organic cage cavity was first determined, and several type III porous liquid systems were successfully constructed, with CO_2 and CH_4 uptakes reaching 3 times and 13 times compared to those of a blank ionic liquid in a sample with 20 wt.% loading of the cage. One system in N-butylpyridinium bis(trifluoromethanesulfonyl)imide was also studied in full detail about its properties (gas uptake capacity, stability, rheology, recyclability and so on).

Chapter 4 studied replacing volatile organic solvents with ionic liquids to construct type II porous liquids, which required both solubilising ability and size-exclusion of the solvents. Solubility of several porous organic molecules (Noria, cyclodextrin, **CC19** and scrambled cage) was screened among a range of ionic liquids with imidazolium, pyridinium, ammonium, phosphonium cations paired with fluorine containing anions. Though no type II system was constructed, corresponding initial

solubility data in ionic liquids was first determined, which would help provide design considerations for future systems.

Chapter 5 explored a new method to construct type I porous liquid, where a tying method which involved a ring-forming reaction between aldehydes and secondary amines was studied as a post-functionalisation method to modify reduced [4+6] imine cage molecules (**RCC1** and **RCC3**). One product **RCC1-ILSA-S3** showed a low melting point below 90 °C, which was qualified to be termed as a general type of porous liquid, just as that a general ionic liquid had a melting point below 100 °C. And **RCC1-ILSA-S3** presented three-fold CO_2 uptake compared to that of the monomer.

Chapter 6 summarised the thesis content and introduced relevant future work.

Chapter 7 gave the instrument information, experiment procedures and related data.

Abbreviations

BET	Brunauer–Emmett–Teller
CD	Circular dichroism
DLS	Dynamic light scattering
DSA	Drop shape analyser
DSC	Differential scanning calorimetry
FT-IR	Fourier transform infrared spectroscopy
HPLC	High-performance liquid chromatography
HT	High tension
IR	Infrared spectroscopy
MALDI-TOF	Matrix-assisted laser desorption/ionisation time-of-flight mass spectrometry
MS	Mass spectroscopy
NMR	Nuclear magnetic resonance spectroscopy
PXRD	Powder X-ray diffraction
RCF	Relative centrifugal force
RP	Reflection positive
RPM	Revolutions per minute
RT	Room temperature
SEM	Scanning electron microscope
STEP	Space and time-resolved extinction profiles
TGA	Thermal gravimetric analysis
TLC	Thin layer chromatography
UV	Ultraviolet

Chemical Abbreviations

AcOH	Acetic acid
COF	Covalent organic framework
CsI_3	Caesium triiodide
DCM	Dichloromethane
DCTB	Trans-2-[3-(4-*tert*-butylphenyl)-2-methyl-2-propenylidene]malononitrile
DMSO	Dimethyl sulfoxide

EtOH	Ethanol
HCP	Hexachloropropene
HCS	Hollow carbon sphere
HS	Hollow silica
IL	Ionic liquid
$LiNTf_2$	Lithium bis(trifluoromethylsulfonyl)imide
MeOH	Methanol
$MgSO_4$	Magnesium sulphate
MOF	Metal organic framework
$NaHCO_3$	Sodium hydrogen carbonate
NaOAc	Sodium acetate
Na_2SO_4	Sodium sulphate
PAF	Porous aromatic framework
PEG	Polyethylene glycol
PL	Porous liquid
POC	Porous organic cage
POP	Porous organic polymer
R, R-CHDA	(1R, 2R)-cyclohexane-1,2-diamine
SC	Scrambled cage
S, S-CHDA	(1S, 2S)-cyclohexane-1,2-diamine
TFA	Trifluoroacetic acid
TFB	1,3,5-Triformylbenzene
TsCl	4-Toluenesulfonyl chloride
ZIF	Zeolitic imidazolate framework
ZSM	Zeolite socony Mobil

Chapter 1

Introduction

Porous materials tend to have physical voids in their structures and they can be classified according to their pore size. [1] Pore sizes less than 2 nm are termed micropores; pore sizes between 2 and 50 nm are termed mesopores, and pore sizes over 50 nm are termed macropores. In addition, there are other less standardised ways to classify porosity in materials, for example, extrinsic and intrinsic porosity. Extrinsic porosity refers to pores located between molecules, which originate from inefficient packing of molecules in crystalline or amorphous solids. Intrinsic porosity refers to an internal void within a molecule, such as a cage molecule with a cavity. [2] Another important aspect of porosity is its connectivity in a particular structure. Some porous organic molecular crystals have 0-D voids (or isolated voids), [3] which is usually the case when the interconnecting channel between voids is too narrow to incorporate guest molecules. By contrast, most porous organic solids tend to have 1- or 3-D pore structures. 1-D porous solids have interconnected molecular-accessible 1-D channels while porous materials with 3-D voids tend to have channels connecting the voids across the structure, thus guest molecules tend to diffuse more efficiently through materials with 1- and 3-D pore structures.

When it comes to the adjective word “porous”, one may intuitively correlate it with solid-state materials containing atoms that are inefficiently packed but tightly bound, which grants the substance structural rigidity and little tendency to change its shape and volume. Rather than a stereotype, this impression implies some key characteristics of porosity. If a porous material has a framework structure with good mechanical strength, then the material will have permanent pores with well-defined shapes that will be maintained. [1,4] Natural porous substances include wood, sponges, coral, bones and so on. Synthesized porous solids materials include MOFs, [5] ZIF, [6] POPs, [7] COFs, [8] porous oxide materials, [9] POCs and so on. [10,11] These materials can be used in a variety of applications, such as energy storage, [12] gas separation, [13] catalysis, [14] enantioseparation, [15] drug delivery and release, [16] to name a few. However porous materials are not limited to porous solids nowadays, thanks to the pioneering work by Stuart James and co-workers there is a new class of porous material, referred to as, porous liquids. [4]

1.1 General types of porous liquids and a brief history introduction

"Porous liquids" was conceptualised by Stuart James in 2007, [4] and realised in the laboratory within these 15 years. In a conventional sense, liquids all contain pores which are only transient due to the thermal motion of liquid molecules. The shape of these pores is ill-defined and much smaller than typical molecules, thus conventional liquids cannot be utilised as porous materials. By contrast, porous liquids have well-defined, permanently accessible voids. [17] There used to be three types of porous liquids, based upon corresponding construction methods according to the first paper which coined 'porous liquid' (**Figure 1.1**). A type I porous liquid is a neat homogenous liquid which contains cavities at room temperature. Type II and type III porous liquids are both composed of unoccupied hosts with cavities and size-excluded solvents. If the hosts can be dissolved in a bulky solvent which cannot enter the cavities of hosts, a type II porous liquid is formed, while the type III porous liquid is prepared by dispersing a non-soluble porous framework in a bulky solvent. As porous liquids combine the properties of liquids and porosity in the same material, it grants porous liquids many advantages and makes them a good supplement to porous materials. For example in an adsorption process, liquids are more efficient in mass and heat transfer compared to solids. [18] In addition, the sorption of porous liquids is based upon physisorption, which could present advantages in industrial-scale CO_2 collection as less energy consumption is needed to recycle the material compared with chemical solvents on one hand; and on the other hand, porous liquids could show better capacity than physical solvents. [19] There has been a new classification that put forward a type IV porous liquid recently by Bennet *et al.*, [20] which was defined as 'neat microporous hosts that form transient, strongly associated liquids'. This kind of materials, for example, could seek porosity in liquid MOFs at higher temperatures, [21] which is discussed as a pseudo-type I porous liquid in this introduction.

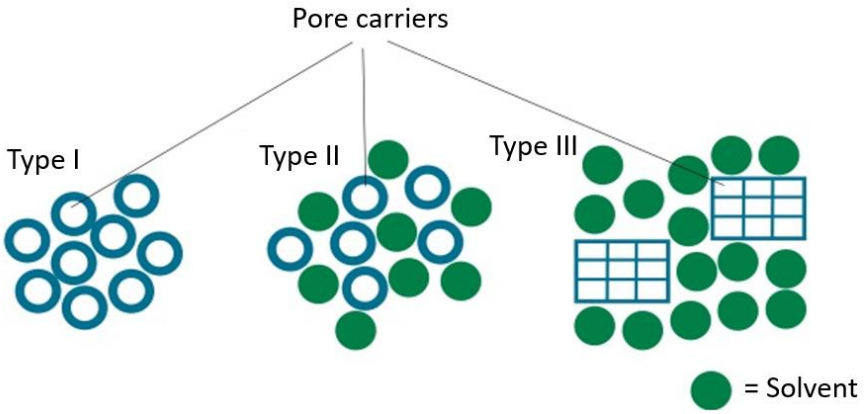

Figure 1.1: Three types of porous liquids. (Reproduced with permission, [4] Copyright 2007, Wiley-VCH)

The first experimental trial of constructing porous liquids had not been reported until 2012 since the concept was put forward, which explored developing porous organic imine cage-based type I porous liquids. [22] Earliest-realised porous liquids were reported in 2015, which included type II porous liquids based upon imine cages dissolved in size-excluded solvents, [23] and a type I porous liquid composed of hollow silica spheres functionalised with long chains. [24] Type III porous liquids were first reported in 2018, [25–27] where ZIF-8 was dispersed in ionic liquids. Starting in 2020, more researchers entered this field and the number of published papers about porous liquids doubled than earlier years, with other kinds of porous solid materials such as coordination cages and covalent organic frameworks employed to construct porous liquids. [28,29]

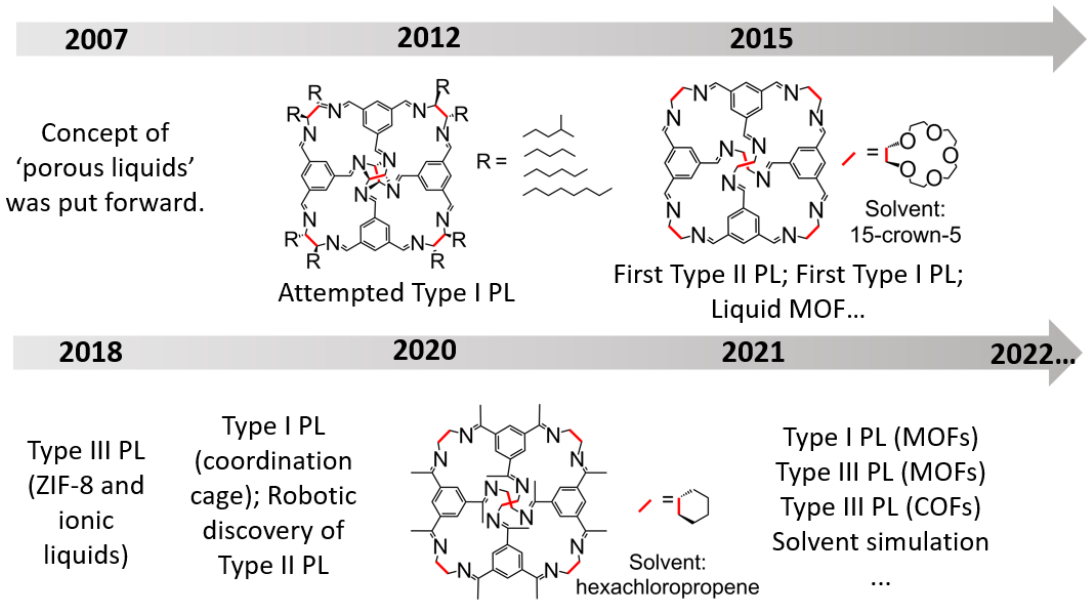

Figure 1.2: A brief timeline of porous liquids history.

1.2 Porosity characterisation method

Compared with transient porosity in conventional liquids, it is less challenging to prove permanent porosity in porous liquids. Both computational and experimental methods have been established with the development of porous liquids. [22–26,29] Computational methods mostly use molecular dynamic (MD) simulations, where the porosity within a liquid would be simulated to see whether it would maintain within a given time scale. For example, in an MD simulation to characterise a ZIF-8 based type III porous liquid which was prepared in the ionic liquid trihexyltetradecylphosphonium bis(trifluoromethanesulfonyl)imide ($[P_{6,6,6,14}][NTf_2]$), [26] both solvents molecules and porous framework were modelled in a periodic simulation box and intermolecular interactions were used with a suitable, system specific, force field. The results showed that the voids in the liquid can be maintained after equilibration (**Figure 1.4 a-b**). [23,26,30,31]

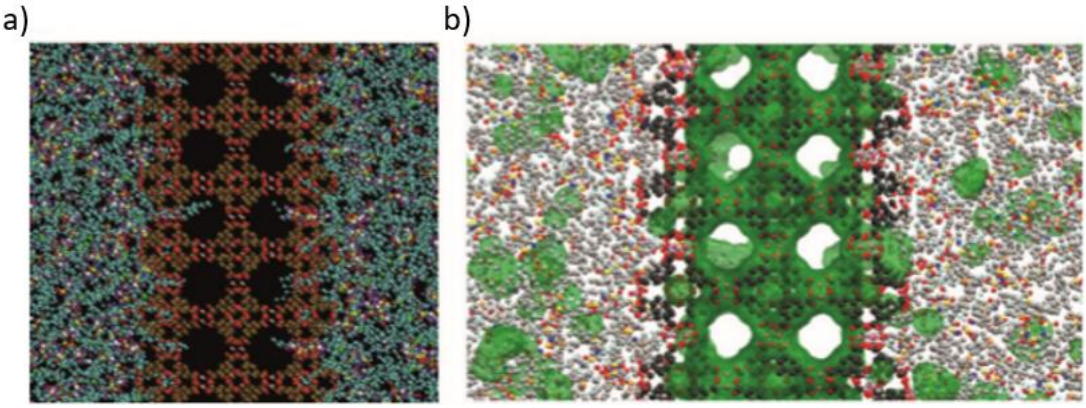

Figure 1.3: Molecular simulation of porous liquids shows empty pores in ZIF-8. a) Snapshots of simulation box consisting of $[P_{6,6,6,14}][NTf_2]$ and ZIF-8; b) Identification of free volume (green regions) in simulation snapshot and the white region inside the MOF are also free volume. (Reproduced with permission, [26] Copyright 2018, Wiley-VCH)

Experimental methods involve density measurement, [26,32,33] positron annihilation lifetime spectroscopy (PALS), [23,25,27,28,34,35] and gas solubility measurement.[36,37] PALS measures the positronium e^+ lifetime pattern in a sample under different conditions to determine the sizes of cavities in a material where the longer the positronium lifetime, the larger the cavity size. Gas solubility measurement, which usually includes carbon dioxide, methane, and nitrogen, could be employed to characterize all three types of porous liquids. The neat solvents or precursors constitute the main part of corresponding porous liquids and usually have less gas solubility than the corresponding porous liquids prepared. Thus, by comparing the gas uptakes of the

blank non-porous solvents or tethered precursor groups with the gas uptake of porous liquids prepared, it is possible to evaluate the porosity in the porous liquid. The operations involved in the solubility difference method are easy to perform and now tend to be commonly used. The gas solubility could be measured by gas evolution measurement, [23,30,38,39] IR, [30,40] NMR, [23,30,38,41] and standard gas sorption. [25,42,43,35,44] For type II porous liquids where volatile solvents are generally involved, experimental methods of IR, NMR and gas evolution tests are utilised apart from simulation methods. CO_2 presents an IR adsorption band at 2335 cm^{-1}, thus IR is usually used to determine CO_2 solubility of samples by integration; While NMR signals of gases such as CH_4 (^1H NMR) often show different chemical shifts within a cage cavity and outside the cage, and gas solubility can be measured by integration of the peak corresponding to gases in the cage cavity. The gas evolution test is performed by saturating porous liquids with gases at first, then adding smaller guests such as chloroform to replace the gases, and at last measuring the volume of gases bubbled out. [30] Standard sorption instruments which normally measure gas uptakes of porous solids could be used for measuring gas solubilities in type I and III porous liquids, which usually have higher boiling points. [25,26,29,35,42–46]

1.3 Progress of porous liquids

1.3.1 Type I porous liquids

1.3.1.1 Pore generators and general construction methods

A type I porous liquid is a neat homogenous liquid which contains cavities at room temperature. Until now, one main method to prepare type I porous liquids is the functionalisation of existing porous solids to lower the melting temperature. Actually, a similar strategy of functionalising surface of nanoparticles with oligomers or polymers to prepare solvent-free nanofluids with liquid-like behaviours had already been studied in 2005, [47] which was before the conception of porous liquids was put forward. A thorough understanding of all kinds of existing porous solid materials is thus necessary for the design and construction of type I porous liquids. According to the published papers about type I porous liquids, brief introductions of related porous solids will be given at first.

1.3.1.1.1 Hollow materials

Hollow materials are a kind of micro-/nanostructures with vacant internal voids and shells, which can take a variety of shapes such as spheres, rods and fibres. [48,49] The shells could be composed of multiple materials, such as inorganic materials like carbon, silica (SiO_2), or titanium oxide; polymers, [50] COFs [51,52] and MOFs. [53–55] The choice of shell material can be based upon chemistry, structure controllability, and composition tunability. For example, inorganic materials are low-cost, biocompatible, and thermally stable, but can be sensitive toward acids/bases. On the other hand, MOFs could be more chemically stable and have a more tailored structure and constitution. [53] Hollow materials not only have porosity in the shells, but extra cavity in the centre. Take hollow microporous silica as an example, the microporosity refers to pores within the shell structure and the much larger internal voids dimensions are related to silica particle size and shell thickness. The introduced holes in the centre of hollow materials grant higher surface areas and lower density, and could be used in loading drugs and catalysts, guest adsorption and storage, or thermal insulators. [56–58] The main preparation method of hollow materials is based upon the template method developed by Caruso in 1998, which involved assembling silica or silica-polymer onto colloidal templates (polymer composites) and removing the colloids to afford corresponding hollow spheres. [59] Other templates could also be used. Take hollow silica spheres (**Figure 1.4**) as an example, micelles/emulsions, organisms (bacteria and viruses), and inorganic particles could all be used to prepare hollow silica.

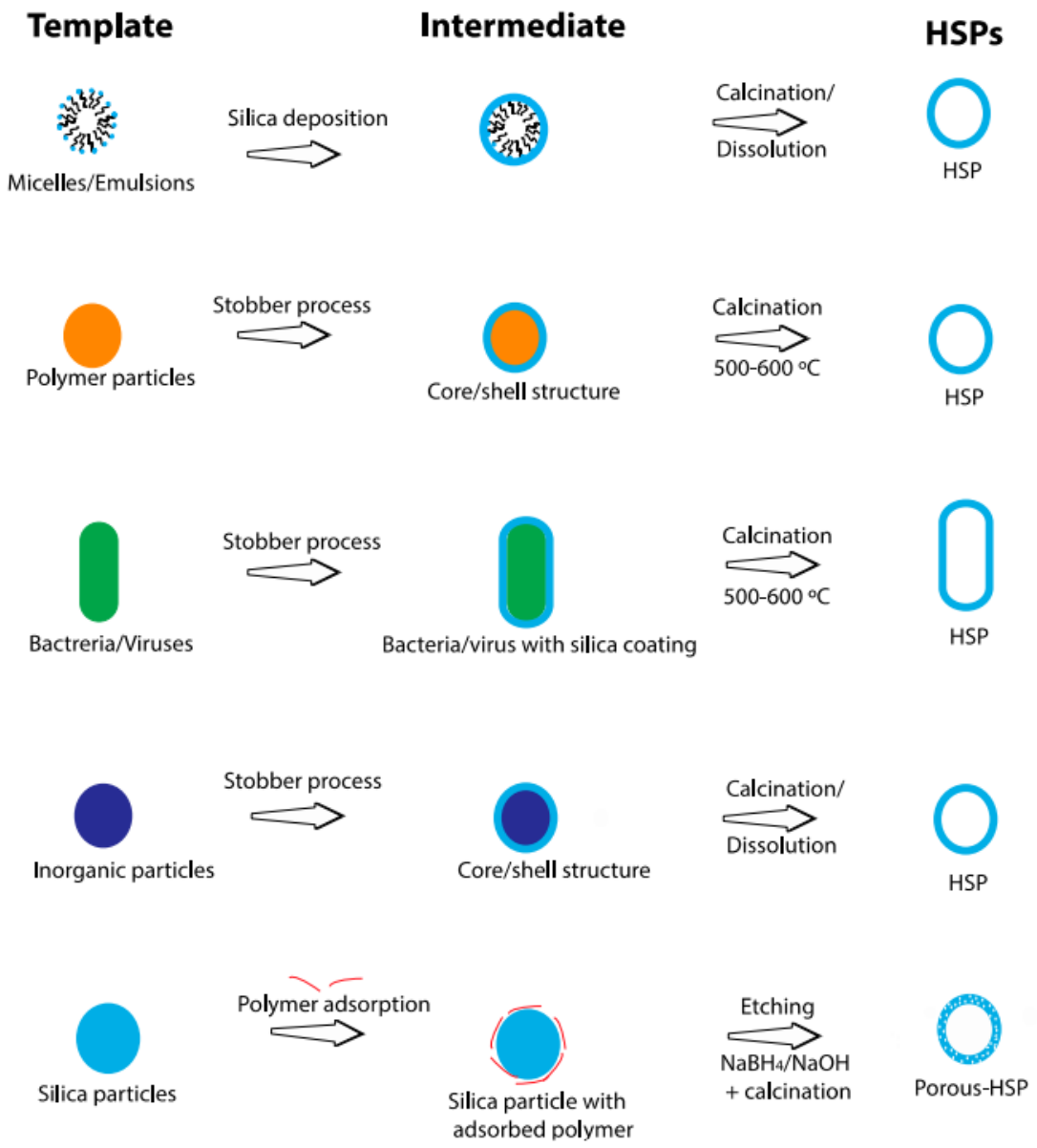

Figure 1.4: Schematic illustration of common strategies used for hollow silica particle synthesis. (Reproduced, [48] Open access)

In the published papers, hollow silica spheres, hollow silica rods and hollow carbon spheres have been studied and prepared to form type I porous liquids.[24,60–68] As silica has abundant hydroxyl groups which are easy to modify, and carbon network has strong π interactions, type I porous liquids were either constructed by surface functionalisation with organosilane on the surface of hollow silica, where the silica shell was usually microporous to prevent self-filling by the functionalised polymeric coronas or canopies; or by binding poly(ionic liquid)s onto the hollow carbon via the strong π -cation/ π -electronic/π-CH interactions. These grafted functional groups either already had an ionic end, or the end could be neutralised to form a salt. And then anion exchange with PEG salts could be performed to lower the melting points,

which on one hand was due to the introduced flexible chains that disturb the structure symmetry, and on the other hand, the delocalised charge on the bulky exchanged PEG ions lead to decreased coulomb interactions between cation and anion. The hollow void in the centre of each entity could function well as a storage place, thus other hollow materials like hollow polymers or MOFs should also possess good potentials in being fabricated to type I porous liquids. And due to their versatile chemistry, more diverse applications such as selectivity or sensing may also be realised in porous liquids.

1.3.1.1.2 Metal organic framework

Metal organic frameworks are a kind of organic-inorganic hybrid materials, where the organic linkers and inorganic metal ions form a framework with internal spaces and aperture windows whose sizes are dependent on the organic linker size. MOFs could date back to 1965 when E. A. Tomic published the paper describing using 1,5-dihydroxynaphthalene-2,6-dicarboxylic acid coordinated with Zn, Ni, Al and Fe ions, and pyromellitic acid with Th and U ions to form 'coordination polymers' and studied their thermal stability. [69] However, the real potential of this strategy of coordination polymer synthesis had not been discovered until the 1990s, when Omar Yaghi developed the method futher and prepared a family of highly porous, stable, crystalline coordinated materials which was coined by him as MOFs. This strategy Yaghi pioneered is widely known as reticular chemistry nowadays. [70–72] Reticular chemistry studies linking molecular building blocks (or linkers) with strong interactions to construct extended frameworks. As the distance among building blocks in the network structure formed could be maintained by the strong interactions, the linkers could be designed and manipulated to form highly porous materials. For MOFs, coordination bonds act as the strong interaction which stitches metal ions and organic linkers to form porous framework structures. The organic linkers in MOFs tend to have oxygen or nitrogen donors, such as polycarboxylates or imidazolates, which could be easily coordinated, [5,73] and the metal ions can direct linkers to form a variety of framework topologies, such as polyhedral, cluster, chains and layers. Owing to the various combination of the inorganic and organic units, over 90000 different MOFs have been fabricated and characterized. [74] Apart from that, the pore sizes, crystal shapes, and chemical compositions can be easily tuned by manipulating different metal ions or functional groups introduced onto the organic linkers, to prepare MOFs with versatile

properties, performances and applications, such as luminescence, magnetism, electrochemistry or catalytic activity (**Figure 1.5**). [75,76] Take MOF-5 as an example, by using different organic linkers with varied molecular length or functional groups, a serial of 12 derivative MOFs with the same cubic topology, but different internal void volumes, window sizes and functionalities could be fabricated. With nearly thirty years of development, MOFs have become one of the hottest fields in chemistry, [77] and are playing key roles in a wide range of applications including sorption, separation, storage, sensing, catalysis, electrochemistry and so on.

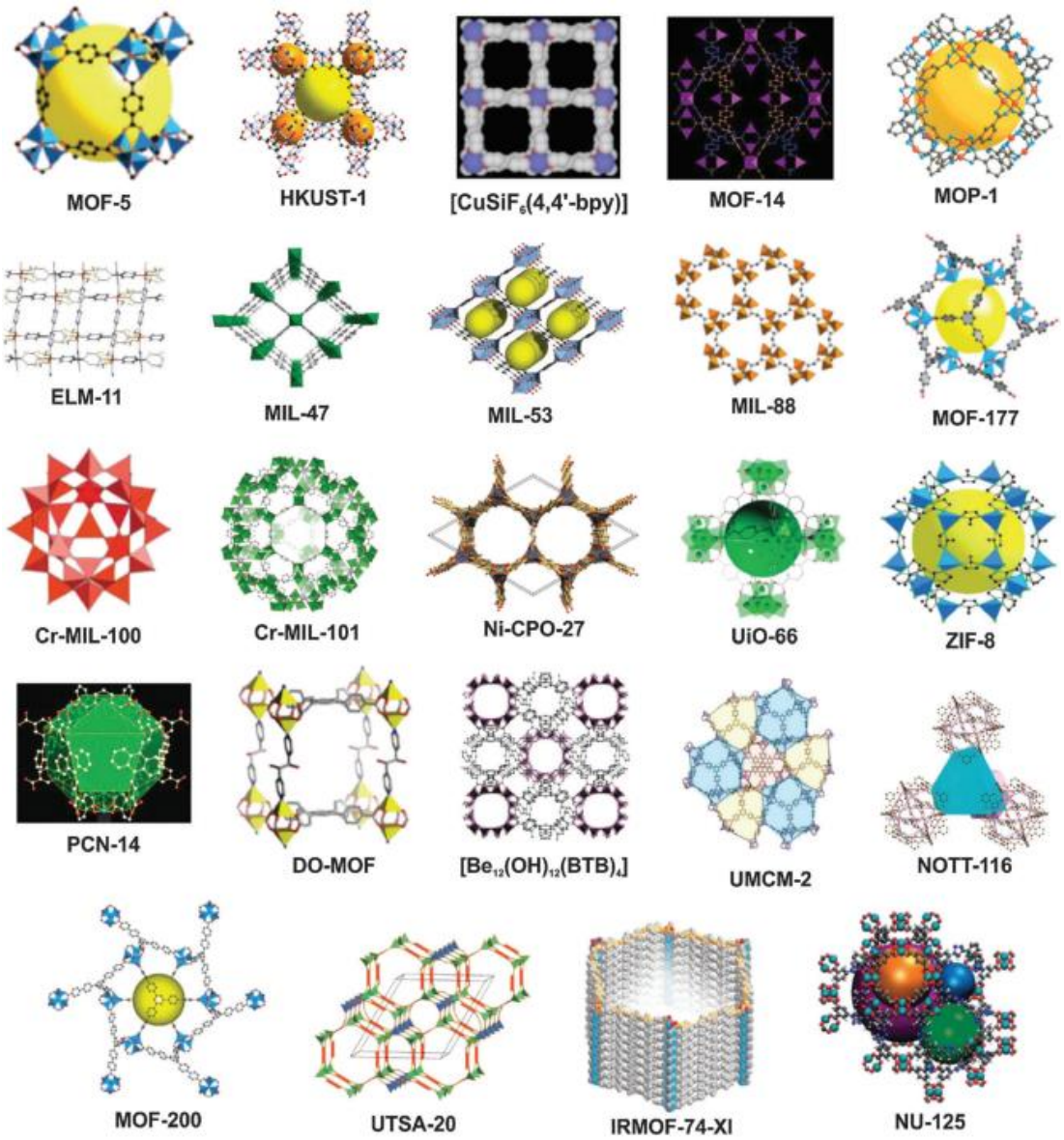

Figure 1.5: Porous MOFs prepared by several research groups aiming for the accommodation/retention of chemical species in their pores/channels. (Reproduced with permission, [75] Copyright 2015, RSC Pub)

An ideal MOF host for preparing a porous liquid should not only have large cavities, which ensure good capacity in applications such as sorption; but also small pore aperture window sizes, which avoid penetration by its own groups to remove porosity; and lastly enough functional groups for post-modification to be made into liquids. The versatile MOFs family indeed provides a variety of options to meet these structural requirements. Currently the published paper describing preparing type I porous liquids based upon MOFs also used the same strategy as that with hollow materials, which employed surface engineering with polymetric chains to disturb crystal symmetry and thus decrease the melting points. [45,78–80] Another strategy for preparing type I porous liquids based on MOFs is to seek porosity at higher temperatures, by screening stable MOFs while heating them into melted states and with potential porosity. [21]

1.3.1.1.3 Porous organic molecules

Unlike extended frameworks such as MOFs, porous organic molecules are discrete organic molecules, where their porosity is usually fabricated through crystallisation after the synthesis. [81] Apart from porous organic crystals, porous organic molecules also could form porous amorphous organic materials. The classification of intrinsic and extrinsic porosity mentioned earlier could be used to describe porosity in porous organic molecules quite well. A molecule with specific geometry or functional groups, such as hydrogen organic framework (HOF) molecules, tends to have inefficient packing which forms voids between molecules. If an array of voids among molecules could form an interconnected porosity network in the crystals after solvent removal, they are called porous organic crystals with extrinsic porosity. Intrinsic porosity refers to those molecules with internal cavities within their molecular structures, where the cavities could be accessible through apertures or windows in the structures. The ‘accessible’ here could be evaluated by the practically absorbed smallest hydrogen molecules, which have a kinetic diameter of 2.4 Å. If the aperture size is less than the kinetic hydrogen diameter, there is not any practical application in gas sorption for the molecule as it would fail to include hydrogen gas. Take calix[4]arene as an example, it is a cone-shaped macrocycle with a wide upper rim and a narrow lower rim, where the lower rim is generally considered too narrow to allow guests to pass through. Thus, the cavities within the molecular are generally isolated and could not transfer guests. Or for a cage molecule **CC1** (**Figure 1.6a**), these molecules tend to pack in a window-to-arene way where pore aperture of one molecule is blocked by the face of another

molecule and the cavities thus isolated. However, in some cases, these molecules can absorb guests through cooperative diffusion mechanisms, [82–85] and this porosity is termed as 0-D. Some molecules such as pillararenes or cyclodextrins, have upside and downside apertures with the same diameter, thus their internal voids could be aligned to form tube-like 1-D porosities. Or for a cage molecule **CC2** with a window-to-arene packing trend, it could pack into 1-D pore channels with the methyl group frustrating the crystal alignment (**Figure 1.6b**). [2] And the last group of molecules could pack to form a 3-D connected porous structure, such as **CC3** which packs in a window-to-window trend (**Figure 1.6c**). These porous organic molecules are good candidates for preparing type I and II porous liquids, due to their generally lower molecular weight and better solubility in solvents than other porous materials. And even poor solubility is encountered, type III porous liquids could also be an alternative. Structural requirements for porous organic molecules to be made into porous liquids usually include a rigid porous structure which could avoid collapsing and maintain cavities while in the liquid state, and small windows to prevent self-filling which may also remove porosity.

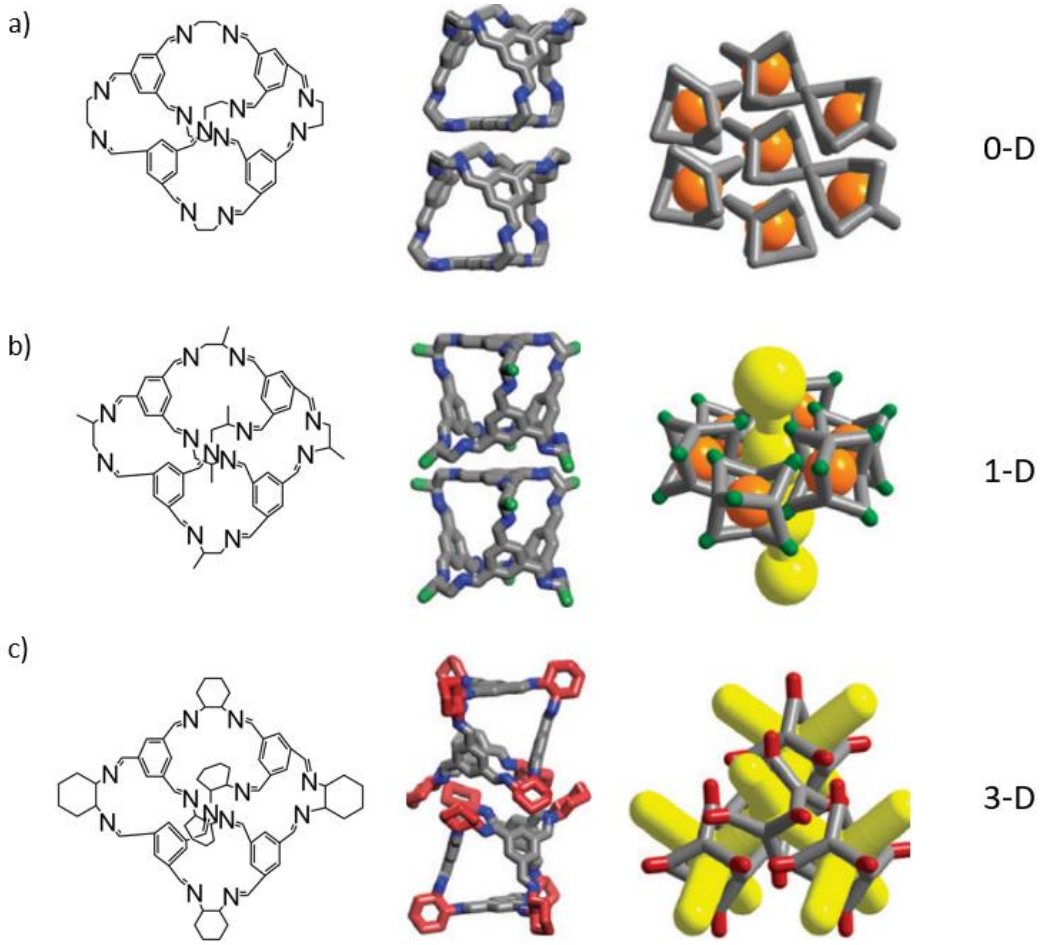

Figure 1.6: a) Molecular structure and crystal packing of **CC1**; b) Molecular structure and crystal packing of **CC2**; c) Molecular structure and crystal packing of **CC3**. (Reproduced with permission, [2] Copyright 2009, Nature Pub)

Compared with MOFs or inorganic hollow materials, porous molecules have generally smaller molecular weights, and their melting points tend to be lower. Methods of constructing type I porous liquids based on porous organic molecules include functionalisation with flexible alkyl chains to disturb the molecular symmetry which could decrease molecular melting points; [22,31] or introduction with ionic liquids moieties and then anion exchange to afford room-temperature porous organic liquids. [86]

1.3.1.1.4 Coordination cages and metal organic cages

Coordination cages are a kind of cage-like structures with internal voids, which are assembled by coordination bonding between pre-designed organic linkers and metal ions. [87] Unlike MOFs with an infinite and extended structure, coordination cages are discrete entities, thus usually having better solubility in common solvents. Another conceptually similar kind of material is metal organic cages, which can be confused

with coordination cages though scientifically they have a range of differences if clear terminology is considered. One main key feature that could distinguish the two is that coordination cages refer to those assembled from neutral linkers (such as pyridine), while metal organic cages are constructed by anionic linkers (such as carboxylates). Other differences between these two groups could be described from several parameters including counter anions, base additive, ligand structure, metal ions, reaction time, temperature, solvent, and geometry of cages (**Figure 1.7**). [87]

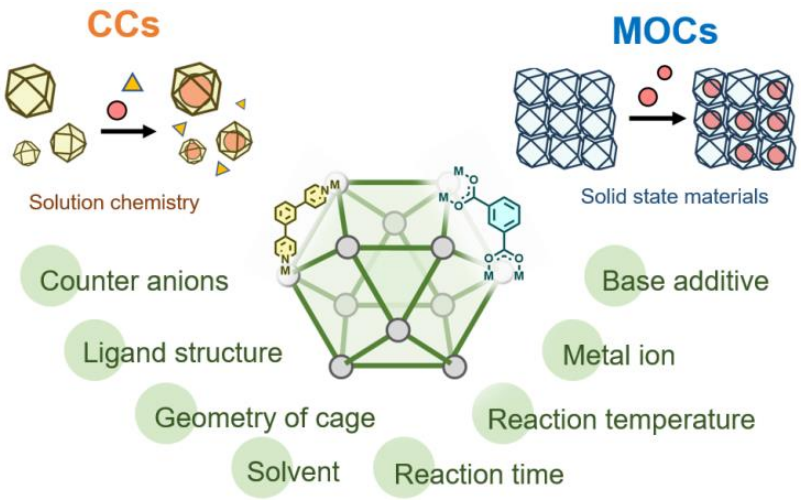

Figure 1.7: Meta-analysis of differences between coordination cage and metal organic cages in terms of structural and synthetic parameters. (Reproduced with permission, [87] Copyright 2022, Elsevier B.V.)

Coordination cages could have a variety of geometries (**Figure 1.8**), which provides a library for the selection of suitable structures for the construction of porous liquids. Due to the diversity of linkers' design, they could offer active sites for post-functionalisation. And due to the host-guest interaction of the coordination cage cavity, they are also termed as metal organic capsules with the capabilities of molecular recognition, chirality sensing, separations, stabilisation of reactive species, and catalysis. [88] Type I porous liquids based upon coordination cages take a similar strategy as mentioned above, by functionalising long chains to disturb cage symmetry and lower melting points. In the following section, the progress and realised examples of type I porous liquids will be discussed more in detail.

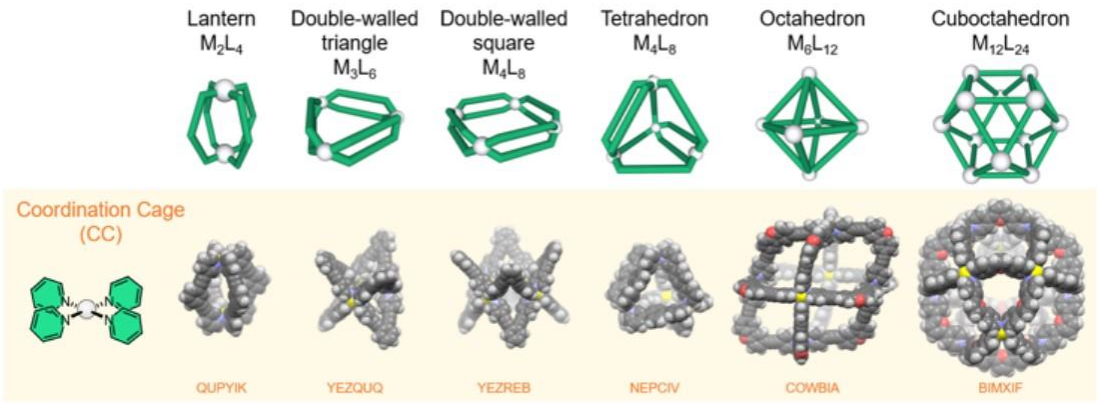

Figure 1.8: Schematic representation of coordination motifs of coordination cages (M represents metal ions; L represents linkers) and examples of corresponding coordination cage crystal structures with CSD reference codes appended below accordingly. (Reproduced with permission, [87] Copyright 2022, Elsevier B.V.)

1.3.1.2 Progress

1.3.1.2.1 Type I porous liquids based upon porous organic cages

The very first trial of synthesising type I porous liquid was attempted in 2012 by Giri *et al.*, using an approach that involved appending alkyl chains (5-8 carbons) to the vertexes of [4+6] imine-based cages to lower their melting points whilst maintaining the internal cavity within the rigid cage structure (**Figure 1.9**). [22] As the flexible alkyl chain used could point in different directions and disturb the cage symmetry, the intermolecular interaction could be easier to break for the molecules to flow. The melting point of one cage with alkyl chains containing eight carbons (**CC9**) was as low as around 50 °C. However, the cage did not present satisfying gas uptakes at the melted state, and it was supposed that the ends of alkyl chains tended to penetrate the internal void of the cage and remove the porosity [22]. Then an iso-hexyl chain was tethered to increase the bulkiness of the ends in the hope of avoiding penetration according to the paper. The corresponding cage (called **CC8**) can crystallise in a highly symmetrical cubic packing with a Brunauer–Emmett–Teller (BET) surface area 289 $m^2 g^{-1}$, but a high melting point of 198 °C. [22] Thus, a paradox occurred here where porosity and fluidity failed to be reconciled.

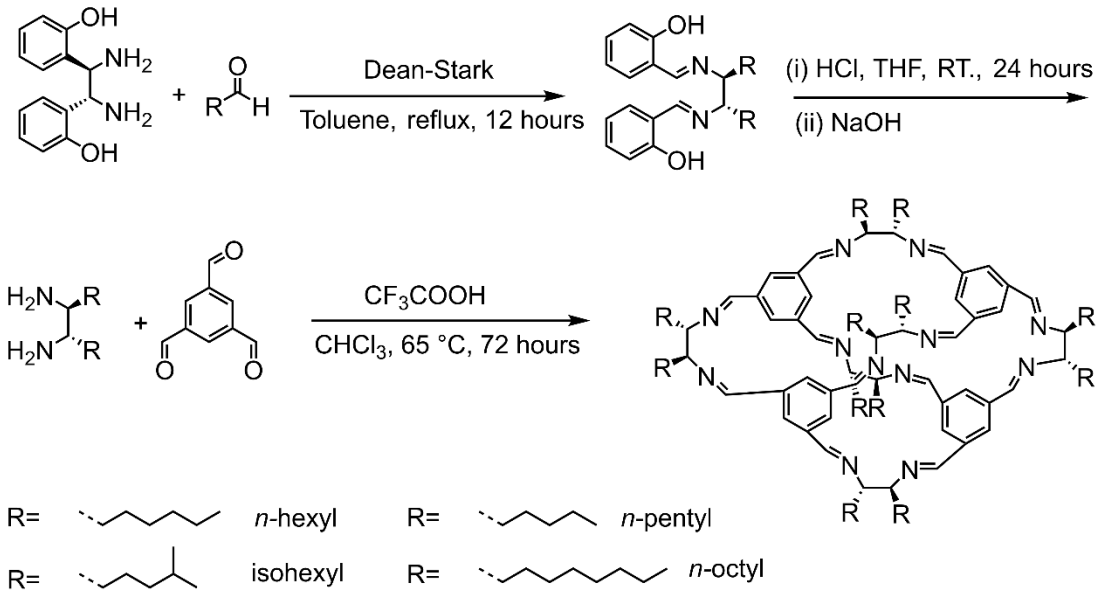

Figure 1.9: Scheme of synthesis of alkylated organic cages. (Reproduced with permission, [22] Copyright 2012, RSC Pub)

A further in-depth study in 2014 studied the similar serial of cages with even longer chains (12 to 22 carbons) and took advantage of modelling to study the porosity (**Figure 1.10a**). [31] According to experimental results, the cage with twelve n-dodecyl chains (n-C_{12}) had the melting a point of around 40 °C, while the one with t-tetradecyl chains (neo-C_{14}) had a slightly higher melting point of around 55 °C. Modelling results revealed that cages with shorter alkyl chains and bulky alky ends (neo-C_{14}) tended to remain empty and were more likely to accommodate guests such as methane. For example, the cage neo-C_{14} had 30% cage empty in the liquid state (**Figure 1.10b**). Though it was concluded in the paper that this porosity could not be comparable with solids, this strategy of disturbing molecular symmetry was successfully proved to be effective in lowering the melting of porous organic cages, and porosity could be maintained to some extent by using alky chains with bulky ends.

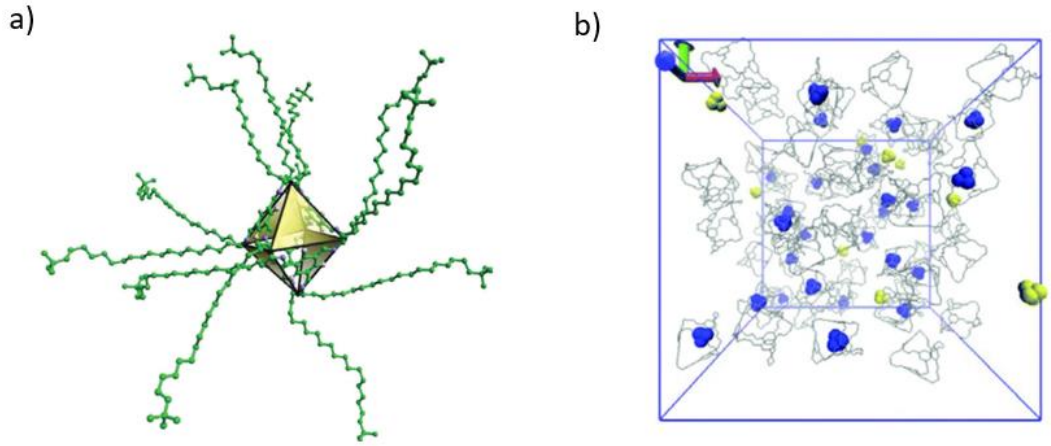

Figure 1.10: a) Representation of a cage molecule with 12 alkyl chains; [30] b) Snapshot of neo-C_{14} with methane molecules in a simulation box, where the yellow colour represents methane molecules outside the cage while blue colour the ones inside the cage. (Reproduced with permission, [31] Copyright 2014, RSC Pub)

Another strategy of liquification is to introduce ionic liquid moiety into porous organic molecules. W. Lin *et al.* successfully synthesised pillar[5]arene-based ionic liquids by the introduction of carboxylic groups (**Figure 1.11**) in 2019. [89] The viscosity of one of the ionic liquid [P_{66614}][DCP_5] was a bit high, which was 1885 mPa·s at 20 °C, however, the melting point could be lowered to room temperature. The CO_2 uptake of [P_{66614}][DCP_5] at 50 °C was 5.52 mol/mol at 1 bar, which roughly equalled 1.53 mmol/g if converted to more commonly used unit. This capacity is much larger compared to other type I porous liquids which usually present CO_2 uptakes at higher pressure, [90] and it was about 11.5 times that of the neutral analogue DCP5 (0.48 mol/mol), and around 9.5 times the ionic liquid monomer [P_{66614}][DC] (0.58 mol/mol). With quantum chemical calculations, NMR, and IR studies of the sorption, they concluded that the increased CO_2 uptake was on one hand due to strong interaction between CO_2 and the carboxylic anion, and on the other hand, the cavity within pillar[5]arene reinforced the CO_2 sorption by separating the carboxylic groups, adjusting to favourable structure conformer and distributing more negative charge on the binding sites.

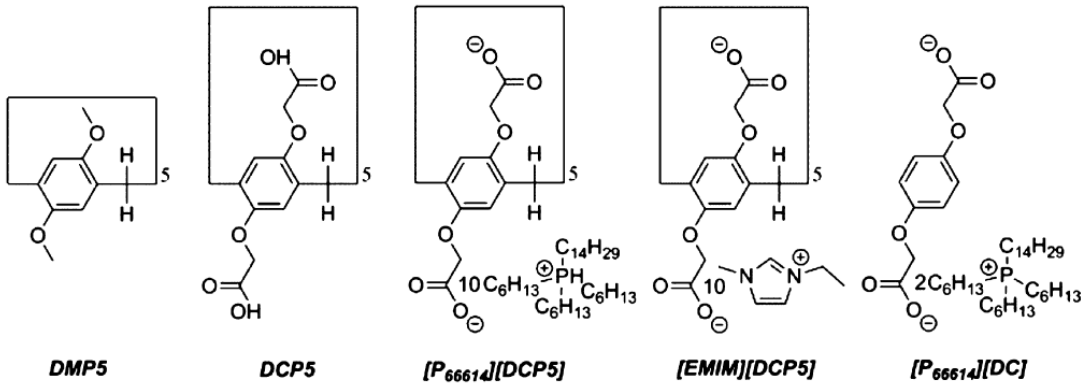

Figure 1.11: Structures of pillar[5]arene based ionic liquids. (Reproduced with permission, [89], Copyright 2019, ACS)

Another study by Sheng Dai's group also exploited the carboxylic group, where they introduced a potassium carboxylate group into a porous organic cage molecule (**Figure 1.12a**). [86] And the porous organic cage salt (KACC) synthesized was fabricated into porous liquids by mixing it with dicyclohexano-18-crown-6 (18-C-6) or 15-crown-5 (15-C-5), where the K^+ ion was complexed into the cavity of the crown via supramolecular interactions. [86] Both porous liquids fitted the definition of type II porous liquids judging by the ratio of solvents they used, which is 7:1 (15-C-5:KACC) for 15-C-5-PL and 3:1 (18-C-6:KACC) for 18-C-6-PL (**Figure 1.12b**). However, they claimed that 18-C-6-PL was a type I porous liquid because 18-C-6 was solid at RT and 18-C-6-PL only showed one melting peak in the DSC curve. [86] Though 18-C-6-PL appears more like a two-component eutectic system where the 18-C-6-KACC complex and remaining 18-C-6 share the same decreased melting point to this author, it is overall a good strategy and opens new routes to liquefication methods. The CO_2 uptakes of 15-C-5-PL and 18-C-6-PL were reported as 0.375 mmol/g and 0.429 mmol/g at 10 bar respectively, [86] which were not very high compared to the above pillar[5]arene based porous liquid. But they were much better than the nearly zero uptakes of 18-C-6 and 15-C-5, and molecular simulation was also performed in the paper which proved that the cavity of KACC remained empty in 15-C-5-PL and 18-C-6-PL. Yin *et al.* utilised density function theory calculations and molecular simulation to study these crown ether and cage complex systems further. And they concluded that the K^+ formed alkali metal complexes with crown ether through ion-dipole interactions, and CO_2 was absorbed through hydrogen bonding. [91]

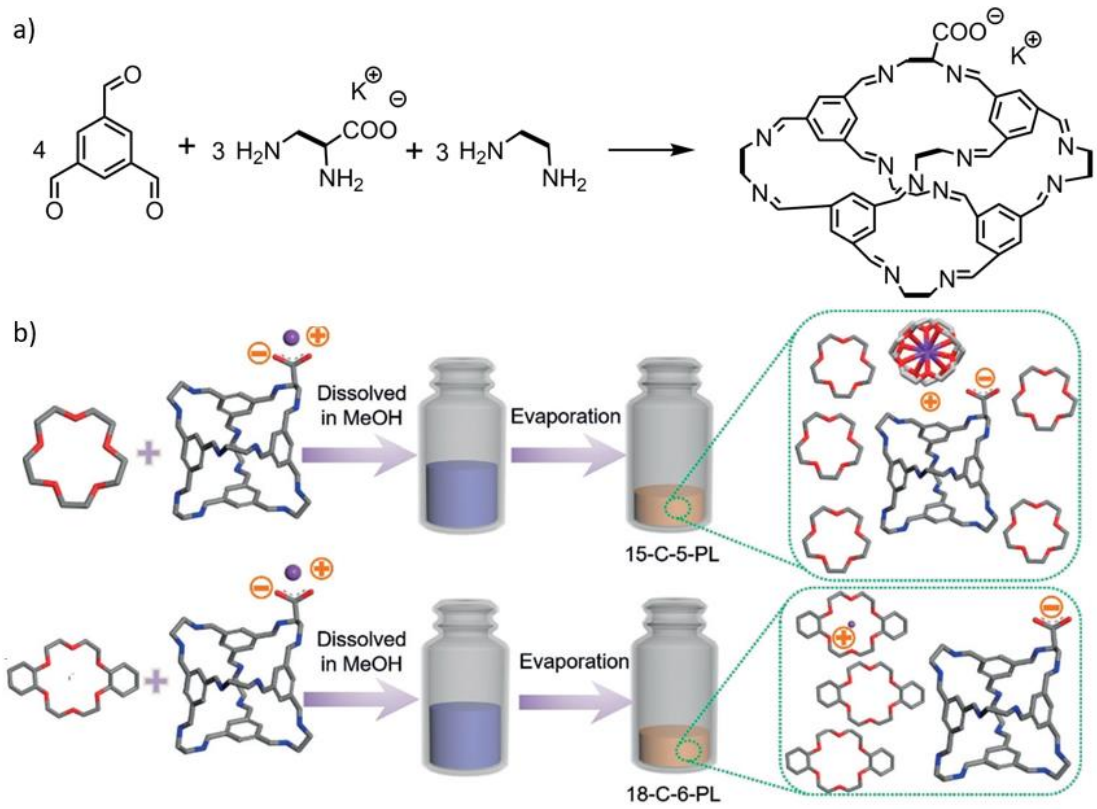

Figure 1.12: a) Synthesis scheme of KACC; b) Preparation scheme of 15-C-5-PL and 18-C-6-PL. (Reproduced with permission, [86] Copyright 2019, Wiley-VCH)

Wang *et al.* explored the construction of type I porous liquid from another porous organic molecule of cyclodextrin by functionalising it with imidazolium ionic liquid. [92] And instead of the gas sorption study, they exploited the specific host-guest interaction properties of the cyclodextrin cavity and used the cyclodextrin porous liquid in chiral separation. [92] Though instead of using the cyclodextrin porous liquid directly, they performed the separation experiment by introducing the aqueous solution into the system, and it turned out to be a reasonable strategy. By adding another organic solvent which was not miscible with water, the unbounded enantiomer could be extracted and thus separated.

1.3.1.2.2 Type I porous liquids based upon hollow inorganic materials

In 2015 Sheng Dai's group first applied the strategy of constructing solvent-free nanofluids in preparing a type I porous liquid (**Figure 1.13**). [24] The transparent liquid (HS-liquid) was fabricated by ionic organosilane attachments (corona) onto hollow silica nanospheres with an internal diameter of 14 nm, and then anion exchange with PEG glycol chains (canopy). [47] The glycol chains introduced in one way lowered the density of charge and decreased the electrical interactions with the corona cation, and

in another way introduce flexibility, thus the composite material had a melting point below room temperature. However, this method may produce HS-liquids which vary from batch to batch, as tethering each hydroxyl group may be hard to control and each hollow silica sphere may have different degrees of organosilane attachments. Thus, in the paper, thermogravimetric analysis was performed to calculate that an average of four corona–canopy chains covered per square nanometre of hollow sphere surface. The viscosity of the HS-liquid was a little high, which was determined as 6800 mPa·s and 4200 mPa·s at 40 and 50 °C respectively in the paper. As the pore size in the spheres of silica shell is about 1.9 nm which could restrict self-penetration by the tethered organosilane corona and the anions of glycol chains canopy, thus porosity could be maintained. [24] The material was used to prepare a supported liquid membrane, though the gas permeability and selectivity were considered to be moderately low. [24]

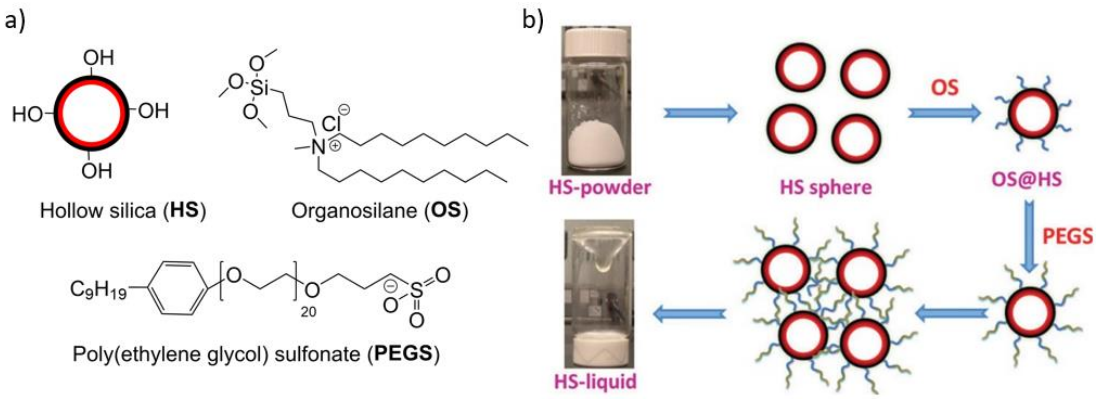

Figure 1.13: a) Chemicals used in the construction of type I porous liquids based upon hollow silica sphere; b) Construction process. (Reproduced with permission, [24] Copyright 2015, Wiley-VCH)

Type I porous liquids using hollow materials published later were mostly based upon this liquefication strategy. In 2017, hollow silica spheres with different sizes (9, 14 and 32 nm) were fabricated into transparent liquids using the same strategy by Shi *et al.*, but with slightly different reagents which included 3-(trihydroxysilyl)-1-propanesulfonic acid as the corona and poly (ethylene glycol) amine as the canopy. [60] And these liquids displayed lower viscosities which were 670, 470, and 250 mPa·s respectively compared to the HS-liquid. [24,60] They discovered that the larger diameter of the hollow silica spheres was, the better CO_2 adsorption capacity was, with the one whose diameter was 32 nm displaying CO_2 uptake of 2.18 mmol/g at 25 bar and 25 °C. [60] And they put forward a mechanism of CO_2 binding sites for the hollow silica-based

type I porous liquids, which included the internal voids in the hollow sphere, interspaces of organic chains and the Lewis acid-base pairing sites between oxygen in the PEG chain and CO_2 (**Figure 1.14**). [60] The interaction nature between CO_2 and hollow silica porous liquids was studied further using density functional theory by Zhang *et al.* in 2020, where they concluded that the strongest absorption sites were on the PEG chains by hydrogen bonding. [63] In 2021, Liu *et al.* systematically studied using hollow silica based porous liquids as fillers in preparing mixed matrix membrane for CO_2, where for one optimum membrane the permeability of CO_2 could reach 229.4 Barrer and CO_2/N_2 selectivity was 71.7, [68] which improved a lot compared to the material in Sheng Dai's 2015 paper. [24] The type I porous liquids prepared from hollow silica not only could absorb CO_2, but they may also be used to remove SO_2, according to a modelling prediction study by Yin *et al.* in 2020. [64] Their results showed that strong noncovalent interactions, such as hydrogen bonding and S (from SO_2) to O (from PEG chains) interactions, play important roles in the SO_2 absorption process. [64]

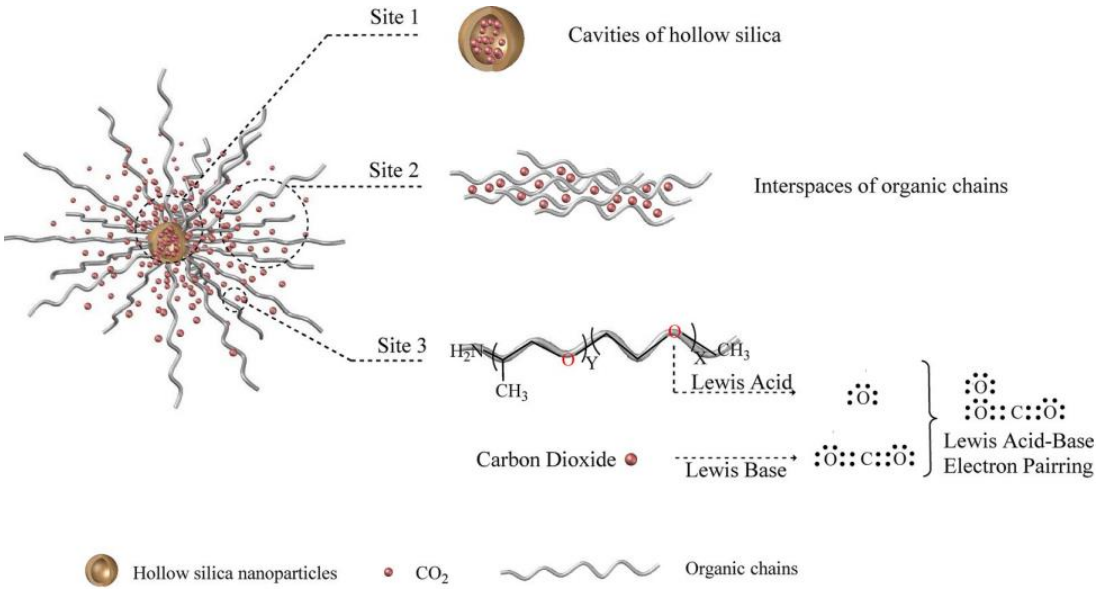

Figure 1.14: Scheme of CO_2 sorption mechanism of a hollow silica sphere based porous liquid. (Reproduced with permission, [60] Copyright 2018, Wiley-VCH)

The stability of hollow silica-based type I porous liquids was studied with molecular dynamic (MD) simulation by Sheng *et al.* in 2020. They deemed the liquid as a colloid comprised of silica spheres dispersed in their surface-functionalised corona and canopy groups, and held the point that the hollow silica nanospheres were prevented from aggregation by increased interface distance with both polymeric corona and

canopy chains grafted on the surface of silica spheres. [62] Another MD simulation by the same group studied the effect of pore size in the silica shell and different canopy structures. [93,94] where they concluded that the pore size in the shell should be small enough to avoid self-penetration by the tethered chains.

Apart from the hollow silica sphere, hollow materials with other shapes have also been studied to prepare porous liquids. Kumar *et al.* prepared hollow silica nanorods and used the same corona and canopy strategy to construct anisotropic porous liquids. [61] The nanorods synthesised had different aspect ratios (2.5, 8 and 11), and the liquid constructed from the nanorod with the largest aspect ratio presented a CO_2 uptake of 0.233 mmol/g at 0.03 bar and 20 °C, which were better than previously reported hollow silica sphere porous liquids. This improvement may be due to the increased internal voids of hollow nanorods, and anisotropic properties may arise in different directions due to the length ratio difference of the nanorods, such as rheology, though further details were not given. The same group published another paper in 2021, where they further explored the application of using porous liquid based on silica nanorods in storage and in situ catalytic conversion of CO_2 (**Figure 1.15**). [66] The hollow internal space was used to temporarily store CO_2, and the attached enzyme outside hollow silica rods converted CO_2 to HCO_3^- in situ, and at last ions of HCO_3^- were precipitated by pre-added Ca^+ to further push the reaction to completion. [66]

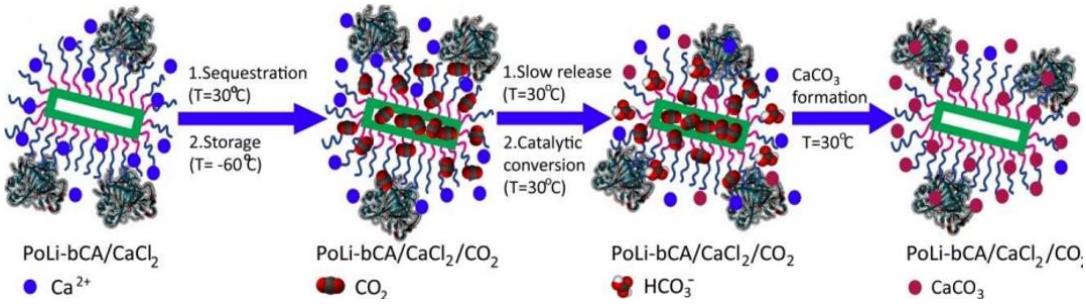

Figure 1.15: Diagram of CO_2 conversion by the type I porous liquid based on hollow nanorods and enzyme PoLi-bCA.(Reproduced with permission, [66] Copyright 2021, Wiley-VCH)

Another application study of hollow-silica-based type I porous liquids attempted encapsulation of metal nanoparticles and studied corresponding catalysis activities. [95–97] Metal nanostructures show remarkable catalytic performances due to their large surface area and rich active sites, [98] but the large surface area may lead to nanoparticle aggregation, irregular distribution and some other issues. Thus, stabilisers are usually used to facilitate the synthesis of metal nanoparticles, such as porous organic cages

which possess well-defined microporous cavities, [98] or porous inorganic materials. [99] Hemming *et al.* first studied the encapsulation of gold (Au), platinum (Pt) and palladium (Pd) in a hollow silica type I porous liquid in 2019. [95] The processes included the encapsulating metal in hollow silica spheres at first and then constructing porous liquid using the above-mentioned corona-canopy method, instead of encapsulating metal nanoparticles directly with porous liquids. These metal-loaded type I porous liquids were further applied in catalysis studies. [96] But unfortunately, these systems could be highly viscous and their catalytic capabilities of several reactions were not as good as the analogues, such as the metal loaded hollow silica spheres. [96] These studies in a way demonstrated that the incorporation of catalysts within the pores of porous liquids and using them in catalysis may not be a good option.

Hollow carbon spheres could also be fabricated to type I porous liquid, where the poly ionic liquid (IL) corona could be firmly bound onto the carbon shell surface through π-cation, π-electronic and π-CH interactions, and the anions were also exchanged into PEGS chains to introduce fluidity. As the poly ionic liquid groups attached to the hollow carbon surface were not affected by the step of anion exchange, it indicated that the interactions between poly ionic liquid and carbon surface were strong enough. The liquid (HCS-liquid) with poly(imidazolium)PEGS prepared by Sheng Dai's group in 2017 showed a CO_2 uptake of 0.568 mmol/g at 10 bar and 25 °C. [100] Su *et al.* prepared HCS liquid with different HCS sizes and poly ionic liquid cations, the best one of which showed a CO_2 uptake of 2.06 mmol/g at 25 °C and 30 bar. However, their viscosities were also high, which could reach 8900 mPa·s at 50 °C [67,90] P. Li *et al.* prepared a similar HCS-based structure, where they synthesized the poly(ionic liquid) with PEGS chains at first and then graft it onto the surface of HCS via π-cation interactions. However, they claimed it should be a type III porous liquid system as the HCS precipitated in a water dispersion when NaCl salt was added. [65] Still, the system was considered by the author to be more a type I system, as the interactions between HCS and poly(ionic liquids) were strong enough to stand the anion exchange step. And the precipitation that occurred in the H_2O+NaCl+HCS-liquid system was probably caused by the stronger π-cation interactions between HCS and NaCl in water, and the poly(ionic liquid) grafting may be replaced.

Another inorganic material zeolite without the hollow structure, which was a microporous aluminosilicate S-1 zeolite, was also explored for the construction of type I porous liquid. [35] It employed a surface sol-gel process (SSP) to increase the surface hydroxy groups on S-1 zeolite with titanium (IV) butoxide, and then used the organosilane-PEGS functionalisation method as well to liquefy zeolite. [35] The CO_2 uptake of the porous liquid S-1-liquid prepared was 0.474 wt% (roughly 0.1 mmol/g) at 1 bar, [35] which would have been higher if a hollow structure was present.

1.3.1.2.3 Type I porous liquids based upon MOFs

One strategy for preparing MOFs based on type I porous liquids is to seek porosity at higher temperatures. It was first observed by Bennett *et al.* in 2015 that ZIF-4, which was composed of zinc ions and imidazolate linkers (**Figure 1.16a**), could be melted and underwent a series of phase changes to form a low-density glass phase. [101] The series of phase changes included a liquid-liquid transition from a low-density liquid to a high-density liquid. [101] And the liquid state and its nature were studied in detail later by Gaillac *et al.* in 2017, [21] where ZIF-4 was heated until 865 K and the process was characterized by neutron and X-ray total scattering experiments and modelling. It was proved in the paper that the coordination network and porosity of ZIF-4 were retained in the liquid phase. Both above papers mentioned attempts to study the melting behaviour of ZIF-8, which was composed of Zn^{2+} and methyl imidazolates, and had a higher surface area compared to ZIF-4. However, ZIF-8 decomposed before melting due to the instability of linkers, and its melting point was predicted to be over 1,250 K by a simulation study. [21] Nozari *et al.* developed a method to facilitate the melting of ZIF-8 by incorporation of an ionic liquid of 1-ethyl-3- methylimidazolium bis(trifluoromethylsulfonyl)imide ([EMIM][TFSI]). [102] The IL-ZIF-8 composite melted at 381 ºC before degradation (410 ºC), which was ascribed to the introduced electrostatic interactions from [EMIM][TFSI] stabilise the rapidly dissociating linkers in ZIF-8 upon heating. [102] Studies of melting of MOFs are currently more focused on melting and quenching to form glass, whereas the melted MOFs have yet to be studied more.

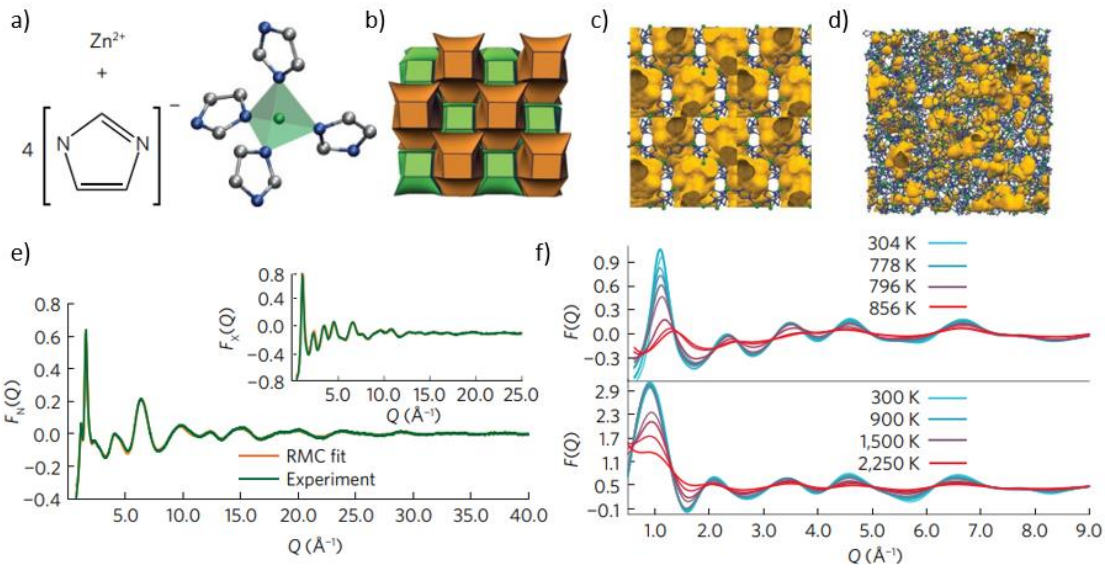

Figure 1.16: a) ZIF-4 composition; b) ZIF-4 topology; c) Crystal structure of ZIF-4; d) Atomic configuration of the melted-quench glass of ZIF-4; e) Experimental neutron structure factor F(Q) data and the fit from the configuration shown in d) (Inset: X-ray data and fit); f) Experimental glass (top) and computational (bottom) ZIF-4 X-ray structure factors upon heating. (Reproduced with permission, [21] Copyright 2017, Nature Pub)

Another strategy in preparing type I porous liquids from MOFs was like the one that was used to liquefy hollow inorganic solids, which also included surface modification with flexible chains and anion exchange with larger groups. Zhao *et al.* performed surface modification to Uio-66, which was a MOF constituted from zirconium ion Zr^{4+} and 1,4-benzenedicarboxylic acid (H_2BDC) in 2020. [45] They functionalised the hydroxyl group in the H_2BDC with organosilanes and changed anions to PEGS to form a transparent MOF-based type I porous liquid (**Figure 1.17**), which showed a CO_2 uptake of 0.636 mmol/g at 25 °C and 10 bar. [45]

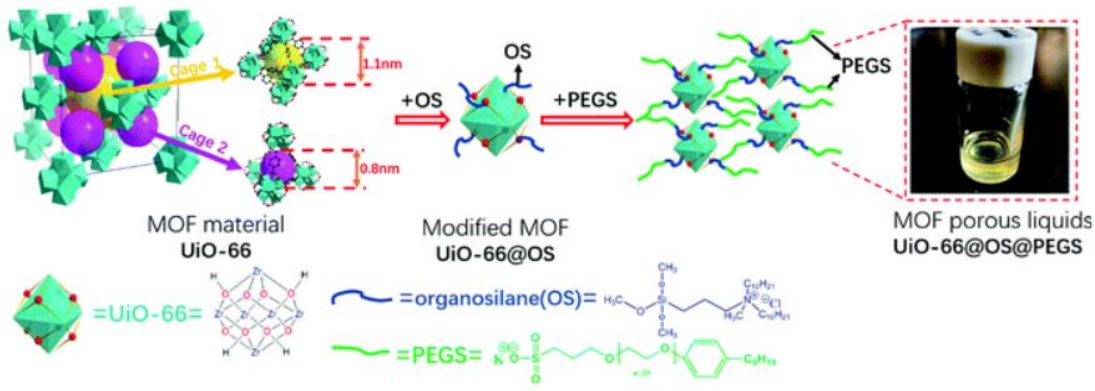

Figure 1.17: Schemic of Uio-66 porous liquids fabrication. (Reproduced with permission, [45] Copyright 2020, RSC Pub)

D. Wang *et al.* used a derivative of Uio-66 which was prepared from 2-hydroxyterephthalic acids and Zr^{+}, called Uio-66-OH (**Figure 1.18**). Uio-66-OH

was post-functionalised with the organosilane 3-(trihydroxysilyl)-1- propanesulfonic acid which worked as coronas and then paired with different polyether amine lengths (M1000, Eth, M2070) canopies to construct several opaque porous liquids. [78] Among them, the as-prepared Uio-66-liquid-M1000, UiO-66-liquid-Eth and Uio-66-liquid-M2070 had CO_2 uptakes of 1.95, 3.53 and 2.68 mmol/g at 25 °C and 10 bar respectively. [78] The same group used a similar strategy to functionalise Uio-66-OH with some oligomer species synthesized from polyether amine and organosilane, and the liquids formed had CO_2 uptakes ranging from 0.0581 to 0.276 mmol/g at RT and 10 bar. [79]

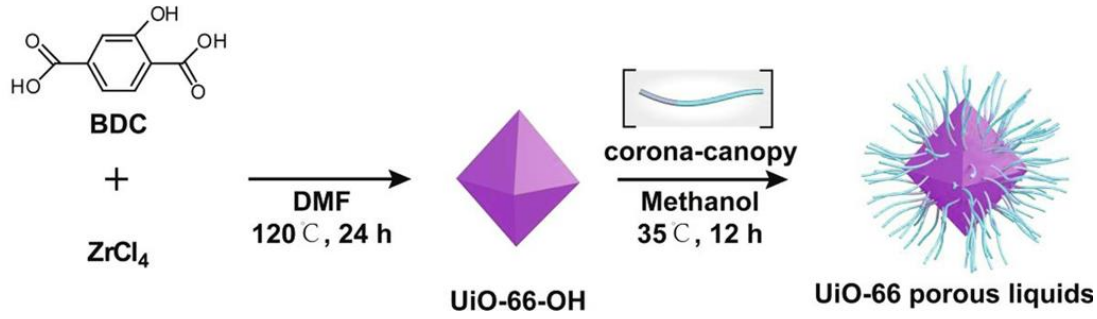

Figure 1.18: Schemic of Uio-66 porous liquids fabrication. (Reproduced with permission, [78] Copyright 2020, Elsevier B. V.)

D. Wang *et al.* also developed methods to construct ZIF-8 based type I porous liquids. The first strategy performed ligand exchange with 3-amino-1,2,4-triazole (Atz), which was NH_2 functionalised, to synthesise modified ZIF-8-NH_2. [103] And by controlling the ratio of added diglycidyl ether-terminated poly (dimethylsiloxane) (PDMS) to ZIF-8-NH_2 (10:1-2.5:1), where epoxy groups of PDMS reacted with amine groups from ZIF-8-NH_2, the resulting porous liquids had much decreased viscosities ranging from 133.4 to 238.9 mpa·s. [104] Corresponding CO_2 uptakes increased from 0.1061 to 0.1931mmol/g at 25 °C and 1 bar with increasing ZIF-8-NH_2 content. [104] This method indicated that by increasing the content of tethered flexible chains, the resulting liquids may have decreased viscosities; however, at the same time the relatively decreased porosity would lead to lower gas uptakes. Another strategy also takes advantage of a similar idea, which employed a higher ratio of flexible groups to decrease viscosities. Branched polyethyleneimine (BPEI) functionalised ZIF-8 was synthesized in two methods, where BPEI replaced water molecule and coordinated to Zn^+, and further used PDMS with different molecular weights to tether with BPEI. The porous liquids prepared with 5% content of ZIF-8 core could present viscosity value as low as 49

mPa·s, however its CO_2 uptake was also low, which was 0.0475 mmol/g at 25 °C and 1 bar. [105]

Another Uio-66 based type I porous liquid constructed from an imidazolium ionic liquid functionalised MOF Deim-Uio-66, which was formed by coordination between Zr^{4+} ion and a modified ligand 2-[(3-decyl-imidazol-1-yl) chloride]-terephthalic acid (Deim-H_2BDC) (**Figure 1.19**). [80] Anion exchange was then performed on Deim-Uio-66 with a PEG ion to receive the porous liquid Im-Uio-PL, which showed a CO_2 uptake of 5.93 mmol/g at 25 °C and 9 bar. [80] And they explored the catalytic performance of Im-UiO-PL in cyclocarbonate synthesis in an autoclave under a CO_2 atmosphere at 20 bar. Im-UiO-PL showed the highest yield of 79.6%, while PEGS, Deim-Uio-66 and a mixture of both had yields of 20.9%, 19.7% and 25.9% respectively. [80]

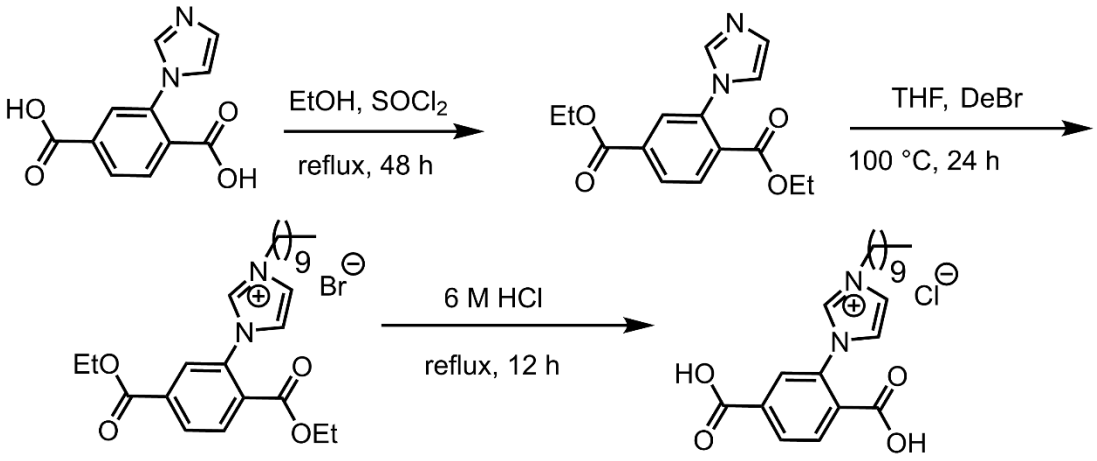

Figure 1.19: Schemic of Deim-H_2BDC synthesis. (Reproduced with permission, [80] Copyright 2021, Wiley-VCH)

1.3.1.2.4 Type I porous liquids based upon a coordination cage

Ma *et al.* prepared the first type I porous liquid based upon coordination cage in 2019, [28] where they synthesised an imidazolium ionic liquid tethered PEG_{1000} benzylamine **B**, and assembled it with a trialdehyde **A** and $Zn(NTf_2)$ to form a tetrahedral cage **2** (**Figure 1.20**). Cage **2** was a brownish opaque liquid at room temperature, which was quite viscous but still flowable. Unfortunately, gas sorption uptake was not reported shown in the paper, but cage **2** was demonstrated to have good size and shape selectivity among a range of different propanol and butanol isomers, and could take up three gaseous chlorofluorocarbon guests (trichlorofluoromethane,

dichlorodifluoromethane and chlorotrifluoromethane). [28] This actually is a good example that opens up other applications for porous liquids.

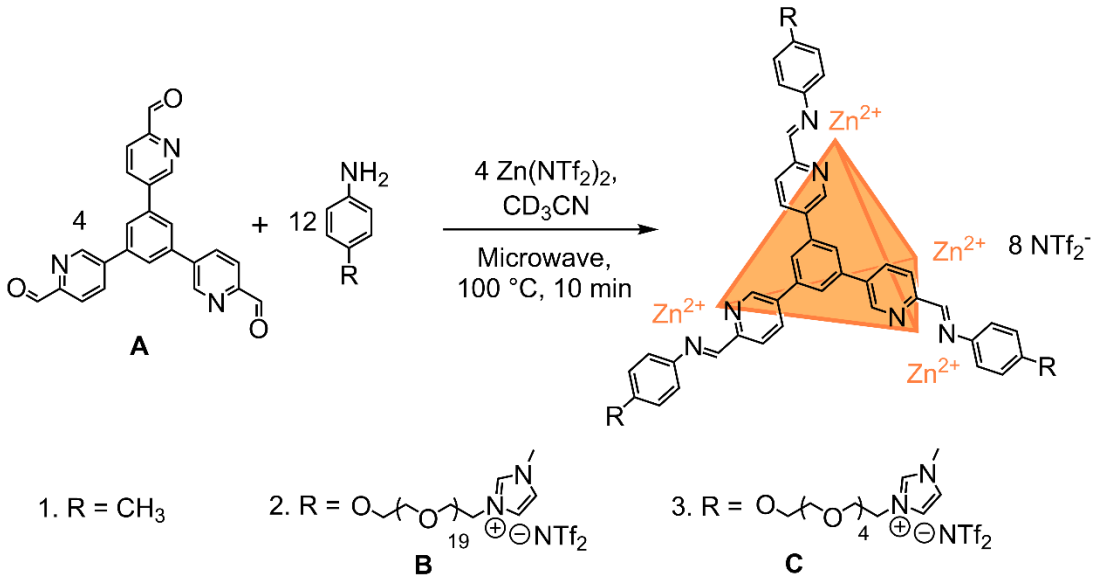

Figure 1.20: Synthesis scheme of coordination cage based porous liquid Cage **2**. (Reproduced with permission, [28], Copyright 2020, Springer Nature Limited)

1.3.1.3 Summary

Though it does not really matter as to a clear-cut classification of one certain liquid material into an absolute type of porous liquid, strong interactions such as covalent bonding, coordination bonding or ion-ion electrical interaction should exist for a complexly constructed material to be a type I porous liquid. For the existing type I porous liquids, one main issue is that the absolute gas sorption uptakes are low, though they display improved gas uptakes to indicate their potential porosity. N_2 uptakes are generally not mentioned, and CO_2 uptakes are not high enough to compete with porous solids either. This is probably caused by the diluted porosity concentration by the larger molecular weight of functionalised groups, for example, the corona-canopy strategy which is used for hollow inorganic materials or MOFs usually employs PEGs whose molecular weight usually overpasses 1000. According to the definitions, type I porous liquids should have better sorption performance compared to type II and III, as the other two are diluted after mixing with flowable media. However, the porosity concentration of type I was also lowered based on the construction method explored so far, thus new construction methods need to be explored. High viscosity is another issue for porous liquids, which is not favourable for them to flow easily, but it may help bind the gas molecules strongly at higher temperatures.

1.3.2 Type II porous liquids

1.3.2.1 Pore generators

Type II porous liquids are two-component materials constructed from dissolving porous solids in size-excluded solvents. In the total published papers related to porous liquids, type II porous liquids systems still constitute a small portion, which was due to the requirement of good solubility of porous solids in the flowing media. Until now, most of the realised type II porous liquids used porous organic molecules as pore carriers, as these materials are known for their solution-processibility feature. [2] The strategy of using metal organic cage (MOC) to prepare type II porous liquids has also been developed recently. [105,106] MOCs resemble MOF, but they are distinct discrete complexes with monodispersed size, structure and molecular weight, [107] thus having better solubility in solvents. Apart from solubility, the ideal porous hosts should also have large internal voids which don't contain any molecules and at the same time, a small window size to prevent solvents from entering the cavity of the host molecule.

1.3.2.2 Solvent selection

Basic considerations of solvent selection for any use would involve low-cost, low toxicity and no damage to the chemical and phase structures of other components. [33] But initially for the purpose of realising constructing a system like type II porous liquids, good solubility, size-exclusion and stability are considered at first. Thus, HCP which is an irritant chemical was also used as a solvent in preparing type II porous liquids. [23,30,41]

The initial screening of solvents with good solubility and size-exclusion for pore carriers is done manually by experiments, which could be both time and labour-consuming. In 2020, Kearsley *et al.* reported the method of using a high-throughput automation system to screen among all possible solvent candidates for dissolving scrambled cage systems, which produced a library of solubility data with ease. [34] Chang *et al.* further improved the solvent selection approach in 2022, where they used computational methods to establish a machine learning model with COSMO-RS calculations and predictions of solvent pKa for solubility simulations. The model was based upon preliminary experimental solubility test results for a porous organic cage

CC13, and then used to screen computationally among 11,000 compounds, which saved both labour and time. [39]

1.3.2.3 Progress

The first two type II porous liquids were reported in 2015, where Giri *et al.* developed two strategies to increase the solubility of porous organic cage hosts in the bulky solvents whilst also maintaining the internal cavities of cages. [23] One strategy was to functionalise the cage vertexes with groups like the solvent molecules. A crown ether tethered imine cage with the topology of T_4D_6 was synthesised from triformaldehyde and crown ether functionalised diamine (**Figure 1.21**). [23] And the crown ether cage could be dissolved in the size-excluded 15-crown-15 at high concentration (44 wt%), with a viscosity over 140 mPa·s at 25 °C. [23] The porosity within the liquid was confirmed by MD, PALS and methane solubility, where methane uptake of the porous liquid was 52 μmol/g at 30 °C and 1 atm, roughly 8 times more soluble than that of the pure 15-crown-5 solvent (6.7 μmol/g). [108] Zhang *et al.* further utilised molecular simulation to study the thermodynamics and kinetics of gas storage in this crown-ether cage in 2016. [109] It was found that gas affinity followed the order $CH_4 > CO_2 > N_2$, and binding sites were different for different gases, where for example, CH_4 molecules favoured both the cage core and regions outside. [109] In 2020, Yin *et al.* used molecular dynamics simulations to study the CO_2 selectivity of the crown-ether cage in binary gas mixtures CO_2/N_2 and CO_2/CH_4. [110] They came to similar results, where for the bulky phase, diffusion of gas molecules followed the order of $CO_2 > N_2$ and $CH_4 > CO_2$ in the mixture of CO_2/N_2 and CO_2/CH_4, respectively; And at the interface, N_2 diffused faster than CO_2 while CH_4 remained faster than CO_2. The sorbent selection parameters could reach ~120.9 and ~32.0 in the mixture CO_2/N_2 and CO_2/CH_4 respectively. [110]

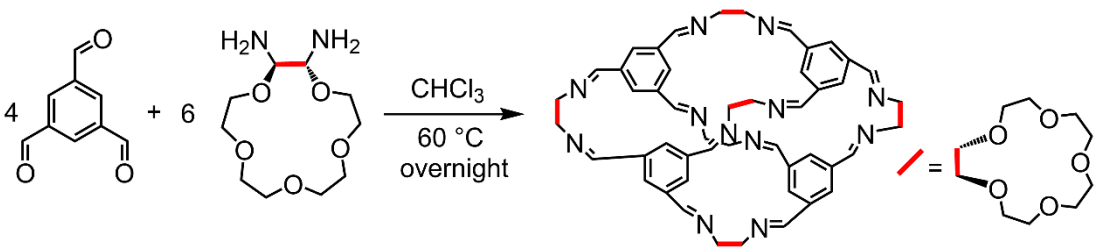

Figure 1.21: Scheme of crown-ether cage synthesis. (Reproduced with permission, [23], Copyright 2015, Nature Pub)

As the synthesis of the crown-ether cage involved explosive and dangerous chemicals, and the yield was too modest, another strategy in the 2015 paper explored applying scrambled cage **$T^4:3^3:13^3$** in preparing type II porous liquids, where the same ratio of diamines mixture of (R, R)-1,2-cyclohexanediamin (for **CC3** synthesis [2]) and 1,2-diamino-2-methylpropane (for **CC13** synthesis [111]) were used in forming cages (**Figure 1.22**). Due to the broken symmetry of the resulting cage molecule and a distribution of cage compositions, the solubility of scrambled cages was largely improved, where it could be dissolved in one size-excluded solvent of HCP at the concentration of over 10 wt% (0.112mmol of scrambled cage per gram of HCP). [23] This scrambled cage porous liquid showed a CH_4 solubility of 51 μmol/g, which was nearly 8 times that of the blank HCP solvent (6.7 μmol/g) at 293 K and 1 atm. And its viscosity (11.7 mPa·s at 295K) was decreased about 10 times compared to the crown ether porous liquid. [108]

The scrambled cage based porous liquids were further explored by Greenaway *et al.* in 2017, where new scrambled cages were synthesised by using combinations of dimethyldiamine and other diamines at different ratios. 25 scrambled cages were screened among six different solvents for targeting possible new type II porous liquids systems, where it was still **$T^4:3^3:13^3$** in HCP that turned out to be the best system with the highest solubility. [30] This **$T^4:3^3:13^3$** scrambled cage porous liquid system was studied in detail about its properties of gas uptakes (N_2, CO_2, CH_4, Xe and SF_6), chiral selectivity, gas retention and so on. [30] Kearsley *et al.* expanded the library of the scrambled cages further and screened more bulky solvents with the aid of a high throughput system, identifying 29 cage-solvent combinations which sped up the discovery of type II porous liquids in the cage system and provided initial data for machine learning. [38]

The scrambled cage porous liquid of **$T^4:3^3:13^3$** in HCP was further studied by two molecular simulation papers. One by Yin *et al.* studied the interaction of CO_2 with the only scrambled cage, showing that CO_2 preferred to locating at the window of the cage through π–π interaction, and its optimal CO_2 absorption capacity was 4 equivalences for one cage. [112] And the other one by Atilhan *et al.* proved that HCP did not enter the cavities of **$T^4:3^3:13^3$** in the porous liquid, and CO_2 could be stabilised by the cage cavity confinement and interaction with the cage external surfaces. The CO_2

maintained a dynamic movement of entering and leaving cage cavities, occupying half of the cage cavities. [113]

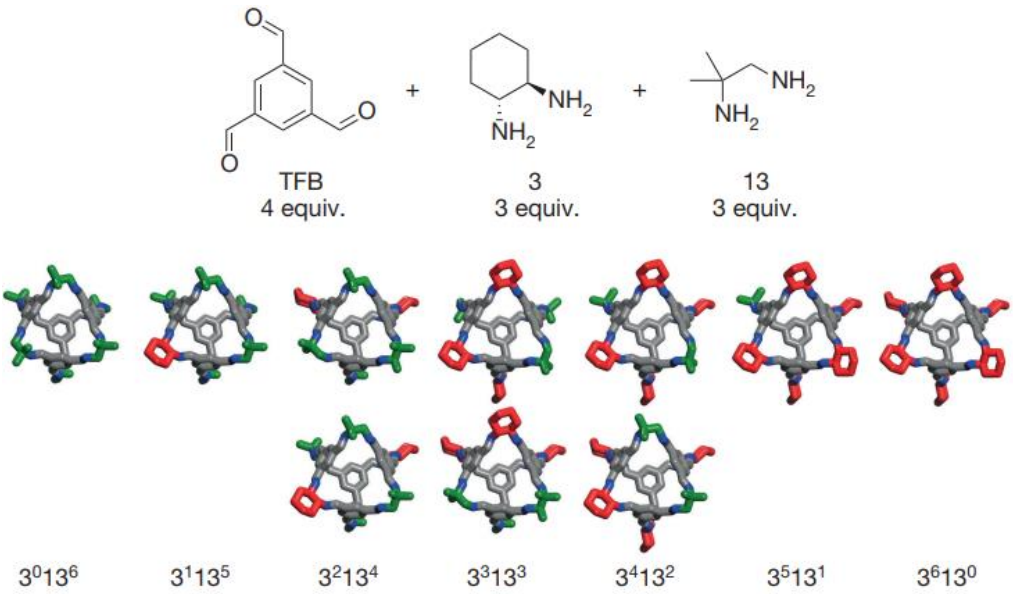

Figure 1.22: Scheme of scrambled cage $\mathbf{T^4{:}3^3{:}13^3}$ synthesis. (Reproduced with permission, [23], Copyright 2015, Nature Pub)

Egleston *et al.* reported the first type II porous liquids with gas selectivity, which was prepared by dissolving an imine cage **CC15**-*R* in HCP with the maximum solubility of < 15.6 mg/mL$_{HCP}$. [41] **CC15**-*R* was an [4+6] imine cage synthesised from triacetylbenzene and (R, R)-1,2-cyclohexanediamine, which was similar to **CC3**-*R* molecular geometry but had smaller window sizes (1.7 Å vs. 4.0 Å respectively). [41] **CC15**-*R* solids had a Xe uptake of 1.283 mmol/g$_{PL}$ while the uptake of the **CC15**-*R* porous liquid in HCP was largely reduced to 4.3 μmol/g$_{PL}$. The reason for the reduction was that Xe preferred to occupy extrinsic pores of solid **CC15**-*R*, while **CC15** molecules in the HCP solution were separated by solvent and lost the extrinsic porosity. [41] Another type II porous liquid system based on porous organic cages was the carboxylic group tethered cage KACC, which has been introduced above in the **1.3.1.2.1** section.

In 2020, Deng *et al.* prepared a type II porous liquid based upon metal organic cage MOP-18, which was assembled from 5-dodecoxybenzene-1,3-dicarboxylic acid and Cu^{2+}. MOP-18 had an inner cavity of 13.8 Å diameter, which is accessible through eight triangular (3.8 Å) and six square windows (6.6 Å). [106] It could be dissolved in 15-crown-5 and formed a stable 5 wt.% solution with a low viscosity of 22.5 mPa·s. By MD simulation, 15-crown-5 was proved to stay outside the MOP-18 cavity, and

the PLs-5 wt.% displayed CO_2 solubility of 6.9 mg/g, which was 17% higher than that of blank 15-crown-5 (5.9 mg/g). [106] A GO-supported PLs membrane was further fabricated, and the PLs-5wt%/GO membrane presented a three-fold CO_2 increase in permeance than that of the 15-crown-5/GO membrane at 60 °C, while the permeance of H_2 and N_2 increased by 4.0 and 2.7 times, respectively. [106]

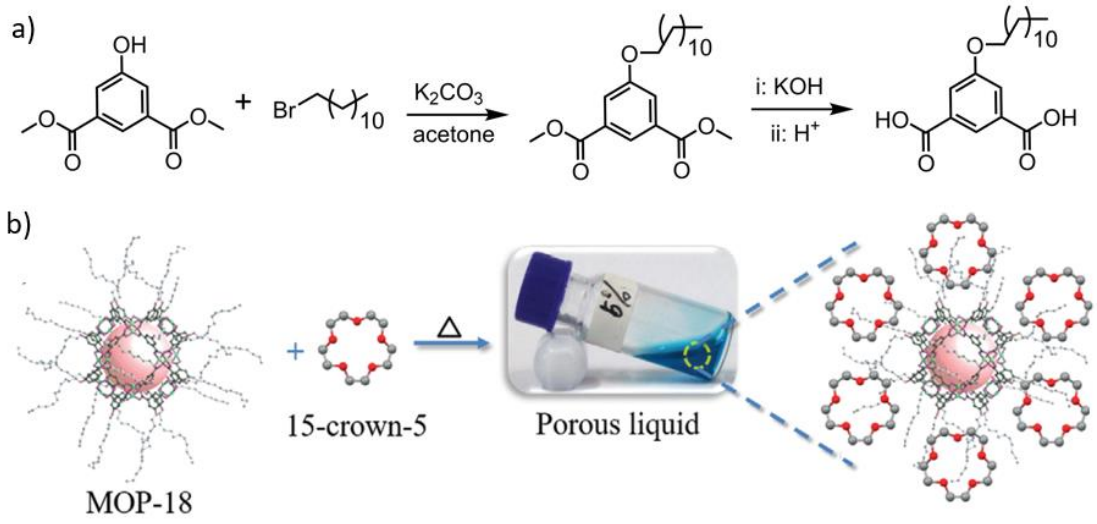

Figure 1.23: a) Scheme of 5-dodecoxybenzene-1,3-dicarboxylic acid synthesis; b) Type II porous liquid formation from MOP-18 and 15-crown-5. (Reproduced with permission, [106] Copyright 2020, Wiley-VCH)

Another type II porous liquid based on a metal organic cage was reported in 2022, [114] where Zhang *et al.* prepared a doughnut-like metal organic cage HD assembled from 5-bromo-1,3-benzenedicarboxylatic acid and vanadium ion V^{3+}, which could be fabricated into a solution in trihexyltetradecylphosphonium chloride (THAP_Cl) in a molar ratio of 1:24. The viscosity of the HD/THTP_Cl solution was 700 mPa·s at 25 °C, and the gravimetric CH_4 uptakes (25 °C, 65 bar) of HD/ THTP_Cl and the blank solvent THTP_Cl were determined as 0.28 and 0.18 mmol/g respectively. [114]

Alexander *et al.* prepared a type II porous liquid using Noria which was a rigid cyclic oligomer composed of resorcinol. [115] Noria was modified to a partially ethylated derivative Noria-OEt, which could be dissolved in 15-crown-5 to with a concentration of up to 80 mg/mL. This solution exhibited a CH_4 uptake of 0.21 mg/g, which was improved compared to that of 15-crown-5 (0.13 mg/g). MD simulation was also employed in the paper to further support the existence of porosity in the liquid and showed that CH_4 occupation within the Noria-OEt cavity was favoured in 15-crown-5. Barnnet *et al.* demonstrated position of methyl groups in cavitands can trigger the

drying of non-polar pockets in water, which suggests new avenues to control guest complexation. [116]

1.3.2.4 Summary

Though type II porous liquids are less common compared to the other two kinds of porous liquids, they have their unique advantages. For example, they could be less viscous compared to type I systems, and less complex in rheology behaviours wtheir its homogeneous nature compared to type III porous liquids.

1.3.3 Type III porous liquids

1.3.3.1 Pore generators and preparation methods

Type III porous liquids are a multiphase kind of fluids, which could be relatively easier to prepare by dispersing porous solid particles in size-excluded liquids. The porous solids typically used are porous materials that do not dissolve well in common solvents, such as MOFs, zeolites and recently porous organic cages and porous organic frameworks (POFs). POFs are linked with purely organic monomers with strong covalent bonds, which include COFs and PAFs. [117] COFs are a kind of crystalline materials with periodic 2D or 3D frameworks. They can be synthesized through reversible dynamic covalent reactions in a predictable way, while PAFs are composed of phenyl-based monomers synthesised through irreversible C-C coupling reactions, which are amorphous and have a rigid diamondoid or other structured frameworks. [117–119] Due to their large pores, it is usually hard to find a bulky solvent that would not penetrate its pores. As solubility is not considered in construction type III porous liquids, pore carriers with large surface areas are much preferred as they will ensure gas uptakes to a certain degree while being diluted with dispersing solvents.

1.3.3.2 Solvent selection

For type III porous liquids, one basic requirement for the solvents used to disperse the pore carriers is size exclusion, which could be proved by molecular dynamic simulations and experimental methods. For general screening, experimental gas uptakes comparison between the blank solvent and the dispersion formed in the solvent works as a direct and convenient method.

Among the reported type III porous liquid systems, ionic liquids and oils are typically used. While ionic liquids, also known as “green solvents”, which are a kind of liquid material by themselves, are widely used in extraction, separation, catalysis, electrochemistry and other areas. [120,121] They have many good properties, such as negligible vapour pressure, good thermal and chemical stability, and wide electrochemical window. What’s more, by pairing different cations and anions, ionic liquids can be easily synthesised, and their properties can be tuned. With the careful and rational design of the solvent of ionic liquids, it may be possible to construct more porous liquids with size-excluded ionic liquids. The use of ionic liquids with low vapour pressure and high boiling points as flowing media in a system, would improve the thermal stability compared to type II porous liquid systems which commonly use organic solvents. And it also brings benefits such as the application of standard sorption measurement for porous solids in liquids, where degassing activation is often involved. However, the generally viscous ionic liquids would cause even higher viscosities in the corresponding dispersions formed. [122] And ionic liquids are relatively more expensive than other solvents, type III porous liquids using ionic liquids as flowing media may be limited in industrial applications.

On the other hand, non-ionic liquids such as silicone oils, triglyceride oils, and polyethylene glycols are much cheaper and less viscous. With equally versatile structures and properties, bulky non-ionic liquids also work as good choices for the construction of type III porous liquids. However, they have disadvantages as well, such as slight volatility, and poor interaction with the pore carriers dispersed which would cause phase separation. And as MOFs are generally used in constructing type III porous liquids, the choice of solvents should also ensure that MOFs do not undergo structural change in the solvents. [33]

1.3.3.3 Phase stability

As a multiphase system, the colloidal stability of type III porous liquids is an important consideration. This could be fulfilled by creating good interaction between pore carriers and solvents, thus preventing aggregation and sedimentation. [33] For example, Dai and co-workers used hydrogen bonding between Zeolite Socony Mobil H-ZSM-5 zeolites and bulky phosphonium ionic liquids to construct a colloidally stable type III system. [43] Surface modification of the pore carriers is usually employed for

stabilisation. For example, a 3D imine-linked COF was functionalized with ionic liquid functionality on its outer shell, forming COF colloids that were extremely stable toward flocculation (>1 year) in an ionic liquid. [29] Alternatively, creating smaller sizes of pore carriers, such as microparticles would help to prevent sedimentation. For example, nanocrystalline particles of ZIF-8 could be prepared by a rapid synthetic method to form stable emulsions while the solid was dispersed. [123]

1.3.3.4 Progress

1.3.3.4.1 ZIF-8

First type III porous liquids were officially reported in 2018 but had already existed before, [25–27,42,124] which opened up a comparatively facile way to prepare porous liquids. The strategy adopted is to disperse non-soluble porous frameworks in bulky ionic liquids, and there is a trend that this type is starting to play a competitive role in the porous liquids field. The main framework involved in these initial explorations was ZIF-8, which had large pores with a surface area that could reach 1297 m^2/g, and at the same time favourably particular small pore aperture (3.4 A) which could limit the size of guests that would be allowed. [25,124] The very first one was published in 2014 by Liu *et al.* They dispersed ZIF-8 in glycol and glycol-2-methylimidazole to improve CO_2 capture. [124] Though the term "porous liquids" was not been adopted by that paper, the concept put up in their way "…to select a material with pores that are sufficiently small to prevent liquid-absorbent molecules from entering the materials, but sufficiently large for the gas molecules to be adsorbed…" is exactly the notion of "porous liquids". [4] In 2018, four papers described suspending ZIF-8 in three sized-excluded ionic liquids were published, [25–27,42] which included a designed-and-synthesised 8,8′-(3,6-dioxaoctane-1,8-diyl)bis(1,8-Diazabicyclo[5.4.0]undec-7-en-8-ium) bis(trifluoromethanesulfonyl)imide ([DBU-PEG][NTf_2]), commercialised N-butyl pyridinium bis(trifluoromethanesulfonyl)imide ([BPy][NTf_2]) and trihexyltetradecylphosphonium bis(trifluoromethylsulfonyl)imide ([$P_{6,6,6,14}$][NTf_2]) (**Figure 1.24**).

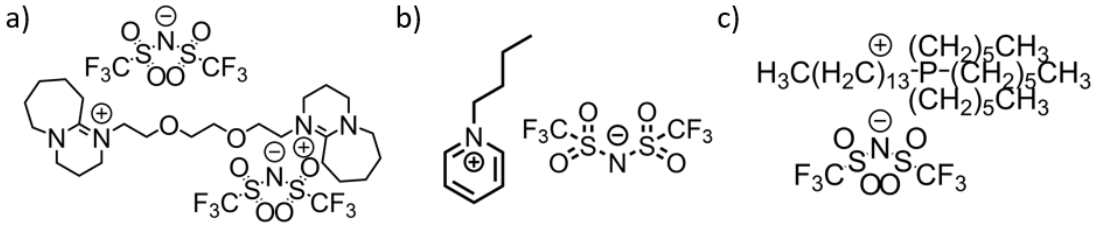

Figure 1.24: a) [DBU-PEG][NTf_2]; b) [BPy][NTf_2]; c) [P_{66614}][NTf_2]

The type III porous liquid based upon the ZIF-8 in [DBU-PEG][NTf_2] was reported by Sheng Dai's group a little earlier. They designed and synthesised [DBU-PEG][NTf_2], where the dimension of the rigid cation reached 1.9 nm × 0.77 nm × 0.40 nm and could be size-excluded from the ZIF-8 pore channel. [25] A 30 wt.% dispersion of ZIF-8 in [DBU-PEG][NTf_2] showed a CO2 adsorption capacity of 1.54 mmol/g at 10 bar, which was 4.7 times than that of blank [DBU-PEG][NTf_2]. [25] The absolute CO_2 uptake was comparable to some of the type I and II porous liquids reported, which demonstrated that the type III porous liquid system, though easier to prepare, was an alternative with advantages. Schott *et al.* further in 2021 used in situ attenuated total reflectance Fourier transform infrared spectroscopy (ATR-FTIR) to study the interfacial properties and mechanisms of CO2 sorption until 7 bar in a 20 wt.% dispersion of ZIF-8 in [DBU-PEG][NTf_2], where they found that slight fluctuations in the ZIF-8 structure happened for both as a solid state and in the ionic liquid [DBU-PEG][NTf_2] after CO_2 was incorporated, suggesting that CO2 interacting more strongly with the ring structure in the ZIF-8 framework during CO_2 sorption. [40] Viscosities of corresponding systems in the [DBU-PEG][NTf_2] have not been mentioned in the above two papers, which may indicate high values. Thus in 2022, Mukesh *et al.* synthesised 8-(2-methoxyethyl)-1,8-Diazabicyclo[5.4.0]undec-7-en-8-ium bis(trifluoromethanesulfonyl)imide ([MEDBU][NTf_2]), a similar DBU-based ionic liquid with relatively low viscosity (210 mPa·s). [125] A 6.66 wt.% ZIF-8 dispersion in [MEDBU][NTf_2] presented an increased viscosity of 350 mPa·s, and a CO_2 uptake of 1.16 mmol/g which was about 1.56 times than that of blank [MEDBU][NTf_2]. [125]

By comparison, the ionic liquid of [BPy][NTf_2] is relatively less viscous, with a viscosity about of 67 mPa·s. [122] However, due to its simpler and less bulky cation structure, it also suffered more risk of penetrating the ZIF-8 framework. The first paper of studying ZIF-8 in [BPy][NTf_2] by Liu *et al.* failed to demonstrate improved gas

uptakes including N_2, CO_2 and CH_4 with a 1.4 wt.% ZIF-8 dispersion sample compared to the blank [BPy][NTf_2]. [124] But Wang *et al.* proved that enhanced CO2 uptakes of ZIF-8 dispersion in [BPy][NTf_2] could be demonstrated at higher loadings of ZIF-8 and pressure, where a 16.96 wt% dispersion of ZIF-8 in [BPy][NTf_2] at 30 °C and 18 bar could take up 24% higher CO_2 than that of blank ILs. [42] The type III porous liquids of ZIF-8 in [BPy][NTf_2] were also studied in liquid-liquid extraction, where in a desulfurization extraction 72.41% and 80.87% of thiophene (TH) and benzothiophene (BT) respectively could be removed, while 88.1% of 2,2,3,3-tetrafluoro-1-propanol, as a solvent and cleaning reagent used in the industry could be recovered. [126]

The ZIF-8 based type III porous liquid in [$P_{6,6,6,14}$][NTf_2]was reported by Gomes *et al.* with both experiments and simulation studies, where a 5 wt.% dispersion could present a 63% increase of CO_2 compared to blank [$P_{6,6,6,14}$][NTf_2] at 30 °C and 5 bar. [26] In 2021 they further used an ionic liquid with the anion replaced with a bulky anion levulinate, which formed a basic ionic liquid [$P_{6,6,6,14}$][Lev] to prepare the type III porous liquid with ZIF-8. [127] The [$P_{6,6,6,14}$][Lev] in the system could improve CO_2 uptake through chemisorption, where a 5 wt.% dispersion of ZIF-8 in [$P_{6,6,6,14}$][Lev] could enhance the CO_2 solubility (1.13 mmol/g) about 100% compared that of that of solid ZIF-8 (0.56 mmol/g) at lower pressure (1 bar, 30 °C). The CO_2 improvement of the 5 wt.% dispersion of ZIF-8 in [$P_{6,6,6,14}$][Lev] (1.97 mmol/g) was less apparent compared to pure [$P_{6,6,6,14}$][Lev] (1.77 mmol/g) with only a 12 % increase at 30 °C and 5 bar, which was actually due to low loading of ZIF-8 and thus less contribution. [127] Zhou *et al.* used the dispersion of ZIF-8 in a range of alkylphosphonium halides ionic liquids to catalyse the coupling reaction of CO_2 with epoxides to form cyclic carbonates, which proved to demonstrate high activity and selectivity under mild conditions. [128]

1.3.3.4.2 Other MOFs

Other MOFs that have been proven to be suitable for constructing type III porous liquids include HKUST-1, Uio-66, ZIF-67 and so on, which were reported by Cahir *et al.* and others. HKUST-1 was composed of 1,3,5-benzenetricarboxylate (BTC) ligands coordinating with copper ions Cu^{2+} in a cubic lattice, forming a 3-D connected porous network where the main channels with the size of 9 Å were connected through 3 Å

triangular windows to the tetrahedral-shaped side-pockets (5 Å). The porosity of HKUST-1 in $[P_{6,6,6,14}][NTf_2]$ was studied by molecular dynamic simulations in the paper by Gomes *et al.* in 2018, where alkyl side chains of the phosphonium cations could be seen in the surface accessible pores but the main channel remained empty. [26] Experimentally, the porosity of dispersion of HKUST-1 in $[P_{6,6,6,14}][NTf_2]$ was proved by CO_2 sorption improvement by the same group in a 2021 paper. [32] Other solvent systems could also be used to construct type III porous liquids with HKUST-1 according to the paper by Cahir *et al.* in 2020, such as polydimethylsiloxane (PDMS), a range of triglyceride oils and so on. [34] The selectivity for ethene over ethane of a sesame oil dispersion of HKUST-1 was also studied by B. Lai et al in 2020, though the system presented not so high selectivity. [129]

Uio-66, which was introduced earlier as candidates to prepare type I porous liquid, could also be used to prepare type III porous liquids. He *et al.* in 2019 reported mixing cross-linked poly(monomethacryloxypropyl-terminated polydimethylsiloxane) (xPDMS) coated UiO-66 serial (including Uio-66-NH_2 and Uio-66-Br_2) with PDMS4k (Mn = 4000 Da) to form a type III porous liquid with excellent homogeneity and colloidal stability, where a 50 wt.% dispersion in PDMS could reach 30.8 cc/g (1.375 mmol/g) and about 13-fold increase compared to blank PDMS4k at 20 °C and 1 bar.[44] The porous liquids formed here could be quite viscous, which easily passed over 10000 mPa·s. In the same paper, a mesoporous MOF-101 with a larger aperture of 16 Å and a smaller aperture of 12 Å was also tried with the same method to construct type III porous liquids. The larger pore aperture would mean a high chance that solvents used to disperse the MOF may enter its pore channel. Though the dispersion presented improved gases uptake compared to blank 4-arm star PDMS by using a bulkier 4-arm star PDMS to mix with xPDMS-coated MIL-101(Cr), the absolute uptakes decreased a lot in comparison with the Uio-66 based system. [44] Zhao *et al.* reported also in 2019 a Uio-66 based type III porous liquid system, where they used another method by modifying nanoparticles of Uio-66 with polyether amine (D2000) and mixing with a polymeric IL of [M2070][IPA], forming a homogeneous and extremely stable liquid. [46] The 50 wt.% dispersion here presented a CO_2 uptake of 7.32 wt.% (1.66 mmol/g) at 25 °C and 10 bar. [46]

ZIF-67, isostructural to ZIF-8, is composed of 2-methylimidazolate ligands coordinated to cobalt ions Co^{2+}, which formed a structure with a small pore aperture

size of 3.4Å. Knebel *et al.* reported in 2020 that ZIF-67 particles with an average size of 264 ± 54 nm could be surfaced functionalised with 1,3-bis(2,4,6-trimethylphenyl) imidazole-2-ylidene (IMes) and 1,3-bis(2,4,6-diisopropylphenyl) imidazole-2-ylidene (IDip) to get solution processible ZIF-67-IMes and ZIF-67-IDip. [130] These modified ZIF-67 could form homogeneous and stable dispersions in mesitylene. A 6 wt.% ZIF-67-IDip in mesitylene presented an apparent increase in the solubility of CO_2, propane and propene. [130] Li *et al.* reported in 2021 by simply mixing ZIF-67 with a synthesized symmetric ionic liquid 1,6-bis(3-buthylimidazolium-1-yl)hexane bis(trifluoromethylsulfonyl)amide ($[C_6BIm_2][NTf_2]_2$), a homogeneous and extremely stable dispersion could be formed without any visible separation for 180 days. [131] A 10 wt.% dispersion of ZIF-67 in $[C_6BIm_2][NTf_2]_2$ presented a CO_2 uptake of 9.54 mmol/g at 25 °C and 1 bar, about 55 times higher than that of the blank $[C_6BIm_2][NTf_2]_2$, which showed the best CO_2 uptake performance among the porous liquids reported so far. Besides the 10 wt.% dispersion also took up 7 times higher toluene uptake than neat $[C_6BIm_2][NTf_2]_2$. [131]

1.3.3.4.3 Other porous materials

In addition to MOFs, other porous materials have been studied to construct type III porous liquids, such as inorganic zeolites, porous organic cages and COFs. Sheng *et al.* studied using inorganic zeolites, including ZSM-5 and silicalite-1, to construct type III porous liquids in their 2018 paper. [25] ZSM-5 and silicalite-1 were mixed with the bulky [DBU-PEG][NTf_2], and dispersions of both were proved to maintain porosity. As the surface areas of ZSM-5 (408 m^2/g) and silicalite-1 (304 m^2/g) were lower than ZIF-8 (1297 m^2/g), and probably with low phase stability in the ionic liquid, they were not so comparable to ZIF-8 based type III porous liquid system in [DBU-PEG][NTf_2]. [25] In 2019, the same group reported a phase-stable type III porous constructed from an H-form zeolite H-ZSM-5 dispersed in several bully ionic liquids such as $[P_{6,6,6,14}][Br]$. [43] The stabilisation force of the system may arise from the mechanical lock of the cation alkyl chains into the pore channels at the surface of H-ZSM-5 nanoparticles and the hydrogen bonding between cation alkyl chains and Brønsted sites in H-ZSM-5. [43] The 40 wt.% dispersion of H-ZSM-5 nanoparticles in $[P_{6,6,6,14}][Br]$ had a viscosity of 9550 mPa·s at 25 °C and presented improved CO_2 uptake compared to blank $[P_{6,6,6,14}][Br]$. [43] Commercialised zeolites such as zeolite 5A and zeolite 13X could also be dispersed in PDMS, paraffin oil, and a range of

triglyceride oils to form type III porous liquids, according to the paper by Cahir *et al.* in 2020. [34] Lai *et al.* also used zeolite in constructing type III porous liquids with ethane/ethene selectivity in the 2020 paper, where they synthesized an Ag^+ containing zeolite AgA and dispersed it in an Ag^+ containing ionic liquid AgIL (1-butyl-3-methylimidazolium bis(trifluoromethylsulfonyl)imide saturated with silver trifluoromethanesulfonate). [129] The 12.5 wt.% dispersion of AgA in AgIL was reported to present an ethene selectivity of 25.6.

POCs which have good solubility in common solvents are usually used to prepare type 2 porous liquids. Some of the properties of POCs can be retained when transferred into the liquid state, such as size-selective guest uptake, [30] while others, such as chiral recognition, [30] are lost. One potential way to retain the solid-state properties of POCs is to form type III porous liquids. POCs with decreased solubility in solvents could be fabricated from cocrystal synthesis, where two solutions of homochiral cages were mixed and more stable packing between the achiral cage molecules due to chiral recognition led to decreased solubility. [132] Fine microparticles could be formed using this method and a range of solvents including oils and ionic liquids were screened to construct type III porous liquids. [122]

POFs based type III porous liquids were first tried in Cahir *et al.*'s paper, where PAF-1 was dispersed in PDMS and a range of triglyceride oils to form type III porous liquids. [34] PAF-1 had the pore size distribution centred around 14 Å, which was quite large that solvents were highly possible to diffuse into its pore channels. But some dispersions of PAF-1 in the screened solvents could display gas uptake improvements, for example, the PAF-1 dispersion in Genosorb® 1753 showed a CO_2 uptake of 0.72 mmol/g, which was over three-fold compared to the pure Genosorb® 1753 (0.23 mmol/g). [34] Mow *et al.* reported a 3D imine-linked colloidal COF based porous liquid. [29] The COF was functionalised with a bulky ionic liquid 3-(3-(4-formylphenoxypropyl)-1-methyl-imidazolium tetrakis[3,5-bis(trifluoromethyl)phenyl] borate (BArF) to produce colloids with pore sizes ranging from 5 to 14 Å. [29] On one hand, the tethered ionic liquid groups could function as steric hindrance that limit penetration of solvents used to disperse the COF colloids; and on the other hand, these ionic liquid groups could interact well with solvents and thus forming a homogeneously stable system. The COF colloids were dispersed in a bulky BArF ionic liquid to form dispersions which stayed stable over a year. [29] And

the 20 wt.% dispersion of COF colloids presented CO_2 and CH_4 uptake increased more than 10 and 20-fold, respectively, compared to blank BArF ionic liquid. [29]

1.3.3.5 Summary

For type III porous liquids, it is feasible to screen a wide range of porous materials and bulky liquids to find suitable combinations. And apart from that improved gas uptake performances could be realised in type III porous liquids, other characteristics of porous hosts, such as gas selectivity and enantioselectivity, can also be expressed in porous liquids. However, one thing that should always be considered is that while choosing MOFs as pore carriers, it is of importance to choose suitable and dry solvents that do not affect the structure of MOFs. And good phase stability of type III systems should be a common standard.

1.4 Applications of porous liquids

As a porous material, we want all the applications that have been reported in porous solids realised in porous liquids, such as sorption, separation, and catalysis. The field of porous liquids has seen significant steps towards realising these applications. For example, a 10 wt.% dispersion of ZIF-67 in $[C_6BIm_2][NTf_2]_2$ had a CO_2 uptake of 9.54 mmol/g at 25 °C and 1 bar, demonstrating good potential in CO_2 capture. [131] An Ag^+ containing zeolite, AgA, dispersed in an Ag^+ containing ionic liquid AgIL could present an ethene selectivity of 25.6 over ethane. [129] A Uio-66-based type I porous liquid constructed from an imidazolium ionic liquid functionalised MOF Deim-Uio-66 showed good in-situ catalytic performance in cyclocarbonate synthesis. [80] However, practical applications have proven more challenging for porous liquids due to their generally low capacity and unfavourable properties like high viscosity. The characterisation method frequently used to determine the porosity of a liquid is CO_2 uptakes, where the porous liquid is compared with the blank solvent or monomer. One reason for choosing CO_2 for these measurements is due to the higher CO_2 uptakes in porous materials at room temperature than other gases like nitrogen. Thus, though the application of CO_2 sorption works to determine the porosity of porous liquids, the adsorbents available are more limited than conventional methods. The high viscosity of porous liquids is also an issue and restricts the utilising the porous liquids directly. For example, a type I porous liquid based upon cyclodextrin had to be diluted in water to perform the chiral separation. [92] An important consideration is that the material

properties are typically closely related to construction methods that determine the application. Thus, application problems encountered by porous liquids would be solved by discovering different construction methods in the future, which might lead to more versatile applications.

1.5 Summary of porous liquids

In summary, porous liquids have seen a lot of developments since it was put forward. However, the field is still at its early stage, and even more, challenges remain, such as the high viscosity and low gas uptakes. To address this, more versatile construction methods need to be developed, and other applications that have been realised in porous solids are also worth exploring for porous liquids.

Chapter 2

Methods

Chapter 2 contains information about the theory associated with the methods used to characterise the materials reported in this thesis.

2.1 Gas laws and gas solubility in liquids

The gas law describes the physical properties of a gas using parameters that describe the amount of substance (*n*), volume (*V*), pressure (*p*), and temperature (*T*). The ideal gas law describes a gas where the distance between each gas molecule is so large that the interactions between each molecule can be ignored. The ideal gas law equation is shown below:

$$pV = nRT$$

For a real gas, there are interactions and collisions among the gas molecules. Repulsion forces are significant when molecules are almost in contact, while attraction forces are influential when molecules are close enough to interact. Thus, a deviation is added to the idealised gas law equation to fit the actual state of a gas. Different scientists have put forward several revised equations. The most used equation is the van der Waals equation:

$$p = \frac{nRT}{V - nb} - a\frac{n^2}{V^2}$$

In the van der Waals equation, *V* - *nb* represents the effect of repulsive interaction between molecules that are restricted to a smaller volume by supposing the gas molecules behave as impenetrable spheres. *nb* is approximately the entire volume taken up by the molecules, which is usually the situation at high pressure. The pressure in the van der Waals equation is reduced by $a\frac{n^2}{V^2}$ if compared with that of the ideal gas law. The term $a\frac{n^2}{V^2}$ represents the effect of attraction forces, which decreases the frequency of collisions with the walls and the force of each collision. Usually, the intermolecular interactions of repulsion and attraction are insignificant at low pressure and high temperature. At low pressure, the gas molecules are often far apart within a large volume, and gas molecules travel more quickly at high temperatures. Thus, intermolecular interactions are less influential in these two conditions, and gas could be seen as ideal gas conditionally.

The gas solubility in a liquid obeys Henry's law shown below, where at a constant temperature, the pressure of the gas is proportional to its fraction in the liquid at low concentrations.

$$p_B = x_B K_B$$

In the above expression, p_B is the gas pressure, x_B is the mole fraction of the gas solute, and K_B is the empirical constant called Henry's law constant. At equilibrium, where the gas molecules escaping from the liquid and gas molecules dissolving in the liquid reach a balanced state, the gas solubility in a liquid will increase with increasing gas pressure in the vessel. Henry's law applies to the more specific situation in this thesis when calculating the CO_2 and CH_4 solubilities in blank ionic liquids at 1 bar. **Figure 2.1** shows CO_2 isotherms of the ionic liquids used in this thesis, where the linear isotherms demonstrate a proportional relationship between the CO_2 solubility and pressure. Different ionic liquids have different Henry's law constants. These constants are affected by the anion type, the free volume effect among the interionic space and the Lewis acid-base interaction. [133] In a porous liquid, the gas solubility is related to the solvent and the extra void volume within the pore carriers used. However, the exact relationship between gas solubility in porous liquids and pressure has not been studied extensively for porous liquids. Thus, the gas solubilities of porous liquids are usually measured and compared with those of pure solvents, which are utilised to indicate porosity in the porous liquid.

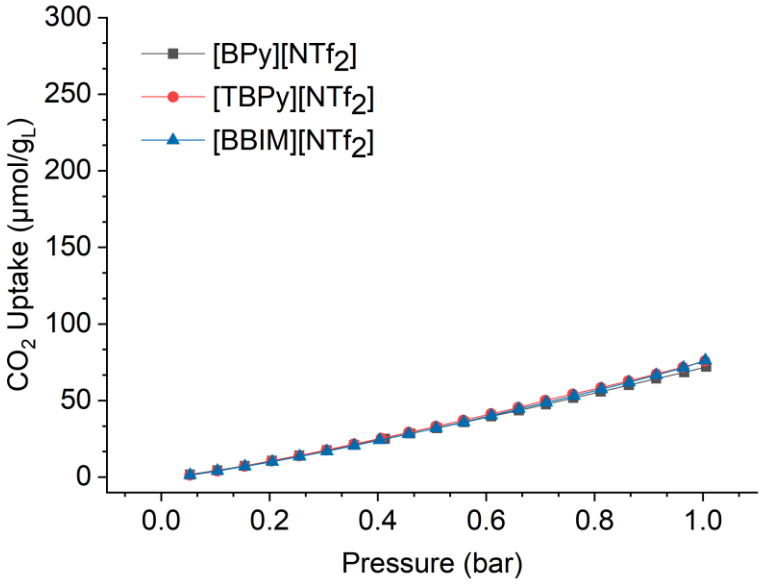

Figure 2.1: CO_2 isotherms of [BPy][NTf_2], [TBPy][NTf_2] and [BBIM][NTf_2].

2.2 Gas sorption and methodology of gas uptake measurement of porous liquids in the thesis

Gas adsorption can be categorised as physisorption and chemisorption. Physisorption describes the adsorption of guest molecules into an empty host driven by interactions between host and guest gas molecules, such as hydrogen bonding, π-π interactions, and Van de Waals interactions. Chemisorption describes the adsorption of guest molecules into a host structure driven by chemical reactions, such as ammonia and CO_2 reacting with amine groups in a host structure. Most of the atoms are bound by other atoms around in the bulk of the solid, while the surface atoms of solids are incompletely bound and tend to attract gas or liquid on the surface to make up for the imbalance of atomic forces. Thus, gas sorption can be used to determine the porosity of solids. During a gas sorption experiment, gas molecules diffuse into a host and cover its internal porosity surface. The theory of using gas sorption to determine a solid's porosity and its pore structure is relatively well explored and established.

In contrast, the relationship between the porosity of porous liquids and gas uptakes remains unknown. At this stage, gas uptakes are only used to indirectly prove the extra porosity in porous liquids. Measuring the gas uptakes of porous liquids by standard gas uptake instruments involves an intelligent gravimetric analyser (IGA) and other instruments, such as Micromeritics ASAP 2020 volumetric adsorption analyser, or Quantachrome Nova 4200e. IGA measures the mass change of samples under the atmosphere of guest gas, while other volumetric adsorption instruments detect the pressure change within a sample tube after dosing with a certain volume of gas. In the thesis, a Quantachrome was utilised to measure the gas uptake of porous liquids due to its easy conversion for running liquids sorption measurement. For example, using liquid stirring to improve mixing and long equilibration time at each pressure point to ensure gas saturation in the liquids. The sorption isotherms reported in this thesis were typically measured at room temperature with stirring and 1800 s equilibrium time at each pressure point. Due to the mathematical operation in the software being designed for solids, only the data of pressure and volume of CO_2 gas during the measurement was extracted and converted to the amount of gas absorbed using the gas law equation. The ideal gas law equation ($n = pV/RT$) was used here due to the situation of low pressure. **Table 2.1** below shows an example of how raw sorption data of CO_2

measured on Quantachrome is converted from p (mmHg) and V (cc/g) to p (bar) and n (µmol). And calculation steps involved are shown below.

Step 1:

$$1\ mmHg = 133.32\ Pa$$

$$1\ cc/g = 1 \times 10^{-6}\ m^3/g$$

Step 2:

$$1\ Pa = 1 \times 10^{-5}\ bar$$

$$n\ (mol) = \frac{p(Pa)V(m^3/g)}{RT(K)}$$

$$R = 8.314\ J \cdot K^{-1} \cdot mol^{-1};\ T = 298\ K$$

Table 2.1: CO_2 sorption data conversion of a 12.5 wt.% dispersion of **CC3-*R*/CC3-*S*** microparticles in [BPy][NTf_2].

Raw data		Step 1		Step 2	
P (mmHg)	**V (cc/g)**	**P (Pa)**	**V (m3/g)**	**P (bar)**	**n (umol/g)**
38.4955	0.1595	5132.312	0.0000001595	0.05	6.5
75.8244	0.3629	10109.09	0.0000003629	0.10	14.7
113.6641	0.5874	15153.97	0.0000005874	0.15	23.8
151.3532	0.823	20178.77	0.0000008230	0.20	33.4
189.2035	1.0563	25225.06	0.0000010563	0.25	42.8
227.183	1.3009	30288.58	0.0000013009	0.30	52.7
265.0652	1.5413	35339.13	0.0000015413	0.35	62.5
303.2438	1.7749	40429.19	0.0000017749	0.40	72.0
341.9118	1.9959	45584.5	0.0000019959	0.46	80.9
380.0258	2.1976	50665.95	0.0000021976	0.51	89.1
417.946	2.4043	55721.56	0.0000024043	0.56	97.5

455.8229	2.6417	60771.4	0.0000026417	0.61	107.1
494.0927	2.8501	65873.62	0.0000028501	0.66	115.5
532.0182	3.0606	70929.94	0.0000030606	0.71	124.1
570.6384	3.2489	76078.87	0.0000032489	0.76	131.7
608.5206	3.4498	81129.42	0.0000034498	0.81	139.8
646.4894	3.649	86191.51	0.0000036490	0.86	147.9
685.485	3.8663	91390.5	0.0000038663	0.91	156.7
722.4317	4.0853	96316.32	0.0000040853	0.96	165.6
753.3287	4.2045	100435.6	0.0000042045	1.00	170.4

2.3 CD

Circular dichroism is an absorption spectroscopic analysis method that uses circularly polarised light to study optically active chiral media. A circularly polarised light is electromagnetic radiation where the electric field vector rotates around the propagation axis with the same magnitude. For example, the vector rotates counterclockwise in a left circularly polarised (LCP) light if looking down the propagation axis. On the other hand, if the vector rotates clockwise, it is a right circularly polarised (RCP) light.

In a typical CD measurement, the sample in a cuvette is irradiated first with LCP. The RCP and corresponding absorption can then be calculated by Beer-lambert law. If the sample is chiral, the interaction between the LCP and RCP will differ due to the asymmetric structure. More absorption of one circularly polarised light than the other would be observed, called the cotton effect. The resulting spectra would present either positive or negative ellipse signals, and one pair of R and S enantiomers would form symmetric spectra. The subject is not limited to chiral molecules but also works for macromolecular structures with chiral chromophores or chromophores placed in an asymmetric environment, such as some polymers or biomolecules. If the sample is not chiral or contains an equal amount of R and S enantiomers, LCP and RCP light would be absorbed to the same amount, and the spectra will give a horizontal line in the

middle. CD measurements were empolyed to prove chirality of **CC3**-*R* and **CC3**-*S* cage molecules in chapter 3.

2.4 PXRD

PXRD is a non-destructive characterisation technique that uses X-ray diffraction to reveal structural information of crystalline or semi-crystalline materials, such as crystallinity and phase purity. Atoms are arranged in a regular order within a crystal. For single crystals, one three-dimensional arrangement of atoms is repeated throughout the entire crystal. In contrast, microcrystalline powders usually contain many smaller crystals with different orientations and are typically characterised by PXRD. X-ray is electromagnetic radiation with a short wavelength ranging from 0.01 to 10 nm, which is at the comparable magnitude as interatomic spacings of the crystalline system. Diffraction of X-ray waves occurs when crystalline samples are irradiated. These X-ray waves scattered by atoms in a crystal can interfere constructively if the relationship between the incident X-ray beam and interatomic spacing satisfies Braggs law, as shown below.

$$n\lambda = 2dsin\theta$$

where *n* represents an integer, and λ is the wavelength of the incident monochromatic X-ray. *D* is the distance between two crystal lattice planes (d-spacing), and θ is the angle between the lattice plane and the incident X-ray beam (**Figure 2.2**). If the relationship between θ, *d* and λ contribute to the path length difference of two waves being equal to an integer number of X-ray wavelength, the X-ray waves scatter in phase and interfere constructively to give diffraction signals. A powder sample is scanned using a monochromatic X-ray beam over a certain 2θ range in degrees. The intensity and angles of diffracted X-ray signals are recorded on a detector. From the measurement, the result is a one-dimensional data set that describes the averaged diffraction signals over a 2θ range from all the crystallites with different orientations.

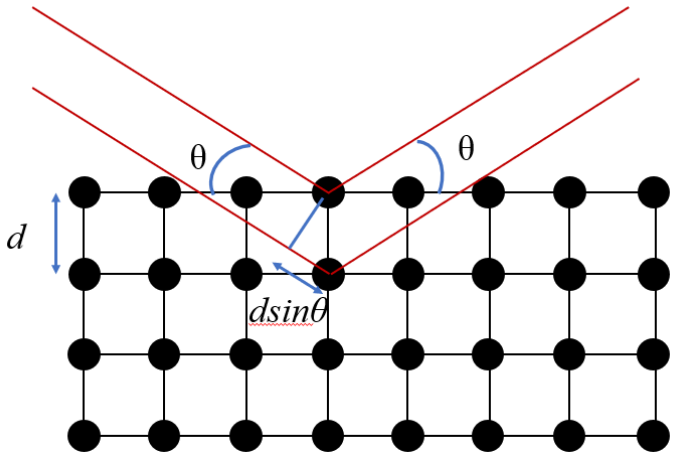

Figure 2.2: Schematic of diffraction of X-rays by crystals.

2.5 DLS

DLS is a technique that measures the size of particles suspended in a solvent, where the Brownian motion of particles is usually monitored and related to the particle diameter. Brownian motion describes a phenomenon in which particles move randomly due to the bombardment of solvent molecules. The velocity of Brownian motion is related to the size of the particles, where the smaller the particle, the faster its motion will be. The size of particles could be calculated by using the Stokes-Einstein equation:

$$d(H) = \frac{kT}{3\pi\eta D}$$

In the equation, *d(H)* is the hydrodynamic diameter, which is the diameter when the particle diffuses in a liquid; *D* is the translational diffusional coefficient recorded during the DLS measurement and depends on particle size, concentration, ions, and surface structure; *k* is Boltzmann's constant; *T* is the temperature, which would affect the viscosity of the liquid; and η is the viscosity of the solvent where particles diffuse. In a DLS measurement, a dilute dispersion is used along with a laser, which is scattered by the particles in the dispersion. If the scattered light interferes constructively, a bright speckle is received by the detector. As the particles are in Brownian motion, the bright speckles show a changing pattern. The particle size information can be revealed by recording the scattered light intensity fluctuation rate and extracting information using the correlation function.

2.6 LUMiSizer®

LUMiSizer® is based on centrifugal technology and space and time-resolved extinction profiles (STEP) technology. According to the instrument configuration in **Figure 2.3**, a clear sample cuvette is placed horizontally into the centrifuge, with a light source above and a detector below. The change in light transmission through the sample cuvette would be detected and recorded during the centrifuge process. The transmitted light intensity *I* would increase over time while phase separation occurs gradually. And each extinction profile line could be described by the Beer-Lambert law:

$$E = -lg\frac{I}{I_0} = \varepsilon cd$$

In the formula, *E* represents extinction; *I* is the transmitted light intensity; I_0 is the incident light intensity; ε is the extinction coefficient; *c* is the particle concentration, which means this method could be utilised to calculate particle concentration; *d* represents path length. The extinction files represent a time-resolved phase separation where particles either cream to the cuvette top or sediment down to the bottom during centrifugation, leaving the clear solvent on the other side. The colour of the extinction files indicates time, where "red" is early profiles, and over time the latest profiles are shown in "green". [134]

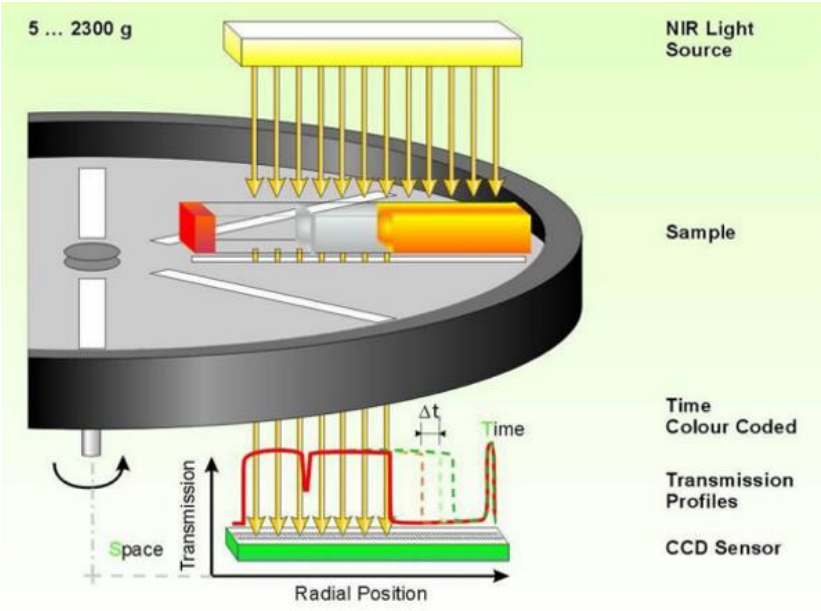

Figure 2.3: Schematic demonstration of the LUMiSizer®. [134]

2.7 TGA

TGA is an analysis method where the mass of a sample is measured over time with changing temperatures. The measurement is usually performed in nitrogen or air where the sample pan and reference pan are heated together from room temperature to 1000 ºC at a constant heating rate, such as 20 ºC/min. Gases are usually used to blow away the compounds released from the sample or provide a controlled oxygen concentration to the system for reactions. A highly sensitive balance in the instrument is used to record the mass change over the heating progress. The mass loss percentage with increasing temperature is calculated to provide information about absorbed moisture or solvents, desorption, decomposition, and solid-gas reactions. For example, if absorbed solvents weakly interact with a sample, then they would likely be removed around their boiling point. For moisture, a mass loss could be observed at around 100 ºC, and the sample's water content could be calculated. At higher temperatures, samples usually undergo decomposition, where a large degree of mass loss can be seen.

TGA is generally used alongside DSC studies and offers information about the decomposition temperature of the sample. The temperature range on the DSC instrument can then be kept below decomposition temperature to avoid degradation of the sample in the DSC pan. However, for the thermal breakage of chemical bonds in the sample that does not involve mass loss, TGA offers incomplete information about the thermal stability of samples. Therefore, DSC, which detects heat change during the heating step, is usually employed at this stage.

2.8 Wettability

Wettability studies how a liquid deposited on a substrate would spread out, which derives from a thermodynamic equilibrium of free energy transition from solid-gas to solid-liquid phase. Wettability is described by Yong's equation shown below.

$$\gamma_s = \gamma_{sl} + \gamma_l cos\theta$$

γ_s, represents the surface free energy of the solid-vapour interface, γ_{sl} the surface free energy of the solid-liquid interface, and γ_l the liquid-vapour interface. The θ is the contact angle between the balanced solid-liquid interface and liquid-vapour interface (**Figure 2.4**). Young's equation relates the contact angle with the balanced interfacial

forced among the solid-liquid-vapour interfaces. And wettability is valued by measuring the contact angle of a liquid drop equilibrated on a surface. Usually, if θ = 0º, the liquid completely wet the solid phase; 0º < θ < 90º, the liquid shows good wettability on the solid; 90º < θ < 180º, the liquid is considered to display incomplete wetting on the solid; θ = 180º, the liquid shows no wetting behaviour on the solid. Good wetting means good adhesion force between the liquid and the solid. Usually, water is selected as the liquid, and the solid surface could thus be described as hydrophilic or hydrophobic. Here, the compatibility of porous solid and ionic liquids was evaluated to determine the phase stability of type III porous liquids. Thus, the ionic liquid was selected as the liquid, and contact angles on the porous solid surface were measured.

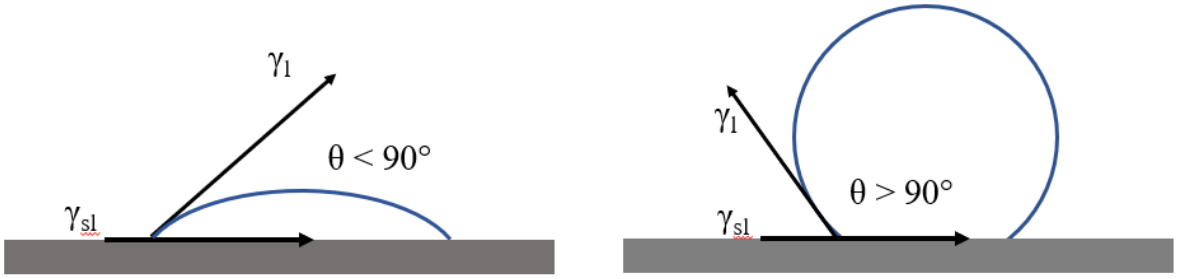

Figure 2.4: Schematic of contact angles.

2.9 Rheology

Rheology studies the flowing and deformation of fluids, and is usually measured on a rheometer where the geometry and plate apply force and perform motions on samples. For example, the above geometry could spin while the lower plate remained stationary (**Figure 2.5a**), and the corresponding flow and deformation of the sample can be studied during different motions between the geometry and the plate. Corresponding rheological terms are defined by using a two-plates model shown in **Figure 2.5b**, which could scientifically describe either shear flow or oscillation tests on the rheometer. When a shear force F (N) is applied to a sample positioned horizontally between two plates, layers of the sample fluid slide over one another, with each layer moving faster than the layer beneath it. And the shear stress τ (N/m^2) equals the shear force applied per unit of the shear area (m^2). The shear strain γ describes the deflection path x (m) per shear gap h (m) under the shear, and the unit of shear strain is 1. The

shear rate $\dot{\gamma}$ (s^{-1}) is the change of shear strain per second, or it could be seen as the velocity v (m/s) of deflection change per shear gap.

According to the law of viscosity, or Newton's law, viscosity η is defined by the shear stress per shear rate. Layers of fluid slide over one another, with each layer moving faster than the one beneath it. The viscosity describes the flow resistance arising from internal friction of the fluid sample while put into motion, and this can be measured by the flow test with a different shear rate on a rheometer. The sample could display ideal viscous flow where its viscosity keeps constant with increasing shear rate, or shear-thinning behaviour where the corresponding viscosity decreases with increasing shear rate.

The oscillation tests on a rheometer characterise a sample's viscoelastic properties, including amplitude sweeps with oscillation motions at a constant frequency but increasing amplitudes (**Figure 2.5c**), and frequency sweeps with oscillation motions at a fixed amplitude but increasing frequencies (**Figure 2.5d**). An ideally viscous behaviour displays constant viscosity during shearing, while an ideally elastic solid shows no elastic deformation with shear applied, and viscoelasticity presents a mixture of viscous and elastic behaviours when sheared. During the oscillation of the geometry, lower plate and the sample in between, shear strain and shear stress undergo a repetitive motion which can be described by sinusoidal functions versus time. Amplitudes of corresponding sinusoidal functions are denoted as shear strain amplitude γ_A and shear stress amplitude τ_A, respectively, which could define the complex shear model G^* below.

$$G^* = \frac{\tau_A}{\gamma_A}$$

Usually, the sinusoidal function of shear strain is pre-set on a rheometer, and the sinusoidal function of shear stress is measured. By comparing the time phase differences, the viscoelasticity could be described. For an ideally elastic behaviour, sinusoidal functions of shear stress and shear strain are in-phase. If samples display viscoelasticity, there is a time lag between sinusoidal curves between shear stress and shear strain, which is called phase lag δ. With the phase lag, the storage modulus G' and loss modulus G'' could be defined.

$$G' = G^* con\delta$$

$$G^{"} = G^{*}sin\delta$$

The storage modulus represents the elastic part of the viscoelasticity, while the loss modulus is the viscous part. If the loss modulus is larger than the storage modulus, the sample is more liquid-like at the measuring point, and more solid-like when the storage modulus is larger. In both amplitude sweeps and frequency sweeps, storage modulus and loss modulus are measured and compared, and for the characterisation of porous liquid samples, liquid properties are always expected in oscillation tests on the rheometer.

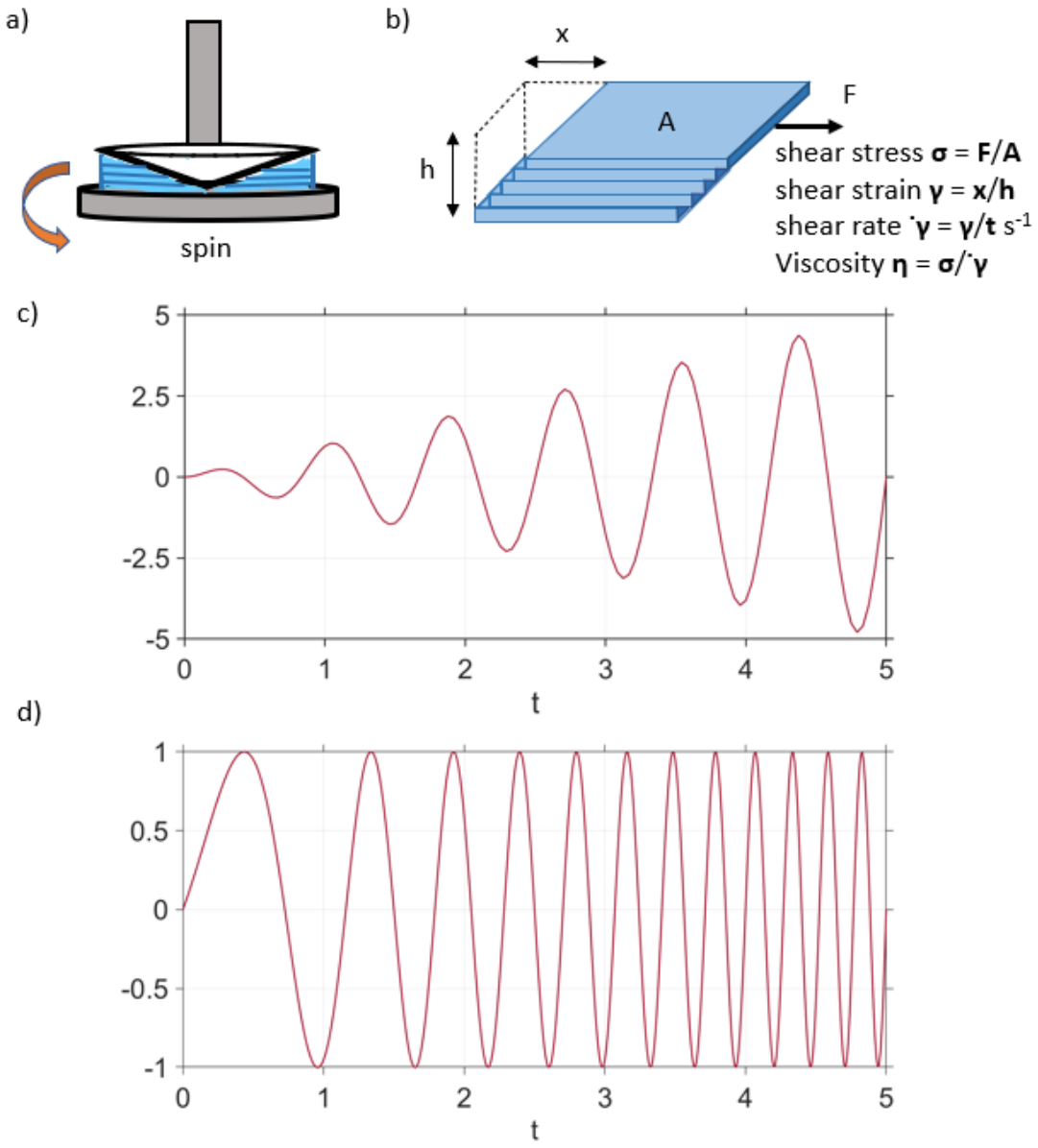

Figure 2.5: a) Representative diagram of rheometer working plates; b) Shear flow and definitions of shear stress, shear strain, shear rate and shear viscosity; c) Amplitude changes during oscillation strain amplitude sweep experiments; d) Frequency changes during oscillation frequency sweep experiments.

Chapter 3

Type III Porous Liquid Based on Porous Organic Cage and Ionic Liquids

3.1 Author contributions

The synthesis of **CC3-*R*/CC3-*S*** microparticles, initial bulky oils screening and optimisation of gas uptake measurement conditions, setup and benchmarking of the Quatanchrome Nova instrument were performed by Dr Greenaway. Ms Xiaoqi Ye performed circular dichroism spectroscopy measurements. The thesis author performed all other experiments, and the associated data interpretation.

This chapter is based upon the publication: A. Kai, B. D. Egleston, A. Tarzia, R. Clowes, M. E. Briggs, K. E. Jelfs, A. I. Cooper and R. L. Greenaway, *Adv. Funct. Mater.*, 2021, **31**, 2106116.

3.2 Introduction

Type III porous liquids are homogeneous dispersions of pore carriers in size-excluded liquids. Porous framework materials, such as MOFs and zeolites, are often used as pore carriers due to their insolubility in most solvents. For example, ZIF-8 has been dispersed in several large and sterically hindered ionic liquids,[25–27] or polymeric glycols to form type III porous liquids.[124] Cahir *et al.* reported the formation of a range of type III porous liquids using various microporous solids, including MOFs and zeolites, in non-ionic oils.[34] As a multiphase system, the colloidal stability of type III porous liquids is an important consideration. For example, Dai *et al.* used hydrogen bonding between H-ZSM-5 zeolites and bulky phosphonium ionic liquids to construct a colloidally stable type III system.[43] He *et al.* [44]and Zhao *et al.* [46] used surface functionalisation to coat particles of UiO-66, with solvent-similar polymeric groups to stabilise these as type III porous liquids. More recently, the surface functionalisation method was used to form a stabilised ZIF-67 dispersion, which could be used directly as a type III porous liquid or conveniently processed further to form mixed matrix membranes with excellent selectivity between propane and propylene.[135] A 3D imine-linked COF was tethered with ionic liquid functionalised aldehydes, which reacted with free amines on its outer shell, forming COF colloids that were extremely stable towards flocculation (> one year) in an ionic liquid.[29] For ZIF-8-based type III porous liquids, an alternative rapid synthetic method was used to produce nanocrystalline particles that allowed stable emulsions to be formed when the solid ZIF-8 was dispersed.[123]

POCs are a type of molecular organic material that contains shape-persistent internal voids in the molecules that are accessible through windows. [136–138] Imine-derived POCs can be synthesised in solution through a reversible condensation reaction, and many derivatives can be produced based on the selection of different synthetic precursors. The window sizes and chemical environment of POCs can be tuned by introducing different functional groups into the precursors.[139] POCs can also have good solubility in organic solvents and are thus good candidates for preparing type II porous liquids.[30,38,108] There have also been attempts to decorate cages with long alkyl chain functionality to lower the melting points in the preparation of type I porous liquids.[22,31] Some of the properties of POCs can be retained when transferred into the liquid state, such as size-selective guest uptake,[41] while others, such as chiral

recognition,[30] are lost. One potential way to retain the solid-state properties of POCs is to form type III porous liquids rather than type I or type II systems.

POC nano- and micro-particles can also be easily fabricated from solution by direct synthesis of a cage in a binary solvent mixture.[140] Another is by exploiting the chiral recognition between two prefabricated homochiral precursor cages, producing co-crystals in a modular way without using any surfactants or templating agents.[132,141] These can be prepared from enantiomeric variants of the same cage species to form a racemate.[142–144] Upon co-crystallisation, the solubility of these racemic cage materials is often significantly reduced if compared to the solution-processable enantiopure cage precursors, thus making them good candidates for preparing type III porous liquids. In a 2012 paper by Hasell *et al.*, a Chemspeed automated liquid handling robot was used to perform systematic experiments by mixing solutions of **CC3**-*R* and **CC3**-*S* to study the effects of mixing rates and temperature on the nanoparticle size and morphology of **CC3**-*R*/**CC3**-*S* microparticles received (**Figure 3.1**). [132] In that study, it was found that the mixing rate affected the morphology of the crystals, with octahedral crystals tending to form with a slow addition rate while spheres formed with a fast addition rate. The mixing temperature also affected the crystallite sizes.

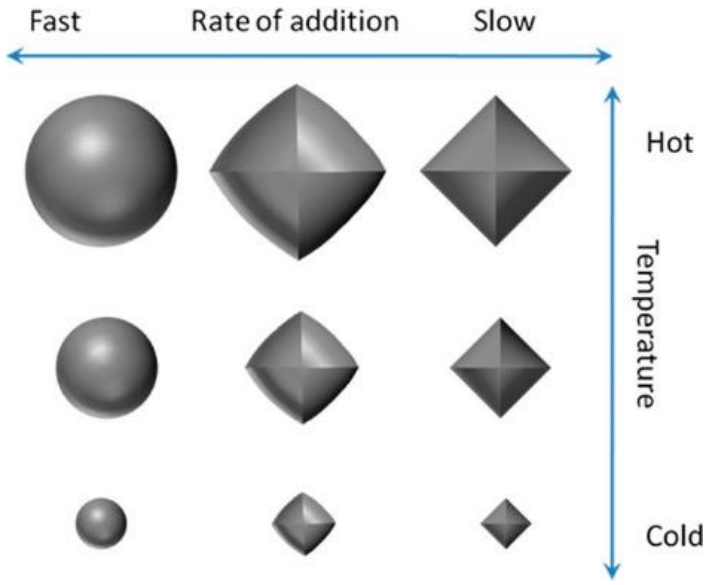

Figure 3.1: Scheme illustrating the size and morphology control in porous organic co-crystals **CC3** synthesis, as achieved by varying the mixing rate and the mixing temperature by Hasell *et al.* (Reproduced with permission, [132] Copyright 2012, American Chemical Society)

The nanoprecipitation method reported by Hasell *et al.* was performed on a scale of up to ~150 mg of **CC3**-*R*/**CC3**-*S* co-crystal microparticles in 100 minutes. The initial screening conditions of scaling up **CC3**-*R*/**CC3**-*S* microparticles was conducted by Dr Greenaway (**Table 3.1**), with the rapid mixing and overhead stirring at RT (method 7) selected as the best preparation method. These reaction conditions were chosen due to the shorter timeframe of the mixing procedure, with large amounts of dilute DCM solutions (1.5 mg/mL, 900 mL each) of **CC3**-*R* and **CC3**-*S* mixed and stirred for only 10 minutes. Overhead mechanical stirring helps mix the solution more thoroughly and afford **CC3**-*R*/**CC3**-*S* microparticles with closer particle sizes. While the isotropic spherical shape of the particle produced in the scaled-up procedure shall have symmetrical pressure applied on it in solvents, which is also likely to help maintain the phase stability of the **CC3**-*R*/**CC3**-*S* dispersion. The **CC3**-*R*/**CC3**-*S* cocrystals produced were microparticles (0.1-100 μm), and they were then screened among a range of solvents, mostly oils, as the size exclusion solvent candidates (**Figure 3.2**).

Table 3.1: Conditions screened for scaling up of synthesis of **CC3**-*R*/**CC3**-*S* microparticles by Dr Greenaway.

	Addition Rate	**Stirring Type**	**Temperature/°C**	**Morphology**	**DLS/nm**
1	Rapid	Prolonged, Magnetic Stirrer Bar	20 °C (RT)	Spherical	503
2	Rapid	Magnetic Stirrer Bar	20 °C (RT)	Spherical	442
3	0.66 mL/min	Magnetic Stirrer Bar	20 °C (RT)	Spherical	946
4	0.66 mL/min	Magnetic Stirrer Bar	0 °C	Spherical	787
5	0.66 mL/min	Magnetic Stirrer Bar	-78 °C	Spherical	1316
6	0.66 mL/min	Overhead	20 °C (RT)	Octahedral	943
7	Rapid	Overhead	20 °C (RT)	Spherical	540

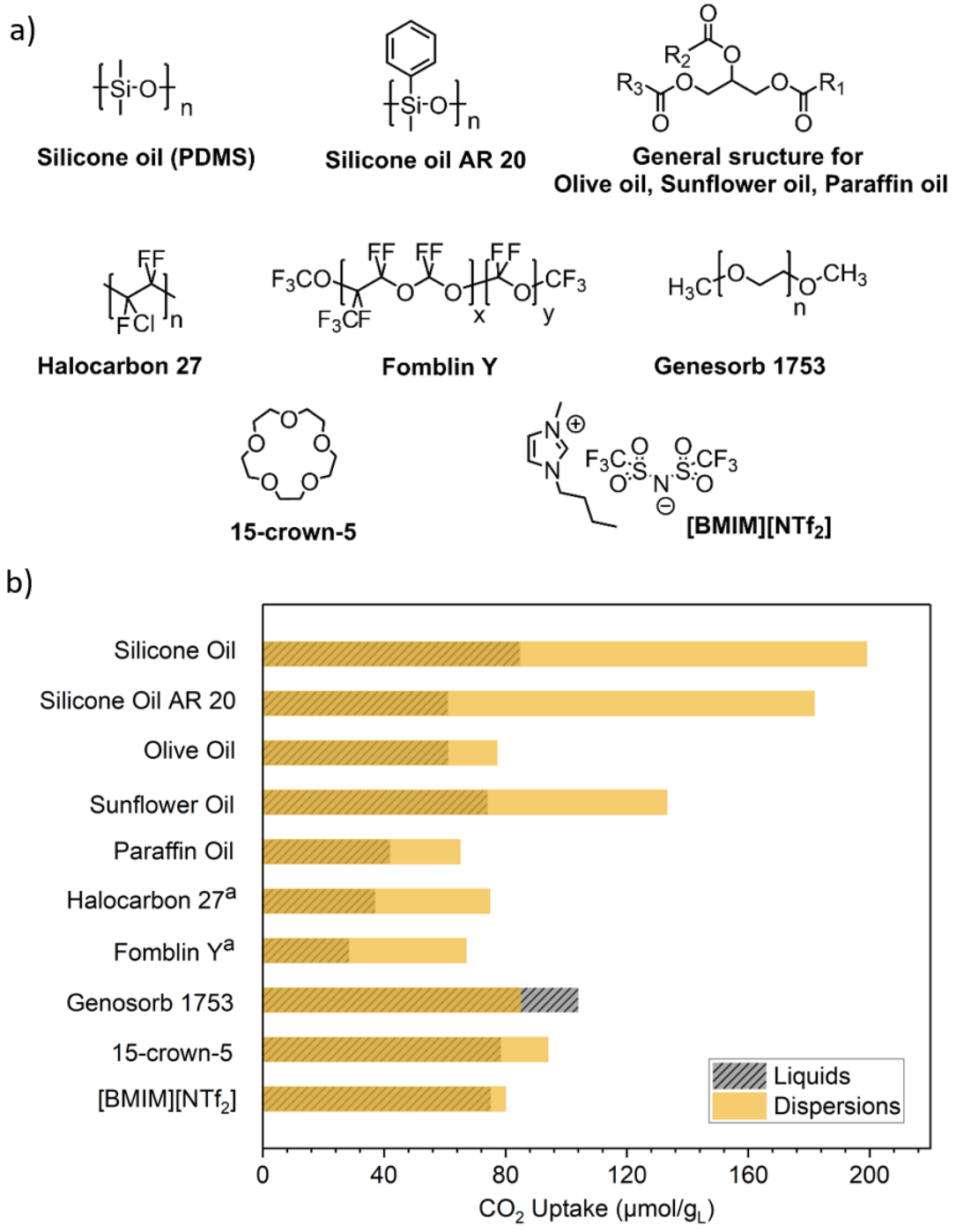

Figure 3.2: (a) Bulky liquids screened previously for the formation of type III porous liquids with **CC3**-*R*/**CC3**-*S* POC microparticles by Dr Greenaway; (b) Comparison of the CO_2 uptakes for the neat bulky liquids and corresponding 12.5 wt.% dispersions of **CC3**-*R*/**CC3**-*S*. [a] A 5 wt.% dispersion was prepared to reduce viscosity.

The optimisation of measurement conditions, setup and benchmarking on a Quatanchrome Nova instrument was also performed by Dr Greenaway (**Figure 3.3**, **Table 3.2**), with an allowed error limit set at 10 μmol/g_L. Previously, the study of gas uptakes in POC-derived type II porous liquids was realised by analytical techniques

such as IR and NMR spectroscopy or gas displacement measurements.[38,41,108] Here, bulky liquids with high boiling points and low vapour pressures allowed studying the gas solubility using more standard sorption measurements for analysing porous solids.

Figure 3.3: Quantachrome Nova 4200e and configuration used to measure gas uptake in liquid samples.

Table 3.2: Comparisons of CO_2 uptakes from literature to those measured with the Quantachrome Nova 4200e by Dr Greenaway.

Sample	**Literature H_{CO2} (bar)** [122]	**Calculated Literature CO_2 Uptake (µmol/g$_L$)**	**Average Measured Experimental Uptake (µmol/g$_L$)**
[BMIM][NTf_2]	33.0 ± 0.3 (25 °C, 1 bar)	71-73	75.1 ± 6.8
15-crown-5	45.8 (30 °C, 1 bar)	85-113	78.5 ± 3.1

The following discussion will only focus on experiments and studies on ionic liquids as solvents performed by the thesis author. Where necessary, comparisons with the systems studied by Dr Greenaway are specified.

3.3 Synthesis and characterisation of POC microparticles

CD spectroscopy, a technique that measures differential absorption of the left (L) and right (R) circularly polarised light, was used to confirm the chirality of **CC3**-*R* and **CC3**-*S*. Usually, no signals are observed if the L and R polarised light is absorbed to equal extents or not absorbed through a liquid sample, like the spectra of the DCM

solvent used (**Figure 3.4a**); [145] However, if L and R circularly polarised light is absorbed to different extents, for example by chiral molecules, the resulting spectra would present signals either positive or negative, and the R and S would form symmetric spectra, [145] just as the spectra of **CC3**-*R* and **CC3**-*S* (**Figure 3.4a**). HT voltage is applied to amplify the detector's signals, and if the HT signal is too high (> 700 V), the CD signals cannot be deemed valid. In **Figure 3.4b**, the wavelength range (225-280 nm) where CD signals of **CC3** appeared showed HT values well below 400 V, which confirmed the reliability of CD signals in **Figure 3.4a**. Then the formation of the POC microparticles was performed using the following conditions (**Figure 3.4c**), where two batches of **CC3**-*R*/**CC3**-*S* microparticles were received by rapidly mixing dilute solutions (1.5 mg/mL) of both **CC3**-*R* and **CC3**-S in DCM at RT with overhead stirring. Rapid precipitation of the POC microparticles was observed upon mixing. The microparticles were then isolated by membrane filtration.

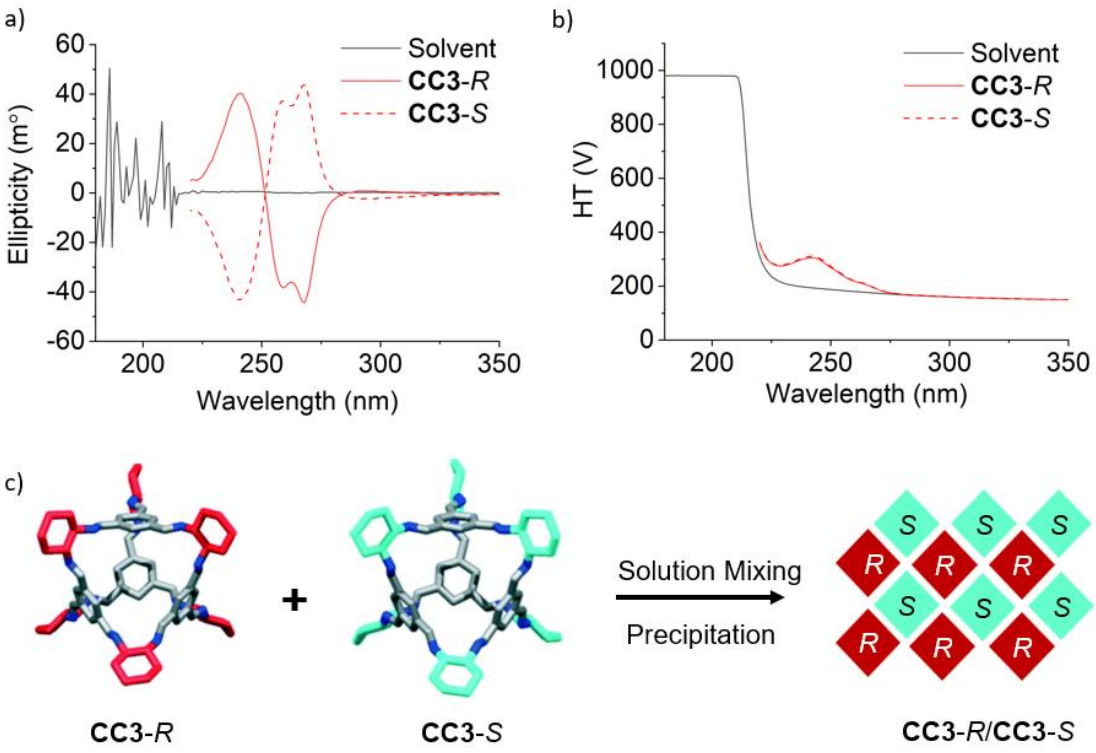

Figure 3.4: a) CD spectra of **CC3**-*R* and **CC3**-*S*; b); High tension voltage signals during CD measurements; c) Scheme of preparation of **CC3**-*R*/**CC3**-*S* microparticles.

Macroscopically, **CC3**-*R*/**CC3**-*S* microparticles were isolated as fine powders, and the PXRD patterns of the particles were recorded to check if the crystal structure had been affected by the mixing and filtration conditions. The PXRD results showed that the peaks of the racemic **CC3**-*R*/**CC3**-*S* microparticles were similar to those of the homochiral cage **CC3**-*R* and **CC3**-*S* (**Figure 3.5**), which all adopted the **CC3**-α window-to-window arrangement. [146] By looking at the diffraction data, the peak positions of microparticles can be found all shift to higher angles. For example, the diffraction peaks at 14.18° and 23.29° of the chiral cage **CC3**-*R* and **CC3**-*S* are shifted to higher angles, 14.39° and 23.73° for batch 1 **CC3**-*R*/**CC3**-*S* microparticles, 14.35° and 23.69° for batch 2, respectively. This indicated that the co-crystals had smaller unit cell sizes with tighter packing due to the use of opposite cage enantiomers, which could pack more closely.

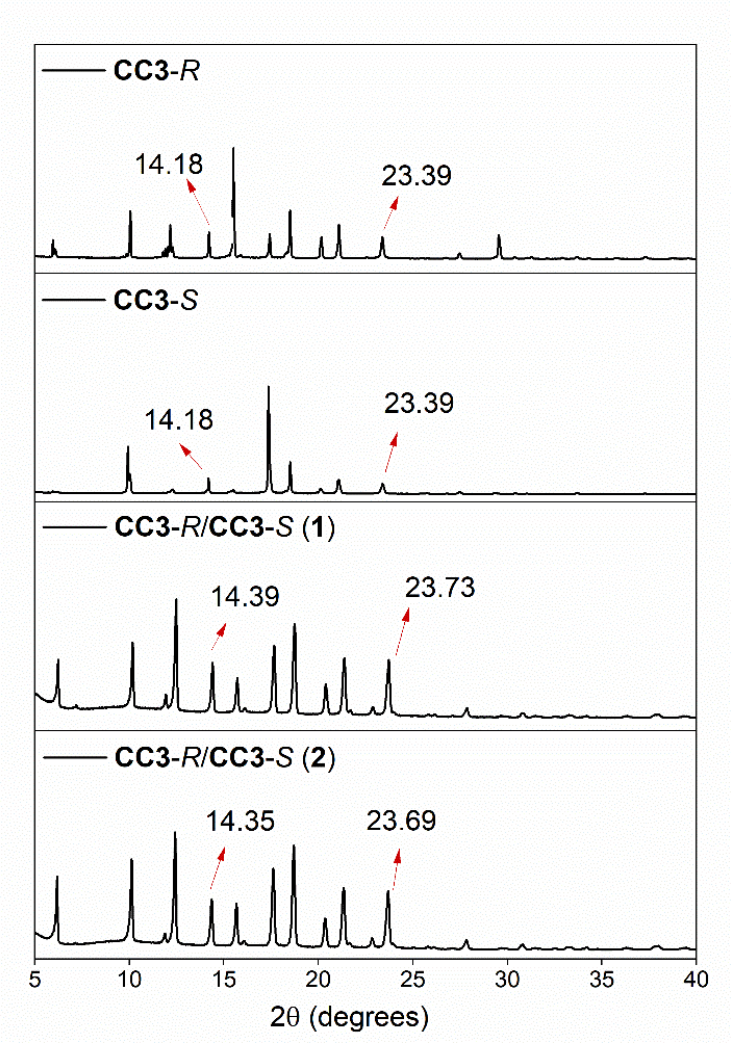

Figure 3.5: PXRD spectra of **CC3**-*R*, **CC3**-*S*, and **CC3**-*R*/**CC3**-*S* microparticles.

Size analysis of the **CC3**-*R*/**CC3**-*S* microparticles confirmed they were the desired microparticles, as determined by DLS measurements and SEM. The DLS size distribution of both batches of **CC3**-*R*/**CC3**-*S* microparticles ranged from 350 to 1000 nm according to plotting (**Figure 3.6**), while corresponding Z-average particle sizes were slightly different, which were 720 and 630 nm, respectively. This slight variation in the average size was due to the uncontrolled nature of the rapid-mixing method used.

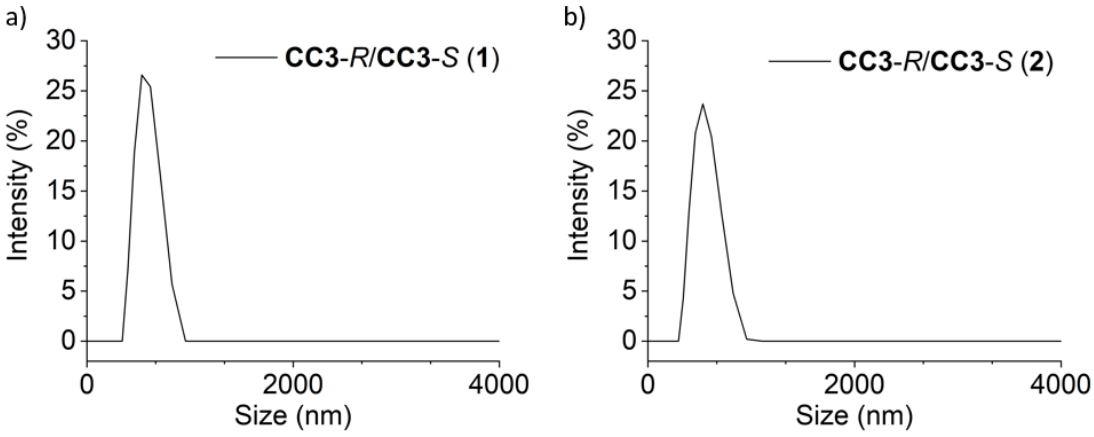

Figure 3.6: DLS of a) **CC3**-*R*/**CC3**-*S* microparticles batch 1; b) **CC3**-*R*/**CC3**-*S* microparticles batch 2.

To further confirm the size of the **CC3**-*R*/**CC3**-*S* microparticles, particle sizes from the acquired SEM images of both batches were also accounted and average sizes were calculated (**Table 3.3**). The SEM size range was mostly in accordance with that of DLS, while average sizes were slightly different, which is likely due to the Z-average by DLS being the light intensity weighted harmonic mean size whilst the average by SEM is the arithmetic mean. SEM also gave an indication of the particle morphology, where **CC3**-*R*/**CC3**-*S* microparticles acquired by the rapid mix-and-filtration method were all uniformly spherical in shape (**Figure 3.7a-d**). Examining the microparticles at increased magnification revealed that the surface of the particles was irregular, with triangle-shaped facets covering the particle surfaces. According to the study of Hassel *et al.*, the addition rate of cage stock solutions affects the shape of the cage microparticles. [132] When the addition rate was increased from slow to fast, the shape of particles could be changed from crystalline octahedrons to round spheres (**Figure 3.1**). Thus, the round particle shape with clear facets on the surface may be due to the medium addition rate used when mixing solutions of homochiral **CC3**.

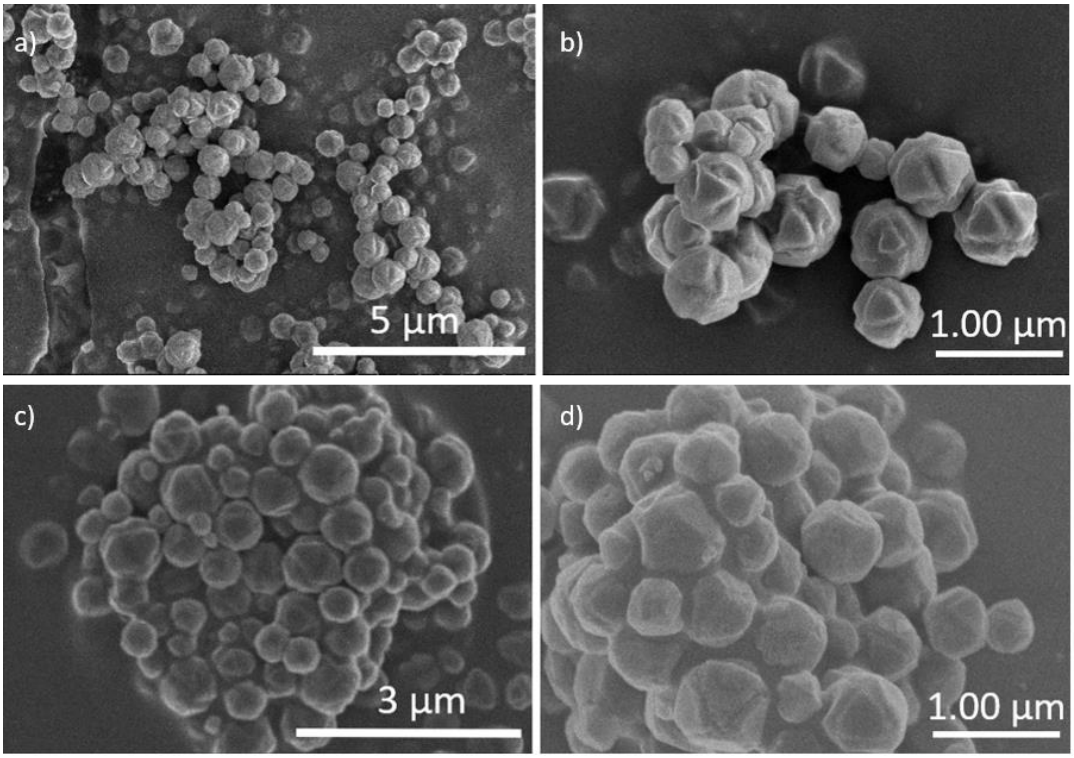

Figure 3.7: SEM images of a) **CC3**-*R*/**CC3**-*S* microparticles batch 1; b) **CC3**-*R*/**CC3**-*S* microparticles batch 1 at magnification; c) **CC3**-*R*/**CC3**-*S* microparticles batch 2; d) **CC3**-*R*/**CC3**-*S* microparticles batch 2 at magnification.

Table 3.3: Summary of the **CC3**-*R*/**CC3**-*S* microparticle compositions investigated, along with the measured particle sizes and observed particle morphology for each sample.

Microparticle Batches	**Z-Average Particle Size by DLS/nm**	**Particle Size Range by SEM/nm**	**Average Particle Size by SEM/nm**	**Particle Morphology by SEM**
CC3-*R*/**CC3**-*S* (**1**)	720	300–1000	613	Spherical
CC3-*R*/**CC3**-*S* (**2**)	630	200–800	599	Spherical

3.4 Screening for type III porous liquids using POC microparticles

The POC **CC3** was studied most extensively among the [4+6] serial of imine cages due to its good chemistry stability, high porosity, and versatile guest binding and separation performances, such as SF_6 sorption and shaping sorting among C8 and C9 aromatic isomers. [147–149] The **CC3-α** crystal adopts a window-to-window packing where an interconnected 3D pore channel runs through all of the packing molecules. And its channel diameter ranges from 5.8 Å, which is the diameter of the cage window, to 7.2 Å, which is the cavity diameter. [136] If static porosity is only considered at this stage, [85] it should be reasonable to compare the sizes of the pore channel and solvents to identify potential size-excluded ionic liquids in advance. As an ionic liquid consists of a cation and anion, the size-exclusion requirement, larger than 7.2 Å for **CC3** in this case, should be satisfied by both ions. However, the ionic radius is not physically meaningful to evaluate the size of ions in ionic liquids due to the poor definition of non-symmetrical ions often encountered in ionic liquids.[150] Thus, it may be challenging to compare the ion size with the window size of **CC3** directly in advance to determine whether the ion is likely to be size excluded. However, an empirical standard may be possible from previous knowledge of **CC3** host-guest properties. For example, anions like $[PF_6]^-$ can be ruled out from the study because their size and shape resemble that of SF_6, which **CC3** can absorb, and even smaller anions, such as Br^-, can also be ruled out.

To determine the porosity of each sample, gas uptakes of the pure liquid and the dispersion made from the liquid and **CC3-*R*/CC3-*S*** microparticles were measured using the same Quantachrome instrument and the same measurement conditions. Typically, at least two gas uptake measurements were performed using each sample during screening, with standard deviations calculated according to the difference between the measured gas uptake values. The reliability of gas uptake measurements was also checked during a recyclability study that was performed using the same material (see section 3.5.6 for full details and results). This is an important consideration as a size-excluded liquid may provide the system with extra capacity to accommodate the gas, thus improving gas uptakes. As data processing on Quantachrome was designed for solid samples, results such as surface area, which required mathematic operation eligible for solids, were not chosen. Only gas isotherms were discussed here, and 1800 s equilibrium time was given to each measuring point

with continuous stirring during sorption to ensure saturation, as the gas diffusion rate was slower in liquids. The former study with 1-butyl-3-methylimidazolium bis(trifluoromethylsulfonyl)imide ([BMIM][NTf_2]) by Dr Greenaway showed that the corresponding dispersion with a 12.5 wt.% loaded **CC3-*R*/CC3-*S*** microparticles in the ionic liquid did not present improved CO_2 uptake (**Figure 3.8**), which indicated the entry of the liquid into particles and failure of meeting size-exclusion requirement. The bis(trifluoromethylsulfonyl)imide anion is a commonly used in synthesising ionic liquids due to its bulky size and dispersed charge. Thus, before changing for more bulky anions, the cation was screened first for more bulky and rigid candidates.

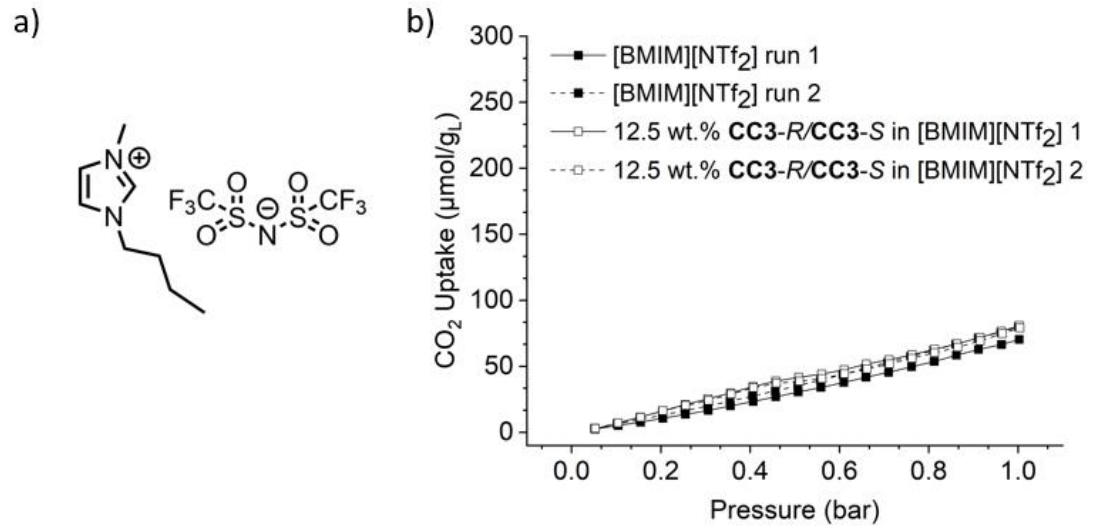

Figure 3.8: a) Structure of ionic liquid [BMIM][NTf_2]; b) CO_2 adsorption isotherms of [BMIM][NTf_2] and the corresponding 12.5 wt.% dispersion of **CC3-*R*/CC3-*S*** microparticles at RT by Dr Greenaway.

In the first screen, dispersions were prepared using the **CC3-*R*/CC3-*S*** microparticles (**Table 3.3, entry 1**) and previously reported size-excluded ionic liquids for MOFs and zeolites, including butyl pyridinium bis(trifluoromethanesulfonyl)imide ([BPy][NTf_2]) and [P_{66614}][NTf_2],[2,3,5] where the anion $[NTf_2]^-$ was remained to study the effect of cations on the gas uptake capability at first. Initially, 5 wt.% dispersions of **CC3-*R*/CC3-*S*** microparticles were prepared in these liquids by mixing and sonication. These dispersions were then screened for porosity, with comparisons of the gas uptakes with the neat ionic liquids.

Interestingly, even with less loading of **CC3-*R*/CC3-*S*** microparticles compared to the 12.5 wt.% [BMIM][NTf_2] dispersion, the [BPy][NTf_2] dispersion led to an improved gas uptake, where the 5 wt.% dispersion had a CO_2 uptake of 111.4 ± 6.4 μmol/g

compared to the blank [BPy][NTf_2]'s 78.3 ± 4.5 μmol/g at 1 bar (**Figure 3.9a-b**). By comparison with the uptakes of the [BMIM][NTf_2] dispersion, it was suggested that the anion $[NTf_2]^-$ was size-excluded, but the 5-membered imidazolium ring in the [BMIM] cation was not. In contrast, the 6-membered pyridyl ring in the [BPy] cation was even with the same n-butyl appended chains. Though [BPy] and [BMIM] cations have similar ionic volumes (0.196 vs 0.198 nm^3), [151] ionic radii differences in certain directions may give rise to the different performances here. The **CC3**-*R*/**CC3**-*S* dispersion in [P_{66614}][NTf_2] took up about 78.6 ± 7.0 μmol/g CO_2, which also presented increased CO_2 uptake in comparison with pure [P_{66614}][NTf_2], which had an uptake of 50.8 ± 4.0 μmol/g (**Figure 3.9c-d**).

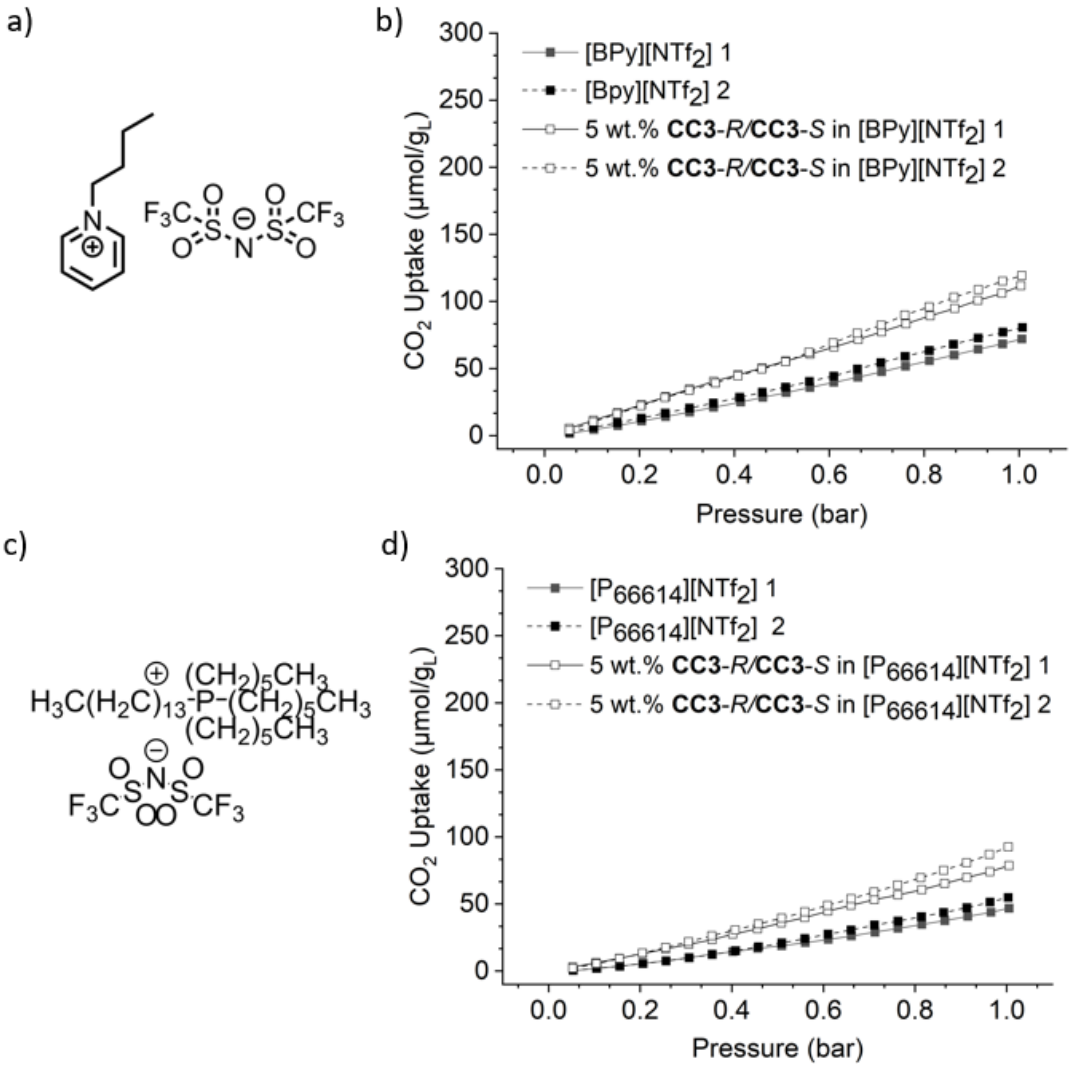

Figure 3.9: a) Structure of ionic liquid [BPy][NTf_2]; b) CO_2 adsorption isotherms of [Bpy][NTf_2] and the corresponding 5 wt. % dispersion of **CC3**-*R*/**CC3**-*S* microparticles at RT; c) Structure of ionic liquid [P_{66614}][NTf_2]; d) CO_2 adsorption isotherms of [P_{66614}][NTf_2] and the corresponding 5 wt. % dispersion of **CC3**-*R*/**CC3**-*S* microparticles at RT.

To further investigate the effect of structures of the ionic liquid (in terms of the effect of the cation) on the overall gas uptake performance, two different ionic liquid samples were also studied. Firstly, benzyl(ethyl)dimethyl ammonium bis(trifluoro-methanesulfonyl)imide ([BEMA][NTf_2]) is a quaternary ammonium salt which has different functional group from the pyridinium salt of [Bpy][NTf_2]. However, the benzene ring and 4-atoms-length of the ammonium alky chain in [BEMA] share a similar size as [BPy], and the ammonium head in the chain grants more bulkiness than the n-butyl chain. Comparison of the CO_2 uptakes at 1 bar and RT in [BEMA][NTf_2] and the corresponding **CC3-*R*/CC3-*S*** dispersions confirmed that the [BEMA] cation was also size-excluded, with a CO_2 uptake increase of 55 μmol/g over solvent (**Figure 3.10a-b**). This improvement was even larger than that of [Bpy][NTf_2], which was 36 μmol/g. The other 1-butyl-4-methylpyridinium bis(trifluoromethanesulfonyl)imide ([MBPy][NTf_2]), which has an extra *para*-methyl group to [BPy] in the cation, however, formed a dispersion with no increased uptake over the pure ionic liquid (**Figure 3.10c-d**). The porosity seemed to be shut off by introducing the methyl group into [BPy], indicating possible entry and blocking of the **CC3** cage window by the methyl group.

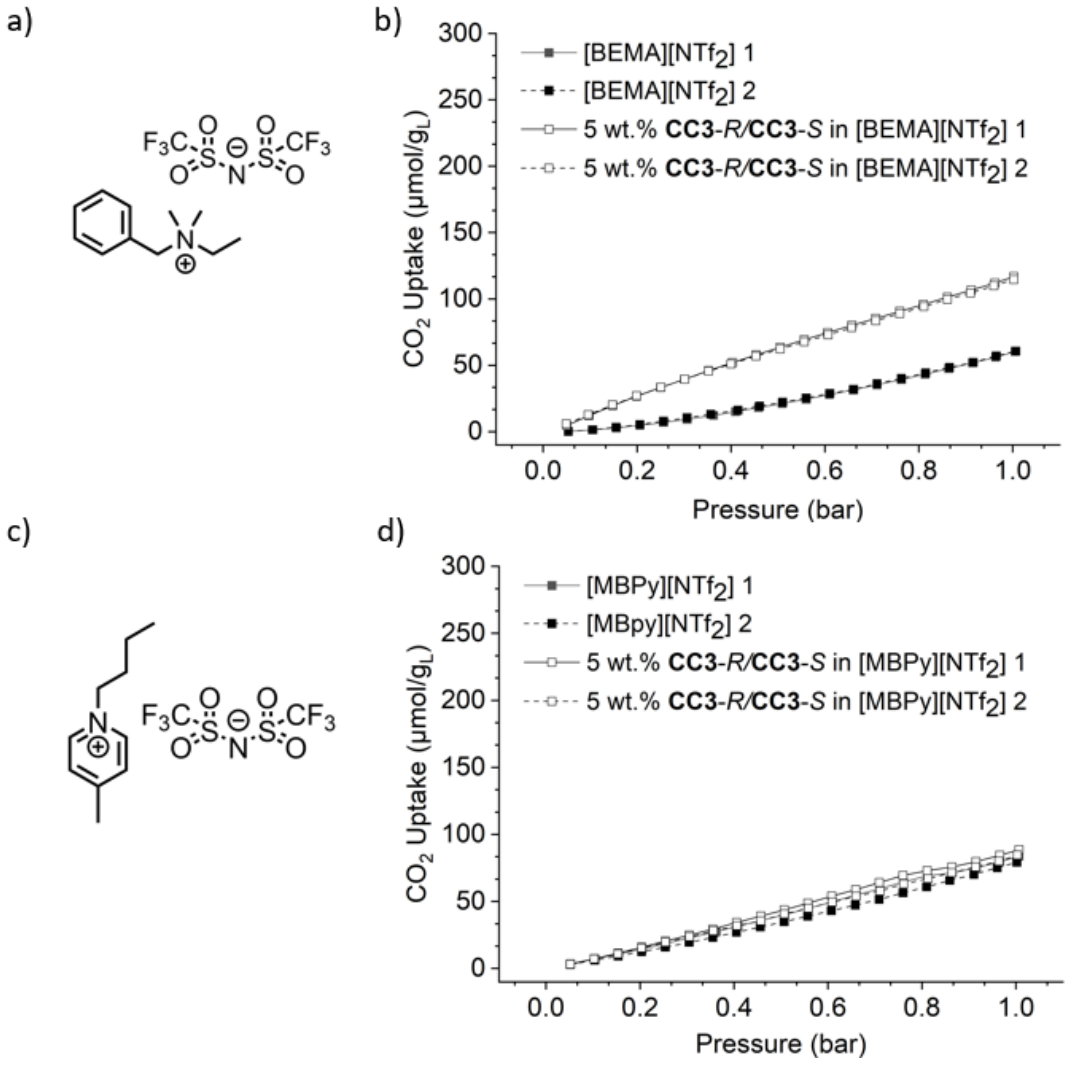

Figure 3.10: a) Structure of ionic liquid [BEMA][NTf_2]; b) CO_2 adsorption isotherms of [BEMA][NTf_2] and the corresponding 5 wt.% dispersion of **CC3-*R*/CC3-*S*** microparticles at RT; c) Structure of ionic liquid [MBPy][NTf_2]; d) CO_2 adsorption isotherms of [MBPy][NTf_2] and the corresponding 5 wt.% dispersion of **CC3-*R*/CC3-*S*** microparticles at RT.

To prove that it was the less bulkier methyl group in the cation [MBPy] that caused loss of porosity in the corresponding **CC3-*R*/CC3-*S*** dispersions, an ionic liquid 4-tertbutyl-1-butylpyridinium bis(trifluoromethanesulfonyl)imide ([TBPy][NTf_2]) was designed and synthesised, where the methyl group on the pyridinium ring was replaced by a bulkier *tert*-butyl group. The porosity was confirmed to be restored by comparing gas uptakes, with the 5 wt.% dispersion in [TBPy][NTf_2] adsorbing 39 μmol/g more CO_2 and 5-fold more CH_4 over the base ionic liquid (**Figure 3.11a-b**). This proved that the small size of the methyl group would shut off the porosity in the system of **CC3-*R*/CC3-*S*** dispersions. To check whether the methyl group on the imidazolium ring in [BMIM] was also the reason for its failure to meet size-exclusion requirements, another ionic liquid 1-butyl-3-butylimidazolium bis(trifluoromethanesulfonyl)imide

([BBIM][NTf_2]) was synthesised, where methyl was replaced by an n-butyl group. The resulting dispersion had an increase of 16 μmol/g CO_2 uptake and twofold more CH_4 uptake, which indicated that [BBIM] may still partially penetrate the molecular cavities of **CC3** and cause the system to lose some porosity (**Figure 3.11c-d**).

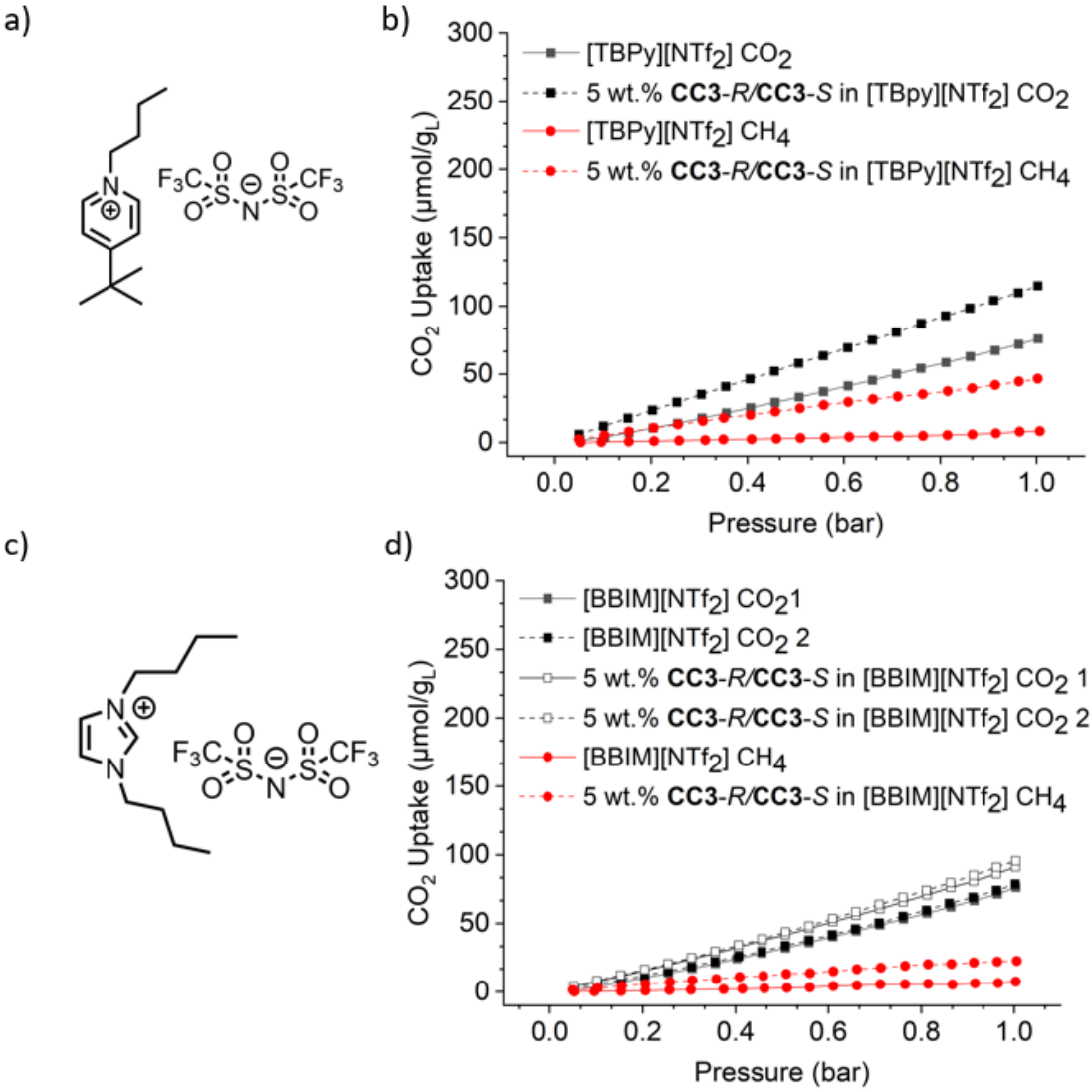

Figure 3.11: a) Structure of ionic liquid [TBPy][NTf_2] and CO_2 adsorption isotherms of [TBPy][NTf_2] and the corresponding 5 wt.% dispersion of **CC3-*R*/CC3-*S*** microparticles at RT.; b) Structure of ionic liquid [BBIM][NTf_2] and CO_2 adsorption isotherms of [BBIM][NTf_2] and the corresponding 5 wt.% dispersion of **CC3-*R*/CC3-*S*** microparticles at RT.

According to gas sorption data of the different ionic liquid dispersions, the anion $[NTf_2]^-$ appeared to fit the requirement of being size-excluded from the **CC3** system, and larger anions, such as tetrakis[3,5-bis(trifluoromethyl)phenyl]borate need not required.[29] For the cation, a benzene or pyridinium ring with a 4-carbon alkyl chain should be bulky enough, though finer tuning of the alkyl chain length, such as two or

three carbons atoms, is still needed to draw this conclusion safely. However, the 1-ethylpyridinium bis(trifluoromethanesulfonyl)imide ([EPy][NTf_2]) and 1-propylpyridinium bis(trifluoromethanesulfonyl)imide ([PPy][NTf_2]) appeared as solids at room temperature, they were not suitable to be used as dispersing liquid and thus not studied in detail here.

Further comparison of the measured gas uptakes alongside theoretical maximum uptakes for each dispersion was calculated by taking into account corresponding proportions of the cage solid uptake and the ionic liquid uptake (Theory uptake = 5 wt.%*$Uptake_{solid}$+ 95 wt.%*$Uptake_{IL}$). The percentage porosity maintained for the microparticles after being dispersed was calculated on the premise that the gas uptake of ionic liquid was not affected after the incorporation of microparticles (**Table 3.4**). In other words, the measured dispersion uptake difference from the theory value was caused by lost porosity from the dispersed microparticles. The calculated remaining porosity in dispersions screened ranged from 6-65% of the maximum theoretical porosity, which suggested that some porosity was lost on moving from the solid to the dispersed state, even for the systems which demonstrated the highest CO_2 uptakes. The observed reductions in uptake were likely due to several factors, including the potential loss of some extrinsic porosity that may be present among the POC microparticles in the solid state when **CC3-*R*/CC3-*S*** microparticles are dispersed, differing degrees of preferential gas binding, or interpenetration of ionic liquids used in forming dispersions to the cavities within the **CC3-*R*/CC3-*S*** microparticles. The ideal ionic liquid is [BEMA][NTf_2], with 65% of **CC3** porosity maintained in the dispersion, while the next two are [BPy][NTf_2] and the synthesised [TBPy][NTf_2], with 41% and 48% of their porosity maintained, respectively. By considering the availability and price of the three ionic liquids, [33] [BPy][NTf_2] is selected as the best option and engaged in further studies as it is commercially available, the cheapest, and has the lowest viscosity.

Table 3.4: Comparisons between the average experimental CO_2 uptakes, the theoretical maximum uptakes of the dispersions, and the percentage porosity maintained from the solid on being dispersed; The average CO_2 uptake of **CC3-*R*/CC3** microparticles (1792 ± 72.0 μmol/g_s, calculated from uptakes of two measurements on a Micromeritics ASAP 2020 volumetric adsorption analyzer) was collected by Dr Greenaway.

Solid	Liquid	Loading (wt.%)	Average Liquid Uptake (μmol/g_L)	Average Dispersion Uptake (μmol/g_L)	Calculated uptake for dispersion (μmol/g)	Percentage Porosity Obtained (%) (Measured vs Calculated)	Percentage Porosity from CC3-*R*/CC3-*S* maintained after Dispersing (%)
CC3-*R*/CC3-*S* [a]	[BMIM][NTf_2]	12.5	75	80	290	28	6
CC3-*R*/CC3-*S*	[BPy][NTf_2]	5	78	111	164	68	41
CC3-*R*/CC3-*S*	[P_{66614}][NTf_2]	5	51	79	138	57	34
CC3-*R*/CC3-*S*	[BEMA][NTf_2]	5	60	115	147	78	65
CC3-*R*/CC3-*S*	[MBPy][NTf_2]	5	81	86	166	52	10
CC3-*R*/CC3-*S*	[TBPy][NTf_2]	5	76	115	162	71	48
CC3-*R*/CC3-*S*	[BBIM][NTf_2]	5	77	93	163	57	22

In the preliminary screen, for **CC3-*R*/CC3-*S*** dispersions made from the size-excluded ionic liquids, gas uptake improvements were observed, indicating that the enhanced gas uptake was related to the **CC3-*R*/CC3-*S*** microparticles introducing extra pore volume into the liquid. To further confirm that the observed improvement in CO_2 uptake was due to the internal pore space of the **CC3-*R*/CC3-*S*** microparticles, rather than, say, certain interaction between groups of **CC3** and ionic liquid or surface adsorption on the microparticles, a control molecule that mimics a fragment of the **CC3** cage was synthesised (**Figure 3.12a, c**).[30] This non-porous control molecule did not dissolve in [BPy][NTf_2], and thus could also be dispersed, allowing us to evaluate the effect of surface adsorption on the particles and interactions between functional groups in the system at the same time. CO_2 isotherms were measured on the 5 wt.% dispersion of the control molecule in [BPy][NTf_2] for direct comparison with the 5 wt.% **CC3-*R*/CC3-*S*** dispersion. No improvement in CO_2 uptake was observed in the 5 wt.% control molecule dispersion system, confirming that neither functional group interactions nor surface adsorption contributed measurably to the observed improvements in gas uptake (**Figure 3.12b**). Additionally, in contrast to the microparticle dispersions in the same liquids, dispersions of the control molecule were not phase-stable, with sedimentation rapidly occurring (< 1 hour) on standing.

Dispersions of different batches of **CC3-*R*/CC3-*S*** microparticles and homochiral cage **CC3**-S in [BPy][NTf_2], were also investigated for their gas solubility – while similar gas uptakes were obtained among these systems (**Figure 3.12d**), the homochiral dispersions were not as colloidally stable as microparticles system, with sedimentation occurring when stirring was not maintained at room temperature. However, this further confirmed that these liquids are size excluded from the cage **CC3**.

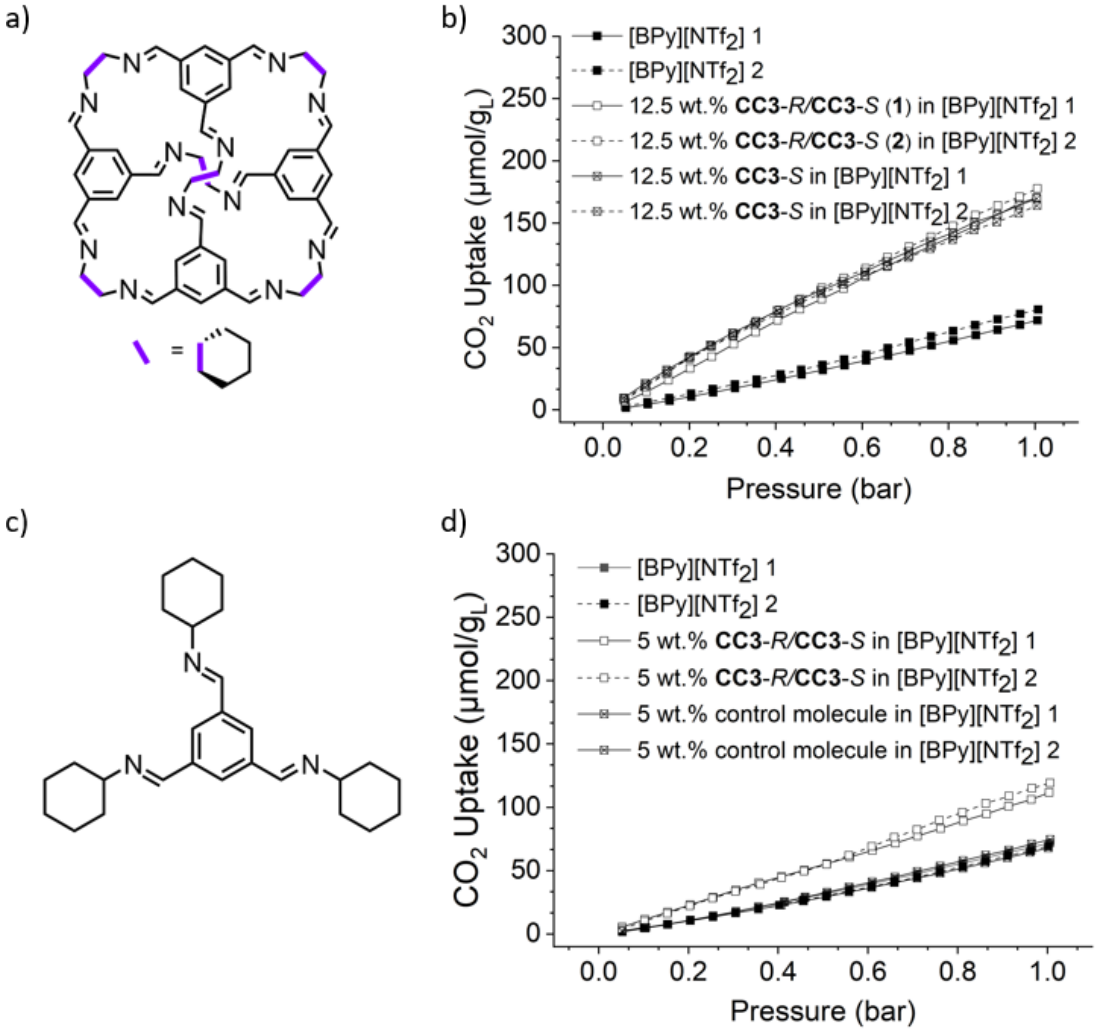

Figure 3.12: a) Structure of **CC3**; b) CO_2 adsorption isotherms of [BPy][NTf_2] and the corresponding 5 wt.% dispersions of different batches of **CC3-*R*/CC3-*S*** microparticles and **CC3-*S*** at RT; c) Structure of control molecule; d) CO_2 adsorption isotherms of [BPy][NTf_2] and the corresponding 5 wt.% dispersions of **CC3-*R*/CC3-*S*** microparticles and the control molecule at RT.

3.5 Properties and stability study of type III CC3-*R*/CC3-*S* microparticle porous liquids

3.5.1 Concentration

The gas uptakes for the dispersions with different **CC3-*R*/CC3-*S*** microparticle concentrations in [BPy][NTf_2] were studied. For the CO_2 sorption measurement (**Figure 3.13**), the gas uptakes of the 5 wt.%, 12.5 wt.% and 20 wt.% dispersions were 111.4 ± 6.4 μmol/g, 172.1 ± 3.6 μmol/g and 209.8 ± 6.7 μmol/g, respectively, which were all higher than that of the pure [BPy][NTf_2] (78.3 ± 4.5 μmol/g). The shape of isotherms for dispersions with higher loadings can be observed to be a little different from that of [BPy][NTf_2]. The isotherms of [BPy][NTf_2] were linear, which was

typical of a physisorption process based on Henry's law. [19] In contrast, the dispersion isotherms showed a slight curve at higher pressure, which may arise from the microporous property of **CC3**, with sorption trending towards saturation. For CH_4 sorption (**Figure 3.14**), as the ionic liquid [BPy][NTf_2] is a poor adsorbent for CH_4 compared to CO_2, the CH_4 uptake improvements of the dispersions were far more pronounced. For the 20 wt.% dispersion, the CH_4 uptake was 103.8 ± 0.7 μmol/g, which was nearly 13 times compared to that of pure [BPy][NTf_2] (7.9 ± 0.1 μmol/g). For the 5 wt.% and 12.5 wt.% dispersions of **CC3-*R*/CC3-*S*** microparticles in [BPy][NTf_2], corresponding CH_4 uptakes were 36.0 ± 0.3 μmol/g and 71.3 ± 3.9 μmol/g, which were nearly 4.5 and 9 times of the [BPy][NTf_2] uptake. And both CO_2 and CH_4 uptakes showed linear improvements with increasing **CC3-*R*/CC3-*S*** microparticles content from 0 to 20 wt.% for [BPy][NTf_2].

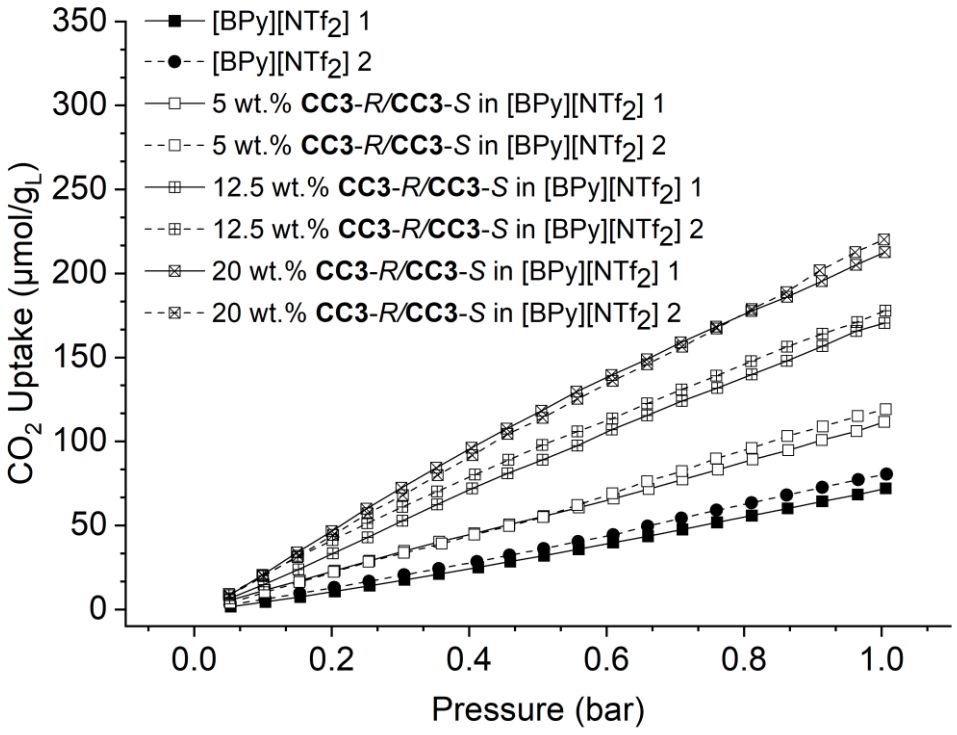

Figure 3.13: CO_2 adsorption isotherms of [BPy][NTf_2] and the corresponding 5 wt.%, 12.5 wt.% and 20 wt.% dispersions of **CC3-*R*/CC3-*S*** microparticles at RT.

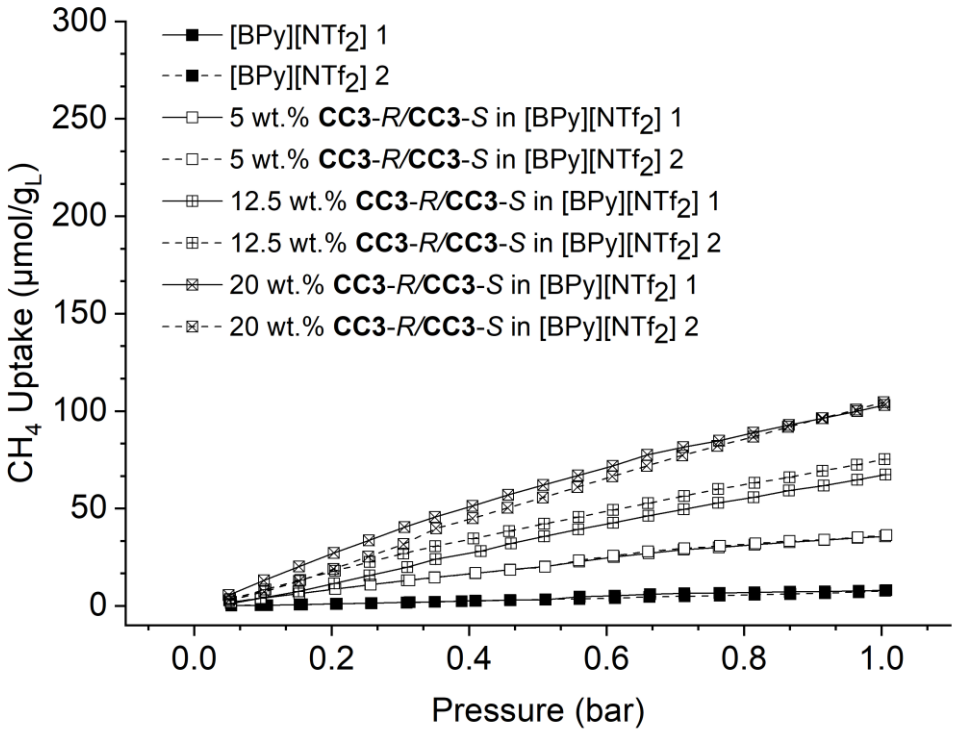

Figure 3.14: CH_4 adsorption isotherms of [BPy][NTf_2] and the corresponding 5 wt.%, 12.5 wt.% and 20 wt.% dispersions of **CC3-*R*/CC3-*S*** microparticles at RT.

Interestingly, the CO_2/CH_4 selectivity which was calculated based on the measured uptakes at 1 bar for dispersions with different wt.% microparticle content in [BPy][NTf_2] (**Table 3.5**) showed a decreasing trend with higher loadings. This may be due to [BPy][NTf_2] having better CO_2/CH_4 selectivity than **CC3-*R*/CC3-*S*** microparticles, which are 9.9 and 1.7, respectively. This indicates that the choice of size-excluded liquid could impact the overall gas uptake in a system and affect gas selectivity in type III porous liquids containing the same pore carrier.

Table 3.5: Summary of the calculated CO_2/CH_4 selectivity at 1 bar and RT for each system based on the measured uptakes.

System	CO_2/CH_4 Selectivity
[Bpy] [NTf_2]	9.9
5 wt.% **CC3-*R*/CC3-*S*** in [Bpy] [NTf_2]	3.1
12.5 wt.% **CC3-*R*/CC3-*S*** in [Bpy] [NTf_2]	2.4
20 wt.% **CC3-*R*/CC3-*S*** in [Bpy] [NTf_2]	2.0
CC3-*R*/CC3-*S*	1.7

Theoretical maximum uptakes of these dispersions, which were calculated by adding gas uptakes of corresponding components' uptake values, were also valued for comparison with experimental data (**Table 3.6-3.7**). For CO_2 sorption, dispersions with different loadings of **CC3-*R*/CC3-*S*** microparticles all presented lost porosity, with maintained porosity ranging from 41% to 46% of corresponding theoretical values toward CO_2. The decreased uptakes could be accounted for by the loss of CO_2 binding sites in the dispersions. As during CO_2 sorption of solid-state **CC3-*R*/CC3-*S*** microparticles, CO_2 was not only absorbed at intrinsic and extrinsic pore surfaces, but also interacted with imine bonds at the windows. [41] Thus CO_2 uptake can be lost quite a lot after **CC3-*R*/CC3-*S*** microparticles were dispersed in solvents. It showed a slightly lifted porosity by increasing **CC3-*R*/CC3-*S*** microparticle loading from 5 wt.% to 12.5 wt.% (from 41% to 46%) but dropped back with 20 wt.% loading (41%). The general decrease trend here may be due to more pronounced extrinsic porosity loss in the dispersions with increased content of **CC3-*R*/CC3-*S*** microparticles. In the situation for CH_4 sorption, dispersions with loadings from 5 wt.% to 20 wt.% showed a linear drop of porosity from 53% (5 wt.% loadings) to 46% (20 wt.% loadings). For CH_4 sorption, three dispersions (5 wt.%, 12.5 wt.% and 20 wt.%) maintained slightly more porosity if compared to CO_2, which probably was due to that CH_4 preferred to staying in the hydrophobic cavity of **CC3**, thus having fewer binding sites lost in the dispersions.

Table 3.6: Comparisons between the average experimental CO_2 uptakes, the theoretical maximum uptakes of the dispersions, and the percentage porosity maintained from the solid after being dispersed. The average CO_2 uptake of **CC3-*R*/CC3** microparticles (1792 ± 72.0 μmol/g_s, calculated from uptakes of two measurements on a Micromeritics ASAP 2020 volumetric adsorption analyzer) was collected by Dr Greenaway.

Solid	Liquid	Loading (wt.%)	Average Liquid Uptake (μmol/g_L)	Average Dispersion Uptake (μmol/g_L)	Calculated uptake for dispersion (μmol/g)	Percentage Porosity Obtained (%) (Measured vs Calculated)	Percentage Porosity from CC3-*R*/CC3-*S* maintained after Dispersing (%)
CC3-*R*/CC3-*S*	[BPy][NTf_2]	5	78	111	164	68	41
CC3-*R*/CC3-*S*	[BPy][NTf_2]	12.5	78	172	292	59	46
CC3-*R*/CC3-*S*	[BPy][NTf_2]	20	78	210	421	50	41

Table 3.7: Comparisons between the average experimental CH_4 uptakes, the theoretical maximum uptakes of the dispersions, and the percentage porosity maintained from the solid after being dispersed. The average CH_4 uptake of **CC3-*R*/CC3** microparticles (1064 ± 77.0 μmol/g_s, calculated from uptakes of two measurements on a Micromeritics ASAP 2020 volumetric adsorption analyzer) was collected by Dr Greenaway.

Solid	Liquid	Loading (wt.%)	Average Liquid Uptake (μmol/g_L)	Average Dispersion Uptake (μmol/g_L)	Calculated uptake for dispersion (μmol/g)	Percentage Porosity Obtained (%) (Measured vs Calculated)	Percentage Porosity from CC3-*R*/CC3-*S* maintained after Dispersing (%)
CC3-*R*/CC3-*S*	[BPy][NTf_2]	5	8	36	61	59	53
CC3-*R*/CC3-*S*	[BPy][NTf_2]	12.5	8	71	140	51	48
CC3-*R*/CC3-*S*	[BPy][NTf_2]	20	8	104	219.2	47	46

3.5.2 Viscosity

Viscosity studies on the 5, 12.5, and 20 wt.% **CC3-*R*/CC3-*S*** dispersions in [BPy][NTf_2] and the pure [BPy][NTf_2] ionic liquid were performed on a viscometer. An automatic data collection mode was used with an optimised and constant shear rate. The results showed that the viscosity of the dispersions increased with increasing particle concentration (**Table 3.8**), ranging from 67.3 ± 0.1 mpa·s for the pure [BPy][NTf_2] to 303.5 ± 0.3 mpa·s for the 20 wt.% dispersion. The high viscosity of the dispersions was due to the employment of the ionic liquids as base solvents, which were generally viscous with the dense coulombic compaction and charge network interactions among cations and anions. [152] To account for higher relative viscosities of the ionic liquid dispersions, which could slow down gas adsorption kinetics, longer equilibration times were employed to ensure saturation during subsequent gas sorption measurements. For comparison, the viscosities of the other ionic liquids screened were also measured. The size-excluded [P_{66614}][NTf_2] and [BEMA][NTf_2] were even more viscous than the 20 wt.% dispersion in [BPy][NTf_2], with viscosities 395.7 ± 0.3 and 496.6 ± 0.8 mpa·s, respectively. As viscous ionic liquids could lead to even more viscous **CC3-*R*/CC3-*S*** dispersions, which may pose a flowing issue and cause trouble in transferring or stirring, [BPy][NTf_2] with the lowest viscosity was considered more suitable as a solvent for constructing a type III porous liquid with **CC3-*R*/CC3-*S*** microparticles.

Table 3.8: Summary of viscosity measurements on the liquids and different concentration dispersions investigated.

Liquids	Viscosity (mpa·s)			
	0 wt.% Dispersion	**5 wt.% Dispersion**	**12.5 wt.% Dispersion**	**20 wt.% Dispersion**
[BPy][NTf_2]	67.3 ± 0.1	86.2 ± 0.2	142.2 ± 0.1	303.5 ± 0.3
[P_{66614}][NTf_2]	395.7 ± 0.3	-	-	-
[BEMA][NTf_2]	496.6 ± 0.8	-	-	-
[MBPy][NTf_2]	61.3 ± 0.1	-	-	-
[TBPy][NTf_2]	108.1 ± 0.1	-	-	-
[BBIM][NTf_2]	74.2 ± 0.2	-	-	-

3.5.3 Rheology

Rheology, a subject describing the deformation and flow behaviour of materials, was employed to study the flow behaviour of the **CC3-*R*/CC3-*S*** dispersion systems in [BPy][NTf_2]. Firstly, flow sweep experiments which studied the viscosity change of a material with increasing shear rate were performed, where the dispersions and pure ionic liquid were scanned over the shear rate from 0.1 to 100 s^{-1} to study their mechanical behaviours. Pure [BPy][NTf_2] had a disruptive dynamic viscosity pattern over the lower shear rate range (<1 s^{-1}), probably due to its low viscosity. Afterwards, pure [BPy][NTf_2] showed a constant viscosity value from 1 s^{-1} to 100 s^{-1} (**Figure 3.15**), which was typical of a Newtonian fluid, where the viscosity did not change as a function of the applied shear rate. The dynamic viscosity resulting from the shear flow on the rheometer (66.7 ± 0.1 mpa·s) was very similar to the viscosity measured on the viscometer (67.3 ± 0.1 mpa·s), which was based on extensional flow with a constant shear rate. In contrast, the dispersions with different concentrations of **CC3-*R*/CC3-*S*** microparticles in [BPy][NTf_2] expressed shear-thinning behaviours, where all the dispersions showed decreased viscosity with increasing shear rates to various degrees.

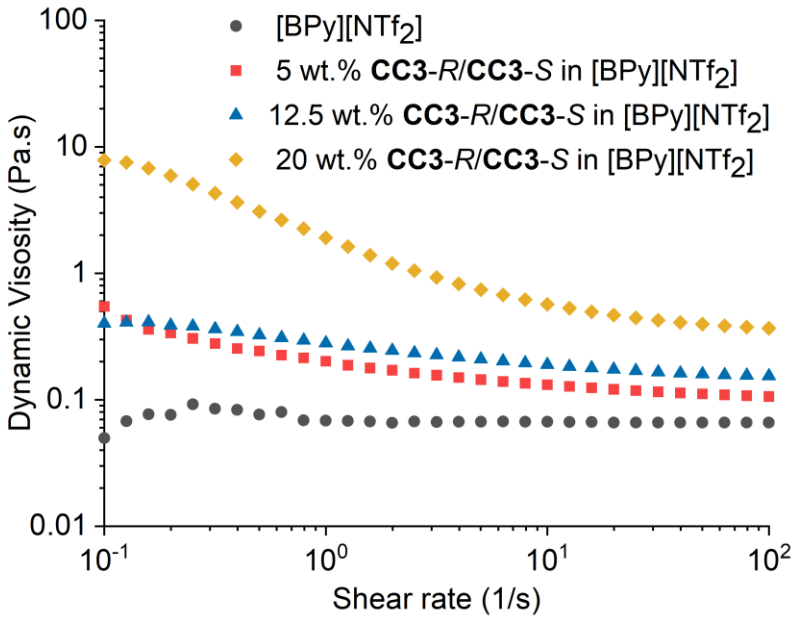

Figure 3.15: Flow Sweep experiments on [BPy][NTf_2] and 5 wt.%, 12.5 wt.% and 20 wt.% dispersions of **CC3-*R*/CC3-*S*** microparticles in [BPy][NTf_2] at RT over shear rate range from 0.1 to 100 s^{-1}.

The 20 wt.% **CC3-*R*/CC3-*S*** dispersion with the most pronounced shear thinning behaviour was studied further in a flow sweep experiment with an expanded shear rate range from 5 × 10^{-5} to 100 s^{-1} (**Figure 3.16**). During the rheology measurements, the 20 wt.% dispersion exhibited a plateau until around 2 × 10^{-3} s^{-1} and then dropped continuously afterwards. On a plot showing the shear viscosity against stress range corresponding to the shear rate from 5 × 10^{-5} to 100 s^{-1}, a peak was observed on the curve at 0.5 pa, demonstrating that the 20 wt.% dispersion had the yield stress. The yield stress indicated that the 20 wt.% dispersion possessed both solid and liquid properties in rheology and should have external stress applied exceeding a certain value (yield stress) for the system to exhibit liquid behaviour or flow. If the applied stress was less than the yield stress, the system would deform elastically like a solid, which matched the character of a highly shear-thinning fluid. The mechanism of this shear thinning behaviour may be related to the rearrangement of **CC3-*R*/CC3-*S*** microparticles in [BPy][NTf_2] in the plane of applied shear rate, where particles may aggregate to form larger agglomerates when at rest or lower shear rate, which would pose higher flow resistance. However, with increasing shear applied, the agglomerates would break down into smaller particles and deform in the direction of the shear, which could enable the flow resistance to decrease and then the material flows.

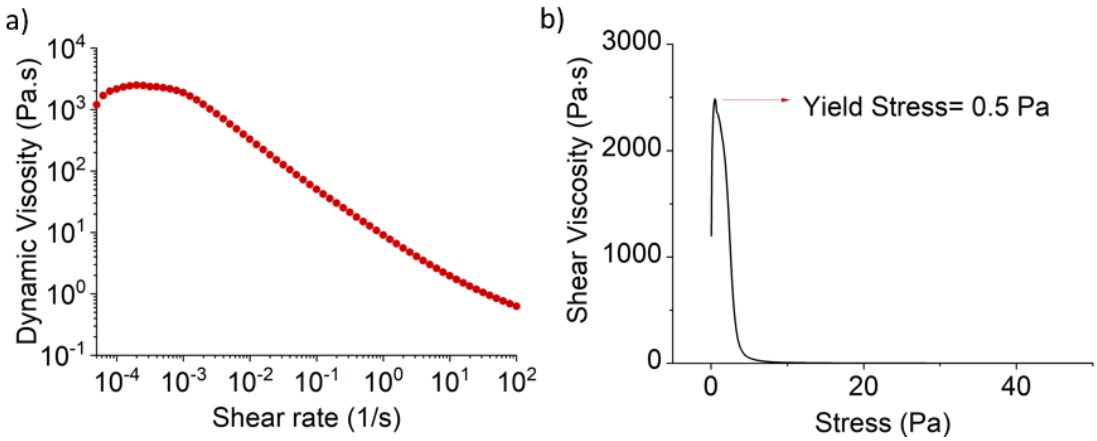

Figure 3.16: a) A flow sweep measurement on the 20 wt.% dispersions of **CC3-*R*/CC3-*S*** microparticles in [BPy][NTf_2] over shear rate range from 5×10^{-5} to 100 s^{-1}; b) Plotting of corresponding shear viscosity over the 5×10^{-5} to 100 s^{-1} range against time.

The flow sweep measurement confirmed that the 20 wt.% dispersion exhibited a yield point, which indicated the dispersion should present a viscoelastic behaviour between an ideal solid and an ideal liquid. To study the viscoelasticity of the system, a dynamic oscillatory amplitude measurement was performed on the 20 wt.% dispersion by increasing oscillatory strain from 1×10^{-2} to 1000% at a frequency of 1 Hz. The results showed that the storage modulus (G', representing a solid property of the system) was larger than the loss modulus (G", representing a liquid property of the system) below around 1% when the system exhibited solid property. G" then became larger than G' until 1000% when the system exhibited liquid property This again demonstrated the existence of the yield stress in the 20 wt.% **CC3-*R*/CC3-*S*** dispersion, where a certain stress threshold exited for the system to flow (**Figure 3.17**). Both G' and G" showed a decreasing trend with increasing oscillation strain applied to the system, but G' experienced a steeper drop starting at 1%, leading the system to exhibit liquid behaviours. Dynamic oscillatory frequency sweep experiments were then performed on the dispersion over the angular frequency range from 0.1 to 100 rad/s at 0.1 % and 10% oscillation strain, respectively (**Figure 3.18**). At 0.1 %, G' was larger than G" over the probed range due to the applied stress being less than the yield stress. Thus, the system behaved like a solid with elastic deformation. While at 10%, where the yield stress was exceeded, G" was larger than G' throughout the measurement and the system should flow like liquid. For both experiments, both G' and G" showed an increasing trend while angular frequency increased from 0.1 to 100 rad/s, indicating a strong relationship.

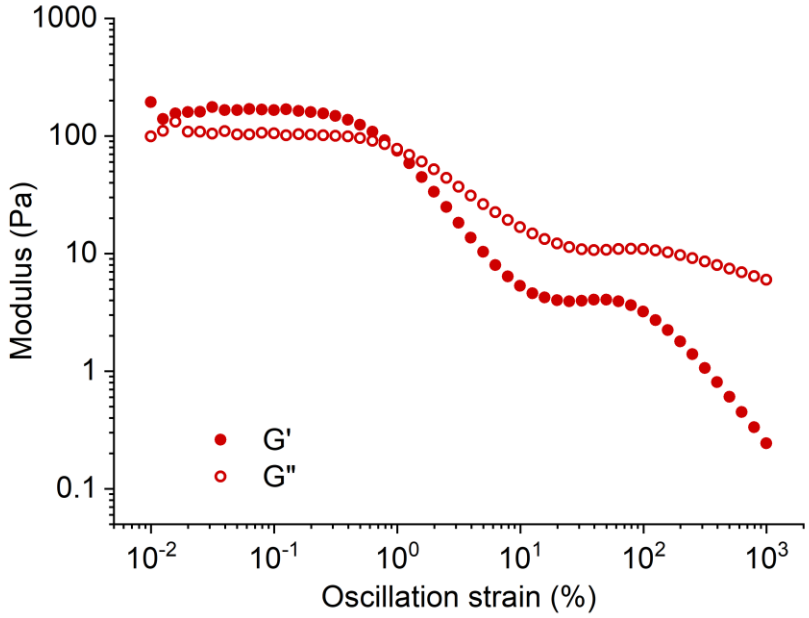

Figure 3.17: A dynamic oscillatory amplitude sweep experiment on the 20 wt.% dispersion of **CC3-*R*/CC3-*S*** microparticles in [BPy][NTf_2] from 1 to 10000% at a frequency of 1 Hz.

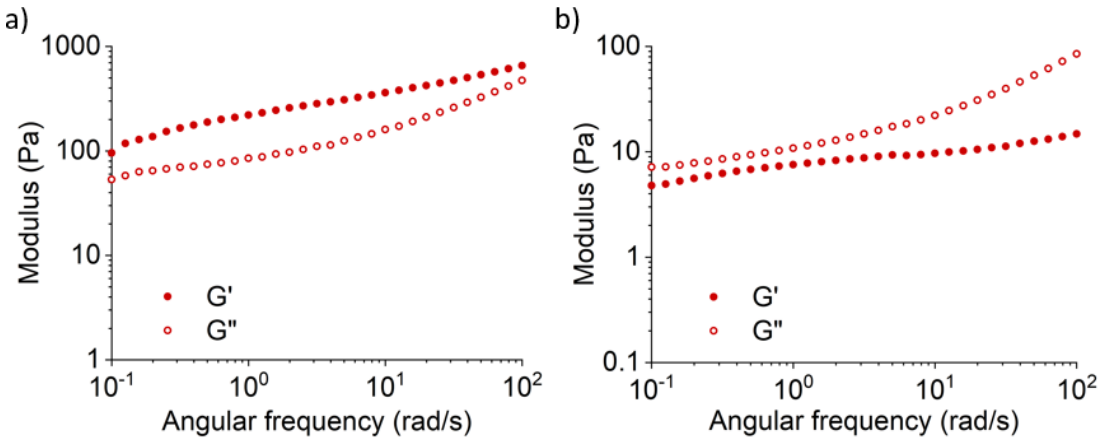

Figure 3.18: a) A dynamic oscillatory frequency sweep experiment on the 20 wt.% dispersion of **CC3-*R*/CC3-*S*** microparticles in [BPy][NTf_2] from 0.1 to 100 rad/s at a 0.1 % oscillation strain; b) A dynamic oscillatory frequency sweep experiment on the 20 wt.% dispersion of **CC3-*R*/CC3-*S*** microparticles in [BPy][NTf_2] from 0.1 to 100 rad/s at a 10 % oscillation strain.

3.5.4 Phase stability

All the [BPy][NTf_2] dispersions of **CC3-*R*/CC3-*S*** microparticles appeared visually stable over extended periods. To evaluate the phase stability of these microparticles in the ionic liquid, the wettability of [BPy][NTf_2] on the particles was first checked on a drop shape analyser to get a rough idea of the interaction between the particles and [BPy][NTf_2]. As **CC3-*R*/CC3-*S*** microparticles had poor solubility in most of the solvents, the microparticles were first pressed into a pellet with a relatively smooth surface for us to try the contact angle measurements. The experiment progressed with the sessile drop analysis, and the instrument was calibrated with contact angle measurements of water on a PTFE surface. Three runs showed a result of 130.7 ± 0.9°, which was in accordance with the values reported in the literature. [153]

Contact angle measurements were then performed by dropping about 4 μL [BPy][NTf_2] with a micropipette onto the **CC3-*R*/CC3-*S*** pellet. The ionic liquid drop appeared to be instantly absorbed into the pellet once it touched the surface. The absorption was likely to be caused by the capillary action occurring within channels formed among the particles in the material during pressing, and this posed difficulty in measuring the exact contact angle. By rewinding the video of the dropping process, the very first image of [BPy][NTf_2] contacting the **CC3-*R*/CC3-*S*** pellet surface was captured (**Figure 3.19a**). The mean contact angle was 46.3°, indicating good wetting of [BPy][NTf_2] on **CC3-*R*/CC3-*S*** microparticles. This roughly gave the impression that the microparticles could interact well with [BPy][NTf_2] ions instead of aggregating with adjacent particles in the dispersions; thus, phase stability could be ensured. In comparison, the contact angle of water on the **CC3-*R*/CC3-*S*** pellet was also measured. After the water drop maintained its shape for 3-4 seconds on the surface with a contact angle of 79.6°, absorption of the water also occurred quickly (**Figure 3.19b**). This sorption might be caused by the porous nature of **CC3,** which can absorb up to 20.1 wt.% water, [154] and the initial contact angle indicated not so good wetting of water on **CC3**, which was reasonable due to the hydrophobic nature of the cage.

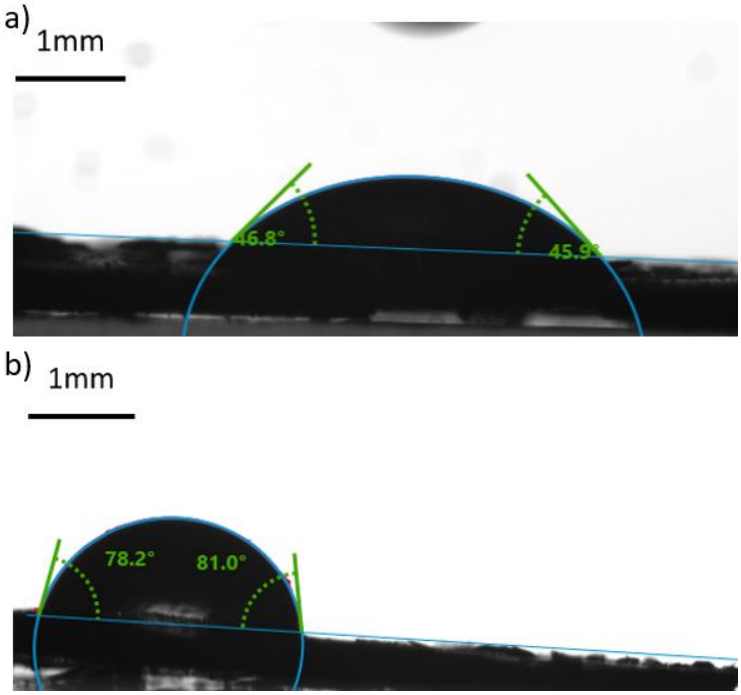

Figure 3.19: a) The image of the contact angles of [BPy][NTf2] on a **CC3-*R*/CC3-*S*** pellet captured in a rewinding video of dropping; b) The image of the contact angles of H_2O on a **CC3-*R*/CC3-*S*** pellet.

PXRD of pressed **CC3-*R*/CC3-*S*** was then measured and compared with an as-synthesised sample to check whether the crystal structure was affected by the high pressure applied during the pressing process (**Figure 3.20**). The PXRD peaks of the pressed microparticles appeared to be broader than the as-synthesised samples, and the intensity of the peaks also seemed to be lower, based on the comparison to the background. Together, the changes in the PXRD data indicate the crystals become smaller and lose some long-range order after the high-pressure pressing. The crystal structure change posed some questions about the reliability of the contact angle results on **CC3-*R*/CC3-*S*** pellets. Thus, another sample preparation method was employed. The second method involved dissolving homochiral **CC3** in DCM, dropping the solution on a glass plate, and then evaporating it into a smooth film. Homochiral **CC3** and **CC3-*R*/CC3-*S*** microparticles share the same chemical and crystal structure and thus should have similar wetting behaviours towards solvents. Both contact angles of [BPy][NTf_2] and water were then measured on the surface of the **CC3** film (**Figure 3.21**). Results showed that contact angles of [BPy][NTf_2] on **CC3**-R film were determined as 19.8 ± 1.8°, which proved its good wetting behaviour, and the water contact angles on the **CC3** film were 78.2 ± 2.9°, similar to that measured on pellets.

Above all, the good interaction between **CC3-*R*/CC3-*S*** microparticles and [BPy][NTf_2] was successfully confirmed.

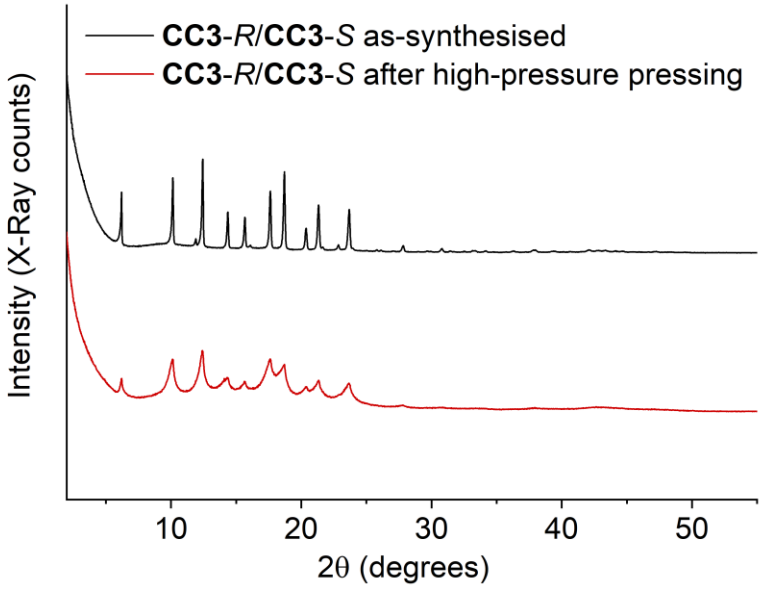

Figure 3.20: PXRD of as-synthesised and pressed **CC3-*R*/CC3-*S*** microparticles.

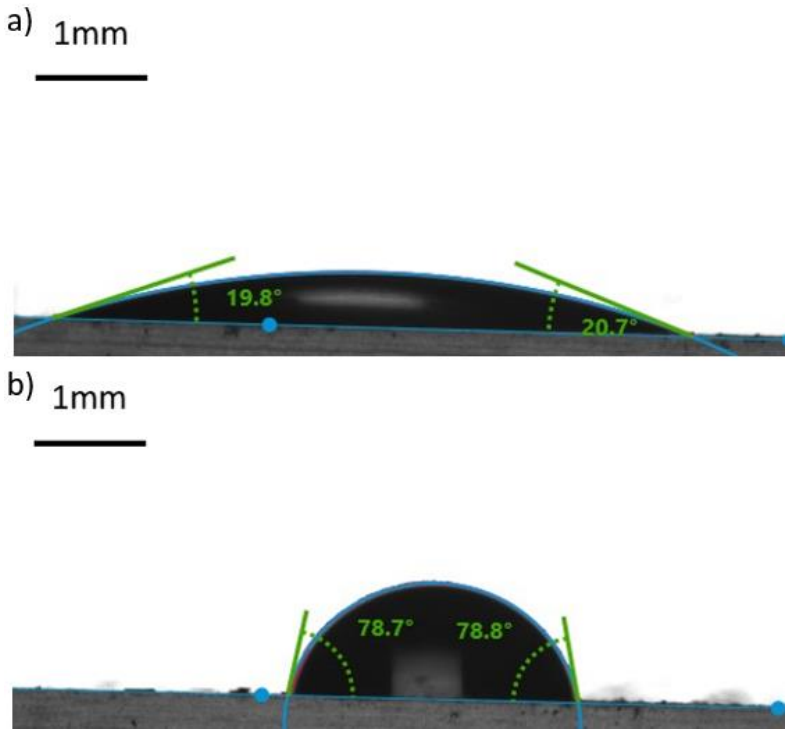

Figure 3.21: a) The image of the contact angles of [BPy][NTf2] on the **CC3-*R*** film formed on a glass plate; b) The image of the contact angles of H_2O on the **CC3-*R*** film formed on a glass plate.

To quantify the dispersion phase stability, LUMiSizer® was then used to accelerate the creaming or sedimentation process for the 5 wt.% and 12.5 wt.% dispersions of **CC3-*R*/CC3-*S*** (particle size: 500–700 nm) in [BPy][NTf_2].[155] According to the Stoke-Einstein equation, particle size plays an important role in determining the ratio of gravitational to Brownian forces applied to the particles in a dispersion. Hence, **CC3-*R*/CC3-*S*** microparticles with reduced particle size can help control the sedimentation velocity in [BPy][NTf_2] and thus stabilise multiphase systems.[156] **CC3-*R*/CC3-*S*** dispersions were pipetted into transparent sample cells (2 mm, rectangular synthetic cell 108-131 mm) and measured at 25 °C and light with a wavelength of 865 nm. Speed and time settings were 2000 RPM with 700 scans at 30 second intervals (or 1000 x 21) for a total run time of 350 min. RCF can be calculated from RPM and the centrifugal radius (r) in mm by the formula below. [157]

$$\mathrm{RCF} = \left(\frac{\mathrm{RPM}}{1000}\right)^2 \times \mathrm{r} \times 1.118$$

With an RPM of 2000 and the relative centrifugal force of 532 × g applied to the dispersion system, the **CC3-*R*/CC3-*S*** microparticles phased out by creaming to the surface of the transparent [BPy][NTf_2], which was indicated by the appearance of light transmission (represented by the colourful part) propagated from right to left in **Figure 3.22.** The average sedimentation velocity was received from the software and converted as 0.1 mm/day for the 5 wt.% dispersion and 0.04 mm/day for the 12.5 wt.% dispersion system (**Table 3.9, Figure 3.22-3.23),** indicating that the dispersions were stable. The stabilised system could be due to the high viscosity of the ionic liquid, or potentially because the cation and anion of [BPy][NTf_2] provided electrostatic stabilisation for the **CC3-*R*/CC3-*S*** microparticles. [158]

Table 3.9: Summary of dispersion stability results from LUMiSizer®

Dispersions	**RPM**	**Stability**	**RCF at midpoint**	**Average V at RCF (um/s)**	**Average V at gravity (um/s)**	**Average V at gravity (mm/day)**
5 wt.% **CC3-*R*/CC3-*S*** in [BPy][NTf_2]	2000	Creaming	532	0.8305	1.560×10^{-3}	0.1
12.5 wt.% **CC3-*R*/CC3-*S*** in [BPy][NTf_2]	2000	Creaming	532	0.2554	4.799×10^{-4}	0.04

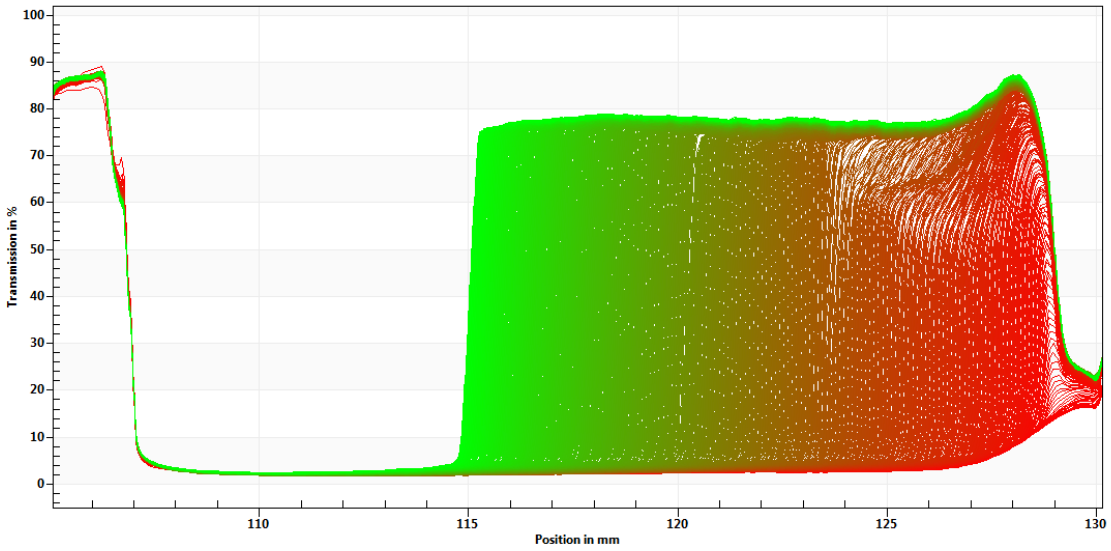

Figure 3.22: 5 wt.% **CC3-*R*/CC3-*S*** dispersion in [BPy][NTf_2] (propagation from right to left indicates creaming).

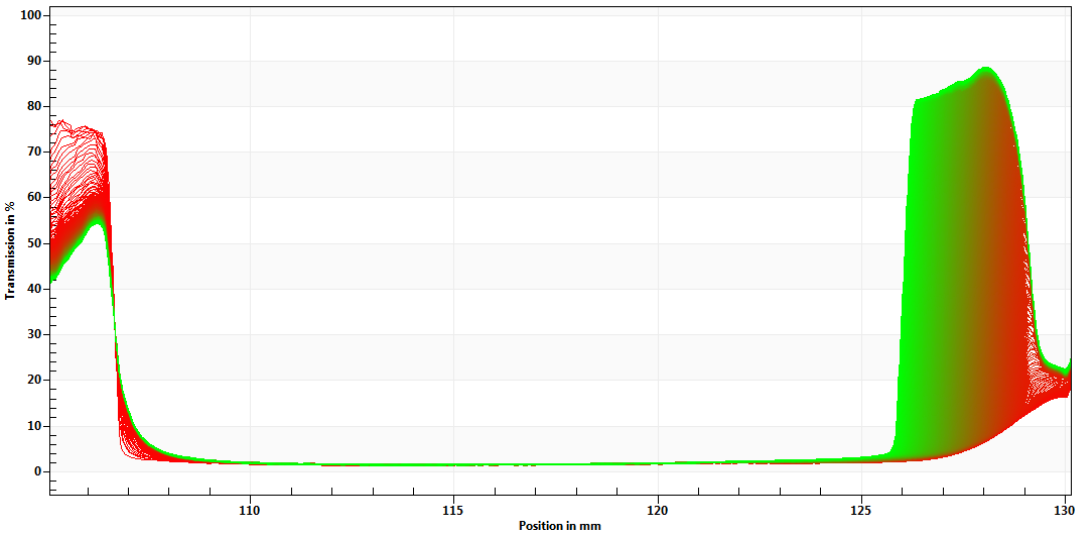

Figure 3.23: 12.5 wt.% **CC3-*R*/CC3-*S*** dispersion in [BPy][NTf_2] (propagation from right to left indicates creaming)

3.5.5 Pore carrier stability

Solvents sometimes have non-negligible effects on porous materials, such as MOFs can undergo structural change in some solvents. [33] The same can be true for porous organic cages, where some imine cages hydrolyse readily in water. However, **CC3** is relatively stable and can absorb water reversibly. [154] To check whether the crystal structure of **CC3-*R*/CC3-*S*** microparticles would be affected by the ionic liquid [BPy][NTf_2], we performed capillary PXRD measurements of **CC3-*R*/CC3-*S*** microparticles and dispersions with different cage concentrations of 5 wt.%, 12.5 wt.%, 20 wt.%, respectively. The PXRD patterns are shown in **Figure 3.24**. As it can be seen in the PXRD patterns, the crystallinity of the **CC3-*R*/CC3-*S*** microparticles retained upon formation of dispersions in [BPy][NTf_2], as the corresponding diffraction peak positions of the **CC3-*R*/CC3-*S*** microparticles all remained in the dispersions, although the baselines were affected by the [BPy][NTf_2] background signal. As expected, the porous liquids with higher wt.% of **CC3-*R*/CC3-*S*** microparticles had more intense diffraction peaks. These results indicated that the dispersions were chemically stable, where the [BPy][NTf_2] neither reacted with **CC3-*R*/CC3-*S*** nor interfered with its crystal packing.

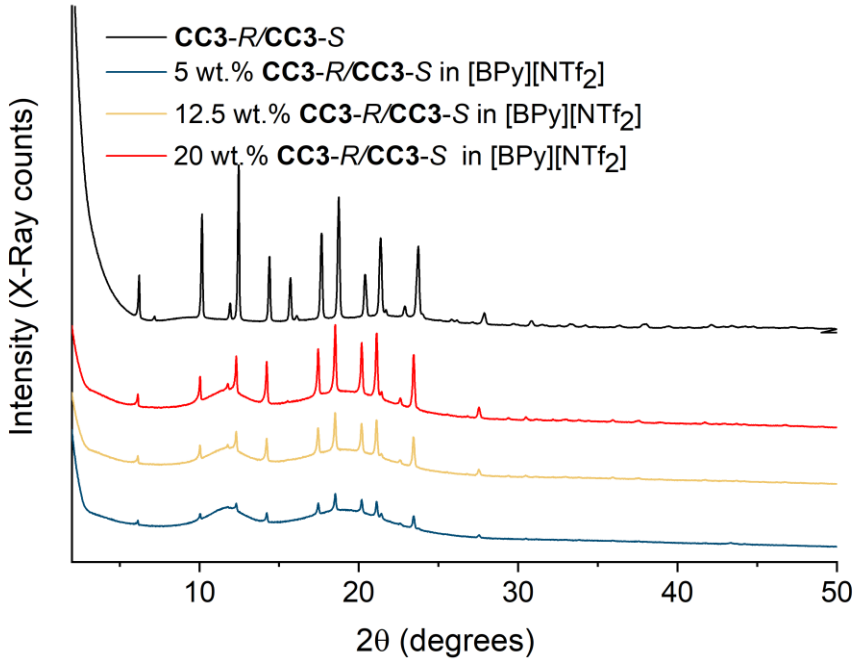

Figure 3.24: Capillary PXRD patterns of **CC3-*R*/CC3-*S*** microparticles and corresponding 5 wt.%, 12.5 wt.% and 20 wt.% dispersions in [BPy][NTf_2].

Infrared spectroscopy was next performed on **CC3-*R*/CC3-*S*** microparticles, [BPy][NTf_2] and corresponding dispersions to check the chemical structure intactness. The IR peaks of **CC3-*R*/CC3-*S*** fitted the data of **CC3** in the literature,[136] where 1648 cm^{-1} corresponded to C=N stretch vibration (**Figure 3.25a**). In the [BPy][NTf_2] spectra, strong peaks between 1250 to 1000 cm^{-1} were C-F vibrations in the anion NTf_2^- while the O=S=O stretch of the sulfonamide appeared at 1345 cm^{-1}. The peak at 1636 cm^{-1} was a C=N bond, which red-shifted to a lower wavenumber due to the conjugation to C=C bond on the pyridinium ring in $[BPy]^+$ (**Figure 3.25b**). For the IR spectra of dispersions, most of the **CC3-*R*/CC3-*S*** peaks were swamped by those of [BPy][NTf_2] except for the 20 wt.% one with higher microparticle loading, where some traces of **CC3** peaks could be found such as 2858 cm^{-1} and 1448 cm^{-1} which were related with C-H vibrations (**Figure 3.25c**). The seeming disappearance of C=N stretch peak of **CC3-*R*/CC3-*S*** in the dispersions was due to overlapping with that of the pyridinium ring. And if another ionic liquid [P_{66614}][NTf_2] with no C=N group in the ionic liquid cation was employed as the solvent (**Figure 3.25d**), the corresponding dispersion spectra could display the stretch vibration peak of imine bonds from **CC3-*R*/CC3-*S*** at 1648 cm^{-1}.

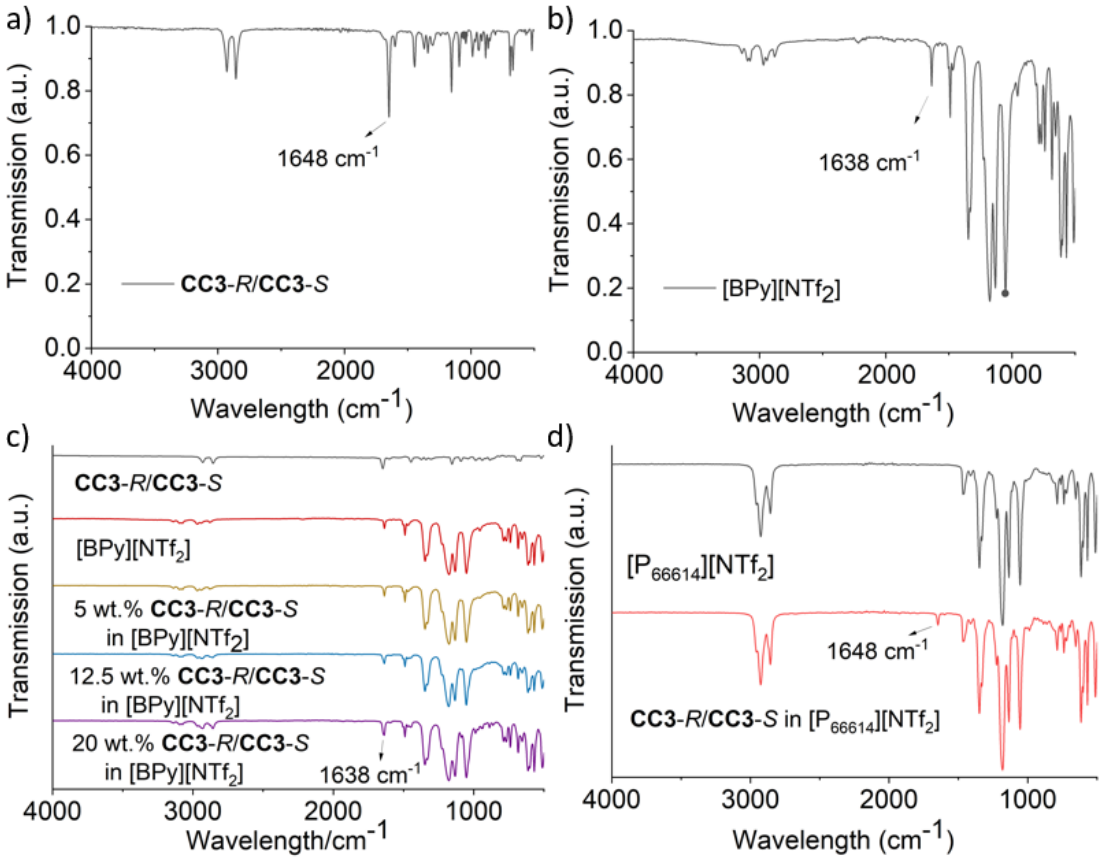

Figure 3.25: IR of a) **CC3-*R*/CC3-*S*** microparticles; b) [BPy][NTf_2]; c) **CC3-*R*/CC3-*S*** microparticles, [BPy][NTf_2] and corresponding dispersions; d) [P_{66614}][NTf_2] and a 5 wt.% dispersion of **CC3-*R*/CC3-*S*** in [P_{66614}][NTf_2].

The crystal structure of **CC3-*R*/CC3-*S*** microparticles was also checked after the CO_2 sorption measurements on the dispersion, where **CC3-*R*/CC3-*S*** microparticles was recovered from a 12.5 wt.% dispersion by filtering out [BPy][NTf_2], washing with ethanol and drying at 90 °C under vacuum overnight. PXRD of the recovered microparticles was compared to that of as-synthesised **CC3-*R*/CC3-*S*** microparticles (**Figure 3.26**). All the peaks were in good agreement between the two samples, indicating the good tolerance of **CC3-*R*/CC3-*S*** towards CO_2 sorption in the ionic liquid dispersion. The morphology of recovered **CC3-*R*/CC3-*S*** microparticles was also checked. From the SEM image, particles maintained the round-shaped morphology, and the average particle size calculated from the SEM was 655 nm, which presented a similar size to that of as-synthesised microparticles. However, the particles did seem to aggregate with another substance, which may be caused by the residual ionic liquid. [159]

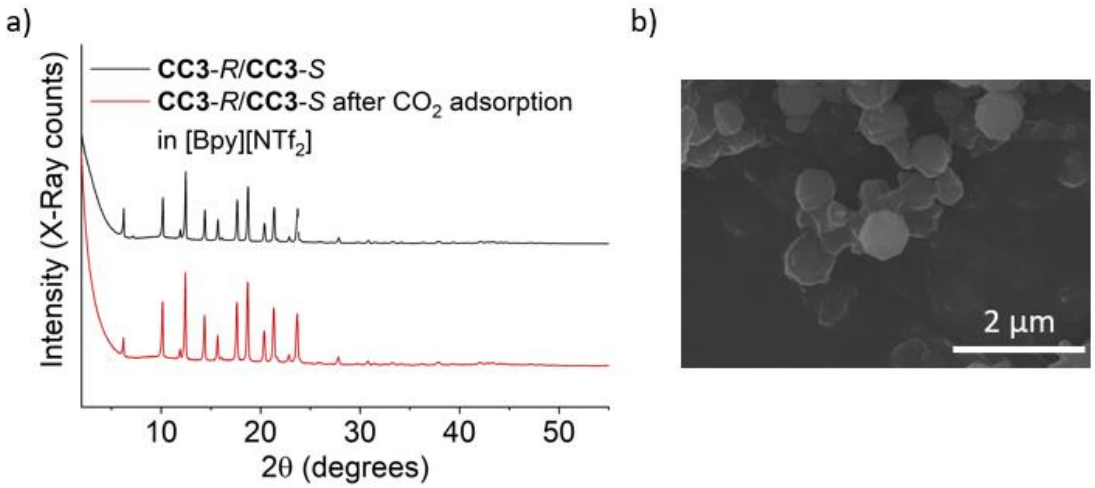

Figure 3.26: a) PXRD b) SEM image of the recovered **CC3-*R*/CC3-*S*** microparticles from a 12.5 wt.% dispersion in [BPy][NTf_2] by filtration after gas sorption studies.

3.5.6 Recyclability and aging

The previously described IR and PXRD measurements indicated that the **CC3-*R*/CC3-*S*** microparticles had good stability in [BPy][NTf_2]. Therefore, the recyclability of the dispersion as gas sorbents was evaluated. The CO_2 uptake of a 12.5 wt.% dispersion of **CC3-*R*/CC3-*S*** in [BPy][NTf_2] was measured over ten cycles (**Figure 3.27**), with re-activation by vacuum degassing for 100 minutes carried out between each measurement. The CO_2 uptakes were reproducible, with no apparent loss in uptake over repeated cycles (average CO_2 uptake in ten cycles: 174.3 ± 4.6 µmol/g), confirming the good recyclability of the system.

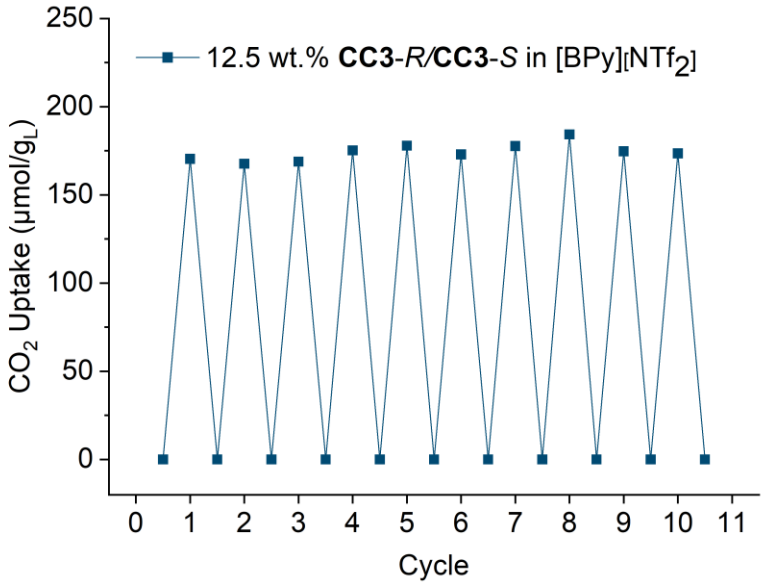

Figure 3.27: Recycling study for CO_2 uptakes (1 bar, 25-27 °C) in a 12.5 wt.% dispersion of **CC3-*R*/CC3-*S*** in [BPy][NTf_2].

One sample of 12.5 wt.% **CC3-*R*/CC3-*S*** dispersion in [BPy][NTf_2] was left covered with parafilm for one month after the first CO_2 sorption measurement, and then it was degassed and measured the CO_2 uptake again to check its long-time stability. The result showed that the isotherm measured after one month was like that of the first day, and the uptakes at 1 bar were almost the same, demonstrating the durable stability of the system (**Figure 3.28**). Overall [BPy][NTf_2] was proved to have a negligible effect on the crystal and chemical structure of **CC3-*R*/CC3-*S*** microparticles, and the dispersion system formed presented recyclable and durable CO_2 sorption properties.

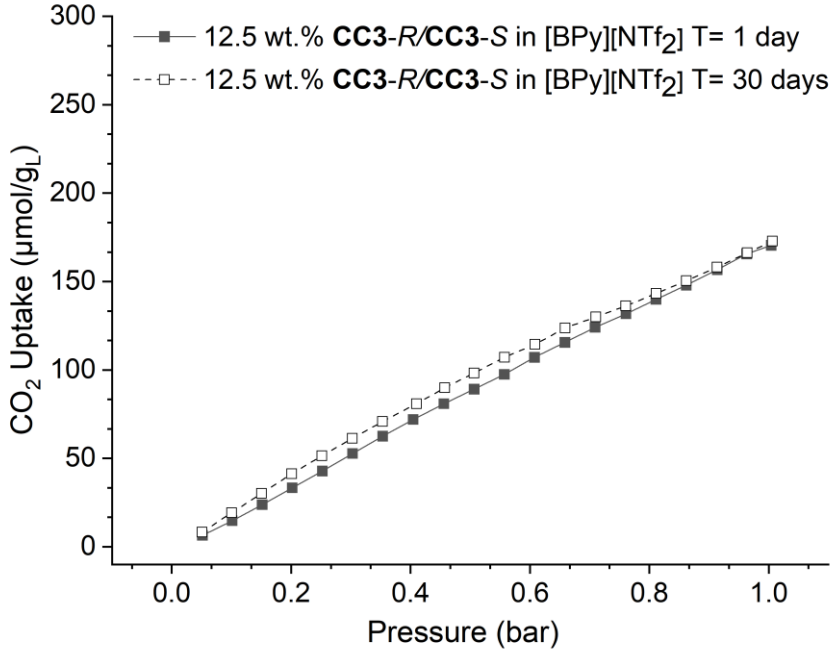

Figure 3.28: CO_2 adsorption isotherm of a 12.5 wt.% dispersion of **CC3-*R*/CC3-*S*** in [BPy][NTf_2] on day 1 and day 30 at RT.

3.5.7 Gas release of the dispersions of CC3-*R*/CC3-*S* microparticles in [BPy][NTf_2] by temperature and pressure

The thermal stability of **CC3-*R*/CC3-*S*** microparticles, [BPy][NTf_2] and three dispersions with 5 wt.%, 12.5 wt.%, 20 wt.% loadings of **CC3-*R*/CC3-*S*** microparticles in [BPy][NTf_2] were checked by TGA (**Figure 3.29**). By comparing the decomposition temperatures of the systems studied, all the dispersions appeared to have comparable thermal stabilities. The decomposition temperature of **CC3-*R*/CC3-*S*** microparticles was comparatively higher (at over 400 °C) than [BPy][NTf_2] which remained stable until around 325 °C. The **CC3-*R*/CC3-*S*** dispersions started to lose weight at around 325 °C, indicating thermal-stability dependence on the ionic liquid

used. Though a little less thermally stable than the pure **CC3-*R*/CC3-*S*** microparticles, these dispersions remain stable up until 300 °C, which should satisfy studies at higher temperatures to assess the possibility of applications such as gas release by temperature swing.

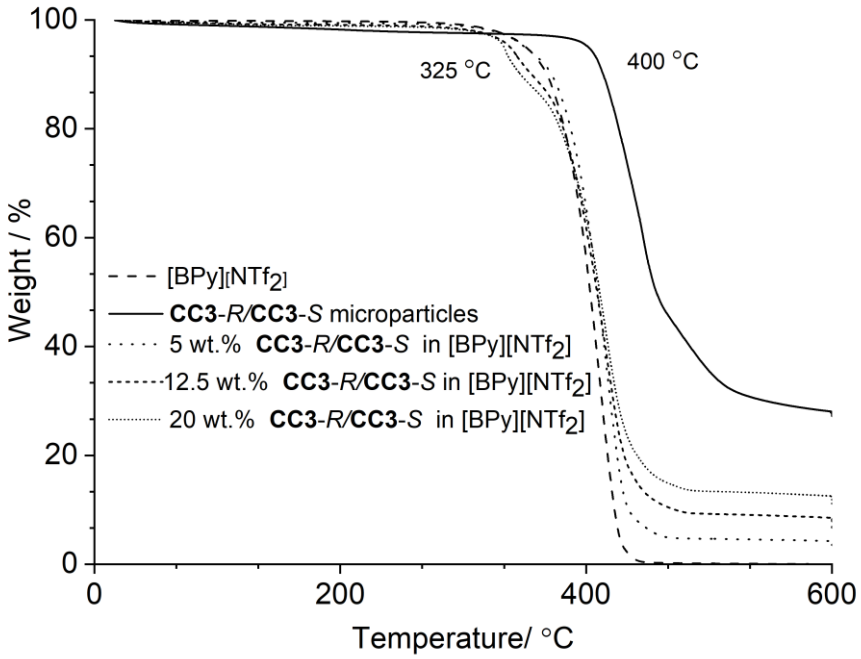

Figure 3.29: TGA of 0 wt.% 5 wt.%, 12.5 wt.% and 20 wt.% dispersions of **CC3-*R*/CC3-*S*** microparticles in [BPy][NTf_2].

Adsorption studies at higher temperatures were further performed to investigate the temperature-swing process for gas uptake and release. The CO_2 uptakes of neat [BPy][NTf_2] ionic liquid and its corresponding 12.5 wt.% **CC3-*R*/CC3-*S*** dispersion were measured at 25, 40, 60, 80 and 100 °C (**Figure 3.30**). The pure ionic liquid and 12.5 wt.% dispersion showed measurable uptakes, even when the temperature was increased to 100 °C, which might arise from the strong interaction of CO_2 with the ionic liquid. Still, the working absorption capacity of **CC3-*R*/CC3-*S*** in [BPy][NTf_2] (104.3 μmol/g_L) was significantly larger than that of the neat [BPy][NTf_2] (37.3 μmol/g_L) between 25 °C and 100 °C (**Table 3.10**). The increased working capacity in the porous liquid was due to the presence of the **CC3-*R*/CC3-*S*** microparticles, with the significant capacity decrease at higher temperatures predominantly dictated by the gas uptake behaviour in the dispersed microporous material. In contrast, the difference in capacity at increasing temperatures in the ionic liquid is much smaller due to the absence of permanent intrinsic porosity.

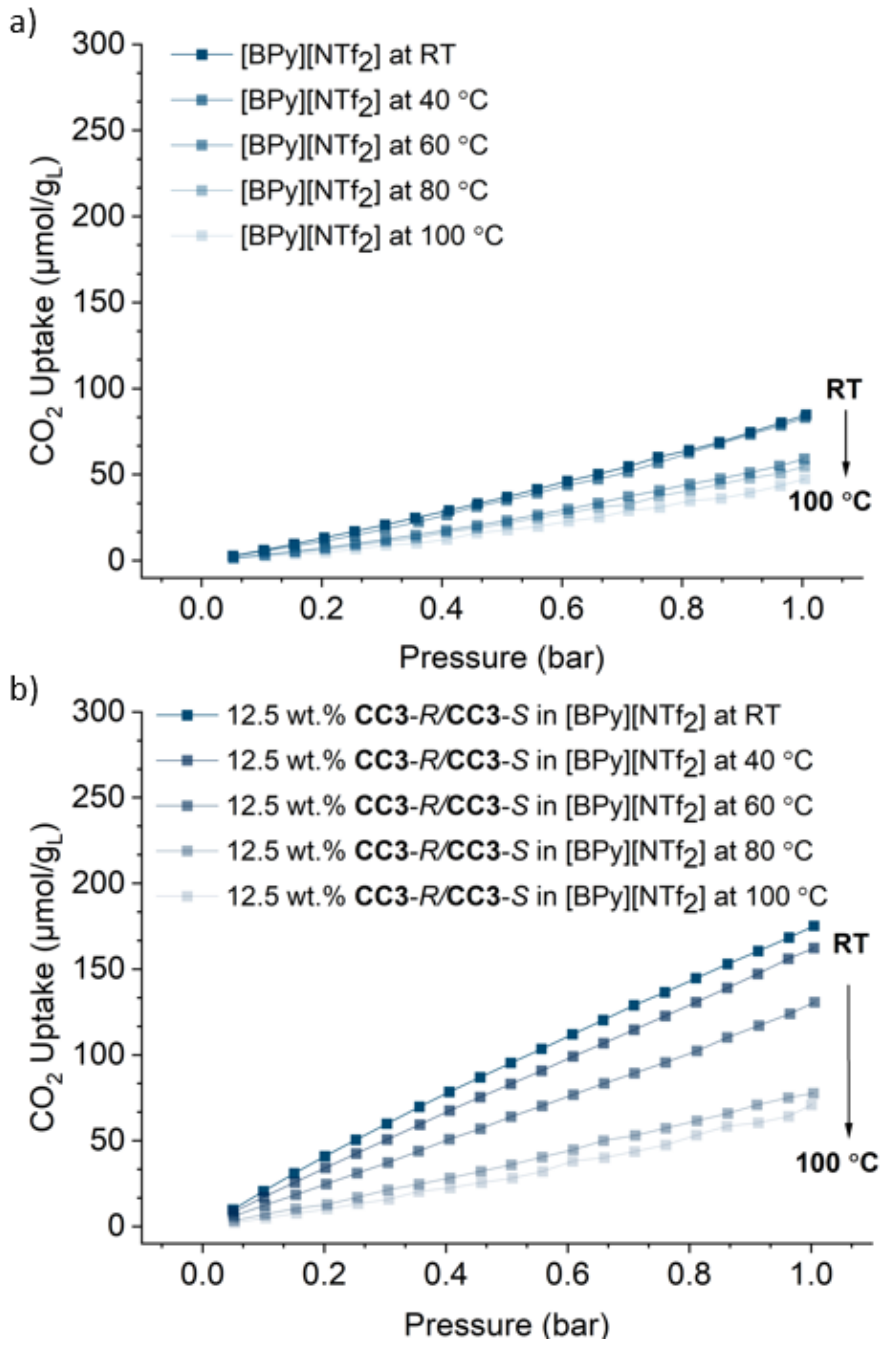

Figure 3.30: a) CO_2 adsorption isotherms of [BPy][NTf_2] at RT, 40, 60, 80, and 100 °C; b) CO_2 adsorption isotherms of a 12.5 wt.% **CC3-*R*/CC3-*S*** dispersion in [BPy][NTf_2] at RT, 40, 60, 80, and 100 °C.

Table 3.10: Summary of CO_2 uptakes of [BPy][NTf_2] and 12.5 wt.% **CC3-*R*/CC3-*S*** dispersion in [BPy][NTf_2] at RT, 40, 60, 80, 100 °C

T (°C)	**CO_2 uptake of [BPy][NTf_2] at 1 bar (μmol/g_L)**	**CO_2 uptake of 12.5 wt.% CC3-*R*/CC3-*S* in [BPy][NTf_2] at 1 bar (μmol/g_L)**
RT	84.8	175.2
40	83.0	162.3
60	59.2	130.8
80	54.8	77.7
100	47.5	70.9

Then the study of pressure control on the CO_2 uptake and release for a 12.5 wt.% **CC3-*R*/CC3-*S*** in [BPy][NTf_2] dispersion was also planned. However, the accurate uptake at high pressure could not be determined due to limitations with our instrument configurations, where it was not possible to stir the cage dispersions on a Micromeritics ASAP 2050 instrument to determine the high-pressure CO_2 isotherm. By comparison, when we recorded CO_2 isotherms on the Quantachrome system we were able to continually stir the viscous ionic liquid dispersions, and it was shown that stirring was important for CO_2 to saturate the ionic liquids and be adsorbed by the cage molecules. A pure [BPy][NTf_2] sample was first attempted to check its CO_2 uptake at higher pressure without stirring on Micromeritics, and different isotherms presented with different equilibration time, with the measurement with shorter equilibration time (35 s) taking up less CO_2 compared that of longer equilibration time of 1800 s at each pressure point (**Figure 3.31a**). In **Figure 3.31b**, which is an enlarged part of the lower pressure range of **Figure 3.31a**, the isotherm of CO_2 adsorption with longer equilibration times on Micromeritics was more comparable to the gas uptakes we determined for our stirred samples recorded on our Quantachrome instrument. These results indicated that a longer equilibration time helped reach saturation without stirring the sample. However, this type of measurement took too long, and its result difference from that of Quantachrome indicated yet unsaturated state and thus was considered as not controllable.

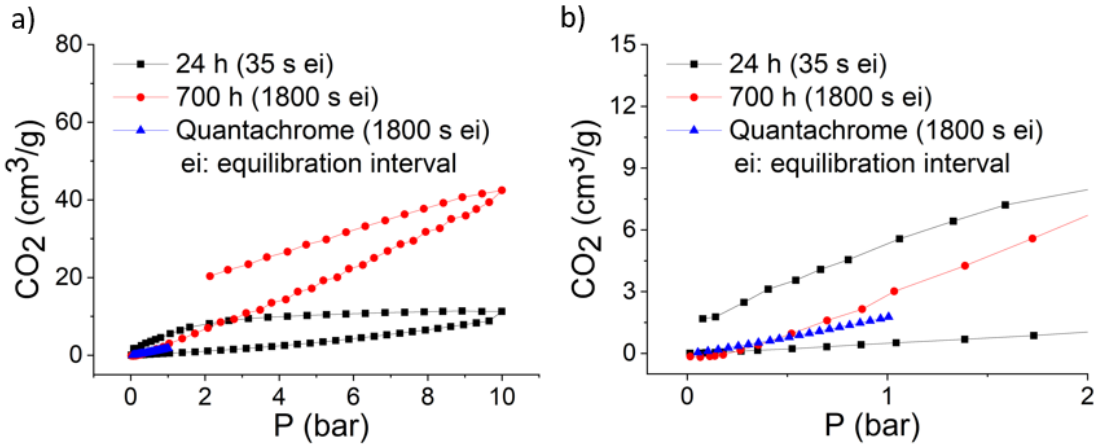

Figure 3.31: a) CO_2 adsorption isotherms of [BPy][NTf_2] at higher pressures with different equilibration time; b) Enlarged CO_2 adsorption isotherms of [BPy][NTf_2].

3.6 Conclusion

In this project, porous organic cage **CC3-*R*/CC3-*S*** microparticles were prepared from two imine cage molecules, **CC3-*R*** and **CC3-*S***, using a chiral recognition crystallisation strategy. Several ionic liquids including [BPy][NTf_2], [P_{66614}][NTf_2], [BEMA][NTf_2], [MBPy][NTf_2], [TBPy][NTf_2] and [BBIM][NTf_2] were screened to prepare new type III porous liquids. All the screened ionic liquid dispersions except [MBPy][NTf_2] displayed improved gas uptake over blank ionic liquids, with 6-65% porosity of **CC3-*R*/CC3-*S*** microparticles remaining intact in corresponding ionic liquids. The lost porosity may be caused by loss of extrinsic porosity among microparticles after being transferred into liquids or partial penetration of ion groups into the cage cavity, such as the case with [MBPy][NTf_2] or [BBIM][NTf_2]. An empirical size-exclusion standard was determined for bulky ionic liquids selection, where for the cation, a benzene ring with a 4-carbon alkyl chain is sufficient. The anion NTf_2^- satisfied the requirement for the **CC3** system. By considering the viscosity, availability, and commercial cost, [BPy][NTf_2] was selected as the ideal ionic liquid to prepare the dispersions of **CC3-*R*/CC3-*S*** microparticles, and the [BPy][NTf_2] dispersions were studied in full details.

Gas sorption isotherms, including CO_2 and CH_4, were performed on the 5 wt.%, 12.5 wt.% and 20 wt.% dispersions of **CC3-*R*/CC3-*S*** microparticles in [BPy][NTf_2] to determine the effect of microparticle concentration on gas uptake. For CO_2 adsorption, dispersions with increasing microparticles loading showed linearly increased uptakes from111.4 ± 6.4 and 172.1 ± 3.6 to 209.8 ± 6.7 μmol/g, which were all improved compared to that of neat [BPy][NTf_2] (78.3 ± 4.5 μmol/g). For CH_4 adsorption, the

gas uptake improvements were more clearly expressed, with corresponding data of 36.0 ± 0.3, 71.3 ± 4.0 and 103.8 ± 0.7 μmol/g for 5 wt.%, 12.5 wt.% and 20 wt.% dispersions compared to around 7.9 ± 0.1 μmol/g of [BPy][NTf_2]. Though both gas uptake improvements increased with more microparticle content, the CO_2/CH_4 selectivity dropped reversely, which is likely because **CC3-*R*/CC3-*S*** was not as good as ionic liquids in CO_2/CH_4 selectivity.

A viscosity study on the ionic liquids screened confirmed the best candidate was [BPy][NTf_2] (67.3 ± 0.1 mpa·s), with the lowest viscosity among the size-excluded ones. More microparticle content in **CC3-*R*/CC3-*S*** dispersions leads to increased viscosity, with the 20 wt.% one (303.5 ± 0.3 mpa·s) 4.5 times that of blank [BPy][NTf_2]. Rheology studies on the dispersions showed that the dispersions presented shear-thinning behaviour. Contact angles were first measured to evaluate the interaction between **CC3-*R*/CC3-*S*** microparticles and [BPy][NTf_2], where good wetting behaviours were observed, indicating that the microparticles could interact well with [BPy][NTf_2] ions instead of aggregating with adjacent particles in the dispersions. Then, the phase stability of dispersions was evaluated quantitively on the LUMiSizer®, where average sedimentation velocity was measured as 0.1 mm/day for the 5 wt.% dispersion and 0.04 mm/day for the 12.5 wt.% dispersion system, indicating that the dispersions were stable. **CC3-*R*/CC3-*S*** microparticles also showed good chemical and crystal stability in [BPy][NTf_2] according to IR and capillary PXRD studies on the dispersions, and the particles maintained their structure and sizes after CO_2 sorption. Good recyclability and ageing studies were also performed to confirm the overall chemical and crystal stability of this dispersion system.

The temperature and pressure control over the porosity of the dispersions of **CC3-*R*/CC3-*S*** microparticles in [BPy][NTf_2] has also been studied. From RT to 100 ℃, the CO_2 uptake of 12.5 wt% dispersion of **CC3-*R*/CC3-*S*** microparticles in [BPy][NTf_2] dropped from 175.2 μmol/g to 70.9 μmol/g, displaying a larger working absorption capacity of 104.3 μmol/g compared to that of pure [BPy][NTf_2] (37.3 $\mu mol/g_L$). As to the pressure control study, as viscous, [BPy][NTf_2] samples could not be stirred on Micromeritics during high-pressure CO_2 measurement, and the adsorption process differed with different equilibration times at each measuring point, which meant this method was not suitable.

Chapter 4

Type II Porous Liquid construction trial

4.1 Author contributions

Dr Michael Briggs synthesised Noria and Boc-Noria. The thesis author performed all other experiments and the associated data interpretation.

4.2 Introduction

This chapter studied the construction of type II porous liquids using porous organic molecules and ionic liquids. Not many type II porous liquid systems are reported, and they are predominately constructed by dissolving cage molecules in size-excluded solvents. [30,38,41,86,108,115] Recently, there were also examples of using metal organic cages in preparing type II porous liquids, [106,114] though the solutions prepared seemed not always transparent. Solvents used to prepare type II porous liquids are mostly organic solvents which have relatively lower boiling points or could be toxic, such as that 15-crown-5 has a boiling point of 93-96 ºC, and HCP could cause irritation. By contrast, ionic liquids are a kind of liquid salts, which could be deemed as a green solvent due to their neglectable volatility and high thermal stability. The solvation and dissolution process of substances in ionic liquids is not fully understood, [160,161] however some interactions, such as ion-ion interaction, hydrogen bonding, van der Waal's forces, and π-πinteractions were proven to act like solute-solvent interaction.[160,162] Thus, ionic liquids may be utilised to prepare type II porous liquids with good thermal stability.

4.3 Solubility screening

The solubility of some selected porous organic solids (**Figure 4.1**) in several ionic liquids (**Figure 4.2**) was screened experimentally. Organic solids include cyclodextrins, **Noria** and **Boc-Noria**, which are rich in hydroxyl or ether groups, apart from two [4+6] imine cages. One cage **CC19** was similar to **CC3** in the molecular structure, except with an extra hydroxyl group on each of the benzene ring; while the scrambled cage $\mathbf{T_4{:}3_3{:}3_{13}}$ had mixed vertex groups and a broken symmetry. Ionic liquids were composed of cations, including imidazolium, pyridinium, phosphonium and ammonium, and anions of tetrafluoroborate ($[BF_4]^-$), hexafluorophosphate ($[PF_6]^-$) and $[NTf_2]^-$. All the anions studied in this chapter contained fluorine atoms, which can, in principle, interact with the porous molecules via hydrogen bonding in C–F···H–O, and C–F···H–C pairs, [163] halogen bonding in SO_2C-F···O pair, [164] C–F···π pair, [165] and multipolar contacts in the C–F···C=N, [166] to help solubilise porous molecules. Due to polarity differences, organic macrocycles normally have poor solubility in ionic liquids. And therefore, the porous solid used here was either rich in polar groups such as the hydroxyl groups or had broken molecular symmetry, which may provide

extra noncovalent bonding sites or easily broken intermolecular packing, thus improving solubility.

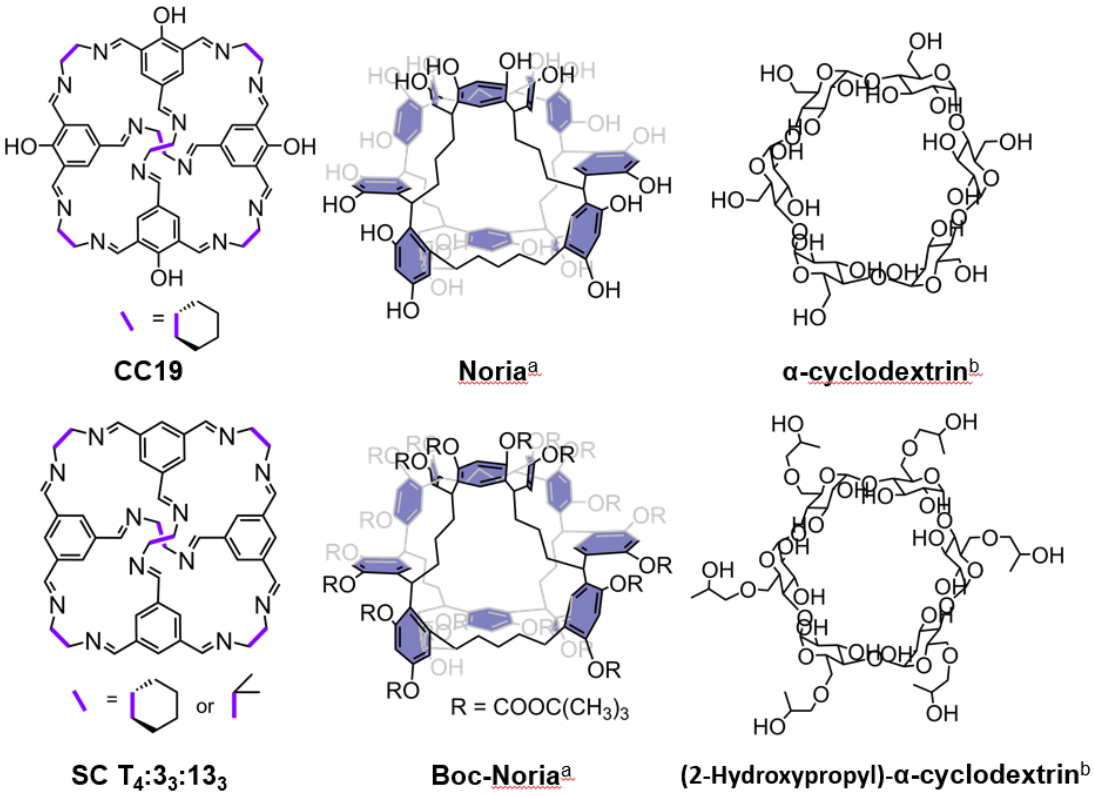

Figure 4.1: Structures and names of porous organic molecules screened for solubility. [a] synthesised by Dr Michael Briggs; [b] commercialised product bought from Sigma-Aldrich.

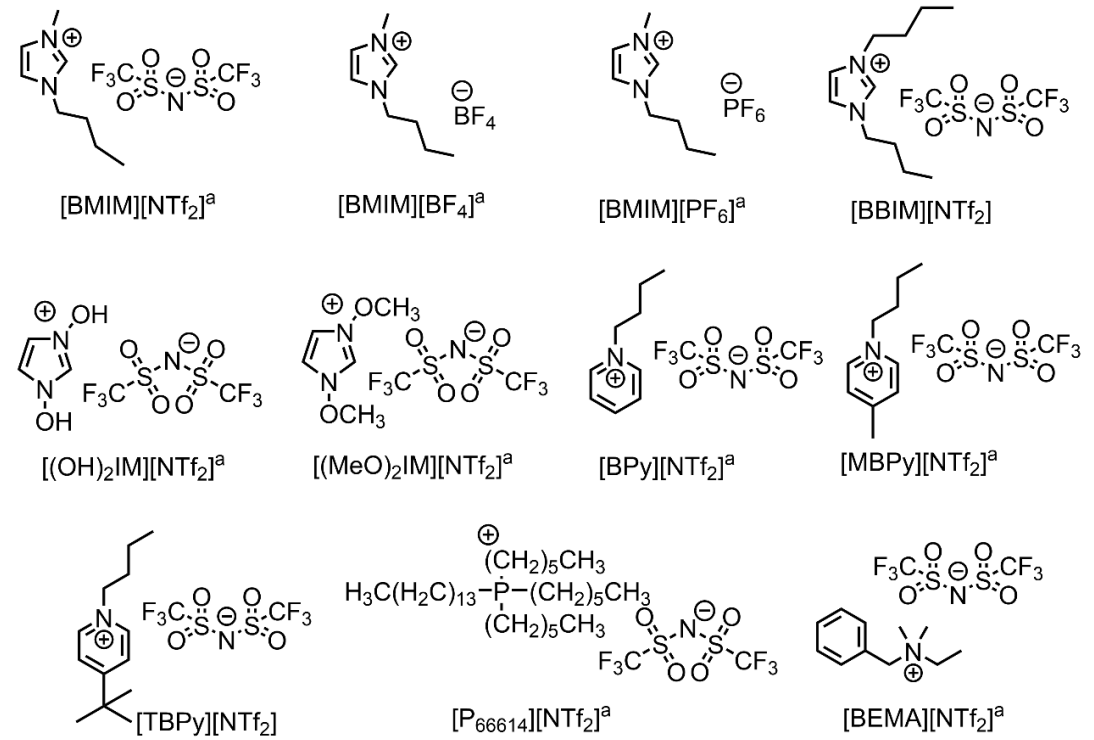

Figure 4.2: Structures and names of ionic liquids screened for solubility. [a] commercialised product.

A typical screen procedure was as follows: a 0.2 mL ionic liquid was weighed, and then a porous solid was added and weighed. Then the mixture with a certain concentration was left to stir and equilibrate at RT for 48 hours. Sonication could sometimes be employed to facilitate solubilisation. Considering that gas uptake increases linearly with the loaded cage concentration [122], there is porosity loss of cages while in liquids, and the error limit of Quantachrome is set as 10 µmol according to the results discussed in Chapter 3, thus, a proper solubilised concentration of porous organic molecules is crucial in porous liquids. Here the threshold 2.5 wt.% was chosen initially, as this value seemed to be the general upper limit for solubilising the porous organic molecules in the ionic liquids screened in this chapter. However, it was also necessary to ensure that the gas uptake improvement value from solubilised molecules should be larger than the allowed error limit of Quantachrome. The scrambled cage **SC T_4:3_3:13_3** was taken as an example to verify the threshold of 2.5 wt.%. **SC T_4:3_3:13_3** solid has a CO_2 uptake of around 1.69 mmol/g, [167]] and the ideal uptake for **SC T_4:3_3:13_3** solid in the 1 g of 2.5 wt.% porous liquid should, therefore, correspond to a CO_2 uptake of 42.5 µmmol/g. By referring to the result of the porosity percentage of **CC3**-*R*/**CC3**-*S* maintained after transferring to size-excluded ionic liquids in Chapter 3 (34-65%), **SC T_4:3_3:13_3** appears to have a CO_2 uptake range of about 14-28 µmmol/g in the 2.5 wt.% solution, which is just above the lower limit of the Quantachrome error. Furthermore, if the unit of the threshold concentration was converted from wt. % to mg/mL, a 2.5 wt.% ionic liquid solution would equal a solution with the concentration range of 25-40 mg/mL (the ionic liquid had a density range of 1-1.6 g/mL, [168] and supposing the solubilised cage would not affect the ionic liquid density,). This threshold concentration (25-40 mg/mL) was lower than the threshold (50 mg/mL) chosen by Dr Kearsey in a type II porous liquids study using organic solvents. [38] Still, 2.5 wt.% was considered a tolerable threshold value as it would not interfere with a qualitative judgement of ionic liquid size-exclusion too much according to the CO_2 calculation above. The solubility screen results are shown in **Table 4.1**.

Table 4.1: Solubility tests results

No.	Ionic Liquid	Porous solids	solubility
1	[BMIM][NTf_2]	**CC19**	Not soluble
		SC T_4:3_3:13_3	Not soluble
		Noria	Not soluble
		Boc-Noria	Not soluble
		α-cyclodextrin	Not soluble
		2-hydroxypropyl-α-cyclodextrin	Not soluble
2	[BMIM][BF_4]	**CC19**	Not soluble
		SC T_4:3_3:13_3	Not soluble
		Noria	Stable colloid at 2.5 wt.%
		Boc-Noria	Stable colloid at 2.5 wt.%
		α-cyclodextrin	Not soluble
		2-hydroxypropyl-α-cyclodextrin	Not soluble
3	[BMIM][PF_6]	**CC19**	Not soluble
		SC T_4:3_3:13_3	Not soluble
		Noria	Not soluble
		Boc-Noria	Not soluble
		α-cyclodextrin	Not soluble
		2-hydroxypropyl-α-cyclodextrin	Not soluble
4	[BBIM][NTf_2]	**CC19**	Not soluble
		SC T_4:3_3:13_3	Not soluble
		Noria	Not soluble
		Boc-Noria	Not soluble
		α-cyclodextrin	Not soluble
		2-hydroxypropyl-α-cyclodextrin	Not soluble
5	[$(OH)_2$IM][NTf_2]	**CC19**	2.5 wt. %
		SC T_4:3_3:13_3	Not soluble
		Noria	Not soluble
		Boc-Noria	Not soluble
		α-cyclodextrin	10 wt.%
		2-hydroxypropyl-α-cyclodextrin	10 wt.%
6	[$(MeO)_2$IM][NTf_2]	**CC19**	2.5 wt. %
		SC T_4:3_3:13_3	Not soluble
		Noria	Not soluble
		Boc-Noria	Not soluble
		α-cyclodextrin	Not soluble
		2-hydroxypropyl-α-cyclodextrin	Not soluble
7	[BPy][NTf_2]	**CC19**	Not soluble
		SC T_4:3_3:13_3	Not soluble
		Noria	Not soluble

		Boc-Noria	Stable colloid at 2.5 wt.%
		α-cyclodextrin	Not soluble
		2-hydroxypropyl-α-cyclodextrin	Not soluble
8	[MBPy][NTf_2]	**CC19**	Not soluble
		SC T_4:3_3:13_3	Not soluble
		Noria	Not soluble
		Boc-Noria	Not soluble
		α-cyclodextrin	Not soluble
		2-hydroxypropyl-α-cyclodextrin	Not soluble
9	[TBPy][NTf_2]	**CC19**	Not soluble
		SC T_4:3_3:13_3	Not soluble
		Noria	Not soluble
		Boc-Noria	Not soluble
		α-cyclodextrin	Not soluble
		2-hydroxypropyl-α-cyclodextrin	Not soluble
10	[P_{66614}][NTf_2]	**CC19**	Not soluble
		SC T_4:3_3:13_3	Not soluble
		Noria	Not soluble
		Boc-Noria	Not soluble
		α-cyclodextrin	Not soluble
		2-hydroxypropyl-α-cyclodextrin	Not soluble
11	[BEMA][NTf_2]	**CC19**	Not soluble
		SC T_4:3_3:13_3	Not soluble
		Noria	Not soluble
		Boc-Noria	Not soluble
		α-cyclodextrin	Not soluble
		2-hydroxypropyl-α-cyclodextrin	Not soluble

4.4 Porosity screening

Four combinations with solubility >2.5 wt. % in ionic liquids were found from the screening, where two ionic liquids of [$(OH)_2$IM][NTf_2] and [$(MeO)_2$IM][NTf_2] (**Figure 4.2**) were involved. It seemed that the hydroxyl and methoxyl groups in the two ionic liquids facilitated the dissolution of the porous solids. We chose the combinations of [$(OH)_2$IM][NTf_2] with **CC19** and **2-hydroxypropyl-α-cyclodextrin** from **Table 4.1** and studied their porosity. Both the 2.5 wt.% **CC19** and 10 wt.% **2-hydroxypropyl-α-cyclodextrin** solutions formed presented a clear and flowable appearance (**Figure 4.3 b** and **Figure 4.4b**). Corresponding CO_2 gas uptakes of solutions were then compared with that of pure [$(OH)_2$IM][NTf_2] to evaluate porosity.

The CO_2 gas adsorption isotherms are shown in **Figures 4.3c** and **4.4c**, and neither of them showed any gas uptake improvements. In the case of the 10 wt.% $[(OH)_2IM][NTf_2]$ solution with a high content of **2-hydroxypropyl-α-cyclodextrin**, the gas uptake of **2-hydroxypropyl-α-cyclodextrin** solution was 33.7 ± 0.3 µmol/g. which even dropped compared to pure $[(OH)_2IM][NTf_2]$ (52.2 ± 0.06 µmol/g). For the 2.5 wt% **CC19** solution in $[(OH)_2IM][NTf_2]$, the CO_2 uptake of the solution was 51.1 ± 1.8 µmol/g, which was also less than that of pure $[(OH)_2IM][NTf_2]$. These initial CO_2 uptake data indicated that the ionic liquid $[(OH)_2IM][NTf_2]$ failed to meet the size-exclusion requirement for both **CC19** and **2-hydroxypropyl-α-cyclodextrin** in preparing type II porous liquids, though it showed good solubilising ability. As the ionic liquid size-exclusion requirement for the [4+6] imine cage system has been studied in the previous chapter, and some conclusions drawn could be applied to the [4+6] imine cage **CC19** as well**.** Thus, the **CC19** system is studied further in making type II porous liquids.

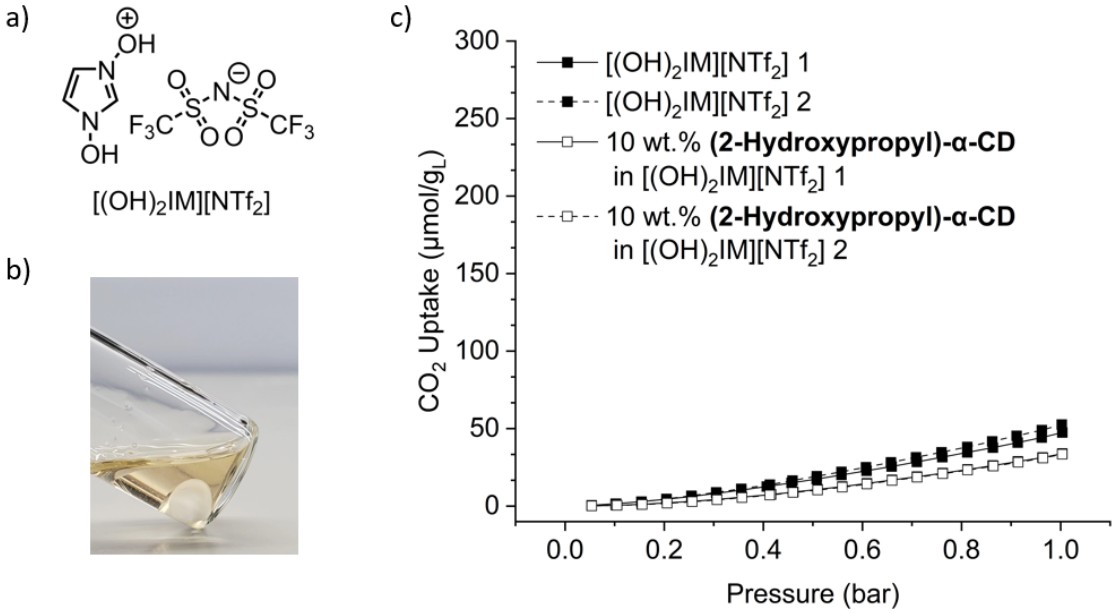

Figure 4.3: a) structure of $[(OH)_2IM][NTf_2]$; b) 10 wt.% of **2-hydroxypropyl-α-cyclodextrin** in $[(OH)_2IM][NTf_2]$; c) CO_2 isotherms of $[(OH)_2IM][NTf_2]$ and 10 wt% of **2-hydroxypropyl-α-cyclodextrin** in $[(OH)_2IM][NTf_2]$ at RT.

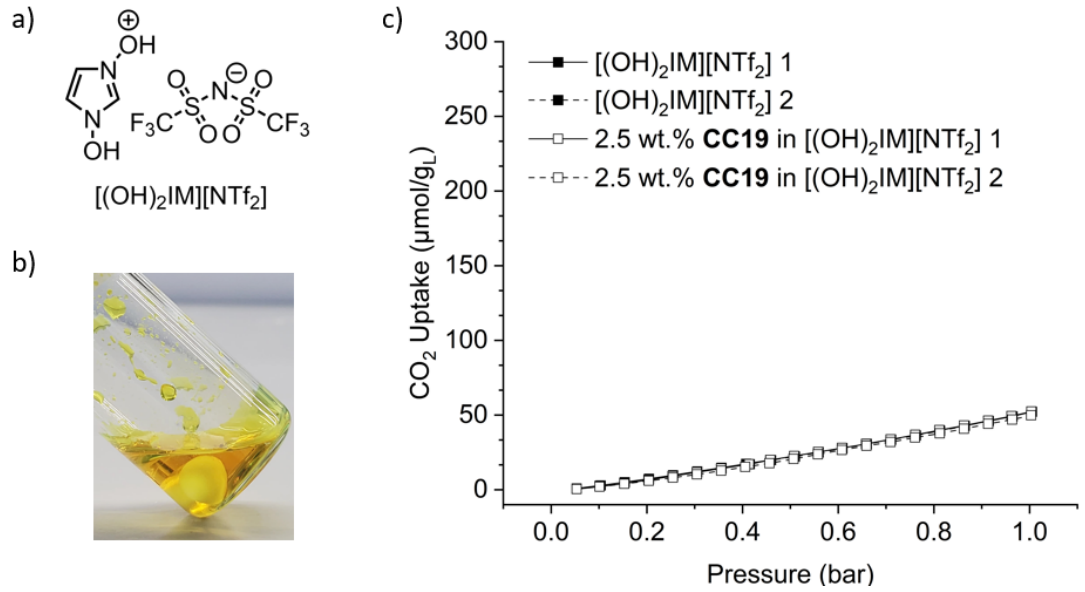

Figure 4.4: a) Structure of $[(OH)_2IM][NTf_2]$; b) 2.5 wt% solution of **CC19** in $[(OH)_2IM][NTf_2]$; c) CO_2 isotherms of $[(OH)_2IM][NTf_2]$ and 2.5 wt% of **CC19** in $[(OH)_2IM][NTf_2]$ at RT.

As discussed in Chapter 3 that $[BPy][NTf_2]$ is size excluded for the imine cage **CC3**, and the imine cage **CC19** shares the same molecular structure with **CC3**. Therefore, we made a dispersion of **CC19** with $[BPy][NTf_2]$ and measured its CO_2 uptake to check whether $[BPy][NTf_2]$ met the size-exclusion requirement for **CC19** (**Figure 4.5**). The 5 wt.% dispersion of **CC19** showed a CO_2 uptake of 137.3 ± 9.3 μmol/g, which clearly improved compared to that of $[BPy][NTf_2]$ (80.2 ± 3.0 μmol/g) and even larger than the 5 wt.% **CC3** dispersion in $[BPy][NTf_2]$ (111.4 ± 6.4 μmol/g). By comparing the structure of $[BPy][NTf_2]$ and $[(OH)_2IM][NTf_2]$, it could be seen that the cation $[(OH)_2IM]^+$ might be so small that it entered into the cavity of **CC19** and removed the solution porosity.

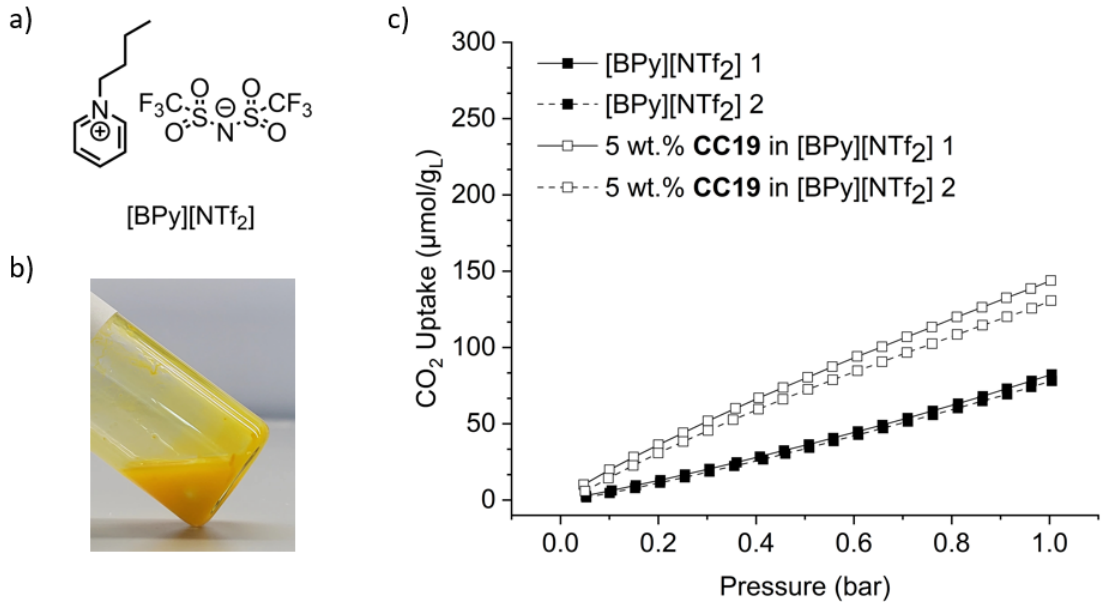

Figure 4.5: a) Structure of [BPy][NTf_2]; b) 5 wt% dispersion of **CC19** in [BPy][NTf_2]; c) CO_2 isotherms of [BPy][NTf_2] and 2.5 wt% of **CC19** in [$(OH)_2$IM][NTf_2] at RT.

Two methods were then tried to fix the size-exclusion issue in preparing type II porous liquids based upon the [4+6] imine cage and ionic liquids. The general logic of the first method is to decrease the window sizes of the cage molecule, which may limit the size of guest molecules that could be allowed into the cage cavity. The first cage with decreased window size tried in preparing type II porous liquids was synthesised using the tying method developed by Dr Liu. [169,170] The tying method involved reducing the imine cage to an amine cage at first, and the vicinal secondary amine groups then formed a five-membered ring by reacting with an aldehyde. The degree of window size decrease depended on the tied groups. For example, **RCC3-6FT,** which was tied with six formaldehyde molecules, had a decreased window size of around 3.5 Å compared to **CC3** (4 Å). Thus, **CC19** was modified by the same tying method to afford **RCC19-6FT** (**Figure 4.6a**), which had a BET surface area of 437 m^2/g and a CO_2 uptake of 1611 μmol/g at room temperature and 1 bar. **RCC19-6FT** also showed good solubility in [$(OH)_2$IM][NTf_2] (> 2.5 wt.%). Still, unfortunately, the 2.5 wt.% solutions of **RCC19-6FT** in [$(OH)_2$IM][NTf_2] showed a CO_2 uptake of 48.7 μmol/g, which did not show any improvement compared to pure [$(OH)_2$IM][NTf_2] (**Figure 4.6c**), indicating the ionic liquids was not size-excluded to **RCC19-6FT**.

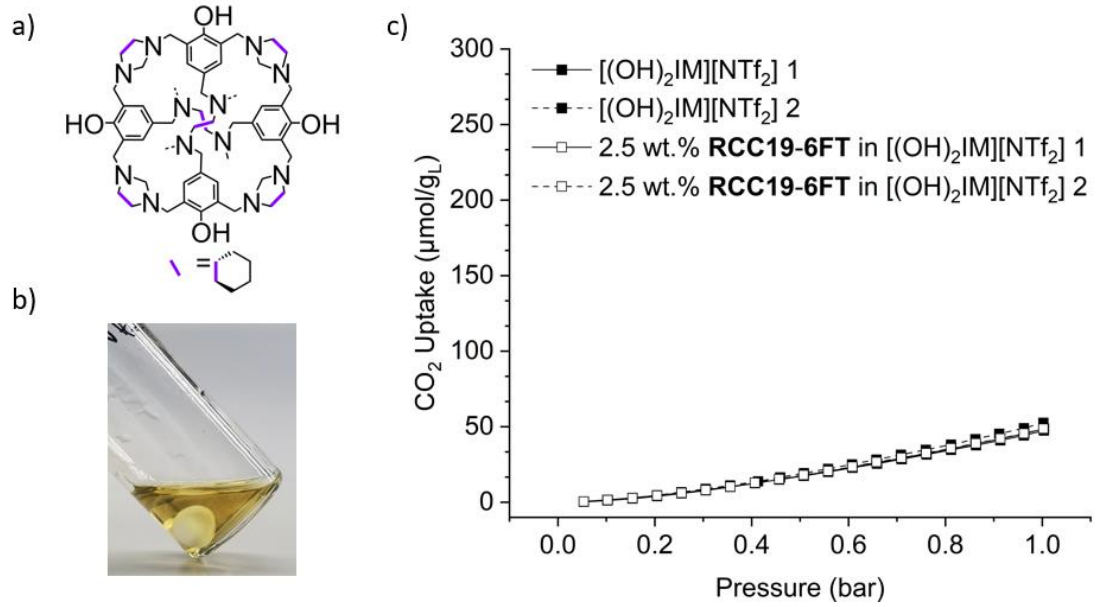

Figure 4.6: a) Structure of **RCC19-6FT**; b) 2.5 wt% solution of **RCC19-6FT** in [(OH)$_2$IM][NTf$_2$]; c) CO_2 isotherms of [(OH)$_2$IM][NTf$_2$] and 2.5 wt% of **RCC19-6FT** in [(OH)$_2$IM][NTf$_2$] at RT.

B. Egleston *et al.* prepared a Type II porous liquid based upon **CC15**, [41] a [4+6] imine cage similar to **CC3** but with extra methyl groups on the carbon atom in each imine bond. The methyl groups decreased the cage window size from 4 Å (**CC3**) to 1.7 Å (**CC15**), thus could not include Xe molecules in a size-excluded solvent HCP. As **CC15** was not so soluble in [(OH)$_2$IM][NTf$_2$], another [4+6] imine cage **TpOMe-CDA** with methoxyl groups around the cage windows which may also have decreased cage window size was chosen (**Figure 4.7a**). [171] Like **CC15**, **TpOMe-CDA** solid had a neglectable BET surface area, and a moderate CO_2 uptake of 800 µmol/g at 25 °C and 1 bar due to the interrupted crystal packing and blocked porosity channels by the methoxyl groups. [41] **TpOMe-CDA** showed good solubility in [(OH)$_2$IM][NTf$_2$] (> 5 wt.%, **Figure 4.7b**), however unfortunately a 2.5 wt.% solution of **TpOMe-CDA** in [(OH)$_2$IM][NTf$_2$] showed a CO_2 uptake of 44.0 ± 0.8 µmol/g (**Figure 4.7c**), which was again even less than that of pure [(OH)$_2$IM][NTf$_2$] (52.2 ± 0.06 µmol/g) and indicated that [(OH)$_2$IM][NTf$_2$] was not size-excluded to **TpOMe-CDA**.

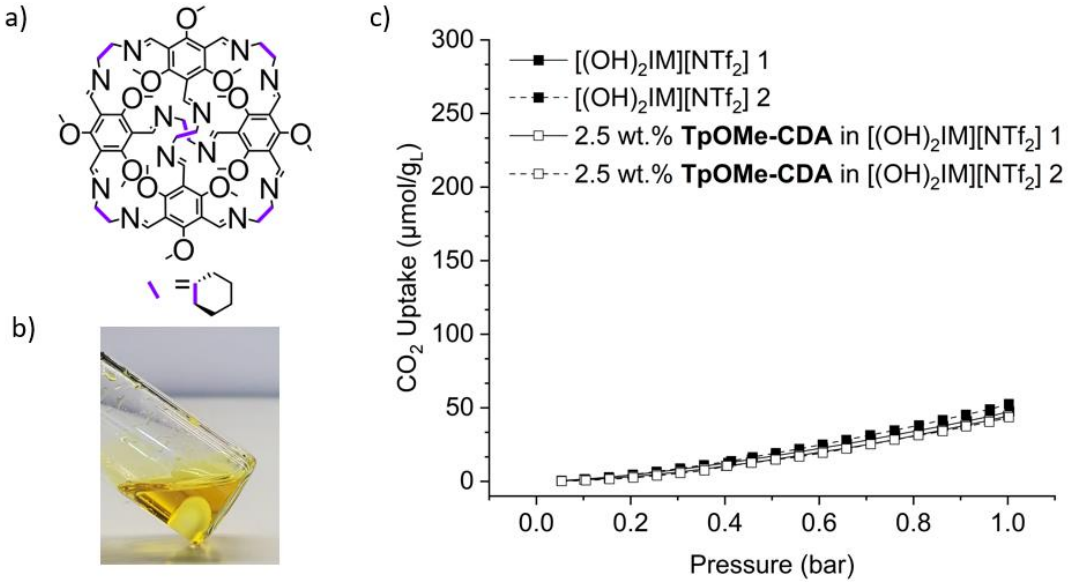

Figure 4.7: a) Structure of **TpOMe-CDA**; b) 2.5 wt% solution of **TpOMe-CDA** in $[(OH)_2IM][NTf_2]$; c) CO_2 isotherms of $[(OH)_2IM][NTf_2]$ and 2.5 wt% of **TpOMe-CDA** in $[(OH)_2IM][NTf_2]$ at RT.

The second method is to combine the size-excluded pyridinium cation with hydroxyl or methoxyl functional groups which seemed to facilitate solubilising porous organic molecules according to the above solubility screening. Thus, several pyridinium ionic liquids functionalised with either hydroxyl or methoxyl groups (**Figure 4.8**), including 4-(tert-butyl)-1-(3-hydroxypropyl)pyridinium bis(trifluoromethylsulfonyl)imide ($[T(OH)Py][NTf_2]$), 1-(2-methoxyethyl)pyridinium bis(trifluoromethylsulfonyl)imide ($[(MeO)Py][NTf_2]$) and 1-(3-hydroxypropyl)-3-(methoxymethyl)pyridinium bis(trifluoromethylsulfonyl)imide ($[(MeO)(OH)][NTf_2]$) were designed, synthesised, and performed solubility screening with **RCC19-6FT**, **TpOMe-CDA** and above porous solids (**Figure 4.1**). Unfortunately, no combination with good porous solid solubility in the modified ionic liquids has been found (**Table 4.2**).

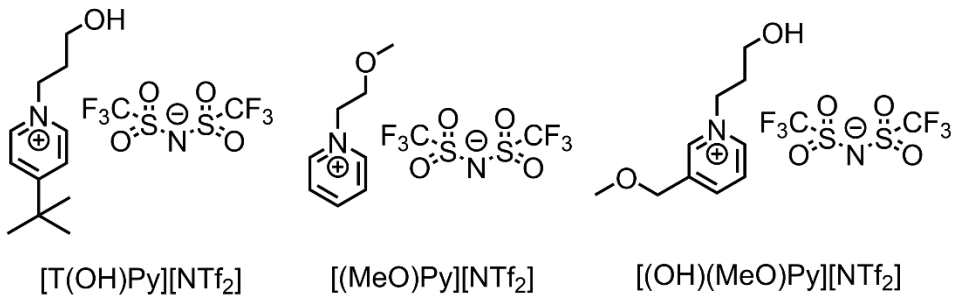

Figure 4.8: Structure of synthesised ionic liquids.

Table 4.2: Solubility screening results in modified ionic liquids.

No.	Ionic Liquid	Porous solids	solubility
1	[T(OH)Py][NTf_2]	**CC19**	Not soluble
		SC T_4:3_3:13_3	Not soluble
		Noria	Not soluble
		Boc-Noria	Not soluble
		α-cyclodextrin	Not soluble
		2-hydroxypropyl-α-cyclodextrin	Not soluble
		RCC19-6FT	Not soluble
		TpOMe-CDA	Not soluble
2	[(MeO)Py][NTf_2]	**CC19**	Not soluble
		SC T_4:3_3:13_3	Not soluble
		Noria	Not soluble
		Boc-Noria	Not soluble
		α-cyclodextrin	Not soluble
		2-hydroxypropyl-α-cyclodextrin	Not soluble
		RCC19-6FT	Not soluble
		TpOMe-CDA	Not soluble
3	[(MeO)(OH)Py][NTf_2]	**CC19**	Not soluble
		SC T_4:3_3:13_3	Not soluble
		Noria	Not soluble
		Boc-Noria	Not soluble
		α-cyclodextrin	Not soluble
		2-hydroxypropyl-α-cyclodextrin	Not soluble
		RCC19-6FT	Not soluble
		TpOMe-CDA	Not soluble

4.5 Conclusion

In this chapter, attempts to prepare type II porous liquids based on porous organic molecules and ionic liquids were tried. Solubility screening was first performed among six porous organic molecules (**CC19**, **SC T_4:3_3:13_3**, **Noria**, **Boc-Noria**, **α-cyclodextrin** and **2-hydroxypropyl-α-cyclodextrin**) with 11 ionic liquids. And it was found that the ionic liquids of [$(OH)_2$IM][NTf_2] and [$(MeO)_2$IM][NTf_2] could dissolve **CC19**, **α-cyclodextrin** and **2-hydroxypropyl-α-cyclodextrin** with concentrations over 2.5 wt.%. It was assumed that the hydroxyl and methoxyl groups in the cations of [$(OH)_2$IM][NTf_2] and [$(MeO)_2$IM][NTf_2] could facilitate the solubilisation of porous organic molecules.

However, CO_2 uptakes comparisons between pure ionic liquids and the corresponding solution as a porosity characterisation method showed that the two ionic liquids were

not size excluded to **CC19** or **cyclodextrin**. Two methods were tried to solve the size-exclusion issue. The first was to dissolve two cages with decreased window sizes (**RCC19-6FT** and **TpOMe-CDA**) in $[(OH)_2IM][NTf_2]$, however it was proved that the cation $[(OH)_2IM]^+$ still failed to meet the size-exclusion requirement. The second method was to combine the size-excluded pyridinium cation and hydroxyl or methoxyl groups. However, the ionic liquids designed could not dissolve the screened porous organic molecules well.

Though the trials of construction of type II porous liquids using porous organic molecules and ionic liquids failed, and the polar ionic liquids seemed not a good solvent choice for nonpolar porous organic molecules. Corresponding initial solubility data in ionic liquids was first determined, which would help provide design considerations for future systems. Future work could try preparing some ionic macrocycles or cages, which as salts should show better solubility in ionic liquids than pure organic compounds. For example, deprotonation of the hydroxyl groups in **CC19** to make it a salt, or introduction of carboxylate groups into cages. In this way, the solubility issue in ionic liquids could be solved to prepare type II porous liquids based on cage or macrocycle derivatives.

Chapter 5

Type I Porous Liquid Based on Ionic Liquid-tethered Organic Cages

5.1 Author contributions

Dr Marc Little provided the initial idea. Dr Xiang Zhou performed HPLC experiments. The thesis author performed all other experiments, and the associated data interpretation.

5.2 Introduction

Type II and type III porous liquids are constructed by either dissolving or dispersing porogen in size-excluded solvents, which would dilute the pore concentration of porous solid. For example, one crown ether functionalised porous imine cage required twelve 15-crown-5 solvent molecules to be dissolved; [108] thus, the solution made had a limit in concentration (44 wt.% of the cage in 15-crown-5). Most type III porous liquids prepared in the literature were usually made into 2.5-20 wt.%. The main reason for the limited concentrations in type III porous liquids was that a higher porogen concentration would lead to more viscous materials, which might contradict the initial purpose of introducing flowing media. Though type II and type III porous liquids may show pronounced gas uptake improvement compared to the blank solvents used, however they have much less gas sorption compared to pure porous solids due to the dilution. This is even more of a disadvantage for porous organic cages, as they generally have much smaller surface areas than MOFs, ZIFs, or COFs. For example, **CC3** had a surface area of around 624 m^2/g and a CO_2 uptake of 1.8 ± 0.07 mmol/g, while a corresponding 12.5 wt.% dispersion in ionic liquid [BPy][NTf_2] had a CO_2 uptake of 170 ± 7.7 μmmol/g at room temperature and 1 bar (pure [BPy][NTf_2] has an uptake of 78.3 ± 4.5 μmmol/g).[122,136] By contrast, the MOF material ZIF-67 had a surface area of 1308.6 m^2 /g and a 10 wt.% ZIF-67 dispersion in the ionic liquid 1,6-bis(3-buthylimidazolium-1-yl)hexane bis(trifluoromethylsulfonyl)amide showed a CO_2 uptake of 9.54 mmol/g at 25 °C and 1 bar. [131]

Thus, type I porous liquids which are composed of solely porogens have an apparent advantage over type II and type III. However, the challenge lies in making a type I porous liquid. The construction methods established so far are based on lowering the melting points of existing porous solids, where two strategies are primarily utilised. The first strategy is to disturb structure symmetry and thus decrease the intermolecular interaction, such as by introducing flexible groups into molecules. As for a covalent compound to melt, energy is needed to break intermolecular forces between molecules for them to flow freely. And the intermolecular force is mostly van der Waals forces, whose strength depends mainly on molecular weight and molecular symmetry of molecules. [172,173] The second strategy is to introduce ionic liquid parts. For ionic compounds, melting points mainly depend on the electrostatic force that holds cations and anions together. Electrostatic force obeys Coulomb's inverse-square law $|F|$ =

$k_e*|q_1*q_2|/(r\text{^}2)$, where the r represents the distance between cation and anion and electrical force is inversely proportional to $r\text{^}2$. If *r* is larger, the corresponding electrostatic force will be vastly decreased. And according to this law, ionic liquids usually use bulky cations and anions to limit electrostatic force and thus lower the melting point.

As discussed in Chapter 1, the types of porous solids that could be used to fabricate type I porous liquids include hollow inorganic materials (silica and carbon), MOFs, coordination cages and porous organic molecules. Hollow porous solids, such as MOFs and coordination cages with high symmetry or large molecular weights, often have high melting points because of their extended coordination or covalent networks. Usually, both flexible alkyl chains and ionic liquids groups are introduced to lower their melting points, such as the corona-canopy method, which uses cations and anions with long flexible chains. However, with the larger molecular weight of the tethered chains introduced, the cavities volume of hosts would constitute less of the materials composition, and absolute gas uptakes of materials constructed are generally low. For example, the tetrahedral coordination cage **2** (**Figure 1.20**), [28] was assembled from trialdehydes and $Zn(NTf_2)$ but appended with large imidazolium ionic liquid tethered PEG_{1000} benzylamines. One PEG chain had a molecular weight of nearly 1800, and each cage **2** had twelve chains, plus four metal ions and eight anions. Therefore, the composition of the cage cavity would take up only a small percentage of one cage **2** entity.

For porous organic molecules with low molecular weight, the strategy of introducing flexible alkyl groups or ionic liquid parts would both successfully lower the melting points. For example, in the 2012 paper, a series of alkyl-chain functionalised diamines was designed, synthesised, and reacted with 1,3,5-triformylbenzene to produce [4+6] imine cages. [22] As the alkyl chains were flexible and may point in different directions which thus broke the molecular symmetry, a cage functionalised with octyl chains with the melting point as low as 50 ºC could be attained. However, unfortunately, these alkyl chains were also inclined to penetrate the hydrophobic internal cavities of the cages. Thus, porosity was lost after melting the cages. The strategy of using ionic liquids also works well. The pillar[5]arene could be functionalised to form a macrocycle ionic liquid $[P_{66614}][DCP_5]$, [89] and this liquid presented the highest CO_2 uptake (5.52 mol/mol, 50 ºC, 1 bar) among all the type I porous liquids reported. Dr

Kearsey also explored this strategy in liquifying porous organic cages, where reduced cage **RCC1** and **RCC3** were first turned into ionic cage salts **RCC1-12HCl** and **RCC3-12HCl** using the method developed by Dr M. Liu. [174,175] Then anion exchange was performed with a variety of bulky anions to screen for salts with low melting points. The **RCC1-12NTf$_2$** showed a decreased melting behaviour from 170 to 220 ^{o}C. However, the reduced cage could lose shape-persistency and thus porosity. By contrast, the cage tying method developed by Dr M. Liu, [169] which used formaldehyde or acetone to react with the secondary amine groups in the reduced cage, would form rigid five-membered rings in the cage structure and regain cage rigidity. Thus, the tying method was employed as a post-modification method for cage functionalisation and studied to construct type I porous liquids in this chapter.

5.3 Study of tying RCC1 with ILSA-S3

An ionic-liquid-functionalised aldehyde was targeted, which could be tethered onto the reduced cage molecule using the tying method of forming aminal bonds between the aldehyde and secondary amines in the cage. Thus, ionic liquid groups could be introduced onto the cage to lower its melting point in a way that maintains the rigidity of the cage core as well. At first, alkyl-aldehydes were attempted in the functionalisation of ionic liquid groups, which unfortunately failed after three synthesis routes trials (**Figure 5.1**). The first approach was to use nucleophilic substitution of TsCl by hydroxyl group in 5-hydroxypentanal using potassium hydroxide as the catalyst. However, this resulted in the aldehyde participating in reactions as well during the functionalisation. The other two tried methods involving weaker bases of potassium carbonate or methylimidazole also failed. The loss of aldehyde during functionalisation may be due to the high reactivity of alkyl aldehydes, where they would readily undergo nucleophilic addition and be attacked by even weak bases, thus could not stand the reaction conditions for functionalisation without protection.

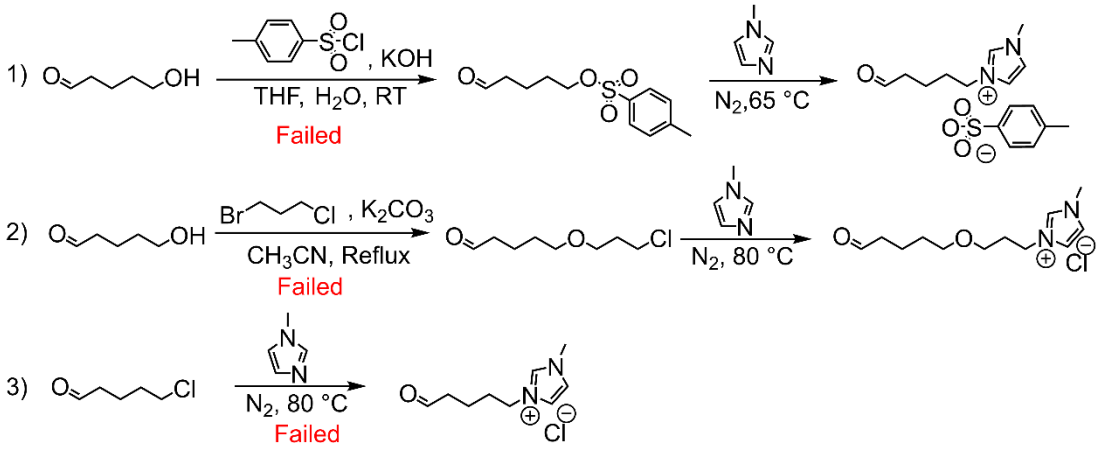

Figure 5.1: Routes to functionalising alkyl aldehydes.

4-hydroxybenzaldehyde was then chosen as the starting material, as this aldehyde was more stable with the conjugation of adjacent benzene p-electrons, which increased the carbonyl group's electric density and reduced the possibility of nucleophilic addition reaction on the aldehyde during functionalisation. A benzaldehyde functionalised with an imidazolium ionic liquid, denoted as **ILSA-S3**, was successfully synthesised using a modified method. [176] According to Chapter 3, the anion [NTf_2]- in **ILSA-S3** should meet the size-exclusion requirement. At the same time, though the imidazolium ring was proven to penetrate the cage cavity of **CC3-*R*/CC3-*S*** in [BMIM][NTf_2] in chapter 3, it might be bulky enough to be size excluded in the situation here as the cage window size decreases more with bulkier tied groups. [170] As **ILSA-S3** had a bulky benzene ring adjacent to the tying sites, the lowered pore limiting envelope could be small enough to reject the imidazolium ring. **ILSA-S3** appeared as an off-white wax with a melting point of about 58 °C, and its ^{1}HNMR was fully interpreted in **Figure 5.2**. Then tying of **RCC1** with **ILSA-S3** was studied, starting with Dr M. Liu's method of tying **RCC3** with formaldehyde in methanol. [169] **RCC1**, instead of **RCC3**, was chosen due to the absence of a bulky cyclohexane group adjacent to the diamine, which should facilitate the tying with bully **ILSA-S3** as it could spin to turn away from the cage cavity. A series of other modified conditions were also screened and listed in **Table 5.1**, where TFA was added to see if it had any catalyst effect, and molecular sieves were used to remove water synthesised from the system. [41]

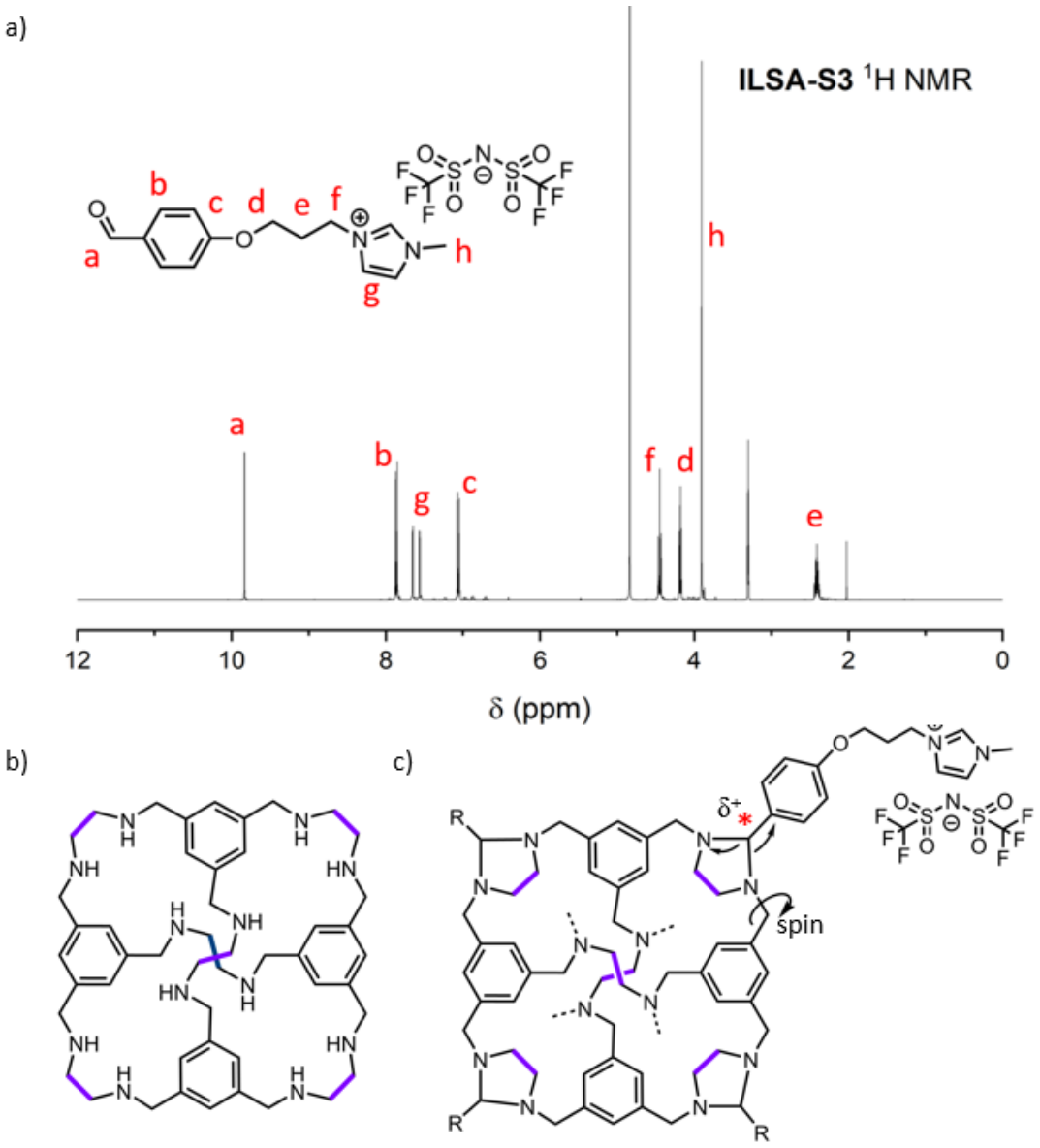

Figure 5.2: a) ^{1}H NMR of **ILSA-S3** (400 MHz, CD_3OD); b) Molecular structure of **RCC1**; c) Molecular structure of **RCC1-ILSA-S3**.

Table 5.1: Tying conditions screened.

	RCC1	**ILSA-S3**	Solvent	Temperature	TFA	Molecular sieves
1	1 equiv.	9 equiv.	Methanol	reflux		
2	1 equiv.	9 equiv.	Methanol	RT		
3	1 equiv.	9 equiv.	Methanol	RT		√
4	1 equiv.	9 equiv.	Methanol	RT	√	
5	1 equiv.	9 equiv.	Methanol	RT	√	√
6	1 equiv.	9 equiv.	DCM	RT		

For methods 1-5 (**Table 5.1**), no apparent ^{1}H NMR change was observed in the spectra of **RCC1-ILSA-S3** product samples after reactions stopped while compared to the spectra of **ILSA-S3**, as the peaks positions in **RCC1-ILSA-S3** spectra resembled those of **ILSA-S3** presented, indicating no reaction happened (**Figure 5.3**). Tying **RCC1** with **ILSA-S3**, which was a nucleophilic addition reaction, formed an aminal bond. The carbon in the aminal bond (marked with an asterisk in **Figure 5.2c**) was a little electron positive with the adjacent electron-withdrawing benzene and nitrogen atoms, thus the aminal bond might be easily attacked by nucleophiles and hydrolysed. The methanol used in the reaction was a relatively polar solvent and thus may pose disadvantages in tying.

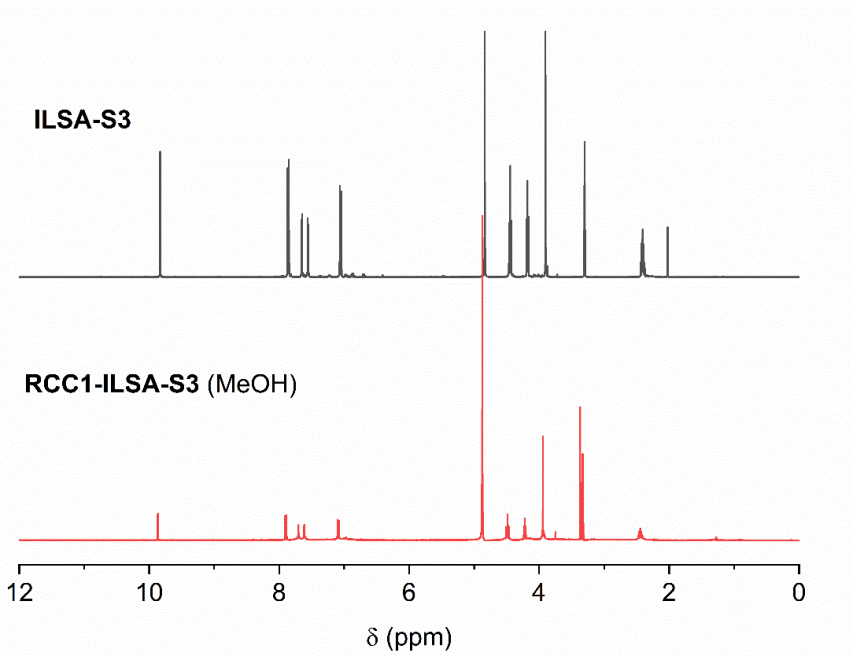

Figure 5.3: Comparison of ^{1}H NMR (400 MHz, CD_3OD) of **ILSA-S3** and **RCC1-ILSA-S3** synthesised in methanol using methods 1-5 in **Table 4.1**.

Next, the less polar solvent DCM was used as the reaction solvent. **RCC1** and **ILSA-S3** were dissolved in DCM respectively and mixed. On mixing, the solution changed from clear to opaque, and the oil-like substance was phased out from the solvent. This oil was separated by decanting the DCM and dried to get an off-white powder. Its ^{1}H NMR (**Figure 5.4**) showed some new broadened peaks, indicating a reaction occurred. Compared with the ^{1}H NMR spectra of **ILSA-S3**, some of the broadened peak positions of **RCC1-ILSA-S3** fitted with those of **ILSA-S3** HNMR peaks. For example, broadened peaks at around 4.4, 4.17, 3.89, and 2.4 ppm in the **RCC1-ILSA-S3** NMR spectra (**Figure 5.4**) corresponded to the H_f, H_d, H_h and H_e in the alkyl chain

and methyl groups of **ILSA-S3** (**Figure 5.2a**), and the broadened peaks were also shifted to the high field. The peak broadening might be caused by the spin of tied **ILSA-S3** groups on the **RCC1** cage (**Figure 5.2c**), thus resulting in the varied environment and chemical shifts. Apart from that, an aldehyde peak could be observed at 9.82 ppm in the **RCC1-ILSA-S3** spectra (**Figure 5.4**), which was a little shifted to high field compared with that of **ILSA-S3**. The shift of aldehyde peak indicated that some monomer aldehyde may be included in the tied product while the NMR of **RCC1-ILSA-S3** was measured, and it took up around 6.7 mol% by integration. The existence of monomer aldehyde in the **RCC1-ILSA-S3** products was assumed to be caused by hydrolysation in the polar methanol used, or a little **ILSA-S3** was incorporated in the product when it was phased out as oil in DCM.

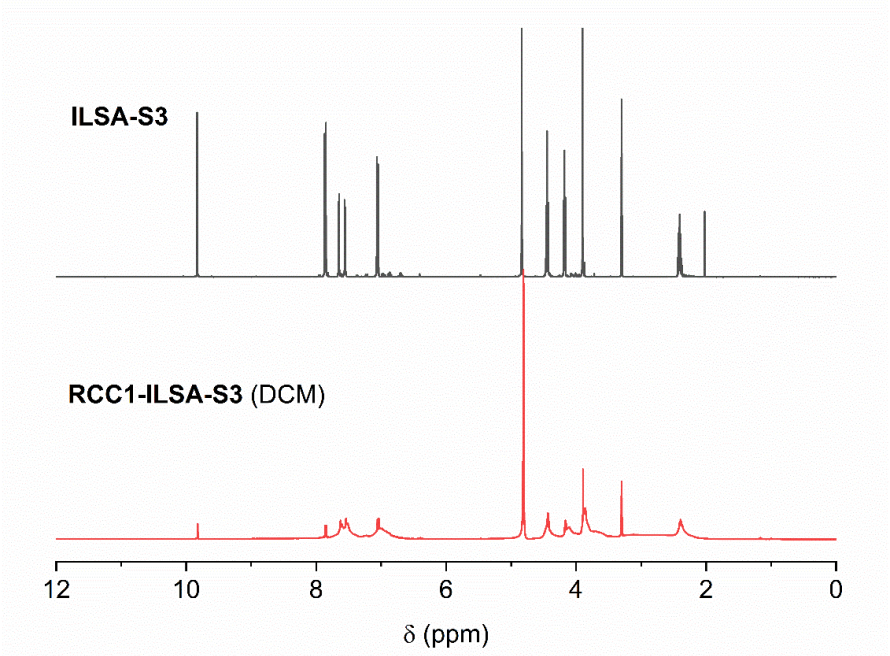

Figure 5.4: Comparison of ^{1}H NMR (400 MHz, CD_3OD) of **ILSA-S3** and **RCC1-ILSA-S3** (Synthesised in DCM) using method 6 in **table 5.1**.

Matrix-assisted laser desorption/ionization time-of-flight mass spectrometry (MALDI-TOF) was then used to check the molecular mass of the synthesised product (**Figure 5.5**), as this method may allow us to get a mass peak of the total molecular weight of the tied cage. The targeted peak $[M\text{-}NTf_2]^+$ = 3579.21 (theory value: 3578.92) was observed, which corresponded to the mass of 6-tied **RCC1** minus an anion $[NTF_2]^-$, and the negative mode gave a clean peak of the anion $[NTF_2]^-$ at 279.89 (theory value: 279.92). Sometimes, a five-tied product peak may appear, which might arise from the aminal bonding breaking with the heavy and bulky **ILSA-S3** groups

attached in the MS measurement or the inclusion of a less-tied product while phasing out from the DCM solution. Elemental analysis was then used to evaluate the purity of **RCC1-ILSA-S3**. The results in **Table 5.2** demonstrated good fitting between the calculated values and experiment values, indicating that most products could be confirmed to be 6-tied **RCC1-ILSA-S3**.

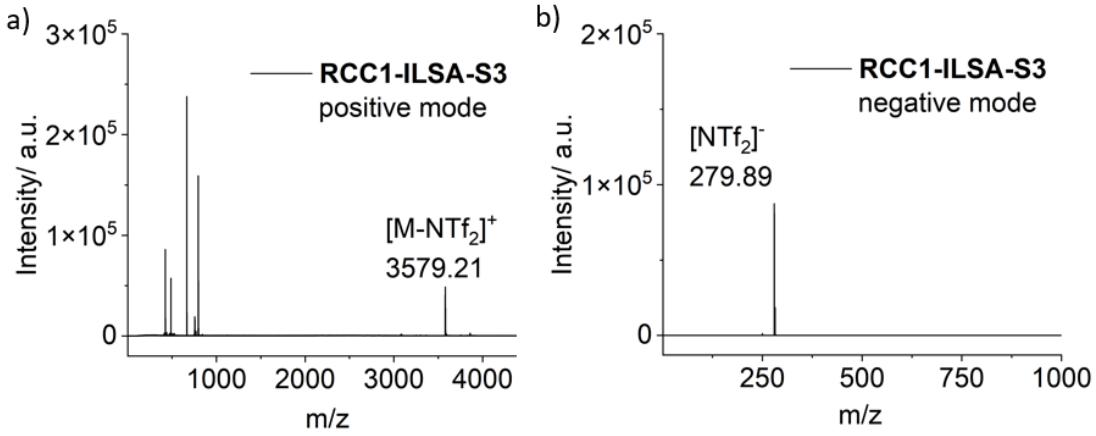

Figure 5.5: a) Mass spectra of **RCC1-ILSA-S3** in positive mode; b) a) Mass spectra of **RCC1-ILSA-S3** in negative mode.

Table 5.2: Elemental analysis of **RCC1-ILSA-S3**

RCC1-ILSA-S3 $C_{144}H_{162}F_{36}N_{30}O_{30}S_{12}$	%C	%H	%N	%S
Calculated value	44.79	4.23	10.88	9.96
Analysis 1	44.04	4.19	10.78	-
Analysis 2	43.75	4.13	10.76	-

After confirming the identity of the targeted 6-tied **RCC1-ILSA-S3**, a thorough wash, which involved dissolving the product in a bit of methanol and then washing with a large quantity of DCM, was employed. The ^{1}H NMR solvent was changed to the less polar DMSO-d_6 in an attempt to get a clean ^{1}H NMR without the aldehyde peak. As is shown in **Figure 5.6**, the peaks were widely broadened due to the freely spinning of tied **ILSA-S3** groups, and it was difficult to analyse and interpret peaks without a low-temperature NMR study. As to ^{13}C NMR spectra, while **RCC1** and **ILSA-S3** were fully interpreted (**Figures 5.7** and **5.8**), it was also not easy to allocate each carbon in **RCC1-ILSA-S3** due to its low-intensity signals (**Figure 5.9**), where only limited peaks could be identified. For example, the R-a peak (**Figure 5.9**) in **RCC1-ILSA-S3** may correspond to the carbon a in **RCC1**, which was a benzene carbon adjacent to

secondary amine groups (**Figure 5.7**); and the IL-i peak corresponded to the carbons (-**C**F_3) in the anion of **ILSA-S3** (**Figure 5.8**), which was a quartet due to its coupling with the fluoride atom. The remaining IL-f, IL-g and IL-h could be assigned to the alkyl chain carbons from **ILSA-S3** (**Figure 5.8**), and the peak of R-c was the carbon adjacent to the benzene ring and nitrogen atom in the cage core **RCC1** (**Figure 5.7**).

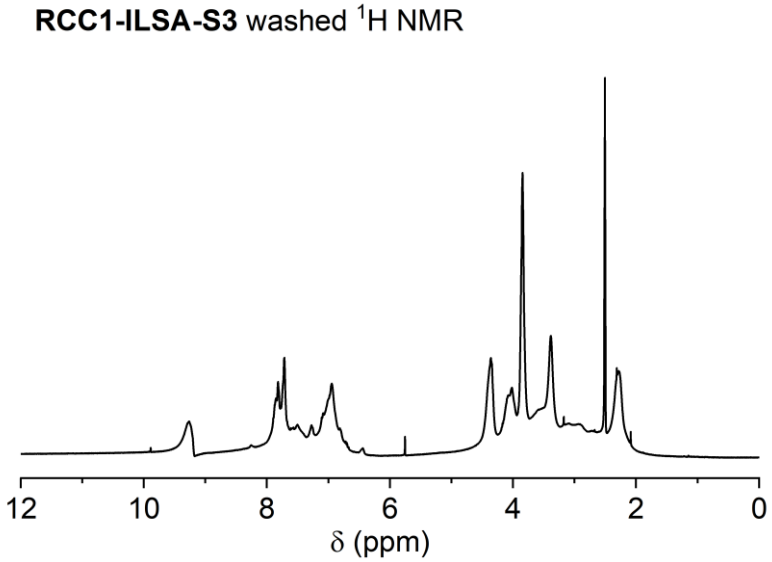

Figure 5.6: ^{1}H NMR (400 MHz, DMSO-d_6) of washed **RCC1-ILSA-S3**.

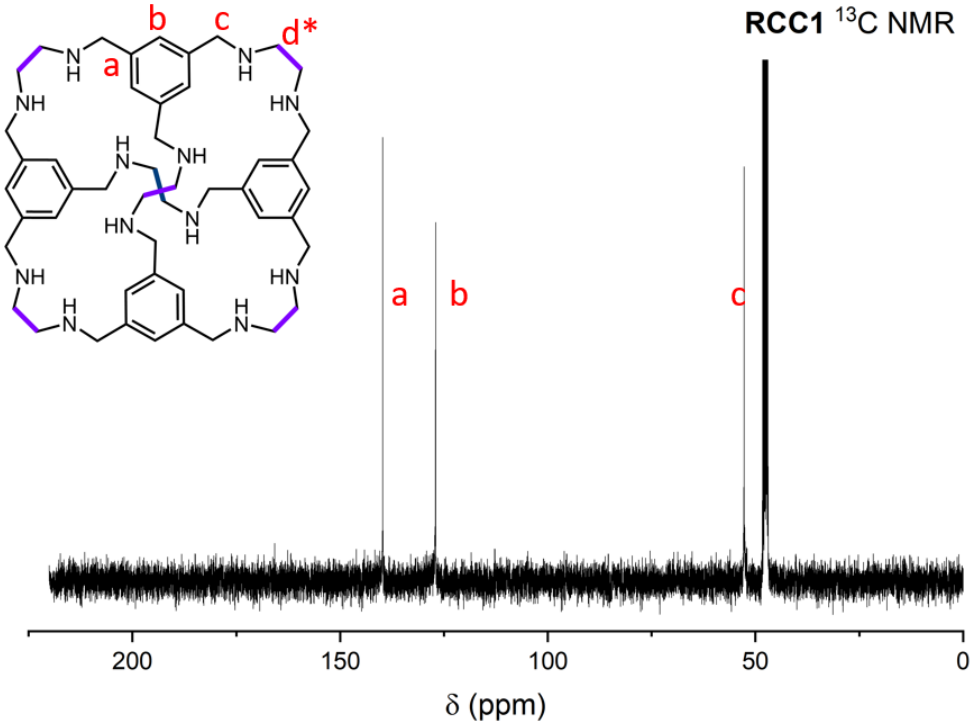

Figure 5.7: ^{13}C NMR (400 MHz, CD_3OD) of **RCC1**. (C(d*) imposed with NMR solvent peaks)

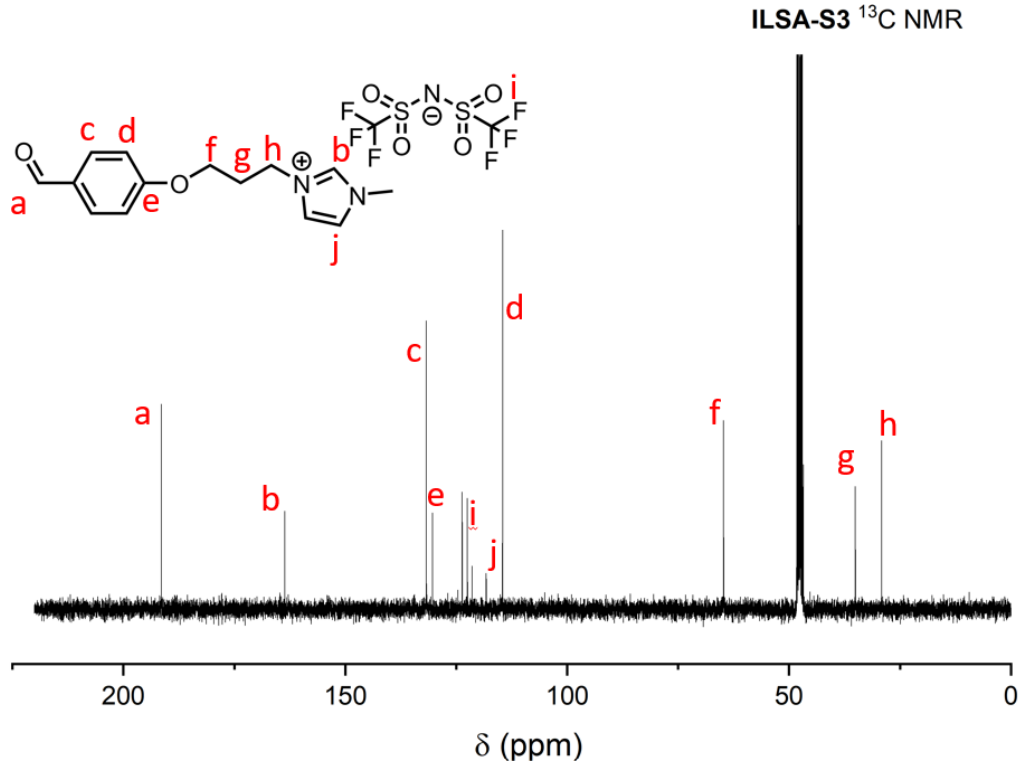

Figure 5.8: ^{13}C NMR (400 MHz, CD_3OD) of **ILSA-S3**.

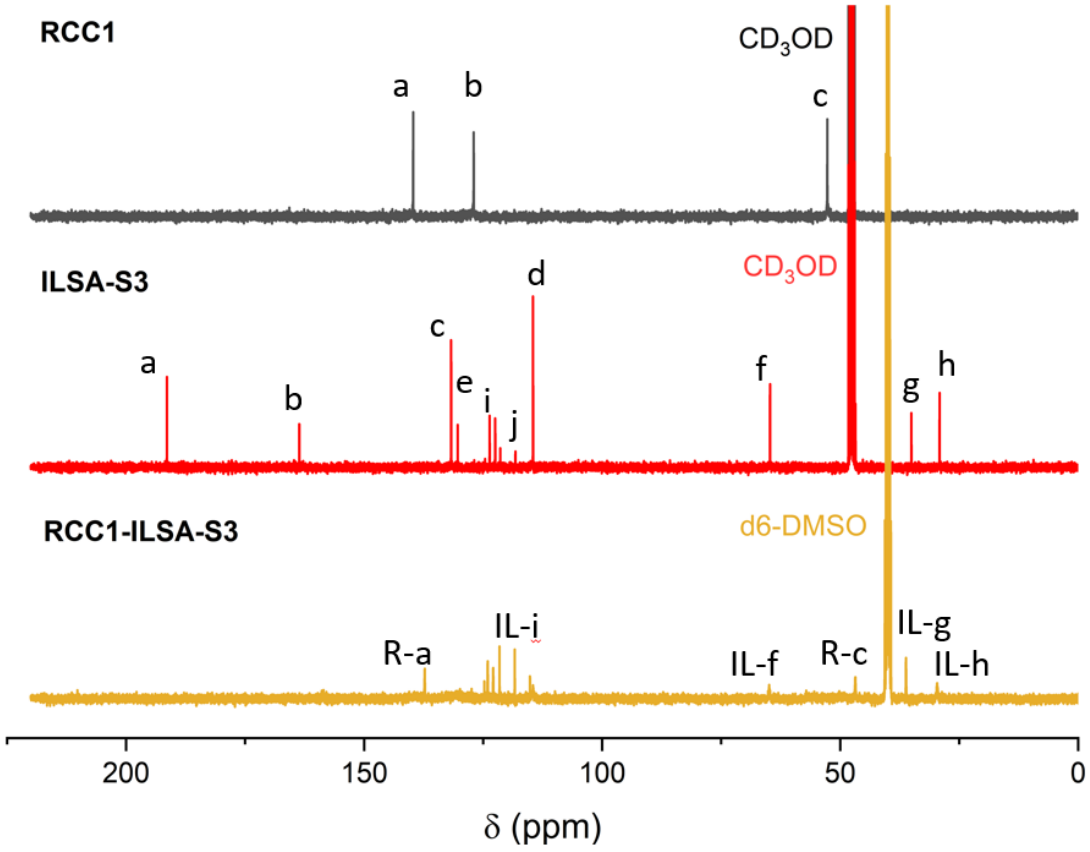

Figure 5.9: Comparison of ^{13}C NMR (400 MHz) of **RCC1** in CD_3OD, **ILSA-S3** in CD_3OD and **RCC1-ILSA-S3** (Synthesised in DCM, method 6 in **table 4.1**) in DMSO-d_6.

HPLC with UV as the detector was also used to check the purity of the washed **RCC1-ILSA-S3**. A C18 column was used as the stationary phase for separation and pure acetonitrile as the mobile phase. Though the sample **RCC1-ILSA-S3** presented a signal at the time of 4.34 minutes at 290 nm (**Figure 5.10b**), it did not show much difference compared to the spectra of **ILSA-S3,** which showed the signal at 4.33 minutes (**Figure 5.10a**). The similar retention time of the ionic liquid tethered cage **RCC1-ILSA-S3** to the precursor **ILSA-S3** may arise from the same interaction sites with the C18 column, where the polar imidazolium ionic liquid ends from both samples could not interact well with the nonpolar column. Due to the indistinguishable interaction sites, it would be hard to determine the purity of **RCC1-ILSA-S3** with HPLC.

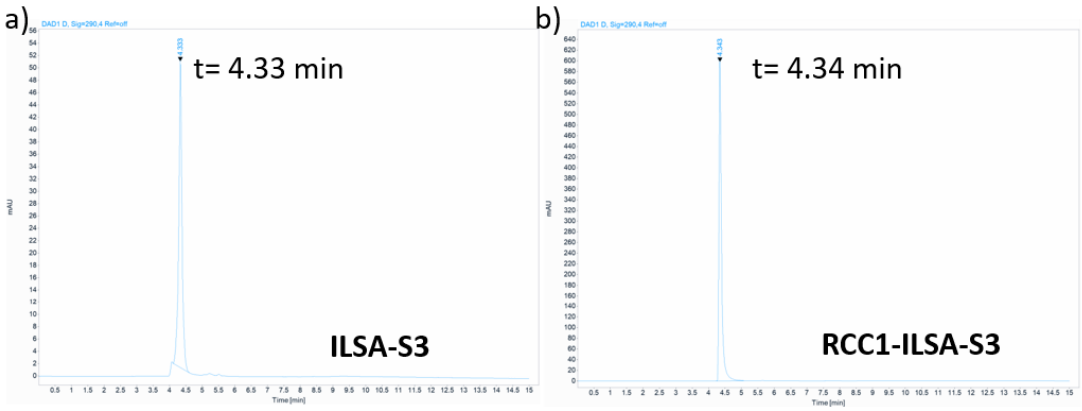

Figure 5.10: HPLC spectra of a) **ILSA-3**; b) **RCC1-ILSA-S3** at 290 nm.

Though explicit NMR assignment and HPLC study of **RCC1-ILSA-S3** failed, elemental analysis and MS spectra could be used to confirm the product. The methanol washing of crude **RCC1-ILSA-S3** though gave a cleaner ^{1}HNMR spectra (**Figure 5.6**), it also caused a lot of mass loss. Thus, the **RCC1-ILSA-S3** product washed with just DCM was used for further studies, as the content of remaining **ILSA-S3** should be low according to the elemental analysis result. And the existence of one or two less-tied products of **RCC1-ILSA-S3** could also be tolerated according to the conclusion by Liu *et al.*, where the cage **RCC3** tied with 5 and 6 formaldehyde molecules had similar pore limiting envelope and gas sorption properties. [170]

5.4 Melting behaviour study

5.4.1 Thermal study

RCC1-ILSA-S3 was first checked with TGA, with the result shown in **Figure 5.11**. **RCC1-ILSA-S3** lost about 2.01% of its mass from room temperature to around 300 °C, which may be due to the absorbed water on the surface of **RCC1-ILSA-S3**. From 300 to 400 °C, **RCC1-ILSA-S3** lost 9.71% mass; after that, until around 500 °C, a steeper loss of 59.9% was observed. Compared to the TGA curves of the precursors, **RCC1** and **ILSA-S3**, the weight loss from **RCC1-ILSA-S3** starting at 300 °C was similar to the onset of the weight loss observed for pure **RCC1**. In the TGA, **RCC1** lost around 5 wt.% while heating the sample to 100 °C, possibly due to weakly bound water on the **RCC1** powders. Concentrated **RCC1** product from the synthesis reaction was first dried under vacuum at RT overnight, changing from a viscous oil to swelling foam, and then dried at 50 °C with a heating block under vacuum for 2-3 hours to give the powder product **RCC1**. [177] And the **RCC1** sample was stored in the air before switching to heating the sample under a dry N_2 gas glow during the TGA measurement. Thus, water could exist in the sample. After 300 °C, **RCC1** underwent a faster weight drop, while **ILSA-S3** stayed stable until 400 °C, and its vast mass loss occurred between 400 and 500 °C. To rule out the possibility that breaking of aminal bonding between **RCC1** and **ILSA-S3** might not cause mass loss, DSC was then employed to check whether bond breaking, which involved heat change, would occur during the temperature range.

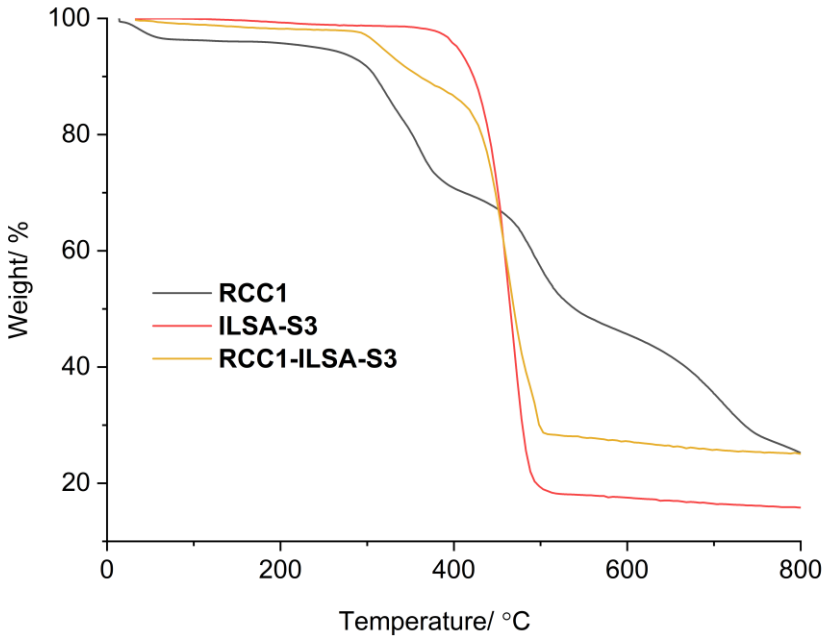

Figure 5.11: TGA of **RCC1**, **ILSA-S3**, **RCC1-ILSA-S3**.

A DSC study of **RCC1-ILSA-S3** recorded between 0 and 150 ºC was shown in **Figure 5.12a**. The heating step in the first cycle presented an overall decreasing trend curve, with a broadened endothermic peak over the range of 55 to 90 ºC. However, the cooling step did not show any exothermic peak, and there was no peak either in the heating or cooling process in the second cycle. Apart from that, samples changed from an off-white powder to a clear yellow glass-like substance (**Figure 5.12d**). Mass spectroscopy of the sample after DSC study was first checked to evaluate the possibility of aminal bond breaking over the temperature range of the peak in the DSC curve. The mass spectra showed an intact 6-tied product of **RCC1-ILSA-S3**, indicating the peak might be due to a phase change behaviour, and it irreversibly transformed into a glass-like state. The broadened appearance of the peak in the heating curve and the lack of a corresponding exothermic peak in the cooling curve indicated the amorphous nature of **RCC1-ILSA-S3**. PXRD study on both as-synthesised and glass-like **RCC1-ILSA-S3** showed no peaks and confirmed its amorphous state (**Figure 5.12b**). To further confirm the phase changing of **RCC1-ILSA-S3**, we used a Stuart digital melting point apparatus SMP 10 to observe its behaviour with increasing temperature. As shown in **Figure 5.12c**, **RCC1-ILSA-S3** first appeared as powders filling the capillary bottom at 25 ºC, but it collapsed onto the capillary wall and looked like a viscous oil with increasing temperature. Thus, it can be concluded that as-synthesised **RCC1-ILSA-S3** was an amorphous solid. It

demonstrated melting behaviour over 55-90 ºC, and **RCC1-ILSA-S3** turned into a glass-like substance after it cooled.

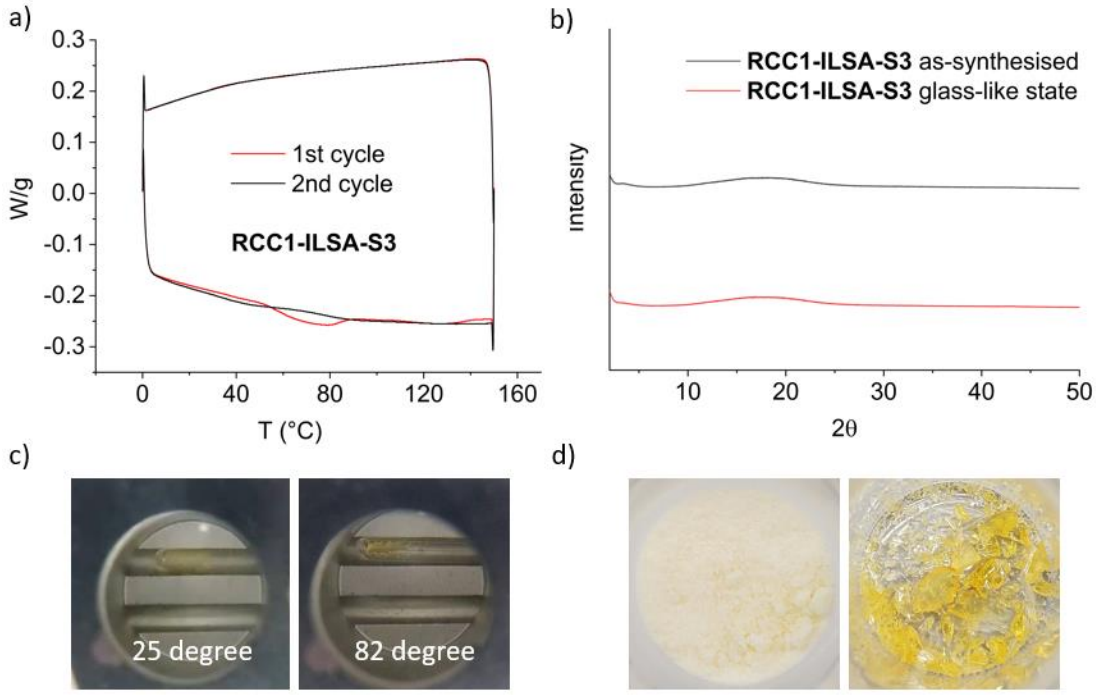

Figure 5.12: a) DSC curve of **RCC1-ILSA-S3**; b) PXRD spectra of as-synthesised **RCC1-ILSA-S3** and glass-like **RCC1-ILSA-S3** after melting and cooling; c) Melting behaviours of **RCC1-ILSA-S3** observed on SMP 10; d) Images of as-synthesised **RCC1-ILSA-S3** and glass-like **RCC1-ILSA-S3**.

The glass-like **RCC1-ILSA-S3** could be turned back to its powder form by soaking in DCM, decanting, and drying under vacuum. Due to these two reversible morphologies of **RCC1-ILSA-S3**, its mechanical processibility was studied, where **RCC1-ILSA-S3** was melted and pressed. A thin and transparent plate was successfully formed (**Figure 5.13a**), and a round plate with a diameter of 1 centimetre could be made by using a mould. The processibility presented here demonstrated that **RCC1-ILSA-S3** has the potential to form a self-supported film.

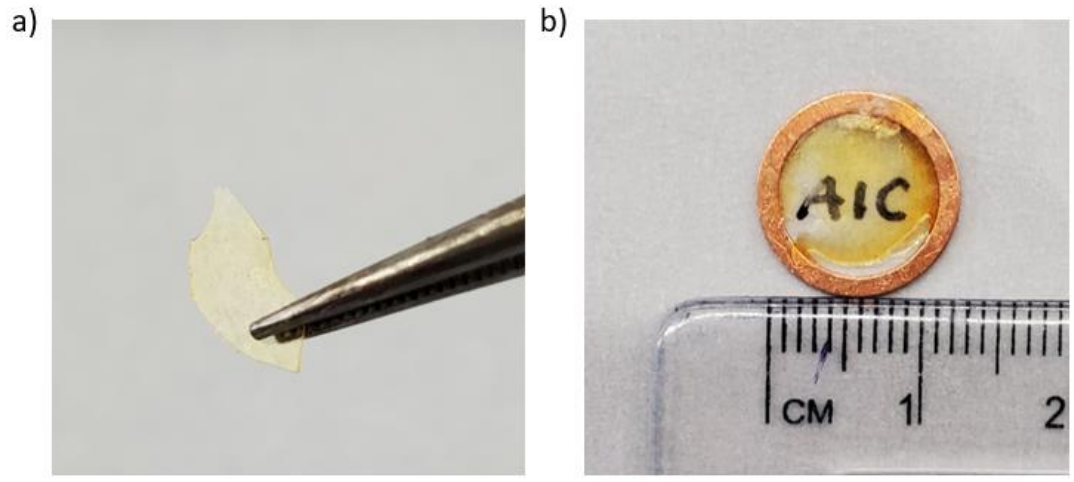

Figure 5.13: a) A thin glass-like plated processed; b) A round-shaped glass-like plate with a diameter of 10 mm processed.

5.4.2 Rheology description

A rheology study was performed on the **RCC1-ILSA-S3** to check whether it could display liquid behaviours at higher temperatures. The sample was heated until 92 °C and equilibrated for 60 seconds before each measurement. It was set that dynamic viscosity was to be measured over the range of the shear rate from 0.1 to 100 s^{-1} in the flow sweep measurement. However, the instrument was overloaded and stopped at a shear rate of 6.31 s^{-1} with a viscosity of 7975 Pa·s (**Figure 5.14a**). The overload was caused by the high viscosity of the melted **RCC1-ILSA-S3**, which would require more shear stress with an increasing shear rate. The dynamic oscillation amplitude measurement also suffered the same issue, where the instrument was overloaded at an oscillation strain of 192.86% with a constant oscillation frequency of 10.0 rad/s. However, the loss modulus G" was overall larger than storage modulus G' within the scanned range from 0.1% to 192.86%, indicating the system exhibited liquid properties (**Figure 5.14b**). These two experiments proved that though **RCC1-ILSA-S3** could behave like a liquid while melted, its viscosity could be massive, posing some disadvantages in melted processing.

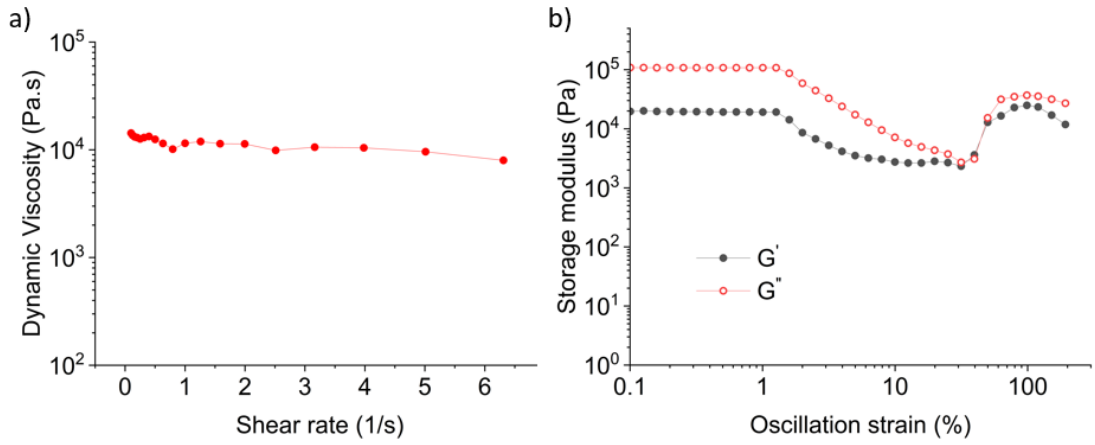

Figure 5.14: a) Flow sweep measurement on **RCC1-ILSA-S3** over the shear rate 0.1-100 s^{-1} (instrument overloaded); b) Oscillation amplitude sweep over the oscillation strain from 0.1 to 1000% with a constant oscillation frequency of 10.0 rad/s (instrument overloaded).

5.4.3 Further melting point decrease strategy

The melting point of ionic liquids could be decreased by increasing the alkyl chain length on the cation to some degree, as this further dispersed the ion charge and reduced the electrostatic interaction with the anion. [150] However, if the alkyl chain length keeps increasing, Van der Waals interaction will also increase with larger molecular weight, thus leading to an increased melting point. [150] To further decrease the melting point of tied-**RCC1**, another ionic liquid functionalised aldehyde was synthesised with three more carbon in the alkyl chain that connected benzaldehyde and imidazolium ring, named **ILSA3-S3**. Tying **RCC1** with **ILSA3-S3** used the same reaction condition as **RCC1-ILSA-S3**, where DCM solutions of **RCC1** and **ILSA3-S3** in a 1:1.5 ratio were mixed, respectively, and the tied product was phased out of the reaction solvent. This approach proved to be successful, with targeted mass peak $[M\text{-}NTf_2]^+$ (3831.40, theory value: 3831.19) and $[NTf_2]^-$ (279.89, theory value: 280.14) observed (**Figure 5.15**). The elemental analysis results (**Table 5.3**) also fitted well with its calculated values.

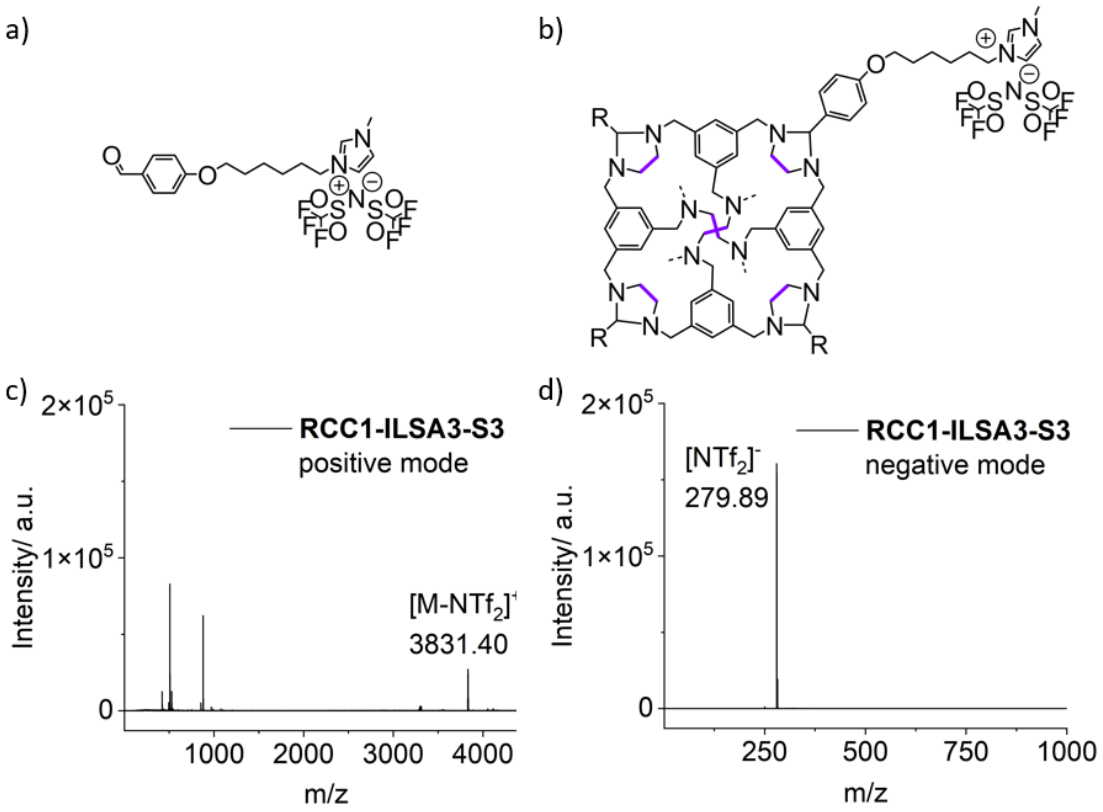

Figure 5.15: a) Molecular structure of **ILSA3-S3**; b) Molecular structure of **RCC1-ILSA3-S3**; c) Mass spectra of **RCC1-ILSA3-S3** in positive mode; d) Mass spectra of **RCC1-ILSA3-S3** in negative mode.

Table 5.3: Elemental analysis of **RCC1-ILSA3-S3**

RCC1-ILSA3-S3 $C_{162}H_{198}F_{36}N_{30}O_{30}S_{12}$	%C	%H	%N	%S
Calculated value	47.29	4.85	10.21	9.35
Analysis 1	46.48	4.79	10.00	-

Tethering ionic liquid with a long PEG chain was proved to successfully lower the melting point of a coordination cage. [28] Thus, a benzaldehyde functionalised with a PEG ionic liquid named **PEG-190-CHO** (**Figure 5.16a**) was also tried. Tying **RCC1** with **PEG-190-CHO** was modified a little due to the good solubility of the tied product in DCM, where DCM solutions of **RCC1** and **PEG-190** in a 1:1 ratio were mixed and stirred with $NaSO_4$ as the drying agent. The DCM solution was then filtered and concentrated to afford the product **RCC1-PEG-190**. Mass spectroscopy again showed targeted peaks (**Figure 5.16c** and **d**), and elemental experimental results also fitted the calculated values (**Table 5.4**).

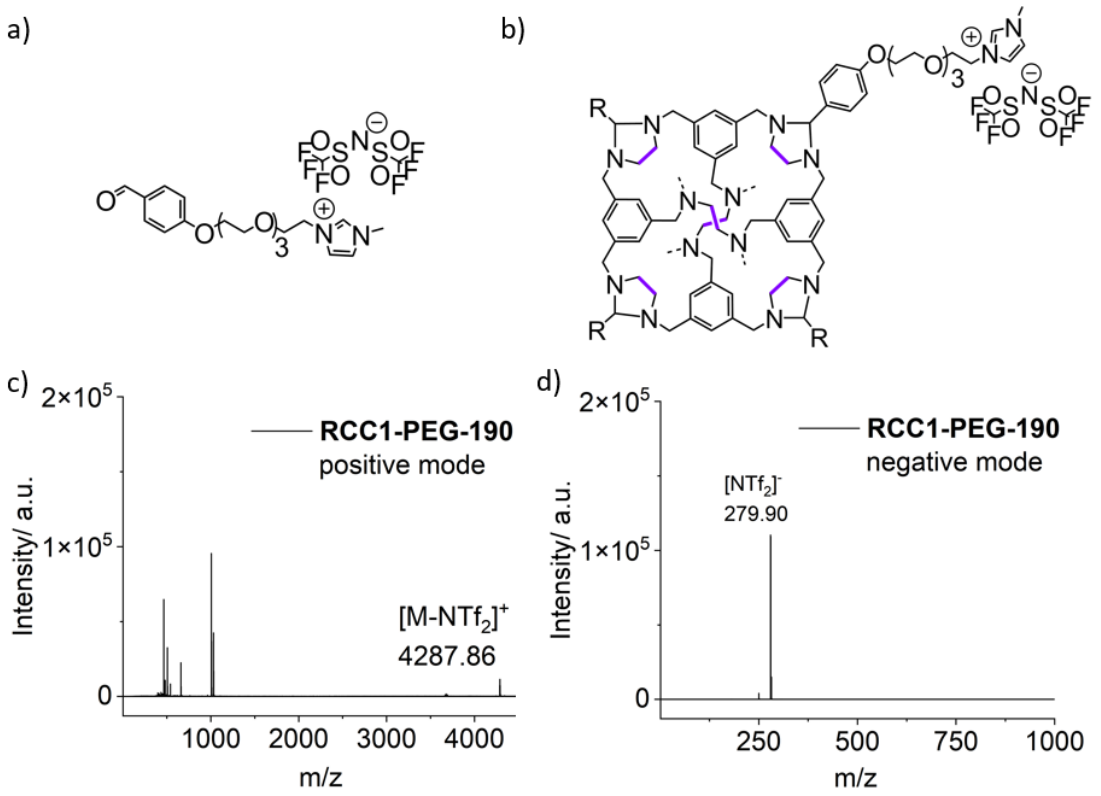

Figure 5.16: a) Molecular structure of **PEG-190-CHO**; b) Molecular structure of **RCC1-PEG-190**; c) Mass spectra of **RCC1-PEG-190** in positive mode; d) Mass spectra of **RCC1-ILSA3-S3** in negative mode.

Table 5.4: Elemental analysis of **RCC1-PEG-190**

RCC1-PEG-190 $C_{174}H_{222}F_{36}N_{30}O_{48}S_{12}$	%C	%H	%N	%S
Calculated value	45.73	4.90	9.19	8.42
Analysis 1	44.84	4.86	8.68	-

DSC studies were then performed on **RCC1-ILSA3-S3** and **RCC1-PEG-190** to check their melting behaviours. Like **RCC1-ILSA-S3**, as-synthesised **RCC1-ILSA3-S3** was off-white powder. However unfortunately, it did not show an apparent decrease in the melting point according to the DSC spectra (**Figure 5.17**), where the melting range only shifted around 5 °C to the lower temperature region (50-85 °C) compared to **RCC1-ILSA-S3** (55-90 °C). **RCC1-PEG-190** appeared as a clear, highly viscous substance stuck to the wall of the vial, which did not show an apparent melting peak but a glass transition around -40 ºC, indicating its liquid nature at room temperature. Another PEG ionic liquid functionalised aldehyde **PEG-370** was also synthesised, which had nearly doubled PEG chain length and may potentially increase the fluidity of the tied **RCC1** salt. However, tying **RCC1** with **PEG-370** failed to give the desired

peak in the mass spectroscopy study, which could be due to that the heavy molecular weight of **PEG-370** posed a disadvantage in tying. Thus, this project was not pursued in lowering melting point further. In conclusion, the melting point of **RCC1** tying serial could be lowered to room temperature while tethered with PEG ionic liquid, however its viscosity could be quite high. This could be fixed by dissolving the product in other bulky solvents with low viscosity to prepare a Type II porous liquid. Though the melting point of **RCC1-ILSA-S3** and **RCC1-ILSA3-S3** failed to be lowered to room temperature, it may be possible to define the two as general type I porous liquids, just as that the general definition of ionic liquids was salts with a melting point below 100 ºC.

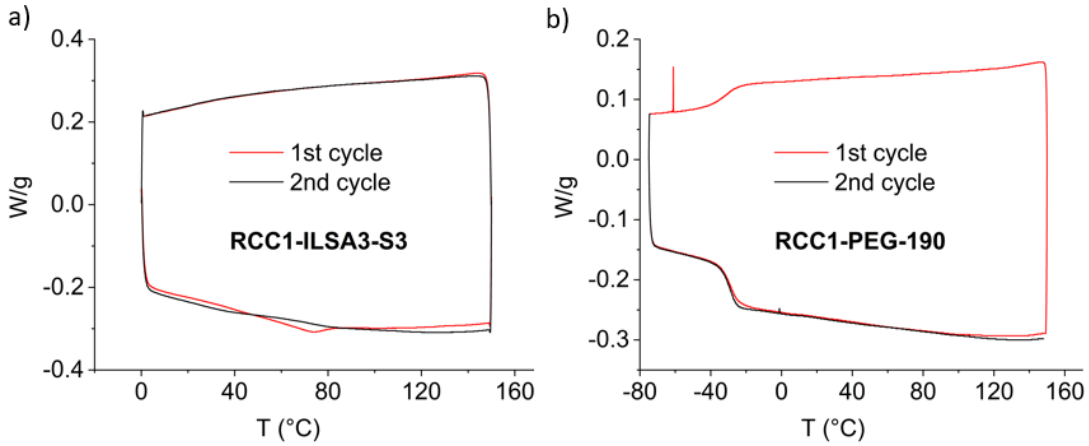

Figure 5.17: a) DSC spectra of **RCC1-ILSA3-S3**; b) a) DSC spectra of **RCC1-PEG-190**.

5.5 Porosity study by CO_2 sorption of RCC1-ILSA-S3

CO_2 uptakes of **ILSA-S3** and **RCC1-ILSA-S3** were first measured on Quantachrome to evaluate the porosity of **RCC1-ILSA-S3,** with the same measuring conditions used for type III dispersions of **CC3-*R*/CC3-*S*** in Chapter 3, which had a longer equilibration time (1800 s) at each measuring point to ensure saturation (**Figure 5.18**). The uptake of the solid-state **RCC1-ILSA-S3** was determined as 218 ± 2.8 µmol/g, nearly three times that of the solid **ILSA-S3** (76 ± 1.3 µmol/g), which successfully demonstrated potential porosity of the **RCC1-ILSA-S3** system.

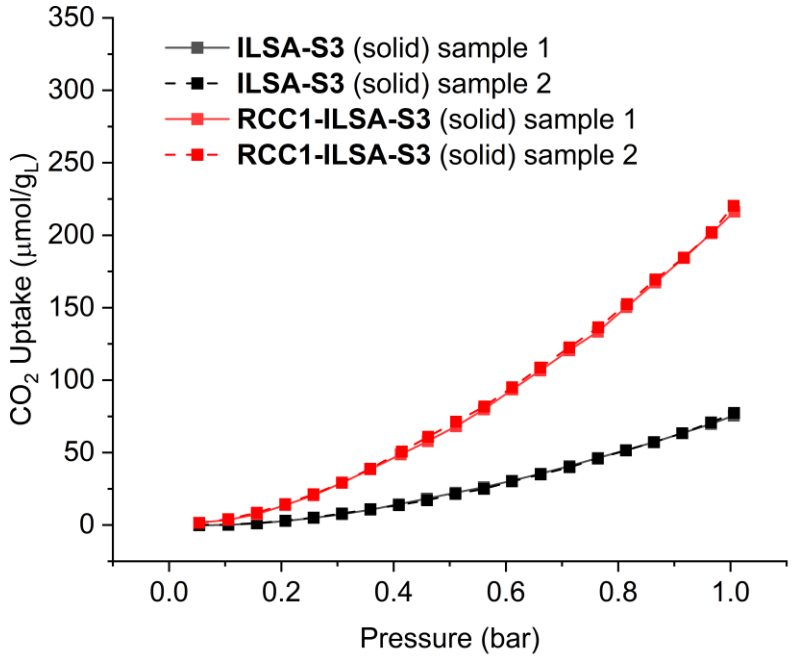

Figure 5.18: CO_2 isotherms of **ILSA-S3** and as-synthesised solid **RCC1-ILSA-S3**.

Then CO_2 sorption of **RCC1-ILSA-S3** at different states was studied. 100 mg **RCC1-ILSA-S3** was heated at 100 ºC to ensure it was melted. The volume of **RCC1-ILSA-S3** decreased a lot after melting, changing from white powders to a thin layer of yellow, clear, viscous oil attached to the tube wall where the stirrer bar did not work. It was assumed that full gas saturation of **RCC1-ILSA-S3** could be reached as each measuring point had a long CO_2 equilibrium time and the thin film of liquid could ensure fully contact with CO_2. The CO_2 uptakes of **RCC1-ILSA-S3** at the liquid state was 198 ± 6.6 µmol/g, which was nearly the same as that of the 20 wt% Type III porous liquid of **CC3-*R*/CC3-*S*** in [BPy][NTf_2] at room temperature (209.8 ± 6.7 µmol/g). **RCC1-ILSA-S3** did not show much of a decreased uptake at 100 ºC compared to room temperature (**Figure 5.19**), which was probably due to the highly viscous state of the liquid formed and binding CO_2 more tightly. This indicates an advantage for the application of sorption at higher temperatures. The CO_2 uptake of the glass-like state was measured on the cooled **RCC1-ILSA-S3** sample, and presented a result of about 204 ± 1.7 µmol/g.

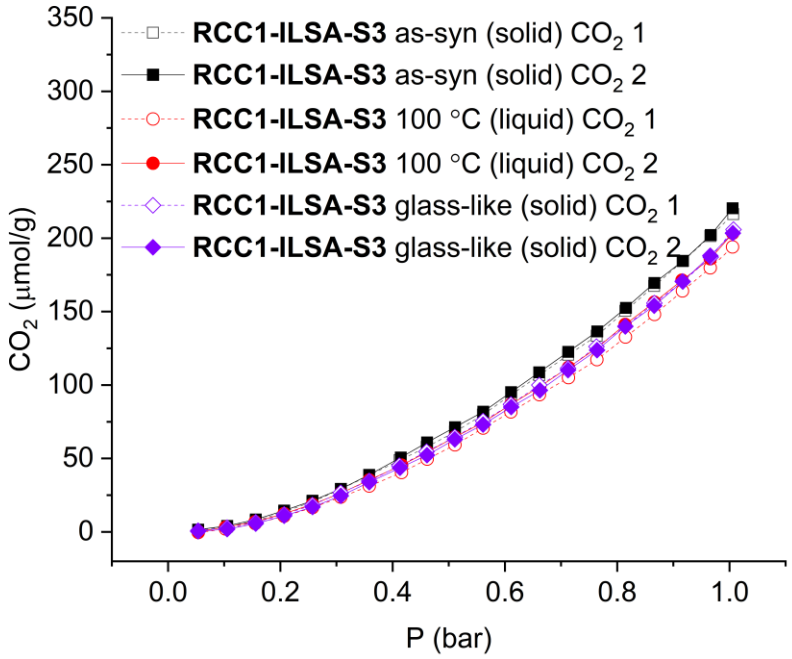

Figure 5.19: CO_2 isotherms of as-synthesised **RCC1-ILSA-S3** at room temperature, **RCC1-ILSA-S3** at 100 ºC and glass-like **RCC1-ILSA-S3**.

Though improved CO_2 uptake of **RCC1-ILSA-S3** over that of the monomer **ILSA-S3** was demonstrated, the absolute CO_2 uptake value **RCC1-ILSA-S3** was still not so high, at least not comparable to that of another type I porous liquid $[P_{66614}][DCP_5]$, [89] which was 5.52 mol/mol (50 °C, 1 bar, roughly 1.53 mmol/g). There could be three reasons for the low uptake of **RCC1-ILSA-S3**. Firstly, the cage we used had a relatively low surface area. Secondly, the tying of **ILSA-S3** decreased the window sizes of the cage, which should pose a pore limiting envelope and reduce the gas uptake. This could be the same situation as Dr M. Liu *et al.*, [170] where they used tied **RCC3** to separate smaller molecules like H_2 and D_2. Lastly, tying **RCC1** with six bulky and heavy ionic liquid groups dilutes the cage concentration like in the situations of type II or type III. As calculated in **Table 5.5,** which divided the relative molecular weight of **RCC1** (minus 12 H) over that of the tied product, **RCC1-ILSA-S3** had just 20.85 wt.% cage core of the whole molecule, which was like making a 20.85 wt.% solution of the cage. To check this theory that the low CO_2 uptake arose from heavily tethered groups, another molecule **RCC1-ILSA-02** was synthesised by tying **RCC1** with the anisaldehyde (MW=136.15), which was similar to **ILSA-S3** (MW=525.44) in structure but much lighter. **RCC1-ILSA-02** had over doubled the percentage of cage core (52.76 wt.%), and it displayed the CO_2 uptake of 307 ± 3.4 µmol/g (**Figure**

5.20), which indeed was 1.5 times that of **RCC1-ILSA-S3**. Thus, with this trend, if the alkyl chain length on the tied groups on **RCC1** were continuously increased to lower the melting point further, the cage core concentration would keep dropping, with **RCC1-PEG-190** having only 17.61 wt.%, and it would have much less gas uptake. However, though the absolute CO_2 uptake of **RCC1-ILSA-S3** at a melted state was not high, it was still comparable to other types I porous liquid systems reported (**Table 5.6**). [90]

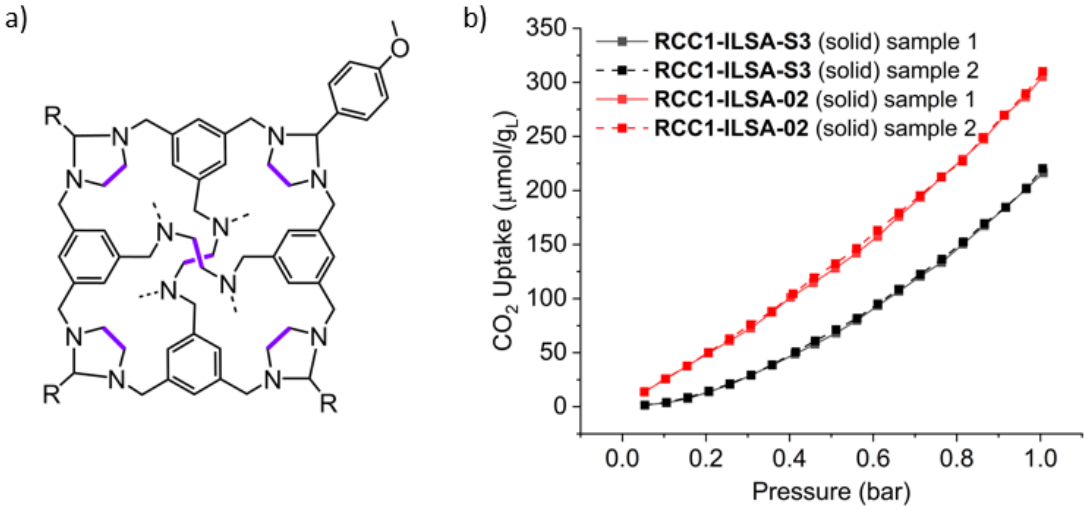

Figure 5.20: a) Molecular structure of **RCC1-ILSA-02**; b) CO_2 isotherms of **RCC1-ILSA-02** and **RCC1-ILSA-S3**.

Table 5.5: Molecular weight list of corresponding tying products of **RCC1**.

	Relative Molecular Weight	Cage Core wt. %
RCC1	817.19	-
RCC1-ILSA-02	1525.97	52.76
RCC1-ILSA-S3	3861.71	20.85
RCC1-ILSA3-S3	4114.19	19.57
RCC1-PEG-190	4570.49	17.61

Table 5.6: CO_2 uptake comparison of **RCC1-ILSA-S3** (melted, 100 ºC) with other type I porous liquid systems.

Type I porous liquids	**CO_2 measure conditions**	**CO_2 uptake (mmol/g)**
HCS-liquid [100]	25 °C, 10 bar	0.568
HCS-PILs-PEGS [67]	25 °C, 10 bar	0.0736-1.05
SIT-M2070 [60]	25 °C, 25 bar	1.5-2.2
UiO-66@OS@PEGS [45]	25 °C, 10 bar	0.636
UiO-66 PLs [178]	25 °C, 10 bar	1.95-3.53
UiO-66- liquid [79]	25 °C, 10 bar	0.254-0.276
Im-UiO-PL [80]	25 °C, 9 bar	5.93
ZIF-8 PLs [104]	25 °C, 1 bar	0.106-0.193 (4.67-8.50 mg/g)
$[P_{66614}][DCP5]$ [89]	50 °C, 1 bar	1.53 (5.52 mol/mol)
PS-OS@SiNR [61]	25 °C, 0.03 bar	0.758-1.115
PoLi-bCA [66]	25 °C, 0.03 bar	0.223
HS-liquid [32]	-	Not reported
γ-CD porous liquid [92]	-	Not reported
Cage **2** [28]	-	Not reported
RCC1-ILSA-S3	398 K, 1 bar	0.198 (this work)

5.6 Stability study

RCC1-ILSA-S3 was found to have relatively good thermal stability and appeared stable until 300 ºC, according to the TGA result. Mass spectroscopy was used further to check the identity of **RCC1-ILSA-S3** after heat treatment, specifically after the DSC study (up to 150 ºC) where **RCC1-ILSA-S3** changed from powder to glass-like solids, and the result showed the presence of the native 6-tied product (**Figure 5.21**). The ageing experiment also demonstrated good stability, where **RCC1-ILSA-S3** remained the 6-tied product in methanol after 1 month. MS was checked after CO_2 sorption because CO_2 may form acid if there was water in the system, and it might decompose **RCC1-ILSA-S3**. The result presented not too much difference from the one before sorption. Before further checking the tolerance of **RCC1-ILSA-S3** towards aqueous acid and base, the effect of water was studied at first. Within one hour of adding 0.2 mL H_2O to 1 mL methanol solution of **RCC1-ILSA-S3** (10 mg/mL), no apparent decomposition of the six-tied product was observed, indicating short-term resistance to H_2O and the capability of studying effects of acids and bases on the system.

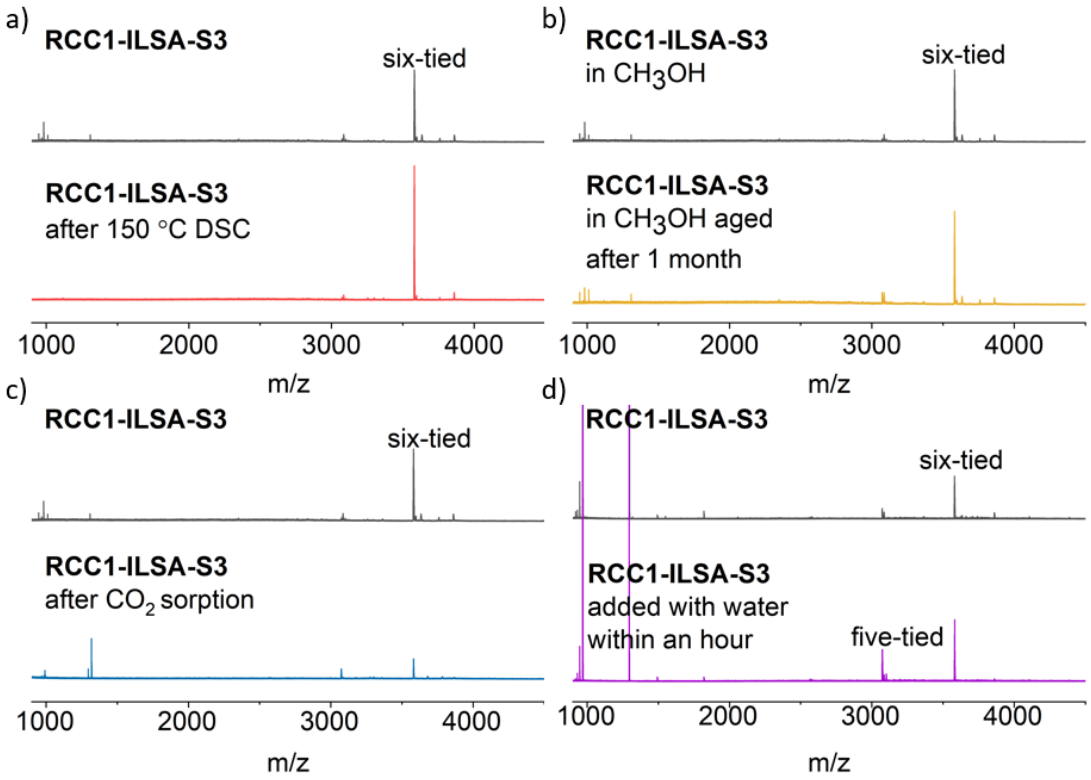

Figure 5.21: MALDI-TOF spectroscopy of **RCC1-ILSA-S3** a) after DSC study (until 150 ºC); b) in MeOH after a month; c) after CO_2 sorption; d) after adding water within an hour.

Aqueous solutions of 1 M HCl, 0.1 M HCl, 1 M acetic acid and 0.1 M acetic acid were made, and 0.2 mL of each was added to the 1 mL methanol solution of **RCC1-ILSA-S3** (10 mg/mL). The 0.2 mL of 0.1M acid was roughly six equivalences of the amount of **RCC1-ILSA-S3** in the methanol solution, corresponding to six tied groups. Mass spectroscopy was then measured within one hour and compared to the blank sample. As can be seen in **Figure 5.22**, both strong acid HCl (pKa = -7) and weak acid CH_3COOH (pKa = 4.76) hydrolysed **RCC1-ILSA-S3** completely after being added, with the peaks of tied products gone.

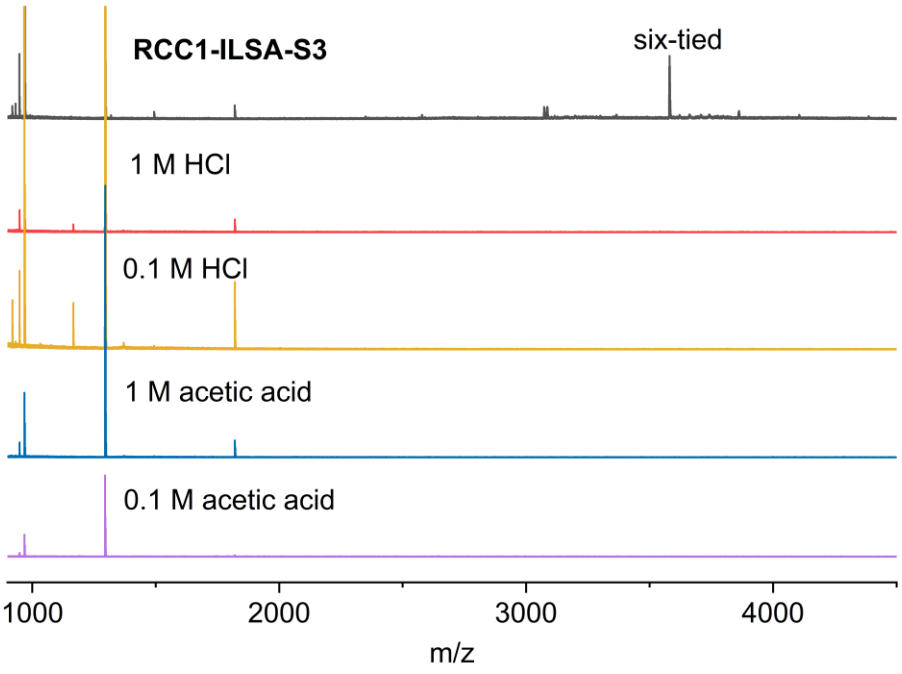

Figure 5.22: Comparisons of mass spectroscopy of **RCC1-ILSA-S3** in methanol and samples with aqueous solutions of 1 M HCl, 0.1 M HCl, 1 M and 0.1 M acetic acid added.

Likewise, aqueous solutions of 0.1 M NaOH, 1 M K_2CO_3, 0.1 M K_2CO_3 and 0.1 M $NaHCO_3$ were made and added to **RCC1-ILSA-S3**. Results showed that **RCC1-ILSA-S3** had better tolerance towards both strong base NaOH (pKa = 15.7) and weak bases of K_2CO_3 (pKa = 10.25) and $NaHCO_3$ (pKa = 6.34) compared to acids, with six-tied product maintained in the solution (**Figure 5.23**) within an hour. Even after a week, samples with 0.1 M K_2CO_3 and $NaHCO_3$ still had the six-tied **RCC1-ILSA-S3** remaining in the solution (**Figure 5.24**). However, decomposition did occur after a week, as peaks of 3 or 4 tied products appeared. For the sample with 1 M K_2CO_3 added, as its concentration was 10 times the 0.1 M K_2CO_3 solution, most of the tied-

product peaks disappeared after a week like the situation where the strong base NaOH solution was added.

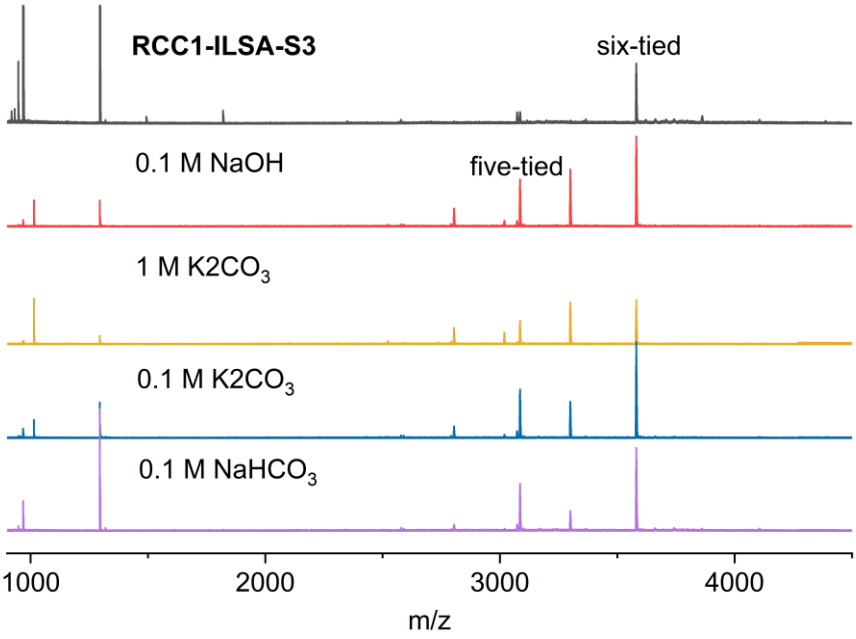

Figure 5.23: Comparisons of mass spectroscopy of **RCC1-ILSA-S3** in methanol and samples with aqueous solutions of 0.1 M NaOH, 1 M K_2CO_3, 0.1 M K_2CO_3 and 0.1 M $NaHCO_3$ added.

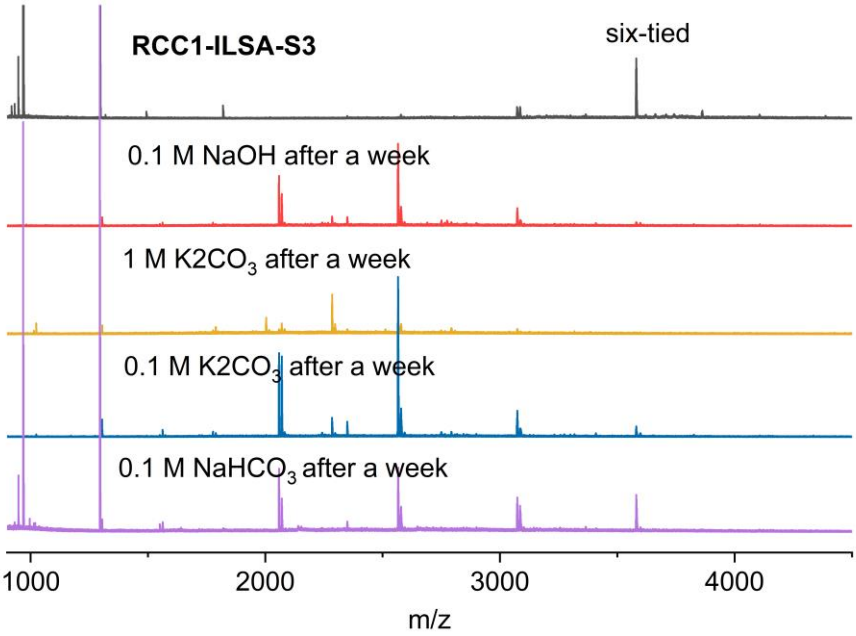

Figure 5.24: Comparisons of mass spectroscopy of **RCC1-ILSA-S3** in methanol and samples with aqueous solutions of 0.1 M NaOH, 1 M K_2CO_3, 0.1 M K_2CO_3 and 0.1 M $NaHCO_3$ added after 1 week.

5.7 Trials to improve porosity

5.7.1 RCC3-5FT-IL

As previously discussed, the lower CO_2 uptake of **RCC1-ILSA-S3** could arise from the relatively lower surface area of cage **CC1** core, deceased window sizes of the cage and the dilution of the cage cavity concentration by functionalising with heavy ionic liquids. One solution to improve porosity was explored by reducing tethered groups while maintaining the rigidity of the cage structure, and the strategy of tuning the number of tied groups on **RCC3** by Liu *et al.*, [179] which utilised the instability of tied acetone, was employed. The design scheme is shown in **Figure 5.25**, and the targeted product **RCC3-5FT-IL**, if could be synthesised, has five lighter formaldehyde groups tied, which could reduce the molecular weight of the whole molecule, and one **ILSA-S3** ionic liquid, which may contribute to a lower melting point.

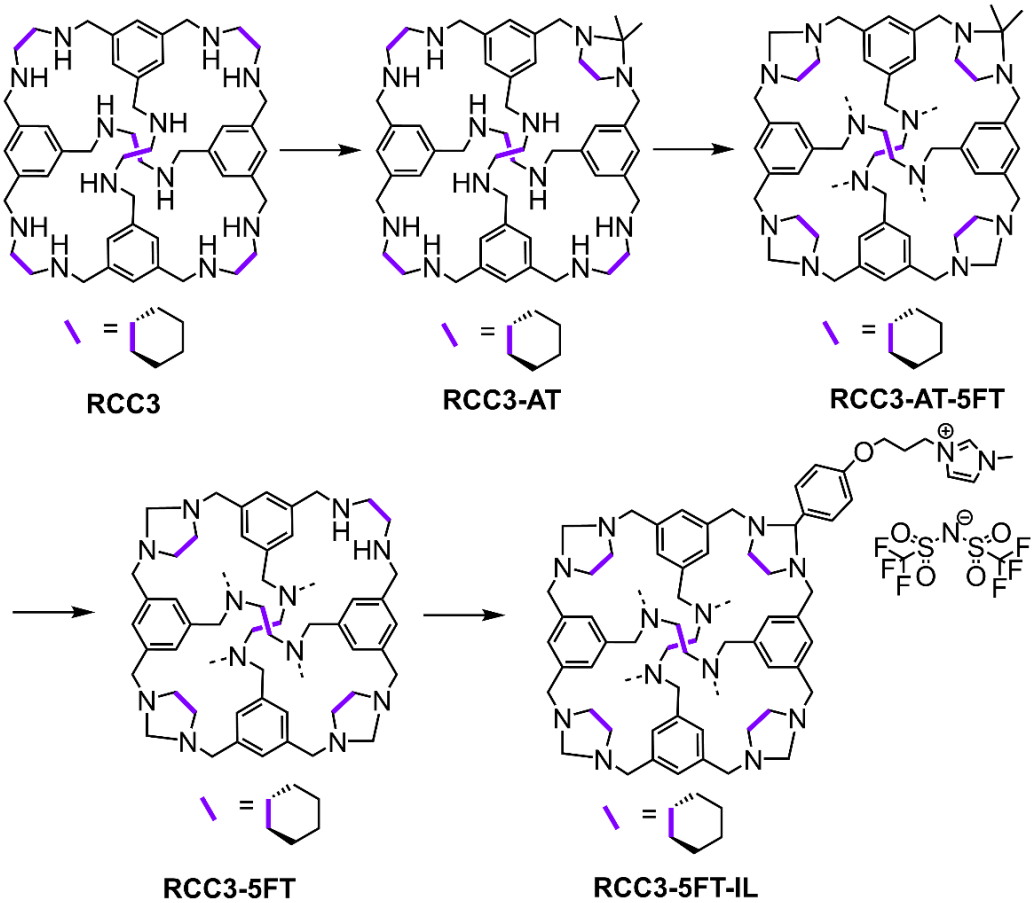

Figure 5.25: Synthesis scheme of **RCC3-5FT-IL**.

However, tying with such bulky groups might be difficult as the cyclopentane groups adjacent to diamines may pose a steric hindrance for the tied ionic liquid groups to

spin and point outward the cage cavity. To explore the best reaction conditions, we first tried the tying reduced cage **RCC3** (**Figure 5.26a**) with only **ILSA-S3**. Tying **RCC3** with small molecules such as acetaldehyde was successful, and the product could be used to separate H_2/D_2. [11] However, the cyclohexane groups on the cage were likely to hinder the tying reaction if bulkier groups such as **ILSA-S3** were used. A series of reaction conditions (**Table 5.7**) covered reaction temperature, solvent and drying agent were then screened for tying **RCC3** with **ILSA-S3**. The first method was tried with the optimum conditions for tying **RCC1** with **ILSA-S3**. However, unlike the phenomenon that had been observed likewise, a minimal oil-like substance appeared in the DCM solution. Mass spectroscopic analysis of the oil substance and the DCM solution showed that a mixture of tied **RCC3** products was presented, and the product with the highest molecular weight was the one tied with just four **ILSA-S3** molecules (4-tied), indicating incomplete tying in the **RCC3** situation. Other reaction conditions were all performed in methanol which could dissolve all the tied products, thus ensuring the reaction to fully completed in the homogeneous medium before it phased out of the reaction.

Table 5.7: Reaction conditions screened for tying **RCC3** with **ILSA-S3**.

	RCC3	**ILSA-S3**	Solvent	T	Molecular sieves	$NaSO_4$
1	1 equiv.	9 equiv.	DCM	RT		
2	1 equiv.	9 equiv.	Methanol	RT		
3	1 equiv.	9 equiv.	Methanol	RT		√
4	1 equiv.	9 equiv.	Methanol	RT	√	
5	1 equiv.	9 equiv.	Methanol	reflux		
6	1 equiv.	9 equiv.	Methanol	reflux		√
7	1 equiv.	9 equiv.	Methanol	reflux	√	

Methods 2-7 with overnight reaction time gave similar results to method 1, with the most tied product as 4-tied; even after 48 hours, results did not show any improvements. However, method 4, which used molecular sieves as the drying agent, displayed a 6-tied ($[M\text{-}NTf_2]^-$=3905.76) product in the mass spectra, with the reaction time extending to a week. And results demonstrated that the reaction could shift to the fully tied **RCC3-ILSA-S3** product after two weeks (**Figure 5.26b**), with the peak of

the less-tied product in the mass spectra disappearing. Though MS spectra still showed the peak of 4 and 5-tied products even after adding more equivalence of **ILSA-S3** into the reaction system and elongating reaction time to 4 weeks, it proved the practicality of tying **RCC3** with bulkier functional groups.

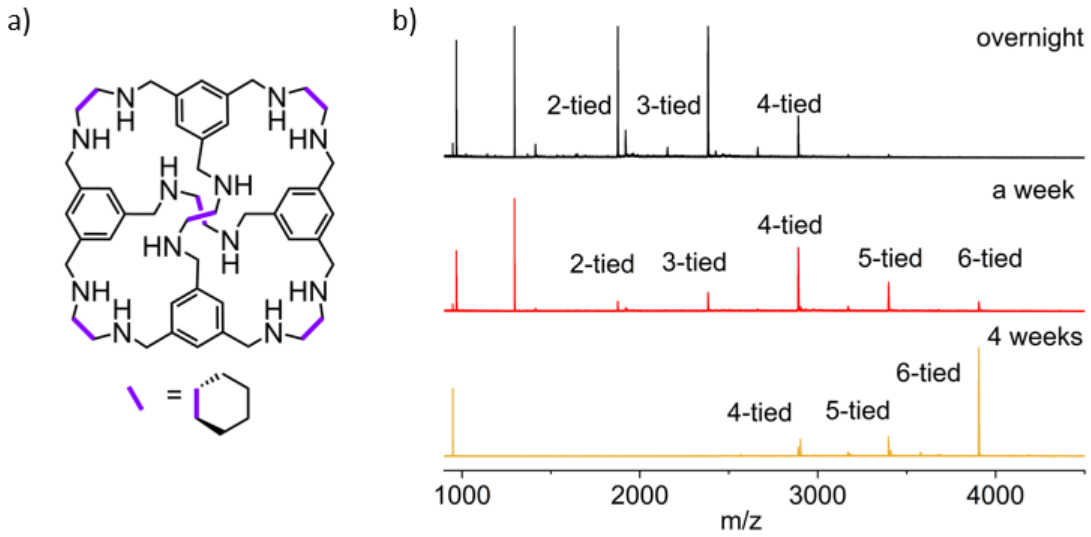

Figure 5.26: a) Molecular structure of **RCC3**; b) Mass spectroscopies of **RCC3-ILSA-S3** products with different reaction times.

Then synthesis scheme in **Figure 5.25** was tried. However, an issue arose at the first step of tying **RCC3** with acetone, where only one (1181.84, theory value: 1181.93) acetone should have been tied to **RCC3** due to steric hindrance according to the conclusion from the original work, [169] while mass peaks of **RCC3** tied with two (1221.85, theory value:1221.96) and three (1261.91, theory value: 1261.99) acetone molecules were also observed (**Figure 5.27a**). Though unexpected, this steric hindrance tolerance of **RCC3** being tied with more acetone molecules seemed in accordance with the above situation of fully tied **RCC3-ILSA-S3**. To check the availability of above scheme (**Figure 5.25**), mixed **RCC3-FT** was then synthesised and tied with **ILSA-S3** using method 4 in **Table 4.7**. And the MS result in **Figure 5.27b** showed the target peak of **RCC3-5FT-IL** at 1428.98 ($[M\text{-}NTf_2]^+$, theory value=1428.90). However, mass peaks corresponding to the product of **RCC3-4FT-2IL** and **RCC3-3FT-3IL** also appeared at 1924.02 (theory value: 1923.99) and 2419.09 (theory value: 2419.01) respectively, indicating that a mixture of equilibrated products existed. The design scheme was thus proved to work. However, the purity of **RCC3-AT** from the first step should be ensured to receive the pure **RCC3-5FT-IL**, and the chemistry of tying **RCC3** was worthy of further study.

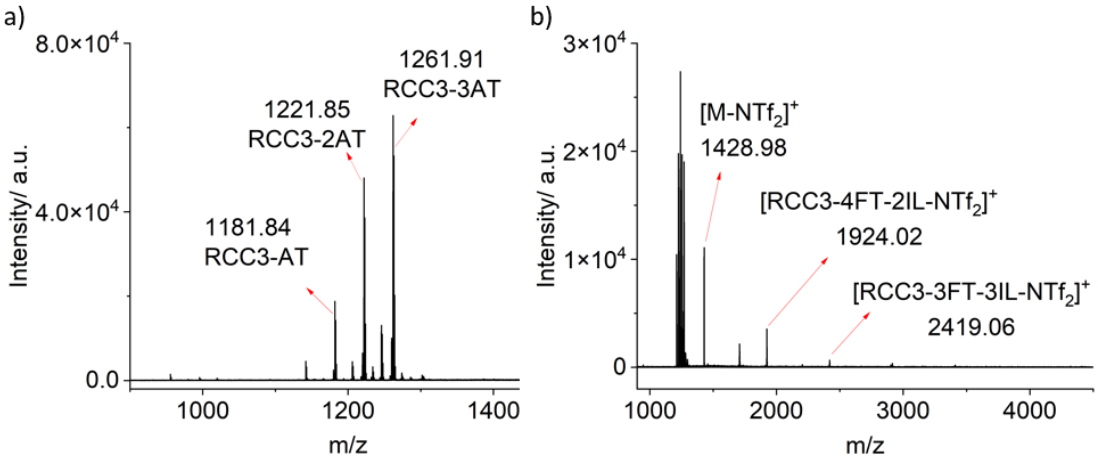

Figure 5.27: MALDI-TOF spectra of a) **RCC3-AT** in positive mode; b) **RCC3-FT-IL** in positive mode.

5.7.2 RCC5-IL

Another solution to fix the low uptake of the tied cage explored the utilisation of a cage with a larger surface area, which was **CC5**. **CC5** has an internal volume of 143.4 $Å^3$, nearly 4 times that of **CC1** (37.9 $Å^3$) (**Figure 5.28**), [142] which may present better uptakes than **RCC1-ILSA-S3** after tying with **ILSA-S3**.

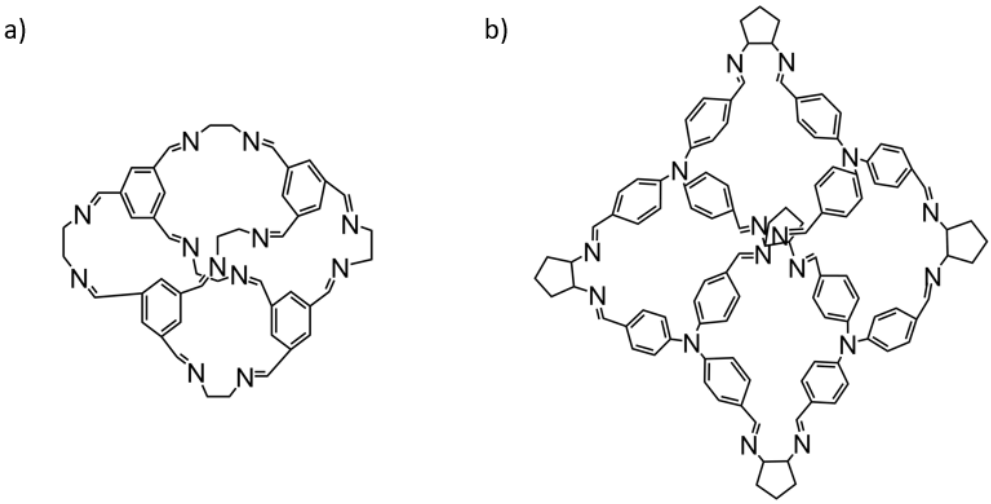

Figure 5.28: Molecular structure of a) **CC1**; b) **CC5**.

Then tying **RCC5** with **ILSA-S3** was tried at first with the above-screened conditions (**Table 5.7**) for **RCC3**, where a methanol solution of **RCC5** was added dropwise into the methanol solution of **ILSA-S3** with molecular sieves, and the mixture was left stirring for two weeks before checking the MALDI-TOF mass spectroscopy. Unfortunately, MS results (**Figure 5.29**) showed that only a mixture of 1, 2, and 3 tied products formed in the solution, indicating steric hindrance might prevent **RCC5** from tying more ionic liquid **ILSA-S3**.

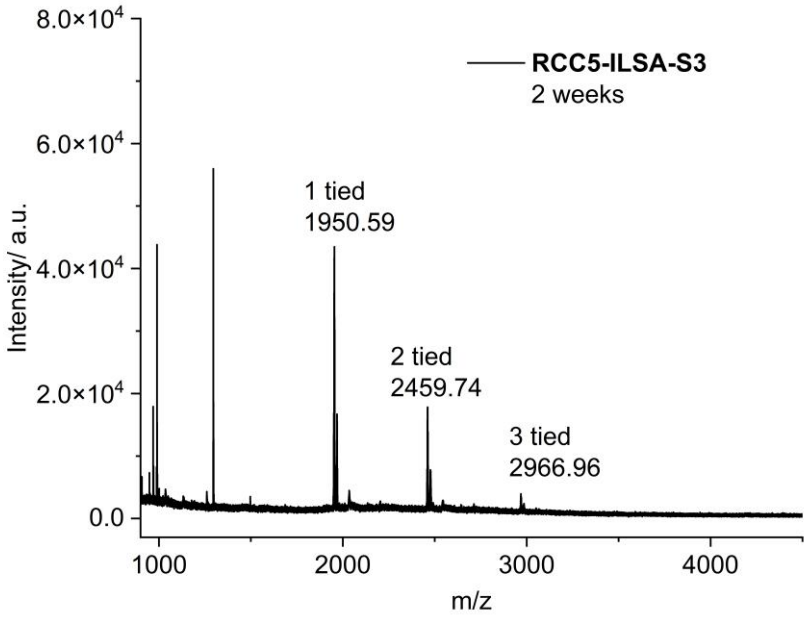

Figure 5.29: MALDI-TOF spectra of **RCC5-5FT-IL** in positive mode.

5.8 Conclusion

Modifying reduced porous organic cages with ionic liquid groups was studied to construct Type I porous liquids. The cages were reduced from [4+6] imine cages formed via dynamic covalent chemistry between precursors of trialdehydes and diamines, and imine bonds in an ortho arrangement within the cage structure were reduced to secondary amine bonds. An ionic liquid functionalised with a benzaldehyde group was reacted with the two ortho secondary amine bonds to form a rigid five-membered ring. The tying disturbed the molecular symmetry of the cage and, in another way, introduced the ionic liquid part, which could contribute to lowering melting points.

One reduced cage **RCC1** without any bulky groups adjacent to the ortho secondary amines was successfully tied with six liquid ionic groups, named **RCC1-ILSA-S3**, which was proved mainly by the MALDI-TOF mass spectroscopy. The spectra showed a main peak confirming the existence of the 6-tied product, though sometimes the 5-tied product could also be found. HPLC was tried to determine the species in the product, but only two broad adjacent peaks appeared and proved unsuccessful. Considering that the tiny amount of 5-tied product may not cause too much effect, the as-synthesised **RCC1-ILSA-S3** was analysed further by DSC to determine the melting point. DSC curve showed a broad melting peak over 55-90 ºC, indicating its

amorphous state, which was confirmed by PXRD. Though the melting point of **RCC1-ILSA-S3** failed to be lowered to room temperature, it could still be possible to call it a general type I porous liquid, just as that the general ionic liquids were salts with a melting point below 100 ºC. The melted-and-cooled **RCC1-ILSA-S3** appeared clear and glass-like, which was also amorphous and remained as a 6-tied structure, confirmed by PXRD and MALDI-TOF MS. Other tied **RCC1** salts were also synthesised to check whether the melting points could be lowered to room temperature, with the one tethered with PEG ionic liquid (**RCC1-PEG-190**) as a successful example, however **RCC1-PEG-190** was too viscous.

The porosity of **RCC1-ILSA-S3** was studied by CO_2 sorption, where CO_2 uptakes were measured using the as-synthesised solid state at room temperature, 100 ºC when it was completely melted, and its glass-like state at 1 bar. CO_2 uptake of the as-synthesised **RCC1-ILSA-S3** at room temperature was over 0.2 mmol/g, which was nearly three times that of the monomer ionic liquid **ILSA-S3**. This absolute uptake was small, which could be ascribed to the low surface area of the cage, decreased window sizes and diluted cage cavity concentration with the tied groups. However, the uptake of **RCC1-ILSA-S3** was still comparable to most type I porous liquids reported so far. Interestingly, the uptakes at 100 ºC and glass-like state were also around 0.2 mmol/g, which indicated applications of sorption at high temperatures and sorption with the processed product.

The stability of **RCC1-ILSA-S3** was studied. **RCC1-ILSA-S3** proved to be thermally stable, which stayed intact after a DSC study. It could stay stable in methanol and during CO_2 sorption. Though **RCC1-ILSA-S3** hydrolyse in acids instantly, it could tolerate bases to some degree.

The tying of bulky **ILSA-S3** could not only be applied to **RCC1** but also proved to be workable for **RCC3**. With the versatile tying chemistry, a cage tied with fewer **ILSA-S3** groups could also be realised, for example, **RCC3-5FT-ILSA-S3,** which was tied with one **ILSA-S3** and five formaldehyde molecules. However pure **RCC3-5FT-ILSA-S3** turned out to be a challenge as an unexpected phenomenon which contradicted former study, where **RCC3** was found to be tied with 2 and 3 acetone molecules. Tying **RCC5,** which had triple internal cavity volume with **ILSA-S3,** was tried to improve the porosity but unfortunately failed.

Chapter 6

Summary and conclusion

This PhD project aimed to explore using new precursors and preparation methods to overcome some of the commonly encountered challenges experienced with porous liquids, such as their low gas capacities and the use of volatile solvents.

In the first project, a stable porous organic imine cage **CC3** was used as a pore carrier to construct type III porous liquids. **CC3** was fabricated into **CC3-*R*/CC3-*S*** microparticles, which have lower solubility than the individual components in solvents. Next, ionic liquids with negligible vapour pressure and good thermal stability were screened as size-excluded solvents for forming **CC3-*R*/CC3-*S*** microparticle dispersions. The ionic liquids studied included imidazolium, pyridinium, ammonium, phosphonium ionic liquids pared with bis(trifluoromethanesulfonyl)imide anion ([BPy][NTf_2], [P_{66614}][NTf_2], [BEMA][NTf_2], [MBPy][NTf_2], [TBPy][NTf_2] and [BBIM][NTf_2]). The porosity of resulting dispersions was determined by comparisons of CO_2 uptakes of pure ionic liquids and corresponding **CC3-*R*/CC3-*S*** dispersions in the ionic liquids. From these studies, several ionic liquids were identified to be size excluded for the **CC3-*R*/CC3-*S*** microparticles: [BPy][NTf_2], [P_{66614}][NTf_2], [BEMA][NTf_2] and [TBPy][NTf_2]. In addition, an empirical size-exclusion standard was determined for ionic liquids, where a pyridinium with a four-carbon alkyl chain was found to meet size-exclusion requirement for cations, while the bis(trifluoromethanesulfonyl)imide anion was bulky enough for the **CC3** [4+6] imine cage system.

One type III porous liquid, comprising **CC3-*R*/CC3-*S*** microparticles dispersed in [BPy][NTf_2] was then studied in detail to determine its properties. It was found that both CO_2 and CH_4 uptakes were increased with an increasing amount of **CC3-*R*/CC3-*S*** microparticle content in the [BPy][NTf_2] dispersions. Viscosity was also found to increase with increasing microparticle content. In rheology studies, the dispersions of **CC3-*R*/CC3-*S*** microparticles in [BPy][NTf_2] displayed shear-thinning behaviours. Good wetting behaviour of [BPy][NTf_2] on a **CC3** film in the contact angle measurement ensured the good phase stability of microparticles in [BPy][NTf_2]. In addition, IR and capillary PXRD studies performed on the **CC3-*R*/CC3-*S*** dispersions in [BPy][NTf_2] were used to prove that **CC3-*R*/CC3-*S*** showed good chemical and crystalline stability in the ionic liquid [BPy][NTf_2], which allowed good CO_2 sorption recyclability and durability. The temperature control over the CO_2 release from the dispersions of **CC3-*R*/CC3-*S*** microparticles in [BPy][NTf_2] was also investigated. It

was found that the CO_2 uptake of a 12.5 wt% dispersion of **CC3-*R*/CC3-*S*** microparticles in [BPy][NTf_2] dropped from 175.2 umol/g to 70.9 umol/g from room temperature to 100 °C, displaying a larger working absorption capacity of 104.3 umol/g compared to that of pure [BPy][NTf_2] (37.27 μmol/g_L). Though this work represented the first example of a III porous liquid based upon porous organic cage and ionic liquids, and the system presented satisfying properties such as good stability, durability and recyclability, the capacity of the **CC3** porous liquid was low. Thus, cages with larger pores and surface areas will likely be required as pore carriers in the future.

The second project focused on attempts to construct type II porous liquids using ionic liquids, which were intended to replace volatile organic solvents that were used in existing type II systems. Six porous organic molecules (**CC19**, **SC T_4:3_3:13_3**, **Noria**, **Boc-Noria**, **α-cyclodextrin** and **2-hydroxypropyl-α-cyclodextrin**), which are rich in hydroxyl or methoxyl groups were employed as pore carriers in solubility screening with 11 ionic liquids with imidazolium, pyridinium, ammonium, phosphonium cations paired with fluorine-containing anions. From this screen, two ionic liquids of [$(OH)_2$IM][NTf_2] and [$(MeO)_2$IM][NTf_2] were found to successfully dissolve **CC19**, **α-cyclodextrin** and **2-hydroxypropyl-α-cyclodextrin** with concentrations over 2.5 wt%. However, further CO_2 sorption measurements and comparisons of the pure ionic liquid [$(OH)_2$IM][NTf_2] and corresponding **CC19** and **2-hydroxypropyl-α-cyclodextrin** solutions demonstrated that the imidazolium ionic liquid cations were too small in size and could enter the cavity of pore carriers to reduce their porosity significantly. Therefore, two strategies were attempted to solve this issue. The first was to dissolve porous organic cages with smaller window sizes (**RCC19-6FT** and **TpOMe-CDA**) in [$(OH)_2$IM][NTf_2]. The second was to modify pyridinium ionic liquids, which were proven to be size excluded to **CC3** (structurally similar to **CC19**), with hydroxyl or methoxyl groups to facilitate solubilisation. Unfortunately, both strategies failed to construct a type II porous liquid. Though no type II system was constructed, corresponding initial solubility data in ionic liquids was first determined, which would help provide design considerations for future systems. Future work could try to prepare some cage salts to be dissolved in ionic liquids, such as deprotonation of the hydroxyl groups in **CC19**.

The third project studied applying tying chemistry in constructing type I porous liquid. The tethering was realised by the formation of a five-membered ring between an ionic liquid functionalised aldehyde and the two ortho secondary amine bonds from a reduced [4+6] imine cages cage. One reduced cage **RCC1** was successfully tied with six liquid ionic groups (**ILSA-S3**), named **RCC1-ILSA-S3**. The amorphous **RCC1-ILSA-S3** powder melted at 90 ºC to become a viscous oil and cooled to form a glass-like morphology, demonstrating the potential of mechanical processability. Another two ionic-liquid aldehydes **ILSA3-S3** and **PEG-190** were also synthesised and tied onto **RCC1** in an attempt to decrease the melting point of resulting cage salts further. However, the melting points failed to be lowered enough to form a room-temperature porous liquid. CO_2 uptakes were measured on the as-synthesised **RCC1-ILSA-S3** powder at room temperature, 100 ºC when it was completely melted, and its glass-like state at 1 bar, where three states of **RCC1-ILSA-S3** all presented similar CO_2 uptakes. The melted **RCC1-ILSA-S3** at 100 ºC presented CO_2 uptake of around 0.2 mmol/g at 1 bar, nearly three times that of the monomer ionic liquid **ILSA-S3** at RT, which proved the porosity of **RCC1-ILSA-S3** at the liquid state. Though the absolute CO_2 uptake was small, it was comparable to most type I porous liquids reported so far. **RCC1-ILSA-S3** was also proved to be relatively stable, which could stay stable towards heat and CO_2 sorption. Though **RCC1-ILSA-S3** hydrolyse in acids instantly, it could tolerate bases to some degree. This versatile tying chemistry could also apply to other reduced cages than **RCC1**. For example, a fully tied **RCC3-ILSA-S3** was also successfully synthesised, thus opening new construction routes to prepare type I porous liquids. For example, further tuning of the number of tied groups on the cage in the future could help improve the gas uptake capacity.

The studies reported in this thesis expand the library of porous liquids reported based upon the use of porous organic cages. This includes the first type III cage porous liquid successfully prepared, provided initial data of using ionic liquids with negligible vapour pressure and good thermal stability as size-excluded solvents for cage-based porous liquid systems, in addition to applying new chemistry to construct type I porous liquids. While this thesis contributes to developments and will help lead to practical applications of porous liquids, further work is required to enhance the capacities of these porous liquids and lower their viscosity. For example, systems like coordination cages with higher surface areas and solubilities than framework materials could be

focused on. Or different chemistry could be explored for the construction of porous liquids, such as employment of molecules containing different functional groups which provide post-functionalisation sites.

Chapter 7

Experimental Data and References

7.1 General synthetic and analytical methods

Materials: TFB was purchased from Manchester Organics, UK. Other chemicals were purchased from Sigma-Aldrich or Key organics. These chemicals were used as received. Ionic liquids were purchased either from TCI UK or Sigma-Aldrich, listed below:

Table 7.1: List of commercial ionic liquids screened.

Chemical	Supplier
1-butyl-3-methylimidazolium bis(trifluoromethylsulfonyl)imide ([BMIM][NTf_2])	Sigma Aldrich 711713
1-butyl-3-methylimidazolium tetrafluoroborate ([BMIM][BF_4])	TCI B2195
1-butyl-3-methylimidazolium hexafluorophosphate ([BMIM][PF_6])	TCI B2701
1,3-dihydroxyimidazolium bis(trifluoromethylsulfonyl)imide ([$(OH)_2$IM][NTf_2])	Sigma Aldrich 691054
1,3-Dimethoxyimidazolium bis(trifluoromethylsulfonyl)imide ([$(MeO)_2$IM][NTf_2])	Sigma Aldrich 690937
butylpyridinium bis(trifluoromethylsulfonyl)imide ([BPy][NTf_2])	TCI B5571
4-butyl-1methylpyridinium bis(trifluoromethylsulfonyl)imide ([MBPy][NTf_2])	TCI B5763
Trihexyltetradecylphosphonium bis(trifluoromethanesulfonyl)imide ([P_{66614}][NTf_2])	Sigma Aldrich 50971
benzyl(ethyl)dimethyl ammonium bis(trifluoro-methanesulfonyl) imide ([BEMA][NTf_2])	TCI B5427

NMR: ^{1}H NMR, ^{13}C NMR and ^{19}F NMR spectra were recorded in deuterated methanol, DMSO or chloroform at 400 MHz using a Bruker Avance 400 NMR spectrometer. Chemical shifts are reported in ppm (δ) with reference to internal residual protonated species of the deuterated solvent. NMR data are presented as follows: chemical shift, integration, peak multiplicity (s = singlet, d = doublet, t = triplet, q = quartet, m = multiplet, br = broad) and coupling constants (J / Hz).

MALDI-TOF MS: Mass spectroscopy was measured on a BRUKER AutoFlex spectrometer. The data was collected by flexControl software and exported by flexAnalysis software. DCTB was used as the matrix and CsI_3 was used to calibrate the instrument each time before measurements. Thus, matrix and samples were made into solutions with a concentration of 10 mg/mL respectively and mixed in a ratio of 10:1 before being deposited onto a steel plate with a micropipette.

PXRD: PXRD patterns were collected in transmission mode on samples held on a thin Mylar film in aluminium well plates on a Panalytical Empyrean diffractometer equipped with a high throughput screening (HTS) XYZ stage, X-ray focusing Page S20 mirror, and PIXcel detector, using Cu-Kα (λ = 1.541 Å) radiation. Capillary PXRD patterns were collected on powder or dispersion samples loaded in borosilicate glass capillaries on a capillary spinner which kept spinning during measurement to improve averaging. PXRD patterns were recorded at room temperature, and diffraction patterns were measured over the range of 2−50°, in 0.013° steps, for 30-60 minutes.

SEM: SEM characterisations were performed on a Hitachi S4800 scanning electron microscope. Samples were prepared by depositing microparticles onto an adhesive high-purity carbon tab on 15mm Hitachi aluminium stubs and coated in chromium before imaging.

DLS: DLS measurements were performed on a Zetasizer instrument. Samples were prepared by dispersing and sonicating a small number of microparticles (0.5 mg) in 20 mL DCM.

IR: IR spectra were collected on a Bruker Tensor 27 FT-IR using ATR mode for ionic liquids or dispersions as samples.

Gas sorption analysis: a) Gas uptakes of the Type III porous liquids were measured on a Quantachrome Nova 4200e. Generally, 0.5 mL sample was injected into a 9 mm sample cell with a large bulb (P/N: 74064) and a glass-coated stir bar was added. The glass-coated stir bar was used instead of the PTFE-coated one because fluorinated structures could show good affinity towards CO_2 and were greatly deployed in CO_2 chemistry, [180] thus was not selected to avoid introducing error. The sample was degassed under vacuum with stirring overnight at room temperature and backfilled with helium before being removed from the degassing station. A filler rod (P/N: 74105-L) was used with the sample cell during sorption measurements at room temperature and the adsorption settings were as follows: 20 pressure points from 0.05 to 1.0 bar in 0.05 increments; pressure tolerance = 0.05 mmHg; equilibration time = 1800 seconds; equilibration timeout = 5400 seconds. Dispersions were kept stirring during all measurements. If a higher temperature was needed during adsorption, a heating block was used. b) CO_2 or CH_4 uptakes of some solid samples were measured using a Micromeritics (RTM) ASAP 2020 volumetric adsorption analyser. Powder samples were degassed offline at 90 °C for 15 h under dynamic vacuum (10^{-5} bar) before analysis. The uptakes were measured at 25 °C (stabilised using a circulating water chiller/heater) and 1 bar and were then used to calculate an expected uptake for the solid present in the dispersions. c) BET surface areas were measured by nitrogen sorption at 77.3 K on the micromeritics ASAP 2420 analyser. Powder samples were first degassed offline at 90 °C for 15 h under dynamic vacuum (10^{-5} bar) before analysis.

Viscosity measurements: Viscosity measurements were carried out with a calibrated RheoSense μVISC viscometer (10-2000 cp) at room temperature. Automatic mode was chosen to measure the viscosity where suitable measuring conditions were primed by the instrument. Measurements were performed three times and the average viscosity was reported.

DSA: Contact angles were measured on a Kruss DSA100 using the method of sessile drop analysis. The width of a needle was measured with a digital calliper and used to calibrate the ADVANCE software. 4-5 microlitre water or ionic liquid was dropped onto the surface of targeted materials using a pipette with the camera recording the process. Images were analysed by the software to get the contact angle and at least three times of measurements were performed to determine a specific contact angle on

a surface. Sample preparation involves two methods. For insoluble materials, pellets were pressed, while for soluble materials, 1 mg/mL solution was prepared, dropped onto a glass plate, and left evaporating to form a film.

LUMiSizer®: Stability of dispersions study was performed on a LUMiSizer® dispersion analyser, using transparent sample cells (2 mm, rectangular synthetic cell 108-130 mm). Measurement conditions were at 25 °C with a wavelength of 865 nm, with speed and scan settings as 2000 RPM and 700 * 30 second intervals (or 1000 * 21) for a total run time of 350 min.

TGA: TGA was performed on a Q5000IR with an automated vertical overhead thermobalance. Samples were heated in an aluminium pan at a ramp rate of 10 °C/min up to 600 °C under a dry nitrogen flow.

DSC: DSC analysis was performed on a TA instruments Discovery DSC. Samples were weighed in Tzero aluminium hermetic pans and sealed with Tzero hermetic lid using the blue set pin hole.

Melting observation: Melting behaviour was observed on a Stuart digital melting point apparatus SMP 10. Samples were first loaded into the capillary glass tubes SMP 10/1 which closed at one end (length = 100mm; inner diameter = 1.3mm; wall thickness = 0.3mm). The sample tube was then inserted into the heating block, and the apparatus heated until plateau which was set at 25 ºC. Afterwards the temperature ramped at a rate of 2 ºC/min and samples could be observed through a magnifying lens at the same time.

Rheology: Rheology studies were performed on ARG2 Rheometer, and the data were analysed with TA instruments TRIOS software. Samples were loaded onto a steel plate at room temperature on the instrument, and another steel cone-shaped geometry plate was set up overhead of the sample. The geometry was then lowered to fully contact the sample on the lower plate. Samples were equilibrated for 30 seconds at 25 °C before each measurement. Flow sweep measurements were carried out between the shear rate 0.1 and 100 s^{-1} or 5 × 10^{-4} and 100 s^{-1}. Flow ramp measurement was performed linearly from 1 to 100^{-1} with a sampling rate of 1s/pt. Dynamic oscillation strain amplitude sweep measurements were carried out from 0.01 to 1000% at 1 Hz, Dynamic oscillation frequency sweep measurements were conducted between 0.1 and 100 rad/s at 0.1 % and 10 % strain respectively.

7.2 Chapter 3 experimental data

7.2.1 Synthesis and characterisation

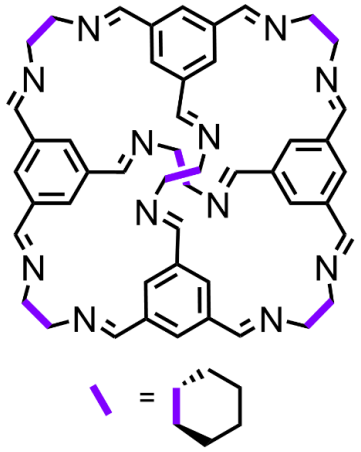

Figure 7.1: Molecular structure of **CC3.**

CC3-*R* and CC3-*S*: **CC3**-*R* and **CC3**-*S* were synthesised according to a previously reported procedure. [136] TFB (2.50 g, 15.42 mmol, 4 eq.) was added to a round bottom flask, and DCM (50 mL) was then slowly added to avoid disturbance of the TFB. R, R-CHDA (2.64 g, 23.19 mmol, 6 eq.) or S, S-CHDA (2.64 g, 23.19 mmol, 6 eq.) was dissolved in DCM (50 mL) and the solution was slowly added to the flask containing TFB with a pipette to form a layer. Trifluoroacetic acid (50 μL) was added, and the mixture was left covered for five days. The crystals that formed were collected by filtration and washed with a mixture solvent (95% ethanol + 5% DCM) to afford **CC3**-*R* or **CC3**-*S* as off-white crystals (3.50 g, yield = 81%). ^{1}HNMR (400MHz, $CDCl_3$) δ_H 8.16 (12H, s, CH=N), 7.90 (12H, s, ArH), 3.34 (12H, m, cyclohexyl CH), 1.9-1.4 (48H, m, cyclohexyl CH_2); ^{13}C NMR (400MHz, $CDCl_3$) δ_C 159.33, 136.76, 129.71, 74.78. 33.15, 24.52; MALDI-TOF MS (RP): m/z: accurate mass calculated for $C_{72}H_{84}N_{12}$ 1116.69, found at 1117.79 ($[M+H]^+$). The NMR data were in accordance with the literature values. [136]

CC3-*R*/CC3-*S*: **CC3**-*R*/**CC3**-*S* microparticles were synthesised using the procedure as follows: A solution (1.5 mg/mL) of **CC3**-*R* (1.35 g) in DCM (900 mL) was poured directly into a solution (1.5 mg/mL) of **CC3**-*S* (1.35 g) in DCM (900 mL) with overhead mechanical stirring. The mixture was stirred for a further 10 minutes to afford a white suspension. Fine, white particles were then collected by filtering the suspension through a nylon membrane with 0.45 μm pore diameter and dried in a

vacuum oven at 90 °C overnight (2.32 g, yield = 86%). The filtration of these particles can be slow, and for a batch of this size can take >6 hours to filter.

CC3-*R*/CC3-*S* Dispersions: Representative preparations of the dispersions are as follows: **CC3-*R*/CC3-*S*** microparticles were de-solvated as above, and [BPy][NTf_2] was dried at 80 °C in a separate vacuum oven for at least 24 hours before mixing with **CC3-*R*/CC3-*S*** microparticles. Then the weighed **CC3-*R*/CC3-*S*** and [BPy][NTf_2] were put into a glass vial with cap and sonicated for at least 10 minutes until a homogenous dispersion was formed.

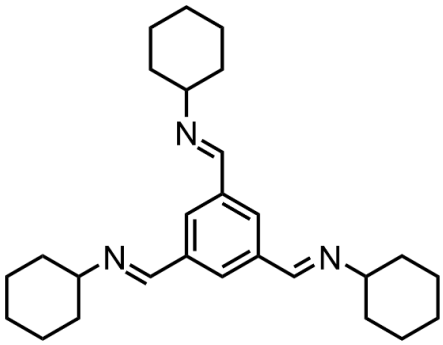

Figure 7.2: Molecular structure of the control molecule **1,1',1''-(Benzene-1,3,5-triyl)tris(N-cyclohexylmethanimine)**.

1,1',1''-(Benzene-1,3,5-triyl)tris(N-cyclohexylmethanimine): The control molecule 1,1',1''-(benzene-1,3,5-triyl)tris(N-cyclohexylmethanimine) was synthesized according to a previously reported method.[30] Cyclohexylamine (1.09 mL, 9.25 mmol, 3 eq.) was added to a solution of TFB (0.5 g, 3.08 mmol, 1 eq.) in DCM (50 mL), and the resulting solution was stirred at room temperature overnight before being concentrated in vacuo. The resulting solid was dried in a vacuum oven at 90 °C to afford the desired product as white powders (1.15 g, yield = 92%). ^{1}H NMR (400 MHz, $CDCl_3$) δ_H 8.38 (3H, s, N=CH), 8.11 (3H, s, ArH), 3.21 (3H, m, NCH), 1.83 (6H, dt, J = 13.2, 3.6 Hz, CH_2), 1.75-1.66 (9H, m, CH_2), 1.60-1.54 (6H, m, cyclohexyl CH), 1.43-1.20 (6H, m, cyclohexyl CH_2); ^{13}C NMR (400MHz, $CDCl_3$) δ_C 157.91, 137.38, 129.22, 70.00, 34.36, 25.63, 24.82; MALDI-TOF MS (RP): m/z: calculated for $C_{27}H_{39}N_3$ 405.31, found at 406.33 ($[M+H]^+$); Elemental analysis (%): C 80.17 H 9.92 N 10.37 (Calculated: C 79.95 H 9.69 N 10.36).

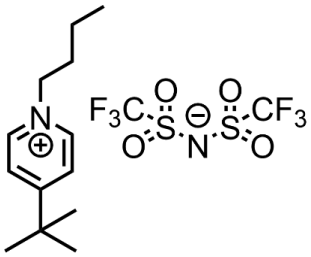

Figure 7.3: Molecular structure of [TBPy][NTf_2].

[TBPy][Br]: 4-tert-Butylpyridine (1.22 g, 9.01 mmol) and 1-bromobutane (2.09 g, 16 mmol) were dissolved in 1 mL of ethanol and refluxed with stirring overnight. The mixture was cooled, suction filtered, and the resulting solid recrystallized from acetone to give the 4-terbutyl-1-butylpyridinium bromide [TBPy][Br] salt (2.13 g, yield = 87%). ^{1}H NMR (400 MHz, CD_3OD) δ_H 8.92-8.89 (2H, m, PyH), 8.14 (2H, d, J = 6.8 Hz, PyH), 4.61 (2H, t, J = 7.6 Hz, N-CH_2), 1.99 (2H, qt, J = 7.6, 2.0 Hz, CH_2), 1.44 (9H, s, CH_3), 1.47-1.37 (2H, m, CH_2), 1.00 (3H, t, J = 7.6 Hz, CH_3); ^{13}C NMR (400MHz, CD_3OD) δ_C 171.21, 143.86, 125.21, 60.48, 36.17, 32.93, 28.88, 19.05, 12.42.

[TBPy][NTf_2]: Aqueous solution of 4-terbutyl-1-butylpyridinium (2.72g, 10 mmol) and $LiNTf_2$ (3.15 g, 11 mmol) was combined and stirred overnight at room temperature. The lower oily phase was extracted with 100 mL DCM and washed with water until no Br^- was detected by $AgNO_3$ solution. The organic phase was then dried over anhydrous Na_2SO_4 and concentrated to afford the light yellow oily [TBPy][NTf_2] (4.20 g, yield = 89%). ^{1}H NMR (400 MHz, CD_3OD) δ_H 8.81-8.78 (2H, m, PyH), 8.09 (2H, d, J = 6.8 Hz, PyH), 4.55 (2H, t, J = 7.6 Hz, N-CH_2), 1.97 (2H, qt, 7.6, 2.4 Hz, CH_2), 1.43 (9H, s, CH_3), 1.45-1.34 (2H, m, CH_2), 1.00 (3H, t, J = 7.2 Hz, CH_3); ^{13}C NMR (400MHz, CD_3OD) δ_C 171.60, 143.66, 125.60, 124.54, 121.44, 118.25, 115.05, 61.24, 36.63, 33.20, 29.86, 19.26, 13.21; ^{19}F NMR (400MHz, CD_3OD) δ_F -78.91; Elemental analysis (%): C 38.29 H 4.74 N 5.89 (Calculated: C 38.13 H 4.69 N 5.93).

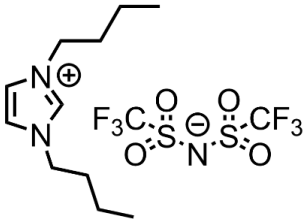

Figure 7.4: Molecular structure of [BBIM][NTf_2].

[BBIM][Br]: 1-Bromobutane (1.37 g, 10 mmol) was slowly added to vigorously stirred 35 ml of acetonitrile solution containing 1-Butylimidazole (1.0g, 8 mmol). The reaction mixture was then refluxed for 72 h. After the reaction stopped, the solvent was evaporated, and the crude product was crystallised from methanol twice to afford 1-butyl-3-butylimidazolium bromide ([BBIM][Br]) (1.69 g, yield = 81%). ^{1}H NMR (400 MHz, CD_3OD) δ_H 9.13(H, s, N=CH), 7.70 (2H, d, J=1.6 Hz, CH=CH), 4.27 (4H, t, J = 7.2 Hz, N-CH_2), 1.95-1.87 (4H, m, CH_2), 1.40 (4H, st, J=7.6, 2.0 Hz CH_2), 1.01 (3H, t, J = 7.6 Hz, CH_3); ^{13}C NMR (400MHz, CD_3OD) δ_C 135.80, 122.43, 49.28, 31.72, 19.08, 12.35.

[BBIM][NTf_2]: Aqueous solution of [BBIM][Br] (2.61g, 10 mmol) and $LiNTf_2$ (3.15 g, 11 mmol) was combined and stirred overnight. 100 mL DCM was used to extract the product, and it was washed with water until no Br^- was detected by $AgNO_3$ solution. The organic phase was then dried over anhydrous Na_2SO_4 and concentrated to afford the light brown [BBIM][NTf_2] (4.01 g, yield = 87%). ^{1}H NMR (400 MHz, CD_3OD δ_H 8.81(H, s, N=CH), 7.33 (2H, d, J=2.0 Hz, CH=CH), 4.19 (4H, t, J = 7.6 Hz, N-CH_2), 1.85 (4H, qt, J = 7.6, 2.0 Hz CH_2), 1.36 (4H, s, J=7.6 Hz CH_2), 0.96 (3H, t, J = 7.6 Hz, CH_3); ^{13}C NMR (400MHz, CD_3OD) δ_C 135.46, 124.54, 122.33, 121.43, 118.23, 114.99, 49.96, 32.00, 19.34, 13.22; ^{19}F NMR (400MHz, CD_3OD) δ_F -79.03; Elemental analysis (%): C 33.87 H 4.60 N 9.07 (Calculated: C 33.84 H 4.59 N 9.11)

7.2.2 Sorption data

Table 6.2: Summary of gas uptakes of ionic liquids and corresponding dispersions. The number in parentheses indicates which batch of microparticles from **Table 3.3** was used for the measurement. The average uptake is based on 2 measurements with the standard deviation shown.

Disp. No.	Solid	Liquid	Loading (wt.%)	Gas	Average Uptake, 25-30 °C, 1 bar (μmol/g_L unless otherwise) stated)	Average increase in uptake over base liquid(μmol/g_L)
1	-	[BPy][NTf_2]	-	CO_2	78.3 ± 4.5	-
2	**CC3-***R*/**CC3-***S* (1)	[BPy][NTf_2]	5	CO_2	111.4 ± 6.4	36
3	**CC3-***R*/**CC3-***S* (1)	[BPy][NTf_2]	12.5	CO_2	170.1 ± 7.7	92
4	**CC3-***R*/**CC3-***S* (2)	[BPy][NTf_2]	12.5	CO_2	172.1 ± 3.6	94
5	**CC3-***R*/**CC3-***S* (2)	[BPy][NTf_2]	20	CO_2	209.8 ± 6.7	131
6	Control molecule	[BPy][NTf_2]	5	CO_2	74.6	0
7	-	[BPy][NTf_2]	-	CH_4	7.9 ± 0.1	-
8	**CC3-***R*/**CC3-***S* (1)	[BPy][NTf_2]	5	CH_4	36.0 ± 0.3	28
9	**CC3-***R*/**CC3-***S* (1)	[BPy][NTf_2]	12.5	CH_4	71.3 ± 3.9	63
10	**CC3-***R*/**CC3-***S* (1)	[BPy][NTf_2]	20	CH_4	103.8 ± 0.7	95
11	**CC3-***S*	[BPy][NTf_2]	12.5	CO_2	164.8 ± 3.7	86
12	-	[P_{66614}][NTf_2]	-	CO_2	50.8 ± 4.0	-

13	**CC3-*R*/CC3-*S*** (1)	$[P_{66614}][NTf_2]$	5	CO_2	85.6 ± 7.0	35
14	-	$[BEMA][NTf_2]$	-	CO_2	60.5 ± 0.1	-
15	**CC3-*R*/CC3-*S*** (2)	$[BEMA][NTf_2]$	5	CO_2	115.6 ± 1.1	55
16	-	$[MBPy][NTf_2]$	-	CO_2	81.4 ± 2.2	-
17	**CC3-*R*/CC3-*S*** (2)	$[MBPy][NTf_2]$	5	CO_2	86.6 ± 1.9	5
18	-	$[TBPy][NTf_2]$	-	CO_2	75.8	-
19	**CC3-*R*/CC3-*S*** (1)	$[TBPy][NTf_2]$	5	CO_2	114.7	39
20	-	$[TBPy][NTf_2]$	-	CH_4	8.1	-
21	**CC3-*R*/CC3-*S*** (1)	$[TBPy][NTf_2]$	-	CH_4	44.4	36
22	-	$[BBIM][NTf_2]$	-	CO_2	77.5 ± 1.3	-
23	**CC3-*R*/CC3-*S*** (2)	$[BBIM][NTf_2]$	5	CO_2	93.4 ± 2.3	16
24	-	$[BBIM][NTf_2]$	-	CH_4	7.4	-
25	**CC3-*R*/CC3-*S*** (1)	$[BBIM][NTf_2]$	-	CH_4	22.5	15

7.3 Chapter 4 experimental data

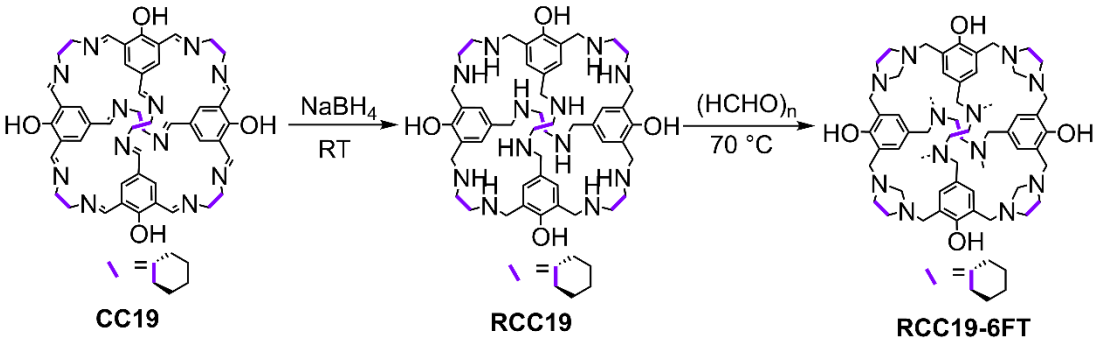

Figure 7.5: Synthesis route of **RCC19-6FT**.

CC19: Synthesis of **CC19** was modified from the method in literature. [181] R, R-CHDA (0.92 g, 8.1 mmol, 12 equiv.) was dissolved in 150 mL methanol in a round bottom flask at room temperature, while 2-hydroxy-1,3,5-benzenetricarbaldehyde (0.48 g, 2.7 mmol, 4 equiv.) was dispersed in the solvent mixture of methanol and DCM (50 mL, 4:1). The aldehyde dispersion was added batchwise into the R, R-CHDA solution within an hour. The resulting mixture was stirred for 3 days and evaporated a little under vacuum to remove DCM. The remaining methanol dispersion was stirred for another 3 days, then filtered and washed with a mixture of methanol and DCM (95:5) and dried at 90 °C to afford the product **CC19** (0.63 g, yield = 79%). ^{1}H NMR (400 MHz, $CDCl_3$) δ_H 13.96-13.79 (m, -OH), 8.62-8.55 (4H, m, -C=NH), 8.28-8.23 (4H, m, -C=NH), 8.09-8.04 (4H, m, -C=NH), 7.90-7.77 (8H, m, benzene H), 3.37-3.26 (12H, br, cyclohexyl CH), 1.82-1.45 (48H, br, cyclohexyl CH_2); MALDI-TOF MS (RP): m/z: accurate mass calculated for $C_{72}H_{84}N_{12}O_4$ 1180.67, found at 1181.66 ($[M+H]^+$).

RCC19-6FT: Reduced cage **RCC19** was synthesised using the similar method used for cage reduction. [169] **CC19** (0.36 g, 0.3 mmol) was dissolved in an 80 mL solvent mixture of chloroform and methanol with 1:1 ratio. Sodium borohydride ($NaBH_4$, 0.76 g, 20 mmol) was then added and the mixture was stirred at room temperature overnight. 1 mL water was added to quench the reaction and it was stirred further for 12 hours. NMR was monitored to ensure the imine peak disappeared and all the imine bonds were reduced. After the reaction stopped, 1 mL water was added, and the mixture was extracted with 3 × 50 mL DCM. The organic phase was dried over $MgSO_4$, filtered, and evaporated to afford the product of **RCC19** (0.34 g, yield = 92 %). Tying **RCC19** with formaldehyde used the similar method that was applied in

tying **CC3**. [169] Paraformaldehyde (0.19 g, 60 mmol) was first dissolved in 40 mL methanol at 70 °C. A 40 mL methanol solution of **RCC19** (0.34g, 0.28 mmol) was then added and the mixture was kept stirring at 70 °C for 3-4 hours. After the reaction stopped, the reaction mixture was filtered, washed, and dried at 90 °C to afford **RCC19-6FT** (0.23 g, yield = 64%). ^{1}H NMR (400 MHz, $CDCl_3$) δ_H 11.79-10.92 (m, -OH), 7.17-6.87 (8H, br, benzene H), 4.34-3.72 (12H, br, N-CH_2-N), 3.61-3.10 (24H, m, benzene-CH_2), 2.26-2.12 (12H, br, cyclohexyl CH), 1.97-1.29 (48H, br, cyclohexyl CH_2); MALDI-TOF MS (RP): m/z: accurate mass calculated for $C_{78}H_{84}N_{12}O_4$ 1276.86, observed at 1277.79.

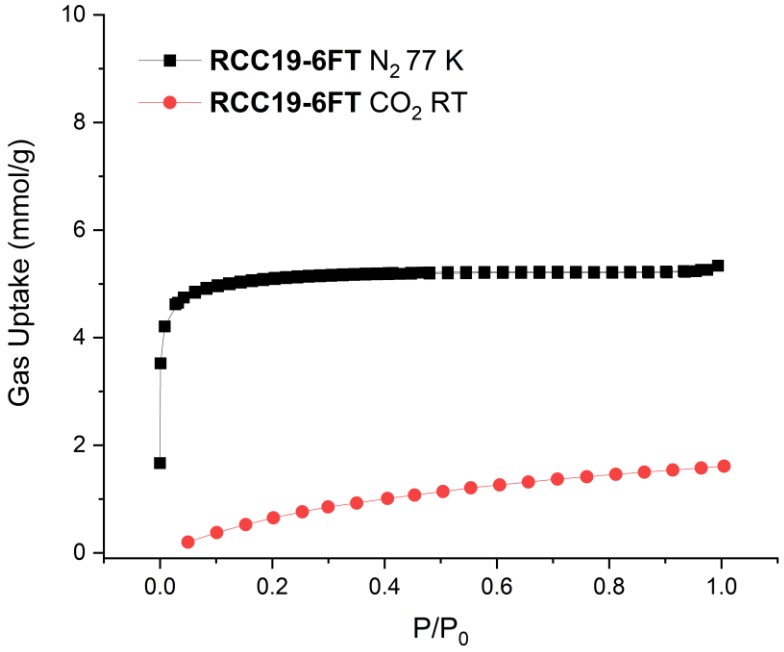

Figure 7.6: Gas sorption of **RCC19-6FT** solids.

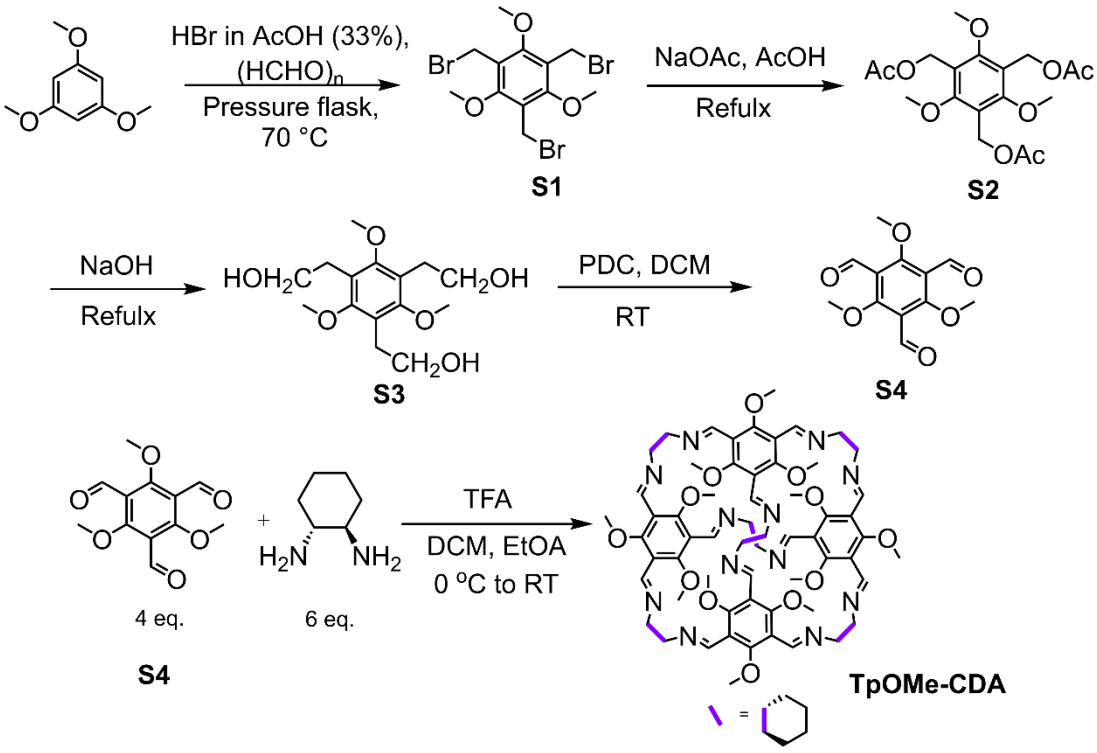

Figure 7.7: Synthesis route of **TpOMe-CDA**.

The aldehyde precursor **S4** and corresponding **TpOMe-CDA** cage were synthesised according to the literature. [171,182,183]

1,3,5-Tris(bromomethyl)-2,4,6-trimethoxybenzene (S1): 1,3,5-trimethoxybenzene 3 (4.5 g, 26.7 mmol), paraformaldehyde (3.0 g, 99.9 mmol) and AcOH (10.5 mL) were mixed and stirred in a 500 mL pressure flask stir for 1 hour. HBr (33% in AcOH, 28.5 mL) was then added, and the reaction mixture was heated in the sealed flask bath at 70 ºC behind a protective screen. The colour of reaction mixture was monitored, and heating was stopped before the colour changed to dark brown. This process usually took less than 2 hours. After cooling to room temperature, the reaction mixture was poured into 170 mL water and white precipitates appeared. The solids were filtered and dissolved in DCM, while the filtrate water was extracted with DCM. The DCM organic layer was combined and washed sequentially with saturated aqueous $NaHCO_3$, water, and brine. The washed DCM layer was concentrated in vacuo and purified with column chromatography using hexanes/ethyl acetate (20:1) to afford the product **S1** (1.6 g, yield =14 %) as a white solid. ^{1}H NMR (400 MHz, $CDCl_3$) δ_H 4.60 (6H, s, Br-CH_2), 4.14 (9H, s, O-CH_3); ^{13}C NMR (400MHz, $CDCl_3$) δ_C 160.17, 123.38, 62.77, 22.58.

1,3,5-Tris(acetoxymethyl)-2,4,6-trimethoxybenzene (S2): **S1** (4.0 g, 8.8 mmol) and NaOAc (9.08 g, 110.8 mmol) was dispersed in 80 mL glacial acid AcOH in a round bottom flask, then heated and refluxed at 120 °C for 4-6 hours. After cooling to room temperature, the resulting suspension was diluted with DCM and cooled in an ice bath. The solid precipitate was removed by filtration, and the filtrate was cooled in the ice bath again to precipitate. The precipitation-and-filtration process was repeated three times. The filtrate was finally concentrated and dissolved in 50 mL ethyl acetate. The organic layer was washed with saturated aqueous $NaHCO_3$ (2 x100 mL), water (100 mL), and brine (100 mL) sequentially, before it dried over $MgSO_4$. The solvent was evaporated in vacuum and the crude **S2** (3.42 g, yield = 98 %) was obtained as a white solid. ^{1}H NMR (400 MHz, DMSO-d_6) δ_H 5.03 (6H, s, AcO-CH_2), 3.77 (9H, s, O-CH_3), 2.04 (9H, s, CH_3 in -Ac).

1,3,5-Tris(hydroxyethyl)-2,4,6-trimethoxybenzene (S3): **S2** (3.46 g, 9 mmol) was then dissolved in EtOH (33 mL) and a 41 mL 3.75 M NaOH solution in water was added. The resulting mixture was refluxed for 12-18 hours. After the reaction mixture cooled, the EtOH in the mixture was then removed in vacuum. The remaining aqueous mixture was neutralized with 1.0 M HCl and saturated with NaCl. The treated water phase was then extracted with ethyl acetate (3 x 100 mL) and the organic layers were combined, dried over Na_2SO_4, and concentrated to dryness to give **S3** (1.82 g, yield = 67%). ^{1}H NMR (400 MHz, DMSO-d_6) δ_H 4.76 (3H, t, J = 4.8 Hz, -OH), 4.45(6H, d, J = 4.8 Hz, HO-CH_2), 3.86 (9H, s, O-CH_3); ^{13}C NMR (400MHz, DMSO-d_6) δ_C 159.21, 124.40, 63.74, 52.99.

2,4,6-Trimethoxy-benzene-1,3,5-tricarbaldehyde (S4): Pyridium dichromate (4.37 g, 11.6 mmol) was added to a stirring mixture of the **S3** (0.6 g, 2.0 mmol) in dry DCM (35 mL) and 4 Å molecular sieves. The resulting suspension was allowed to stir under nitrogen overnight. It was then diluted with DCM (100 mL) and all solid material was removed via filtration over celite. The filtrate was concentrated and purified via column chromatography (3:2 hexanes/ethyl acetate) to afford **S4** (0.3 g, yield = 59%) as a fibrous white solid. ^{1}H NMR (400 MHz, $CDCl_3$) δ_H 10.35 (3H, s, CHO), 4.03 (9H, s, O-CH_3).

TpOMe-CDA: **S4** (50.4 mg, 0.2 mmol) was dissolved in 2 mL ethyl acetate in a vial placed in an ice bath. R, R-CHDA was dissolved in 2 mL DCM and the solution was

slowly added (~1ml/5min) into **S4** solution with the aid of syringe pump (~1ml/5min). TFA was added by dropping a dose of its vapour with a syringe and needle after the complete addition. The vial was then capped with a rubber septum, and a needle was pierced into the septum which allowed slow evaporation. The reaction mixture was left undisturbed at room temperature, and blocked shaped crystals could appear after 48 hours, which was collected, washed with ethanol to afford **TpOMe-CDA** (17 mg, yield = 23%). ^{1}H NMR (400 MHz, $CDCl_3$) δ_H 8.52 (12H, s, -C=NH), 3.53 (9H, s, O-CH_3), 3.40 (12H, m, cyclohexyl CH), 1.84-1.46 (48H, br, cyclohexyl CH_2); ^{13}C NMR (400MHz, $CDCl_3$) δ_C 162.69, 153.83, 121.09, 62.76, 33.85, 24.76; MALDI-TOF MS (RP): m/z: accurate mass calculated for $C_{84}H_{108}N_{12}O_{12}$ 1476.82, found at 1477.75($[M+H]^+$).

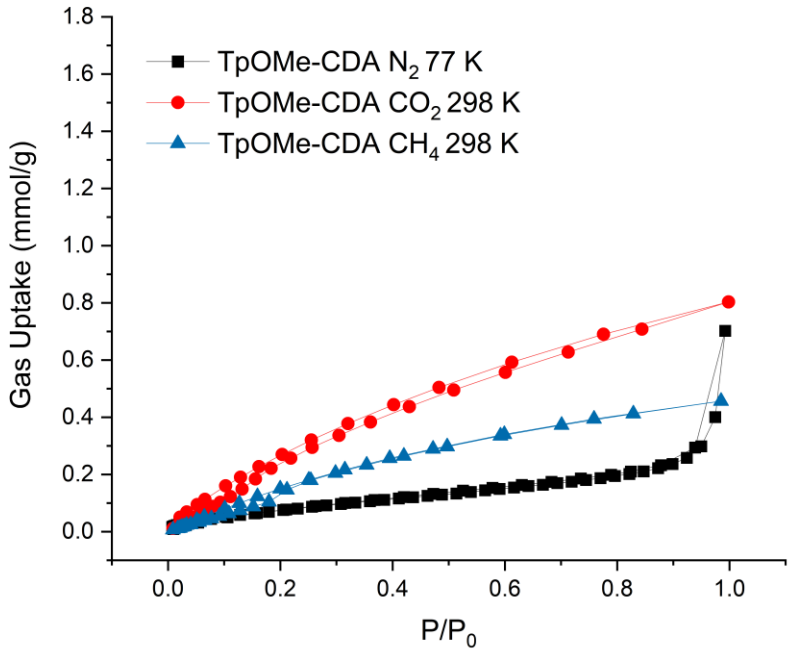

Figure 7.8: Gas sorption of **TpOMe-CDA** solids.

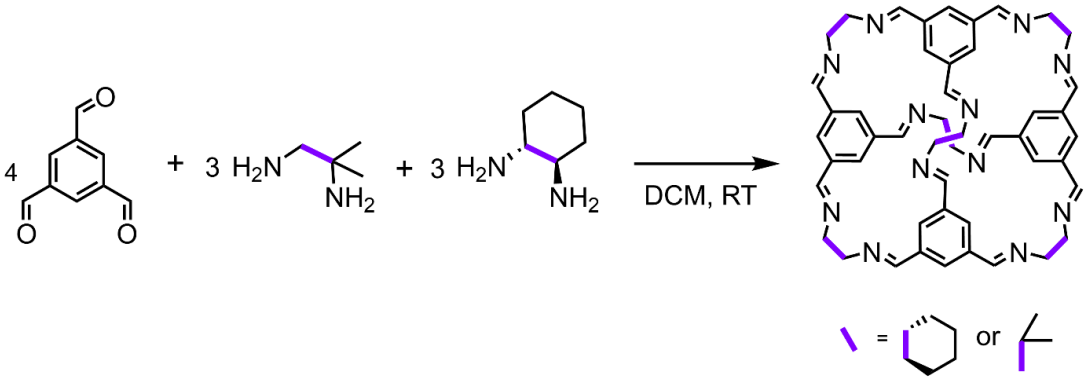

Figure 7.9: Synthesis route of **SC T_4:3_3:13_3**.

SC T_4:3_3:13_3: Scrambled cage **T_4:3_3:13_3** was synthesised according to the literature. [23] TFB (0.6485 g, 4 mmol, 4 eq.) was dissolved in 200 mL DCM, then R, R-CHDA (0.34 g, 3 mmol, 3 eq.) in 20 mL DCM and 1,2-diamino-2-methylpropane (0.22 g, 3 mmol, 3 eq.) in 20 mL DCM solution were added. The reaction mixture was stirred at room temperature under N_2 for three days. After the reaction stopped, the solution was concentrated, washed with ethyl acetate (100 mL) and dried at 90 ºC overnight to afford the product (0.94 g, yield = 91%). ^{1}H NMR (400 MHz, $CDCl_3$) δ_H 8.21-2.28 (24H, br, C=NH and benzene H), 3.95-3.35 (12H, br, CH or CH_2), 1.82-1.32 (42H, cyclohexyl H and CH_3); ^{13}C NMR (400MHz, $CDCl_3$) δ_C 161.09, 159.34, 155.43,137.28,136.78, 129.55, 100.1, 74.89, 72.37, 61.34, 33.23, 29.59, 24.54, 22.2; MALDI-TOF MS (RP): m/z: accurate mass calculated for **T_4:3_{13}:13_3** as **3_0:13_6**= 960.6, **3_1:13_5**= 986.6, **3_2:13_4**=1012.6, **3_3:13_3**=1038.66, **3_4:13_2**=1064.68, **3_5:13_1**=1090.7, **3_6:13_0**=1116.7; found at 961.6, 987.6, 1013.6, 1039.7, 1065.7, 1091.7, 1117.7 ($[M+H]^+$);

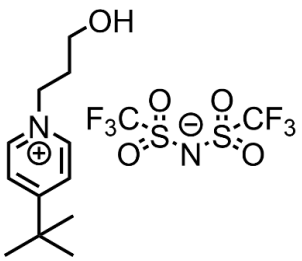

Figure 7.10: Molecular structure of 4-(tert-butyl)-1-(3-hydroxypropyl)pyridinium bis(trifluoromethylsulfonyl)imide ([T(OH)Py][NTf_2]).

[T(OH)Py][Cl]: The mixture of 4-tert-Butylpyridine (2.70 g, 20 mmol) and 3-chloropropanol (2.12g, 22 mmol) was heated at 100 ºC overnight. Solids appeared after the reaction mixture cooled, which was washed with ethyl acetate and filtered to give the product of [T(OH)Py][Cl] (3.90 g, yield = 85%). ^{1}H NMR (400 MHz, CD_3OD) δ_H 8.90 (2H, br, pyridinium H), 8.14 (2H, br, pyridinium H), 4.73 (2H, t, J = 7 .2 Hz, CH_2), 3.63 (2H, t, CH_2-OH), 2.21 (2H, m, CH_2), 1.45 (9H, s, tert-butyl); ^{13}C NMR (400 MHz, CD_3OD) δ_C 172.60, 145.50, 126.47, 59.50, 58.81, 37.52, 34.42, 30.23.

[T(OH)Py][NTf_2]: 100 mL acetonitrile solution of [T(OH)Py][Cl] (2.29 g, 10 mmol) and LiNTf_2 (3.15 g, 11 mmol) was combined and stirred overnight. 100 mL DCM was then added, and the mixture was washed with water until no Cl^- was detected by $AgNO_3$ solution. The organic phase was then dried over anhydrous Na_2SO_4 and concentrated to afford the light brown [T(OH)Py][NTf_2] (4.23 g, yield = 89%). ^{1}H NMR (400 MHz, CD_3OD) δ_H 8.80 (2H, br, pyridinium H), 8.10 (2H, br, pyridinium H), 4.68 (2H, t, J=7.2 Hz, CH_2), 3.62 (2H, t, CH_2-OH), 2.19 (2H, m, CH_2), 1.44 (9H, s, tert-butyl); ^{13}C NMR (400 MHz, CD_3OD) δ_C 172.71, 145.37, 126.47, 125.94, 122.76, 119.57, 116.38, 59.49, 58.77, 37.50, 34.30, 30.16; ^{19}F NMR (400 MHz, CD_3OD) δ_F -80.57; Elemental analysis (%): C 35.73 H 4.30 N 5.92 (Calculated: C 35.44 H 4.25 N 5.90).

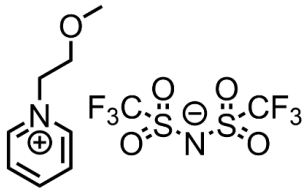

Figure 7.11: Molecular structure of 1-(2-methoxyethyl)pyridinium bis(trifluoromethylsulfonyl)imide ([(MeO)Py][NTf_2]).

[(MeO)Py][Br]: 2-bromoethyl ether (1.02 g, 7.34 mmol) was added into pyridine (0.527 g, 6.67 mmol), and the mixture was stirred at 75 °C for 3 hours. After the reaction stopped and cooled, solids would come out. The crude product was washed with ethyl acetate and dried in vacuo at 80 °C overnight to afford [(MeO)Py][Br] (1.25 g, yield = 86%). ^{1}H NMR (400 MHz, CD_3OD) δ_H 8.97 (2H, br, pyridinium H), 8.63 (1H, m, pyridinium H), 8.12 (2H, br, pyridinium H), 4.83 (2H, t, J = 4.8 Hz), 3.87 (2H, t, 4.8 Hz, CH_2-O), 3,34 (3H, s, O-CH_3); ^{13}C NMR (400 MHz, CD_3OD) δ_C 147.17, 146.51, 129.15, 71.46, 62.65, 59.26.

[(MeO)Py][NTf_2]: 100 mL acetonitrile solution of [(MeO)Py][Br] (2.18 g, 10 mmol) and $LiNTf_2$ (3.15 g, 11 mmol) was combined and stirred overnight. 100 mL DCM was then added, and the mixture was washed with water until no Br^- was detected by $AgNO_3$ solution. The organic phase was then dried over anhydrous Na_2SO_4 and concentrated to afford the light yellow [(MeO)Py][NTf_2] (3.76 g, yield = 90%). ^{1}H NMR (400 MHz, CD_3OD) δ_H 8.94 (2H, br, pyridinium H), 8.62 (1H, m, pyridinium H), 8.11 (2H, br, pyridinium H), 4.81 (2H, t, J = 4.8 Hz), 3.86 (2H, t, 4.8 Hz, CH_2-O), 3,34 (3H, s, O-CH_3); ^{13}C NMR (400 MHz, CD_3OD) δ_C 147.17, 146.46, 129.14, 125.98, 122.80, 119.62, 116.44, 71.39, 62.69, 59.23; Elemental analysis (%): C 28.81 H 2.86 N 6.66 (Calculated: C 28.71 H 2.90 N 6.70).

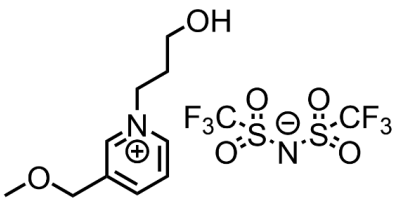

Figure 7.12: Molecular structure of 1-(3-hydroxypropyl)-3-(methoxymethyl)pyridinium bis(trifluoromethylsulfonyl)imide ([(OH)(MeO)Py][NTf_2]).

3-(methoxymethyl)pyridine: Picolyl chloride hydrochloride (4.30 g, 26.37 mmol) was dissolved in 40 mL DMSO, and the solution was slowly added to a suspension of sodium methoxide (4.23 g, 79.11 mmol) in 40 mL DMSO at room temperature. The reaction mixture was stirred for 24 hours and quenched by adding 200 mL water. The aqueous solution was extracted by ethyl acetate (3 x 50 mL), and the ethyl acetate phase was dried over $NaSO_4$ and concentrated. The crude product was purified by column chromatography using neat ethyl acetate eluent to give the product 3-(methoxymethyl)pyridine (2.53 g, yield = 63%). ^{1}H NMR (400 MHz, CD_3OD) δ_H 8.52-8.51 (1H, m, pyridine H), 8.47-8.46 (1H, m, pyridine H), 7.84-7.81 (1H, m, pyridine H), 7.45-7.41 (1H, m, pyridine H), 4.51 (2H, s, CH_2-O), 3.41 (3H, s, O-CH_3). ^{13}C NMR (400 MHz, $CDCl_3$) δ_C 149.33, 149.28, 135.49, 133.66, 123.50, 72.24, 58.47.

[(OH)(MeO)Py][Cl]: 3-chloropropanol (2.12g, 22 mmol) was added to the 3-(methoxymethyl)pyridine (3.02 g, 20 mmol), and the mixture was stirred at 100 ºC overnight. After the reaction stopped and cooled, solids would come out. The crude product was washed with ethyl acetate and dried in vacuo at 80 °C overnight to afford [(OH)(MeO)Py][Cl] (3.57 g, yield = 82%). ^{1}H NMR (400 MHz, DMSO-d_6) δ_H 9.12 (1H, s, pyridinium H), 9.09 (1H, br, pyridinium H), 8.53 (1H, br, pyridinium H), 8.17-8.13 (1H, m, pyridinium H), 4.72 (2H, t, pyridinium-CH_2), 4.65 (2H, s, CH2-O), 3.44 (2H, t, CH_2-OH), 3.39 (3H, s, O-CH_3), 2.09 (2H, q, CH_2); ^{13}C NMR (400 MHz, DMSO-d_6) δ_C 143.98, 143.26, 139.08, 127.57, 69.43, 58.65, 58.28, 57.10, 33.30.

[(OH)(MeO)Py][NTf_2]: 100 mL acetonitrile solution of [(OH)(MeO)Py][Cl] (2.17 g, 10 mmol) and $LiNTf_2$ (3.15 g, 11 mmol) was combined and stirred overnight. 100 mL DCM was then added, and the mixture was washed with water until no Cl^- was detected by $AgNO_3$ solution. The organic phase was then dried over anhydrous Na_2SO_4 and concentrated to afford the light brown [(OH)(MeO)Py][NTf_2] (3.97 g, yield = 86%). ^{1}H NMR (400 MHz, CD_3OD) δ_H 8.94 (1H, s, pyridinium H), 8.87 (1H, br, pyridinium H), 8.51 (1H, br, pyridinium H), 8.08-8.04 (1H, m, pyridinium H), 4.75

(2H, t, pyridinium-CH_2), 4.70 (2H, s, CH2-O), 3.63 (2H, t, CH_2-OH), 3.51 (3H, s, O-CH_3), 2.23 (2H, q, CH_2); ^{13}C NMR (400 MHz, CD_3OD) δ_C 144.97, 144.87, 144.30, 128.90, 125.93,122.75, 119.56, 116.38, 70.96, 60.63, 59.30, 58.80, 34.43. ^{19}F NMR (400 MHz, CD_3OD) δ_F -80.61.

7.4 Chapter 5 experimental data

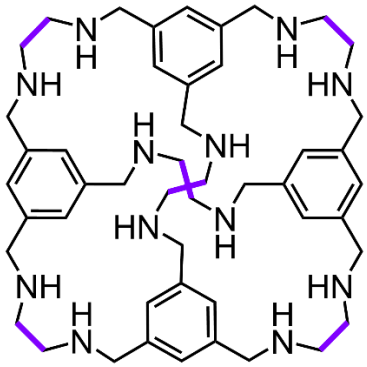

Figure 7.13; The molecular structure of **RCC1**.

RCC1: Reduced cage RCC1 was synthesised according to the literature with minor modified steps. [184] TFB (1.87 g, 0.012 mol) was first dissolved in methanol (575 mL) in a 2 L round-bottomed flask cooled in an ice bath. Ethylenediamine (1.04 g, 0.017 mol) was dissolved in methanol (425 mL) and added in batches over 1 hour to the TFB solution under a nitrogen atmosphere. The reaction mixture was further stirred overnight. After checking NMR of the sample from mixtures that the aldehyde peak has gone, sodium borohydride (1.53 g, 0.040 mol) was added, and the reaction mixture was stirred for a further 12 hours. Water (5 mL) was then added, and the reaction stirred for a further 12 hours. After the reaction stopped, the solvent was then removed under vacuum. The resulting white solid was then extracted with DCM (2 × 100 mL) and the remaining white solid was removed by filtration. The solvent was then removed with a rotary evaporator (water bath at 30 °C) and crude **RCC1** was obtained as an off-white solid (1.47 g, yield = 62%). ^{1}H NMR (400MHz, CD_3OD) δ_H 7.10 (12H, s, H_A), 3.65 (24H, s, H_B), 2.60 (24H, s, H_C); ^{13}C NMR (400MHz, CD_3OD) δ_C 141.09, 128.37, 54.09.

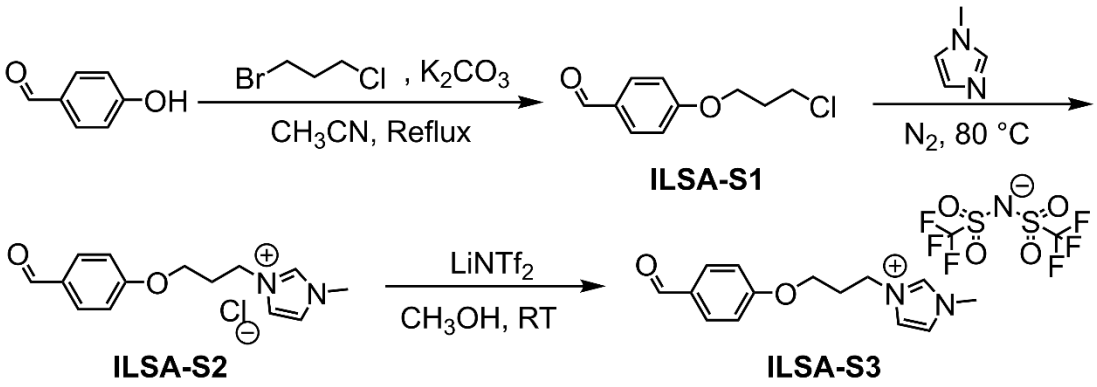

Figure 7.14: Synthesis route of ionic liquid functionalised aldehyde **ILSA-S3**.

ILSA-S3 was synthesised according to the literature with minor modifications. [176]

ILSA-S1: A mixture of 4-hydroxybenzaldehyde (2.44 g, 20 mmol), 1-bromo-3-chloropropane (4.72 g, 30 mmol) and K_2CO_3 (5.53 g, 40 mmol) in acetonitrile (150 mL) was refluxed for 3 hours, during which the reaction was monitored with TLC. After completion of the reaction, acetonitrile was evaporated, and the residue was dispersed in DCM and filtered. The organic layer was then evaporated and purified by column chromatography on silica using 100% DCM to get the targeted product **ILSA-S1** as a light-yellow oil (3.65 g, yield = 92%). ^{1}H NMR (400MHz, $CDCl_3$) δ_H 9.89 (1H, s, CHO), 7.84 (2H, m, ArH), 7.01 (2H, m, ArH), 4.21 (2H, t, J= 6 Hz, OCH_2), 3.76 (2H, t, J= 6 Hz, CH_2), 2.28 (2H, q, J= 6 Hz, CH_2); ^{13}C NMR (400MHz, $CDCl_3$) δ_C 190.91, 163.84, 132.14, 130.25, 130.25, 114.89, 64.74, 41.33, 32.11.

ILSA-S2: A mixture of **ILSA-S1** (1.99 g, 10 mmol) and 1-methylimidazole (1.23 g, 15 mmol) was heated at 80 °C for 6 h to give a thick viscous liquid. The viscous liquid was washed with diethyl ether (3 × 30 mL) to get the crude product **ILSA-S2** (2.02 g, yield = 72%). ^{1}H NMR (400MHz, CD_3OD) δ_H 9.85 (1H, s, CHO), 9.02 (1H, s, C=NH), 7.87 (2H, m, ArH), 7.65 (2H, m, ArH), 7.07 (2H, m, ArH), 4.48 (2H, t, J= 7.2 Hz, OCH_2), 4.20 (2H, t, J= 6 Hz, CH_2), 3.93 (3H, s, CH_3), 2.43 (2H, m, CH_2); ^{13}C NMR (400MHz, $CDCl_3$) δ_C 192.78, 165.02, 138.19, 133.11, 131.73, 125.06, 123.92, 115.93, 66.20, 48.22, 36.50.

ILSA-S3: **ILSA-S2** (1.0 g, 3.56 mmol) is dissolved in 50 mL in acetonitrile, and lithium bis(trifluoromethanesulfonyl)imide ($LiNTf_2$, 1.15 g, 4 mmol) was added. The mixture was then stirred at room temperature for 24 hours. After the reaction stopped, the solution was diluted with 100 mL DCM, washed with water and dried over $MgSO_4$.

The mixture was filtered, and the filtrate was concentrated to yield **ILSA-S3** as an off-white wax (1.53 g, yield = 82%). ^{1}H NMR (400MHz, CD_3OD) δ_H 9.84 (1H, s, CHO), 7.87 (2H, m, ArH), 7.62 (2H, dd, J= 36, 2 Hz, Imi-H), 7.07 (2H, m, ArH), 4.46 (2H, t, J= 7.2 Hz, CH_2), 4.19 (2H, t, J= 5.6 Hz, CH_2), 3.01 (3H, s, CH_3), 2.42 (2H, m, CH_2); ^{13}C NMR (400MHz, CD_3OD) δ_C 192.82, 165.01, 133.12, 131.73, 125.02, 123.86, 122.80, 115.91, 66.12, 36.43, 30.51; ^{19}FNMR (400MHz, CD_3OD) δ_F -80.70; Elemental analysis (%): C 36.86 H 3.22 N 8.05 (Calculated: C 36.57 H 3.26 N 8.00).

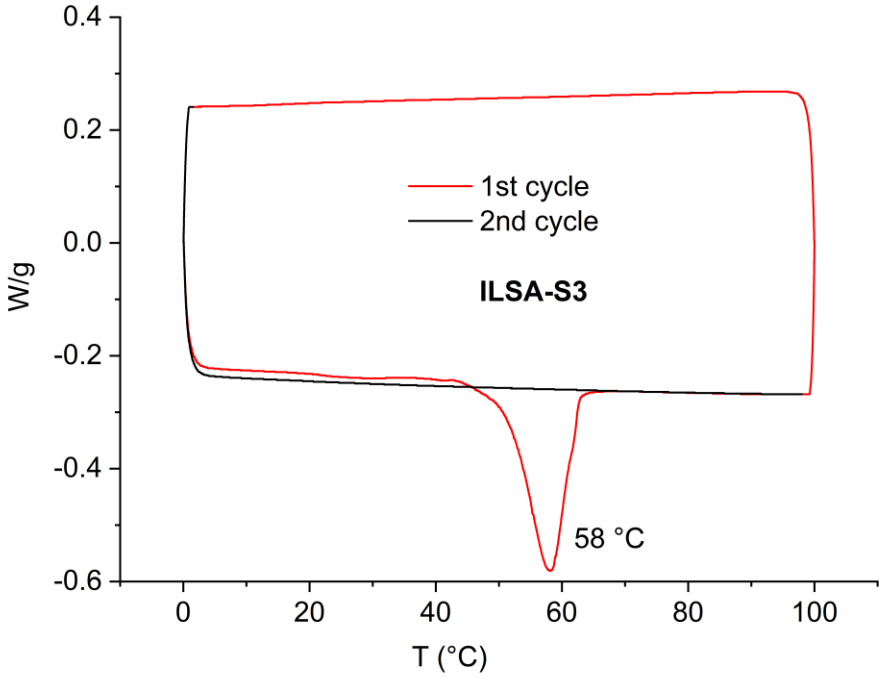

Figure 7.15: DSC of **ILSA-S3**.

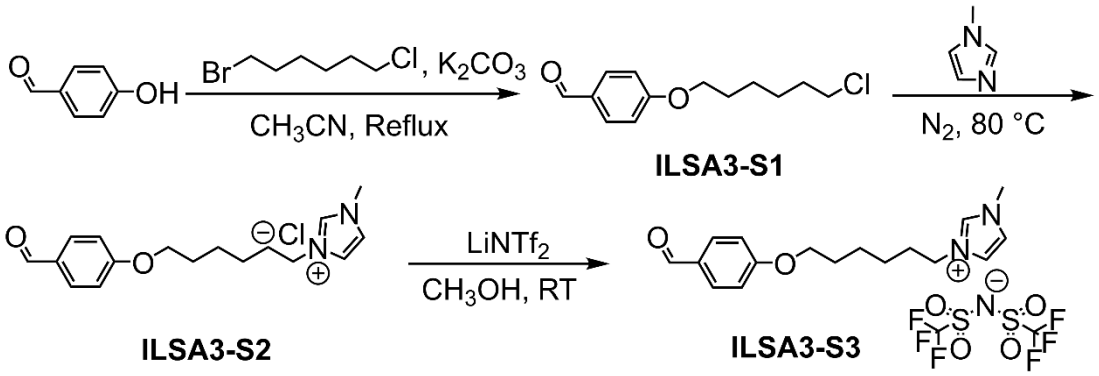

Figure 7.16: Synthesis route of ionic liquid functionalised aldehyde **ILSA3-S3**.

The synthesis procedures were like those used for **ILSA-S3**. And structure information of every step product was listed below.

ILSA3-S1: ^{1}H NMR (400MHz, $CDCl_3$) δ_H 9.88 (1H, s, CHO), 7.83 (2H, m, ArH), 6.99 (2H, m, ArH), 4.05 (2H, t, J= 6 Hz, OCH_2), 3.56 (2H, t, J= 6.4 Hz, $ClCH_2$), 1.83 (4H, m, CH_2), 1.52 (4H, m, CH_2); ^{13}C NMR (400MHz, $CDCl_3$) δ_C 190.96, 164.28, 132.14, 129.96, 114.87, 68.28, 45.09, 32.59, 29.05, 26.72, 25.48.

ILSA3-S2: ^{1}H NMR (400MHz, CD_3OD) δ_H 9.83 (1H, s, CHO), 8.99 (1H, s, Imi-H) 7.85 (2H, m, ArH), 7.62 (2H, dd, J= 31.6, 2Hz, CH=CH), 7.06 (2H, m, ArH), 4.25 (2H, t, J= 7.2 Hz, OCH_2), 4.10 (2H, t, J= 6.4 Hz, CH_2), 3.94 (3H, s, CH3), 1.94 (2H, m, CH_2), 1.84 (2H, m, CH_2), 1.57 (2H, m, CH_2), 1.44 (2H, m, CH_2).

ILSA3-S3: ^{1}H NMR (400MHz, CD_3OD) δ_H 9.82 (1H, s, H_A), 7.85 (2H, m, H_B), 7.57 (2H, dd, J= 30, 2 Hz, H_C), 7.06 (2H, m, H_D), 4.22 (2H, t, J= 7.6 Hz, H_E), 4.08 (2H, t, J= 6 Hz, H_F), 3.91 (3H, s, H_G), 1.93 (2H, m, H_H), 1.83 (2H, m, H_I), 1.56 (2H, m, H_J), 1.43 (2H, m, H_K); ^{13}C NMR (400MHz, CD_3OD) δ_C 192.90, 165.87, 133.12, 131.18, 125.97, 125.42, 124.91, 123.60, 122.79, 119.60, 115.93, 69.27, 50.72, 36.41, 30.97, 29.83, 26.87, 26.43; ^{19}F NMR (400MHz, CD_3OD) δ_F -80.64; Elemental analysis (%): C 40.33 H 4.11 N 7.11 (Calculated: C 40.21 H 4.09 N 7.40).

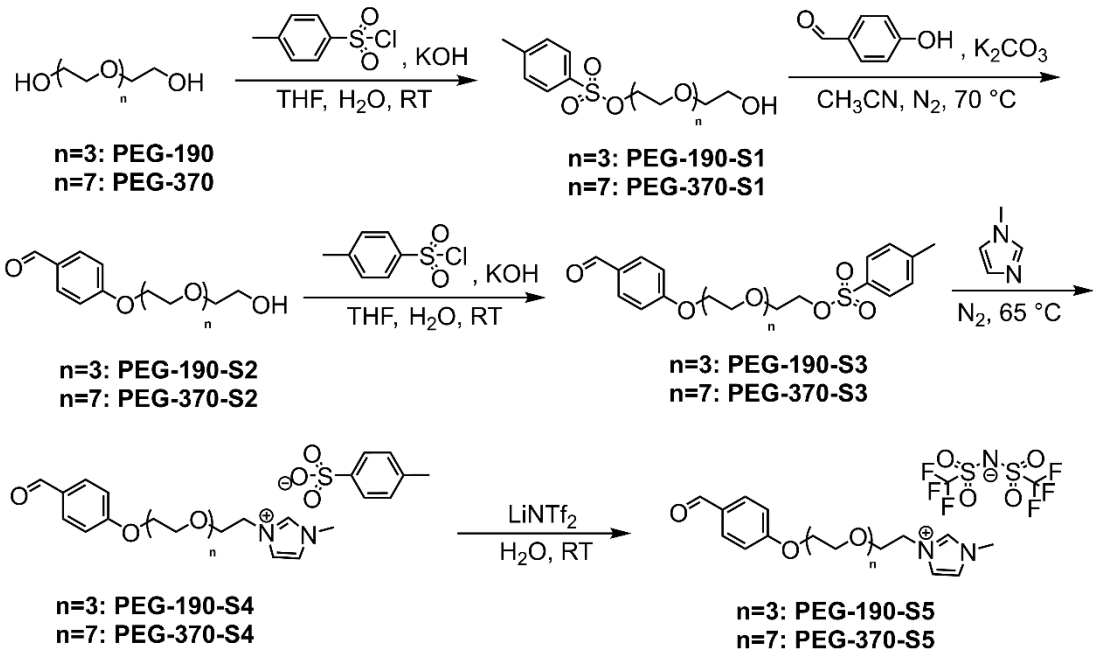

Figure 7.17: Synthesis route of PEG-CHO.

PEG-CHO was synthesised according to the literature with modifications. [28]

PEG-190-S1: A solution of potassium hydroxide (0.49 g, 8.57 mmol, 3 equiv.) in water (7.5 mL) was added slowly to a solution of tetraethylene glycol (**PEG-190**, 4.08g, 21 mmol, 7. equiv.) and TsCl (0.55 g, 2.89 mmol, 1 equiv.) in tetrahydrofuran (THF, 250 ml). The mixture was stirred for 18 hours at room temperature. Water (250 mL) was then added, and the reaction mixture was extracted with DCM (3 x 100 mL). The organic layer was dried over $MgSO_4$, filtered, and the solvent was removed by rotary evaporation. The crude product was purified by flash column chromatography (SiO_2 DCM/methanol 99:1 to 95:5, v/v) to afford the oily **PEG-190-S1** (0.860 g, yield = 86%). ^{1}H NMR (400MHz, $CDCl_3$) δ_H 7.80 (2H, m, ArH), 7.34 (2H, m, ArH), 4.17 (2H, m, CH_2OH), 3.73-3.59 (14H, m, PEG-CH_2 groups), 2.45 (3H, s, CH_3 on benzene); ^{13}C NMR (400MHz, $CDCl_3$) δ_C 144.94, 133.10, 129.95, 128.10, 72.59, 70.85, 70.44, 69.36, 68.82, 61.85, 21.76; **PEG-370-S1** was synthesised with the same method with **PEG-190-S1**. ^{1}H NMR (400MHz, $CDCl_3$)) δ_H 7.80 (2H, m, ArH), 7.34 (2H, m, ArH), 4.16 (2H, m, CH_2OH), 3.71-3.58 (30H, m, PEG-CH_2 groups), 2.45 (3H, s, CH_3 on benzene); ^{13}C NMR (400MHz, $CDCl_3$) δ_C 144.91, 133.14, 129.95, 128.12, 72.72, 70.87, 70.73, 70.69, 70.64, 69.37, 68.81, 61.85, 21.77.

PEG-190-S2: **PEG-190-S1** (0.35 g, 1.00 mmol, 1 equiv.) and 4-hydroxybenzaldehyde (0.244g, 2.00 mmol, 2 equiv.) and K_2CO_3 (0.69g, 5.00 mmol, 5 equiv.) were dispersed

in acetonitrile (10 mL) and heated at 70 °C under N_2 for 18 hours. After the reaction stopped, the mixture was evaporated and extracted with DCM (3 x 50 mL). The DCM phase could be evaporated and used directly for the next step reaction or purified by column chromatography (100% DCM to 100% MeOH) to get the pure product of **PEG-190-S2** (0.22 g, yield = 74%). ^{1}H NMR (400MHz, $CDCl_3$ δ_H 9.88 (1H, s, CHO), 7.83 (2H, m, ArH), 7.02 (2H, m, ArH), 4.22 (2H, m, CH_2OH), 3.89 (2H, m, CH_2), 3.73-3.60 (12H, m, PEG CH_2 groups); ^{13}C NMR (400MHz, $CDCl_3$) δ_C 190.97, 163.91, 132.08, 130.17, 114.99, 72.63, 70.96, 70.75, 70.66, 70.39, 69.57, 67.82, 61.82; **PEG-370-S2**: ^{1}H NMR (400MHz, $CDCl_3$) δ_H 9.88 (1H, s, CHO), 7.83 (2H, m, ArH), 7.02 (2H, m, ArH), 4.22 (2H, m, CH_2OH), 3.89 (2H, m, CH_2), 3.80-3.50 (26H, m, PEG CH_2 groups), 3.20-2.00 (2H, broad, CH_2); ^{13}C NMR (400MHz, $CDCl_3$) δ_C 190.97, 163.98, 132.08, 130.16, 115.01, 72.70, 71.02, 70.73, 70.67, 70.63,70.40, 69.58, 67.88, 61.84.

PEG-190-S3: Potassium hydroxide (0.84 g, 3.20 mmol, 4 equiv.) was dissolved in 5 mL water and added slowly to a THF (20 mL) solution of **PEG-190-S2** (0.30 g, 1.00 mmol, 1 equiv.) and TsCl (0.38 g, 2.00 mmol, 2 equiv.). The mixture was stirred for 18 hours at room temperature and quenched with 150 mL. The mixture was then extracted with DCM (3 x 100 mL) and DCM phase was dried over MgSO4, filtered, and concentrated by rotary evaporation. The crude product was purified by column chromatography (100% DCM to 100% MeOH) to afford **PEG-190-S3** (0.36 g, yield = 79%). ^{1}HNMR (400MHz, $CDCl_3$) δ_H 9.88 (1H, s, CHO), 7.80 (4H, m, ArH), 7.33 (2H, dd, J= 8 Hz, ArH), 7.02 (2H, dd, J= 8 Hz, ArH), 4.21 (2H, t, J= 4.8 Hz, CH_2OH), 4.15 (2H, t, J= 4.8 Hz, CH_2), 3.88 (2H, m, CH_2), 3.73-3.59 (10H, m, PEG CH_2 groups), 2.44 (3H, s, CH_3 on benzene); ^{13}CNMR (400MHz, $CDCl_3$) δ_C 190.93, 163.97, 144.94, 133.13, 132.07, 130.18, 129.95, 128.08, 115.01, 70.99, 70.88, 70.79, 70.68, 69.60, 69.35, 68.82, 67.90, 21.75; **PEG-370-S3**: ^{1}H NMR (400MHz, $CDCl_3$) δ_H 9.88 (1H, s, CHO), 7.81 (4H, m, ArH), 7.34 (2H, dd, J= 8 Hz, ArH), 7.02 (2H, dd, J= 8 Hz, ArH), 4.22 (2H, t, J= 4.8 Hz, CH_2OH), 4.16 (2H, t, J= 4.8 Hz, CH_2), 3.89 (2H, t, J=4.8 Hz, CH_2), 3.74-3.58 (24H, m, PEG CH_2 groups), 2.45 (3H, s, CH_3 on benzene); ^{13}C NMR (400MHz, $CDCl_3$) δ_C 190.96, 163.99, 144.93, 133.13, 132.09, 130.18, 129.96, 128.11, 115.02, 71.03, 70.87, 70.75, 70.69, 70.64, 69.59, 69.37, 68.81, 67.90, 21.77.

PEG-190-S4: In the neat **PEG-190-S3** (0.45 g, 1.00 mmol, 1 equiv.), 1-methylimidazole (0.25 g, 3.00 mmol, 3 equiv.) was added, and the mixture was stirred

at 65 °C under the atmosphere for 18 hours. After the reaction stopped, it was washed with methanol and diethyl ether to afford **PEG-190-S4** (0.44 g, yield = 82%). ^{1}H NMR (400MHz, CD_3OD) δ_H 9.84 (1H, s, CHO), 8.90 (1H, s, ImH), 7.85 (2H, m, ArH), 7.70 (2H, m, ArH), 7.55 (2H, dt, J= 46.4, 1.6 Hz, CH=CH), 7.23 (2H, m, ArH), 7.07 (2H, m, ArH), 4.33 (2H, t, J= 4.8 Hz, CH_2OH), 4.23 (2H, m, CH_2), 3.88 (3H, s, CH_3), 3.87-3.58 (12H, m, PEG CH_2 groups), 2.36 (3H, s, CH_3); ^{13}C NMR (400MHz, CD_3OD) δ_C 192.79, 165.48, 143.66, 141.64, 133.12, 131.52, 129.81, 126.95, 124.50, 124.24, 115.99, 71.69, 71.40, 71.36, 71.32, 69.11, 50.75, 36.44, 21.30; **PEG-370-S4**: ^{1}H NMR (400MHz, DMSO-d_6) δ_H 9.88 (1H, s, CHO), 9.05 (1H, s, ImH), 7.86 (2H, m, ArH), 7.71 (2H, m, CH=CH), 7.47 (2H, m, ArH),7.12 (4H, m, ArH), 4.34 (2H, t, J= 4.4 Hz, CH_2OH), 4.22 (2H, t, J= 4.4 Hz, CH_2), 3.86 (3H, s, CH_3), 3.77-3.49 (30H, m, PEG CH_2 groups), 2.29 (3H, s, CH_3 on benzene); ^{13}C NMR (400MHz, DMSO-d_6) δ_C 191.33, 163.47, 137.52, 136.81, 131.80, 129.66, 128.02, 125.48, 123.35, 122.69, 114.95, 69.93, 69.75, 69.69, 69.51, 68.69, 68.11, 67.69, 48.74, 35.71, 20.77.

PEG-190-S5: **PEG-190-S4** (0.53 g, 1.00 mmol, 1 equiv.) and $LiNTf_2$ (0.57 g, 2.00 mmol, 2 equiv.) were dissolved in 10 mL water and stirred for 6 hours. 100 mL DCM was then added to the system, and the mixture was washed with water (100 mL x 3) until no precipitate was tested by adding $AgNO_3$ solution into the water phase. The DCM layer was then dried over $MgSO_4$, filtered, and evaporated to afford **PEG-190-S5** (0.57 g, yield = 89%). ^{1}H NMR (400MHz, $CDCl_3$) δ_H 9.87 (1H, s, CHO), 8.79 (1H, s, ImH) 7.82 (2H, m, ArH), 7.48 (1H, s, CH=CH), 7.19 (1H, s, CH=CH), 6.99 (2H, m, ArH) 4.32 (2H, t, J=4.4 Hz, CH_2OH), 4.20 (2H, t, J= 4.4 Hz, CH_2), 3.74-3.56 (8H, m, PEG CH_2 groups). ^{13}C NMR (400MHz, $CDCl_3$) δ_C 191.01, 163.80, 136.77, 132.16, 130.27, 123.68, 123.04, 121.53, 118.33, 114.92, 70.84, 70.42, 70.35, 70.32, 69.53, 68.61, 67.95, 49.94, 36.37; ^{19}F NMR (400MHz, DMSO-d_6) δ_F -78.93; Elemental analysis (%): C 39.24 H 4.29 N 6.43 (Calculated: C 39.19 H 4.23 N 6.53). **PEG-370-S5**: DMSO-d_6 was used to receive the ^{1}H NMR. ^{1}H NMR (400MHz, DMSO-d_6) δ_H 9.87 (1H, s, CHO), 9.03 (1H, s, ImH), 7.86 (2H, m, CH=CH), 7.70 (2H, m, ArH), 7.13 (2H, m, ArH), 4.34 (2H, t, J= 4.4 Hz, CH_2OH), 4.22 (2H, t, J= 4.4 Hz, CH_2), 3.86 (3H, s, CH_3), 3.77 (4H, m, CH_2), 3.60-3.49 (24H, m, PEG CH_2 groups); ^{13}C NMR (400MHz, DMSO-d_6) δ_C 191.30, 163.48, 136.80, 131.79, 129.66, 123.35, 122.69, 121.08, 117.88, 114.94, 69.94, 69.75, 69.69, 69.55, 69.52, 68.70, 68.11, 67.68, 35.71;

^{19}F NMR ((400MHz, DMSO-d_6) δ_F -78.72; Elemental analysis (%): C 42.53 H 5.36 N 5.28 (Calculated: C 42.49 H 5.29 N 5.13).

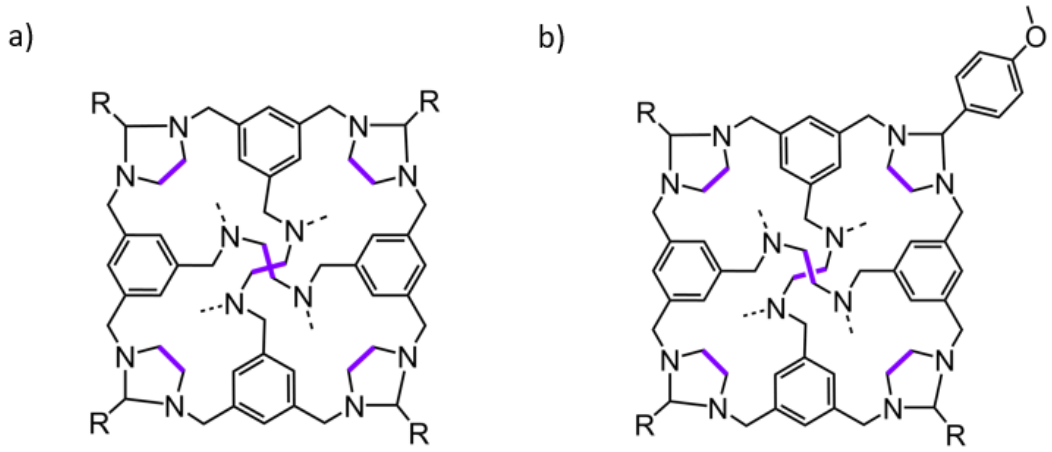

Figure 7.18: Molecular structure of a) **RCC1-CHO** tying serial; b) **RCC1-ILSA-02**.

RCC1-CHO tying serial: The method of tying **RCC1** with **ILSA-S3**, **ILSA3-S3**, **PEG-190-CHO** and **PEG-370-CHO** was similar. Typically, **RCC1** (30 mg, 0.037 mmol, 1 equiv.) was dissolved in 2 mL DCM and added dropwise to the DCM solution of the aldehyde (9 equiv.). Usually, the solution would become opaque after a few minutes and was kept stirring overnight. After the reaction stopped, the mixture was left to stand for the phase separation, where the lower layer of oily phase was the tied product. The upper DCM layer was decanted, and the product was washed by DCM for several times to afford the product **RCC1-ILSA-CHO**. In the case of tying **PEG-CHO**, as the product was soluble in DCM, 6 equiv. aldehyde was used and Na_2SO_4 was added to the system to remove the by-product of water. The reaction mixture was then filtered and evaporated to afford **RCC1-PEG-CHO**.

RCC1-ILSA-02: Tying **RCC1** with p-anisaldehyde was done in methanol with the same concentration and ratio that was used above. As the product was solid, it was filtered and washed with methanol to afford **RCC1-ILSA-02**. Elemental analysis (%): C 73.33 H 7.10 N 11.38 (Calculated: C 75.56 H 7.13 N 11.01).

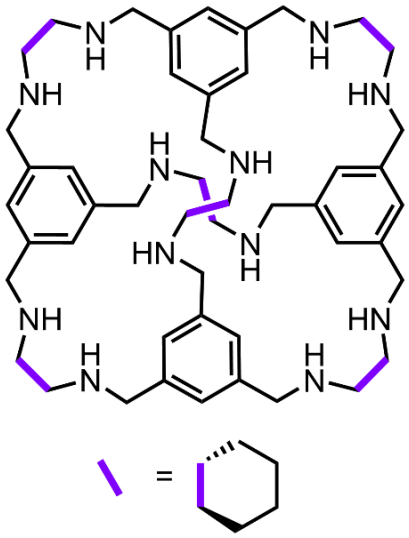

Figure 7.19: Molecular structure of **RCC3**.

RCC3 was synthesised according to the literature. [169] **CC3**-*R* (0.93 g, 0.83 mmol) was dissolved in a 50 mL solvent mixture of chloroform and methanol with 1:1 ratio. Sodium borohydride ($NaBH_4$, 1.00 g, 26.6 mmol) was then added and the mixture was stirred at room temperature overnight. 2 mL water was added to quench the reaction and it was stirred further for 12 hours. After the reaction stopped, 100 mL water was added, and the mixture was extracted with 3 × 50 mL DCM. The organic phase was dried over $MgSO_4$, filtered and evaporated to afford the product of **RCC3** (0.53 g, yield = 57%). ^{1}H NMR (400MHz, $CDCl_3$) δ_H 7.11 (12H, s, ArH), 3.81 (12H, d, Ar-CH_2, J=14 Hz), 3.55 (12H, d, Ar-CH_2, J=14 Hz), 2.21 (12H, br, cyclohexyl CH), 1.64-0.96 (48H, br, cyclohexyl CH_2); ^{13}C NMR (400MHz, $CDCl_3$) δ_C 141.24, 125.17, 61.35, 50.65, 31.72, 25.04.

RCC3-ILSA-S3: **RCC3** (10 mg, 1 equiv.) and **ILSA-S3** (0.11g, 24 equiv.) were dissolved in 5 mL methanol, and molecular sieves were then added. The reaction mixture was stirred at room temperature for over a week. The reaction was monitored by MALDI-TOF.

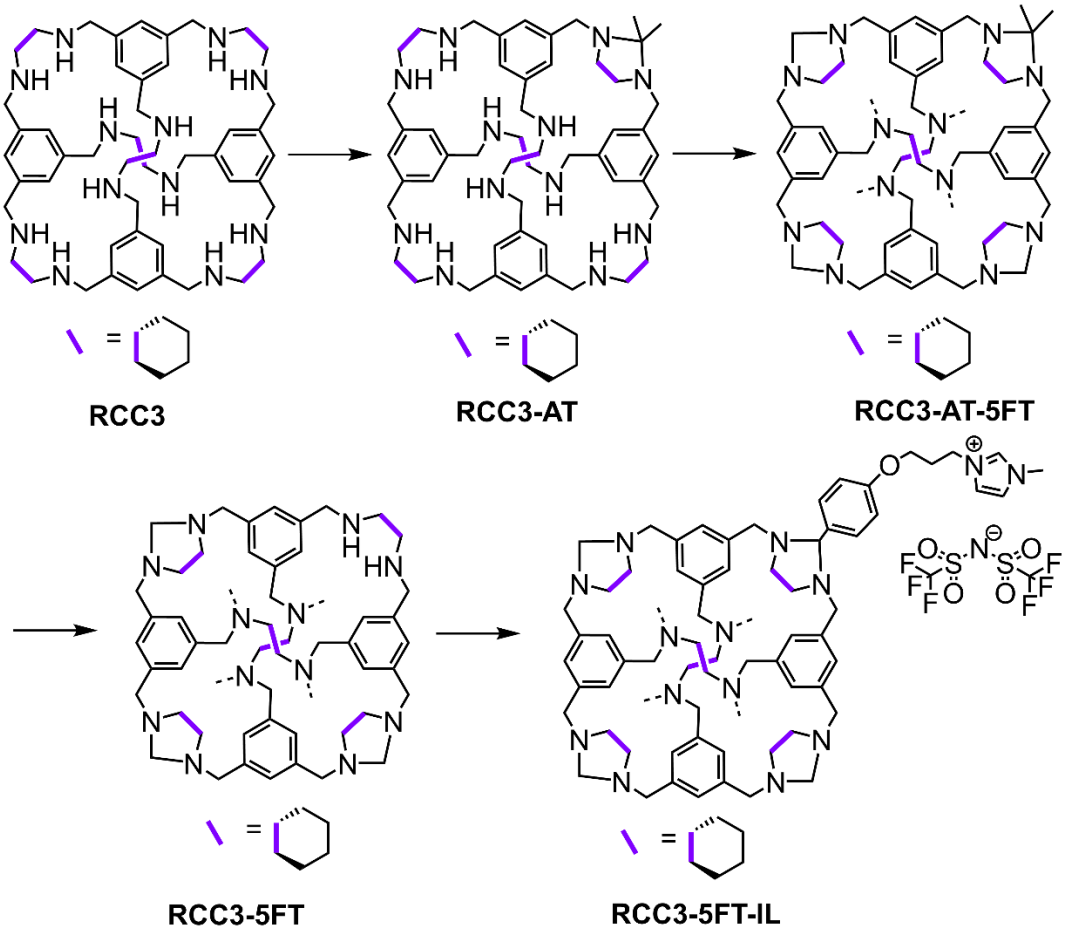

Figure 7.20: Synthesis route of **RCC3-5FT-IL**.

RCC3-5FT was synthesised according to the literature. [169,170] As the tuning of reaction conditions to get pure **RCC3-5FT** has yet to be performed, no detailed characterisation data could be provided here.

RCC3 (100 mg) was dissolved in 6 mL acetone in a vial and the solution was left overnight. Crystals which appeared at the bottom and wall of the vail were collected by filtration and washed with acetone. The crystals were dried at room temperature under vacuum to afford **RCC3-AT**. 50 mg **RCC3-AT** was then added to a small glass tube, while paraformaldehyde was added to a 100 mL pressure vessel. A glass tube containing **RCC3-AT** was placed into the pressure vessel which was then sealed. The pressure tube was heated at 60 °C in an oil bath for 12 hours. After the reaction stopped, the glass tube was taken out and cooled in atmosphere. The product was left in atmosphere for a further 12 hours to remove absorbed formaldehyde. Around 50 mg **RCC3-AT-FT** was dissolved in a 10 mL mixture of $CHCl_3$ and methanol (1:1). A drop of water was added, and the mixture was then stirred at room temperature for 12 hours. After the reaction stopped, the solution was evaporated and dried under vacuum

at 60 ºC to afford **RCC3-FT**. Tying **RCC3-FT** with **ILSA-S3** used the same reaction conditions as **RCC3-ILSA-S3**.

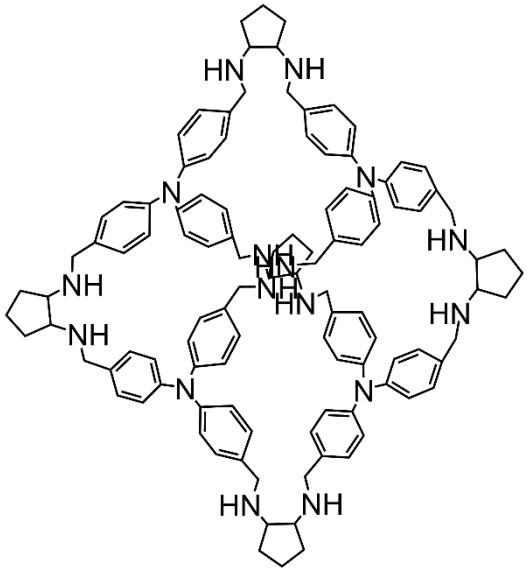

Figure 7.21: Molecular structure of **RCC5**.

CC5: **CC5** was synthesised according to the literature. [142] In an oven-dried flask which was cooled to room temperature under dry N_2, (1R, 2R)-1,2-cyclopentanediamine dihydrocholoride (0.21 g, 1.2 mmol) was first dissolved in 100 mL methanol. Triethylamine (0.24 g, 2.4 mmol) was then added, and the solution was stirred at room temperature for 5–10 min. In another oven-dried and N_2-cooled flask, tri(4-formylphenyl)amine (0.26 g, 0.8 mmol) was dissolved in 100 mL of DCM (100 mL). The first solution was then layered very slowly onto the tri(4-formylphenyl)amine solution by a pipette. A cloudy interface could be seen between these two layers after the addition was completed and the resulting suspension was then capped and kept at room temperature for 7 days. White solids formed in the flask after 7 days were collected by filtration and washed with DCM (3 × 5 mL) to afford **CC5** (0.30 g, yield = 90%). ^{1}H NMR (CDCl3, 400 MHz,) δ_H 7.99 (12H, s, C=NH), 7.51 (24H, d, J = 8.8 Hz, benzene H), 7.01 (24H, d, J = 8.8 Hz, benzene H), 3.62 (12H, m, cyclopentyl CH), 2.12-1.95 (36H, br, cyclopentyl CH_2); MALDI-TOF MS (RP): m/z: accurate mass calculated for $C_{114}H_{108}N_{16}$ 1700.89, found at 1702.11 ($[M+H]^+$).

RCC5: Reduced cage **RCC5** (0.26 g, 0.15 mmol) was synthesised using the similar method used for cage reduction. [4] **CC5** was dispersed in the solvent mixture of methanol and chloroform (1:1, 200 mL), $NaBH_4$ (0.6 g, 15.86 mmol) was then added, and the reaction mixture was stirred at room temperature for 72 hours. The reaction

mixture turned clear gradually. After the reaction stopped, 2 mL water was added and stirring was continued for another 12 hours. The solvent was then evaporated, and DCM was added to extract the product. DCM phase was filtered, dried over Na_2SO_4, and concentrated to afford **RCC5** (0.16 g, yield = 61%). ^{1}H NMR ($CDCl_3$, 400 MHz,) δ_H 7.14-7.12 (24H, br, benzene H), 6.98-6.96 (24H, br, benzene H), 3.78-3.55 (24H, br), 2.81 (12H, br, cyclopentyl CH), 2.06-1.37 (36H, br, cyclopentyl CH_2); ^{13}C NMR ($CDCl_3$, 400 MHz,) δ_C 146.82, 134.88, 129.19, 124.16, 64.73, 52.15, 31.16, 21.30; HR-ESI MS (RP): m/z: accurate mass calculated for $C_{114}H_{132}N_{16}$ 1725.13, found at 1726.09 ($[M+H]^+$).

7.5 Reference

1 Romm Freddy, *Microporous Media: Synthesis, Properties, and Modeling*, CRC Press, 2004.

2 T. Tozawa, J. T. A. Jones, S. I. Swamy, S. Jiang, D. J. Adams, S. Shakespeare, R. Clowes, D. Bradshaw, T. Hasell, S. Y. Chong, C. Tang, S. Thompson, J. Parker, A. Trewin, J. Bacsa, A. M. Z. Slawin, A. Steiner and A. I. Cooper, *Nat. Mater.*, 2009, **8**, 973–978.

3 J. Tian, P. K. Thallapally and B. P. McGrail, *CrystEngComm*, 2012, **14**, 1909–1919.

4 N. O'Reilly, N. Giri and S. L. James, *Chem. A Eur. J.*, 2007, **13**, 3020–3025.

5 H. Furukawa, K. E. Cordova, M. O'keeffe and O. M. Yaghi, *Science*, 2013, DOI: 10.1126/science.1230444.

6 B. Chen, Z. Yang, Y. Zhu and Y. Xia, *J. Mater. Chem. A*, 2014, **2**, 16811–16831.

7 A. Trewin and A. I. Cooper, *Angew. Chem. Int. Ed.*, 2010, **49**, 1533–1535.

8 A. P. Côté, A. I. Benin, N. W. Ockwig, M. O'Keeffe, A. J. Matzger and O. M. Yaghi, *Science*, 2005, **310**, 1166–1170.

9 A. Huang, Y. He, Y. Zhou, Y. Zhou, Y. Yang, J. Zhang, L. Luo, Q. Mao, D. Hou and J. Yang, *J. Mater. Sci.*, 2019, **54**, 949–973.

10 A. Modak and S. Jana, *Microporous Mesoporous Mater.*, 2019, **276**, 107–132.

11 A. G. Slater and A. I. Cooper, *Science*, 2015, DOI: 10.1126/science.aaa8075.

12 Y. Li, Z. Y. Fu and B. L. Su, *Adv. Funct. Mater.*, 2012, 22, 4634–4667.

13 Y. Wu and B. M. Weckhuysen, *Angew. Chem. Int. Ed.*, 2021, **60**, 18930–18949.

14 C. M. A. Parlett, K. Wilson and A. F. Lee, *Chem. Soc. Revv.*, 2013, **42**, 3876–3893.

15 C. Zhu, K. Yang, H. Wang, Y. Fang, L. Feng, J. Zhang, Z. Xiao, X. Wu, Y. Li, Y. Fu, W. Zhang, K. Y. Wang and H. C. Zhou, *ACS Cent. Sci.*, 2021, **2022**, 570.

16 G. Ahuja and K. Pathak, *Indian J. Pharm. Sci.*, 2009, **71**, 599-607.

17 A. I. Cooper, *ACS Cent. Sci.*, 2017, **3**, 544–553.

18 S. L. James, *Adv. Mater.*, 2016, **28**, 5712–5716.

19 P. Pakzad, M. Mofarahi, M. Ansarpour, M. Afkhamipour and C.-H. Lee, *Adv. Carbon Capture*, 2020, 51–87.

20 T. D. Bennett, F.-X. Coudert, S. L. James and A. I. Cooper, *Nat. Mater.*, 2021, **20**, 1179–1187.

21 R. Gaillac, P. Pullumbi, K. A. Beyer, K. Chapman, D. A. Keen, T. D. Bennett and F. X. Coudert, *Nat. Mater.*, 2017, **16**, 1149–1155.

22 N. Giri, C. E. Davidson, G. Melaugh, M. G. Del Pópolo, J. T. A. Jones, T. Hasell, A. I. Cooper, P. N. Horton, M. B. Hursthouse and S. L. James, *Chem. Sci.*, 2012, **3**, 2153–2157.

23 N. Giri, M. G. Del Pópolo, G. Melaugh, R. L. Greenaway, K. Rätzke, T. Koschine, L. Pison, M. F. C. Gomes, A. I. Cooper and S. L. James, *Nature*, 2015, **527**, 216–220.

24 J. Zhang, S. Chai, Z. Qiao, S. M. Mahurin, J. Chen, Y. Fang, S. Wan, K. Nelson, P. Zhang and S. Dai, *Angew. Chemie*, 2015, **127**, 946–950.

25 W. Shan, P. F. Fulvio, L. Kong, J. A. Schott, C. L. Do-Thanh, T. Tian, X. Hu, S. M. Mahurin, H. Xing and S. Dai, *ACS Appl. Mater. Interfaces*, 2018, **10**, 32–36.

26 M. Costa Gomes, L. Pison, C. Červinka and A. Padua, *Angew. Chemie*, 2018, **130**, 12085–12088.

27 S. Liu, J. Liu, X. Hou, T. Xu, J. Tong, J. Zhang, B. Ye and B. Liu, *Langmuir*, 2018, **34**, 3654–3660.

28 L. Ma, C. J. E. Haynes, A. B. Grommet, A. Walczak, C. C. Parkins, C. M. Doherty, L. Longley, A. Tron, A. R. Stefankiewicz, T. D. Bennett and J. R. Nitschke, *Nat. Chem.*, 2020, **12**, 270–275.

29 R. E. Mow, A. S. Lipton, S. Shulda, E. A. Gaulding, T. Gennett and W. A. Braunecker, *J. Mater. Chem. A*, 2020, **8**, 23455–23462.

30 R. L. Greenaway, D. Holden, E. G. B. Eden, A. Stephenson, C. W. Yong, M. J. Bennison, T. Hasell, M. E. Briggs, S. L. James and A. I. Cooper, *Chem. Sci.*, 2017, **8**, 2640–2651.

31 G. Melaugh, N. Giri, C. E. Davidson, S. L. James and M. G. Del Pópolo, *Phys. Chem. Chem. Phys.*, 2014, **16**, 9422–9431.

32 J. Avila, C. Červinka, P. Dugas, A. A. H. Pádua and M. Costa Gomes, *Adv. Mater. Interfaces*, 2021, DOI: 10.1002/admi.202001982.

33 H. Mahdavi, H. Zhang, L. K. Macreadie, C. M. Doherty, D. Acharya, S. J. D. Smith, X. Mulet and M. R. Hill, *Nano Res.*, 2022, **15**, 3533–3538.

34 J. Cahir, M. Y. Tsang, B. Lai, D. Hughes, M. A. Alam, J. Jacquemin, D. Rooney and S. L. James, *Chem. Sci.*, 2020, **11**, 2077–2084.

35 Y. Liu, Y. Bai and T. Tian, *Materials*, 2019, **12**, 3984–3991.

36 Y. Li, *ChemistrySelect*, 2020, 5, 13664–13672.

37 B. D. Egleston, A. Mroz, K. E. Jelfs and R. L. Greenaway, *Chem. Sci.*, 2022, 13, 5042–5054.

38 R. J. Kearsey, B. M. Alston, M. E. Briggs, R. L. Greenaway and A. I. Cooper, *Chem. Sci.*, 2019, **10**, 9454–9465.

39 C.-W. Chang, I. Borne, R. M. Lawler, Z. Yu, S. S. Jang, R. P. Lively and D. S. Sholl, *J. Am. Chem. Soc.*, 2022, **144**, 4071–4079.

40 J. A. Schott, C.-L. Do-Thanh, W. Shan, N. G. Puskar, S. Dai and S. M. Mahurin, *Green Chem. Eng.*, 2021, **2**, 392–401.

41 B. D. Egleston, K. V. Luzyanin, M. C. Brand, R. Clowes, M. E. Briggs, R. L. Greenaway and A. I. Cooper, *Angew. Chemie Int. Ed.*, 2020, **59**, 7362–7366.

42 X. Wang, D. Shang, S. Zeng, Y. Wang, X. Zhang, X. Zhang and J. Liu, *J. Chem. Thermodyn.*, 2019, **128**, 415–423.

43 P. Li, H. Chen, J. A. Schott, B. Li, Y. Zheng, S. M. Mahurin, D. E. Jiang, G. Cui, X. Hu, Y. Wang, L. Li and S. Dai, *Nanoscale*, 2019, **11**, 1515–1519.

44 S. He, L. Chen, J. Cui, B. Yuan, H. Wang, F. Wang, Y. Yu, Y. Lee and T. Li, *J. Am. Chem. Soc.*, 2019, **141**, 19708–19714.

45 X. Zhao, S. An, J. Dai, C. Peng, J. Hu and H. Liu, *New J. Chem.*, 2020, **44**, 12715–12722.

46 X. Zhao, Y. Yuan, P. Li, Z. Song, C. Ma, D. Pan, S. Wu, T. Ding, Z. Guo and N. Wang, *Chem. Commun.*, 2019, **55**, 13179–13182.

47 A. B. Bourlinos, R. Herrera, N. Chalkias, D. D. Jiang, Q. Zhang, L. A. Archer

and E. P. Giannelis, *Adv. Mater.*, 2005, **17**, 234–237.

48 J. Sharma and G. Polizos, *Nanomaterials*, 2020, DOI: 10.3390/nano10081599.

49 A. Q. Zhang, H. J. Li, D. J. Qian and M. Chen, *Nanotechnology*, 2014, DOI: 10.1088/0957-4484/25/13/135608.

50 B. Li, X. Yang, L. Xia, M. I. Majeed and B. Tan, *Sci. Rep.*, 2013, **3**, 2128.

51 Y. Li, C. Wang, S. Ma, J. Xu, X. Li, Y. Wei and J. Ou, *RSC Adv.*, 2021, **11**, 20899–20910.

52 S. Kandambeth, V. Venkatesh, D. B. Shinde, S. Kumari, A. Halder, S. Verma and R. Banerjee, *Nat. Commun.*, 2015, **6**, 1–10.

53 Z. Cai, Z. Wang, J. Kim and Y. Yamauchi, *Adv. Mater.*, 2019, DOI: 10.1002/adma.201804903.

54 H. Chen, Z. G. Gu, S. Mirza, S. H. Zhang and J. Zhang, *J. Mater. Chem. A*, 2018, **6**, 7175–7181.

55 A. Jayakumar, R. P. Antony, R. Wang and J. M. Lee, *Small*, 2017, DOI: 10.1002/smll.201603102.

56 Y. Yang, S. Jin, Z. Zhang, Z. Du, H. Liu, J. Yang, H. Xu and H. Ji, *ACS Appl. Mater. Interfaces*, 2017, **9**, 14180–14186.

57 Y. Li and J. Shi, *Adv. Mater.*, 2014, **26**, 3176–3205.

58 T. Liu, L. Zhang, B. Cheng and J. Yu, *Adv. Energy Mater.*, 2019, DOI: 10.1002/aenm.201803900.

59 F. Caruso, R. A. Caruso and H. Möhwald, *Science*, 1998, **282**, 1111–1114.

60 T. Shi, Y. Zheng, T. Wang, P. Li, Y. Wang and D. Yao, *ChemPhysChem*, 2018, **19**, 130–137.

61 R. Kumar, P. Dhasaiyan, P. M. Naveenkumar and K. P. Sharma, *Nanoscale Adv.*, 2019, **1**, 4067–4075.

62 L. Sheng, Z. Chen and Y. Wang, *Appl. Surf. Sci.*, 2021, DOI: 10.1016/j.apsusc.2020.147951.

63 J. Zhang, N. Lv, Y. Chao, L. Chen, W. Fu, J. Yin, H. Li, W. Zhu and H. Li, *J. Mol. Graph. Model.*, 2020, DOI: 10.1016/j.jmgm.2020.107694.

64 J. Yin, J. Zhang, W. Fu, D. Jiang, N. Lv, H. Liu, H. Li and W. Zhu, *J. Mol. Graph. Model.*, 2021, DOI: 10.1016/j.jmgm.2020.107788.

65 P. Li, D. Wang, L. Zhang, C. Liu, F. Wu, Y. Wang, Z. Wang, Z. Zhao, W. Wu, Y. Liang, Z. Li, W. Wang and Y. Zheng, *Small*, 2021, DOI: 10.1002/smll.202006687.

66 A. Bhattacharjee, R. Kumar and K. P. Sharma, *ChemSusChem*, 2021, **14**, 3303–3314.

67 F. Su, X. Li, Y. Wang, Z. He, L. Fan, H. Wang, J. Xie, Y. Zheng and D. Yao, *Sep. Purif. Technol.*, 2021, DOI: 10.1016/j.seppur.2021.119410.

68 S. Liu, L. Meng and J. Fan, *ChemistrySelect*, 2021, **6**, 5027–5033.

69 E. A. Tomic, *J. Appl. Polym. Sci.*, 1965, **9**, 3745–3752.

70 O. M. Yaghi, *ACS Cent. Sci.*, 2019, **5**, 1295–1300.

71 O. M. Yaghi, *J. Am. Chem. Soc.*, 2016, **138**, 15507–15509.

72 O. M. Yaghi, M. J. Kalmutzki and C. S. Diercks, *Introduction to reticular chemistry: Metal-organic frameworks and covalent organic frameworks*, Wiley-VCH, 2019.

73 M. Safaei, M. M. Foroughi, N. Ebrahimpoor, S. Jahani, A. Omidi and M. Khatami, *Trends Anal. Chem.*, 2019, **118**, 401–425.

74 S. M. Moosavi, A. Nandy, K. M. Jablonka, D. Ongari, J. P. Janet, P. G. Boyd, Y. Lee, B. Smit and H. J. Kulik, *Nat. Commun.*, 2020, **11**, 1–10.

75 P. Silva, S. M. F. Vilela, J. P. C. Tomé and F. A. Almeida Paz, *Chem. Soc. Rev.*, 2015, **44**, 6774–6803.

76 D. Li, H. Q. Xu, L. Jiao and H. L. Jiang, *EnergyChem*, 2019, DOI: 10.1016/j.enchem.2019.100005.

77 Q. Xu and H. Kitagawa, *Adv. Mater.*, 2018, DOI: 10.1002/adma.201803613.

78 D. Wang, Y. Xin, X. Li, F. Wang, Y. Wang, W. Zhang, Y. Zheng, D. Yao, Z. Yang and X. Lei, *Chem. Eng. J.*, 2021, DOI: 10.1016/j.cej.2020.127625.

79 D. Wang, Y. Xin, X. Li, H. Ning, Y. Wang, D. Yao, Y. Zheng, Z. Meng, Z. Yang, Y. Pan, P. Li, H. Wang, Z. He and W. Fan, *ACS Appl. Mater. Interfaces*, 2021, **13**, 2600–2609.

80 Y. H. Zou, Y. B. Huang, D. H. Si, Q. Yin, Q. J. Wu, Z. Weng and R. Cao, *Angew. Chem. Int. Ed.*, 2021, **60**, 20915–20920.

81 M. A. Little and A. I. Cooper, *Adv. Funct. Mater.*, 2020, DOI: 10.1002/adfm.201909842.

82 S. A. Herbert, A. Janiak, P. K. Thallapally, J. L. Atwood and L. J. Barbour, *Chem. Commun.*, 2014, **50**, 15509–15512.

83 J. L. Atwood, L. J. Barbour, A. Jerga and B. L. Schottel, *Science*, 2002, **298**, 1000–1002.

84 J. L. Atwood, L. J. Barbour and A. Jerga, *Science*, 2002, **296**, 2367–2369.

85 D. Holden, S. Y. Chong, L. Chen, K. E. Jelfs, T. Hasell and A. I. Cooper, *Chem. Sci.*, 2016, **7**, 4875–4879.

86 K. Jie, N. Onishi, J. A. Schott, I. Popovs, D. Jiang, S. Mahurin and S. Dai, *Angew. Chem. Int. Ed.*, 2020, **59**, 2268–2272.

87 T. Tateishi, M. Yoshimura, S. Tokuda, F. Matsuda, D. Fujita and S. Furukawa, *Coord. Chem. Rev.*, 2022, DOI: 10.1016/j.ccr.2022.214612.

88 D. Zhang, T. K. Ronson and J. R. Nitschke, *Acc. Chem. Res.*, 2018, **51**, 2423–2436.

89 W. Lin, Z. Cai, X. Lv, Q. Xiao, K. Chen, H. Li and C. Wang, *Ind. Eng. Chem. Res.*, 2019, **58**, 16894–16900.

90 H. Mahdavi, S. J. D. Smith, X. Mulet and M. R. Hill, *Mater. Horizons*, 2022, 9, 1577–1601.

91 J. Yin, J. Zhang, C. Wang, N. Lv, W. Jiang, H. Liu, H. Li, W. Zhu, H. Li and H. Ji, *J. Mol. Liq.*, 2021, DOI: 10.1016/j.molliq.2021.117676.

92 Y. Wang, Y. Sun, H. Bian, L. Zhu, D. Xia and H. Wang, *ACS Appl. Mater. Interfaces*, 2020, **12**, 45928.

93 L. Sheng and Z. Chen, *J. Mol. Liq.*, 2021, **333**, 115890.

94 L. Sheng, Z. Chen, B. Xu and J. Shi, *J. Phys. Chem. B*, 2021, **125**, 5387–5396.

95 E. B. Hemming, A. F. Masters and T. Maschmeyer, *Chem. Commun.*, 2019, **55**, 11179–11182.

96 E. B. Hemming, A. F. Masters and T. Maschmeyer, *Chem. Eur. J.*, 2020, **26**, 7059–7064.

97 E. B. Hemming, A. F. Masters and T. Maschmeyer, *Aust. J. Chem.*, 2020, **73**, 1296–1300.

98 X. Yang, J. K. Sun, M. Kitta, H. Pang and Q. Xu, *Nat. Catal.*, 2018, **1**, 214–220.

99 Y. Zheng, X. Zhang, Y. Yao, X. Chen and Q. Yang, *RSC Adv.*, 2015, **5**, 105747–105752.

100 P. Li, J. A. Schott, J. Zhang, S. M. Mahurin, Y. Sheng, Z. Qiao, X. Hu, G. Cui, D. Yao, S. Brown, Y. Zheng and S. Dai, *Angew. Chem. Int. Ed.*, 2017, **56**, 14958–14962.

101 T. D. Bennett, J. C. Tan, Y. Yue, E. Baxter, C. Ducati, N. J. Terrill, H. H. M. Yeung, Z. Zhou, W. Chen, S. Henke, A. K. Cheetham and G. N. Greaves, *Nat. Commun.*, 2015, **6**, 1–7.

102 V. Nozari, C. Calahoo, J. M. Tuffnell, D. A. Keen, T. D. Bennett and L. Wondraczek, *Nat. Commun.*, 2021, **12**, 1–13.

103 K. Y. Cho, H. An, X. H. Do, K. Choi, H. G. Yoon, H. K. Jeong, J. S. Lee and K. Y. Baek, *J. Mater. Chem. A*, 2018, **6**, 18912–18919.

104 Y. Wu, D. Wang, P. Li, X. Li, C. Wang, Z. He, Y. Xin and Y. Zheng, *J. Mol. Liq.*, 2021, DOI:10.1016/j.molliq.2021.117522.

105 X. Li, D. Yao, D. Wang, Z. He, X. Tian, Y. Xin, F. Su, H. Wang, J. Zhang, X. Li, M. Li and Y. Zheng, *Chem. Eng. J.*, 2021, DOI: 10.1016/j.cej.2021.129239.

106 Z. Deng, W. Ying, K. Gong, Y. J. Zeng, Y. Yan, X. Peng, Z. Deng, W. Ying, X. Peng, Y. Zeng, K. Gong and Y. Yan, *Small*, 2020, DOI: 10.1002/smll.201907016.

107 B. S. Pilgrim and N. R. Champness, *Chempluschem*, 2020, **85**, 1842–1856.

108 N. Giri, M. G. Del Pópolo, G. Melaugh, R. L. Greenaway, K. Rätzke, T. Koschine, L. Pison, M. F. C. Gomes, A. I. Cooper and S. L. James, *Nature*, 2015, **527**, 216–220.

109 F. Zhang, F. Yang, J. Huang, B. G. Sumpter and R. Qiao, *J. Phys. Chem. B*, 2016, **120**, 7195–7200.

110 Z. Yin, H. Chen, L. Yang, C. Peng, Y. Qin, T. Wang, W. Sun and C. Wang, *Langmuir*, 2021, **37**, 1255–1266.

111 T. Hasell, J. L. Culshaw, S. Y. Chong, M. Schmidtmann, M. A. Little, K. E. Jelfs, E. O. Pyzer-Knapp, H. Shepherd, D. J. Adams, G. M. Day and A. I. Cooper, *J. Am. Chem. Soc.*, 2014, **136**, 1438–1448.

112 J. Yin, W. Fu, J. Zhang, H. Ran, N. Lv, Y. Chao, H. Li, W. Zhu, H. Liu and H. Li, *RSC Adv.*, 2020, **10**, 42706–42717.

113 M. Atilhan, A. Cincotti and S. Aparicio, *J. Mol. Liq.*, 2021, DOI: 10.1016/j.molliq.2021.115660.

114 Z. Zhang, B. Yang, B. Zhang, M. Cui, J. Tang and X. Qiao, *Nat. Commun. 2022 131*, 2022, **13**, 1–10.

115 F. M. Alexander, S. F. Fonrouge, J. L. Borioni, M. G. Del Pópolo, P. N. Horton, S. J. Coles, B. P. Hutchings, D. E. Crawford and S. L. James, *Chem. Sci.*, 2021, **12**, 14230–14240.

116 J. W. Barnett, M. R. Sullivan, J. A. Long, D. Tang, T. Nguyen, D. Ben-Amotz, B. C. Gibb and H. S. Ashbaugh, *Nat. Chem.*, 2020, **12**, 589–594.

117 S. Zhang, Q. Yang, C. Wang, X. Luo, J. Kim, Z. Wang, Y. Yamauchi, S. Zhang,

Q. Yang, C. Wang, Z. Wang, X. Luo, Y. Yamauchi and J. Kim, *Adv. Sci.*, 2018, DOI: 10.1002/advs.201801116.

118 F. Zhang, Z. Yang, J. Hao, K. Zhao, M. Hua, Y. Yang and J. Wei, *Commun. Chem.*, 2019, **2**, 1–10.

119 J. Hu, S. K. Gupta, J. Ozdemir and M. H. Beyzavi, *ACS Appl. Nano Mater.*, 2020, **3**, 6239–6269.

120 H. Zhao, S. Xia and P. Ma, *J. Chem. Technol. Biotechnol.*, 2005, **80**, 1089–1096.

121 N. Winterton, *Clean Technol. Environ. Policy*, 2021, **23**, 2499–2522.

122 A. Kai, B. D. Egleston, A. Tarzia, R. Clowes, M. E. Briggs, K. E. Jelfs, A. I. Cooper and R. L. Greenaway, *Adv. Funct. Mater.*, 2021, **31**, 2106116.

123 J. Cravillon, S. Münzer, S. J. Lohmeier, A. Feldhoff, K. Huber and M. Wiebcke, *Chem. Mater.*, 2009, **21**, 1410–1412.

124 H. Liu, B. Liu, L. C. Lin, G. Chen, Y. Wu, J. Wang, X. Gao, Y. Lv, Y. Pan, X. Zhang, X. Zhang, L. Yang, C. Sun, B. Smit and W. Wang, *Nat. Commun.*, 2014, **5**, 5147–5153.

125 C. Mukesh, S. Sarmad, A. Samikannu, D. Nikjoo, W. Siljebo and J. P. Mikkola, *J. Mol. Liq.*, 2022, DOI: 10.1016/j.molliq.2022.119046.

126 J. Wu, X. Wu, P. Zhao, Z. Wang, L. Zhang, D. Xu and J. Gao, *Fuel*, 2021, DOI: 10.1016/j.fuel.2021.121013.

127 J. Avila, L. F. Lepre, C. C. Santini, M. Tiano, S. Denis-Quanquin, K. Chung Szeto, A. A. H. Padua and M. Costa Gomes, *Angew. Chemie Int. Ed.*, 2021, **60**, 12876–12882.

128 Y. Zhou, J. Avila, N. Berthet, S. Legrand, C. C. Santini, M. Costa Gomes and V. Dufaud, *Chem. Commun.*, 2021, **57**, 7922–7925.

129 B. Lai, J. Cahir, M. Y. Tsang, J. Jacquemin, D. Rooney, B. Murrer and S. L. James, *ACS Appl. Mater. Interfaces*, 2021, **13**, 932–936.

130 A. Knebel, A. Bavykina, S. J. Datta, L. Sundermann, L. Garzon-Tovar, Y. Lebedev, S. Durini, R. Ahmad, S. M. Kozlov, G. Shterk, M. Karunakaran, I. D. Carja, D. Simic, I. Weilert, M. Klüppel, U. Giese, L. Cavallo, M. Rueping, M. Eddaoudi, J. Caro and J. Gascon, *Nat. Mater.*, 2020, **19**, 1346–1353.

131 X. Li, D. Wang, Z. He, F. Su, N. Zhang, Y. Xin, H. Wang, X. Tian, Y. Zheng, D. Yao and M. Li, *Chem. Eng. J.*, 2021, **417**, 129239.

132 T. Hasell, S. Y. Chong, K. E. Jelfs, D. J. Adams and A. I. Cooper, *J. Am. Chem.*

Soc., 2012, **134**, 588–598.

133 Z. Lei, C. Dai and B. Chen, *Chem. Rev.*, 2014, **114**, 1289–1326.

134 J. Gross-Rother, N. Herrmann, M. Blech, S. R. Pinnapireddy, P. Garidel and U. Bakowsky, *Int. J. Pharm.*, 2018, **543**, 257–268.

135 A. Knebel, A. Bavykina, S. J. Datta, L. Sundermann, L. Garzon-Tovar, Y. Lebedev, S. Durini, R. Ahmad, S. M. Kozlov, G. Shterk, M. Karunakaran, I. D. Carja, D. Simic, I. Weilert, M. Klüppel, U. Giese, L. Cavallo, M. Rueping, M. Eddaoudi, J. Caro and J. Gascon, *Nat. Mater.*, 2020, **19**, 1346–1353.

136 T. Tozawa, J. T. A. Jones, S. I. Swamy, S. Jiang, D. J. Adams, S. Shakespeare, R. Clowes, D. Bradshaw, T. Hasell, S. Y. Chong, C. Tang, S. Thompson, J. Parker, A. Trewin, J. Bacsa, A. M. Z. Slawin, A. Steiner and A. I. Cooper, *Nat. Mater.*, 2009, **8**, 973–978.

137 F. Beuerle and B. Gole, *Angew. Chem. Int. Ed.*, 2018, 57, 4850–4878.

138 M. Mastalerz, *Acc. Chem. Res.*, 2018, **51**, 2411–2422.

139 A. G. Slater, P. S. Reiss, A. Pulido, M. A. Little, D. L. Holden, L. Chen, S. Y. Chong, B. M. Alston, R. Clowes, M. Haranczyk, M. E. Briggs, T. Hasell, G. M. Day and A. I. Cooper, *ACS Cent. Sci.*, 2017, **3**, 734–742.

140 M. W. Schneider, L. G. Lechner and M. Mastalerz, *J. Mater. Chem.*, 2012, **22**, 7113–7116.

141 S. Jiang, Y. Du, M. Marcello, E. W. Corcoran, D. C. Calabro, S. Y. Chong, L. Chen, R. Clowes, T. Hasell and A. I. Cooper, *Angew. Chem. Int. Ed.*, 2018, **57**, 11228–11232.

142 J. T. A. Jones, T. Hasell, X. Wu, J. Bacsa, K. E. Jelfs, M. Schmidtmann, S. Y. Chong, D. J. Adams, A. Trewin, F. Schiffman, F. Cora, B. Slater, A. Steiner, G. M. Day and A. I. Cooper, *Nature*, 2011, **474**, 367–371.

143 T. Hasell, S. Y. Chong, M. Schmidtmann, D. J. Adams and A. I. Cooper, *Angew. Chemie - Int. Ed.*, 2012, **51**, 7154–7157.

144 S. Tothadi, M. A. Little, T. Hasell, M. E. Briggs, S. Y. Chong, M. Liu and A. I. Cooper, *CrystEngComm*, 2017, **19**, 4933–4941.

145 S. M. Kelly, T. J. Jess and N. C. Price, *Biochim. Biophys. Acta - Proteins Proteomics*, 2005, **1751**, 119–139.

146 M. A. Little, S. Y. Chong, M. Schmidtmann, T. Hasell and A. I. Cooper, *Chem. Commun.*, 2014, **50**, 9465–9468.

147 A. Kewley, A. Stephenson, L. Chen, M. E. Briggs, T. Hasell and A. I. Cooper,

Chem. Mater., 2015, **27**, 3207–3210.

148 T. Hasell, M. Miklitz, A. Stephenson, M. A. Little, S. Y. Chong, R. Clowes, L. Chen, D. Holden, G. A. Tribello, K. E. Jelfs and A. I. Cooper, *J. Am. Chem. Soc.*, 2016, **138**, 1653–1659.

149 T. Mitra, K. E. Jelfs, M. Schmidtmann, A. Ahmed, S. Y. Chong, D. J. Adams and A. I. Cooper, *Nat. Chem.*, 2013, **5**, 276–281.

150 F. Philippi and T. Welton, *Phys. Chem. Chem. Phys.*, 2021, **23**, 6993–7021.

151 J. M. Slattery, C. Daguenet, P. J. Dyson, T. J. S. Schubert and I. Krossing, *Angew. Chem. Int. Ed.*, 2007, **46**, 5384–5388.

152 F. Philippi, D. Rauber, K. L. Eliasen, N. Bouscharain, K. Niss, C. W. M. Kay and T. Welton, *Chem. Sci.*, 2022, **13**, 2735–2743.

153 B. D. Tompkins and E. R. Fisher, *J. Appl. Polym. Sci.*, 2015, DOI: 10.1002/app.41978.

154 T. Hasell, M. Schmidtmann, C. A. Stone, M. W. Smith and A. I. Cooper, *Chem. Commun.*, 2012, **48**, 4689–4691.

155 D. Lerche, *J. Dispers. Sci. Technol.*, 2002, **23**, 699–709.

156 D. Gonzalez Ortiz, C. Pochat-Bohatier, J. Cambedouzou, M. Bechelany and P. Miele, *Engineering*, 2020, **6**, 468–482.

157 M. Sadegh-Cheri, *J. Chem. Educ*, 2020, **97**, 2338-2341.

158 F. Yu, Y. Chen, X. Liang, J. Xu, C. Lee, Q. Liang, P. Tao and T. Deng, *Prog. Nat. Sci. Mater. Int.*, 2017, 27, 531–542.

159 X. Guan, Y. Ma, H. Li, Y. Yusran, M. Xue, Q. Fang, Y. Yan, V. Valtchev and S. Qiu, *J. Am. Chem. Soc.*, 2018, **140**, 4494–4498.

160 C. Chiappe, M. Malvaldi and C. S. Pomelli, *Pure Appl. Chem.*, 2009, **81**, 767–776.

161 D. Yalcin, C. J. Drummond and T. L. Greaves, *Phys. Chem. Chem. Phys.*, 2019, **22**, 114–128.

162 T. G. A. Youngs, J. D. Holbrey, M. Deetlefs, M. Nieuwenhuyzen, M. F. Costa Gomes and C. Hardacre, *ChemPhysChem*, 2006, **7**, 2279–2281.

163 C. Dalvit and A. Vulpetti, *Chem. Eur. J.*, 2016, **22**, 7592–7601.

164 P. Metrangolo, J. S. Murray, T. Pilati, P. Politzer, G. Resnati and G. Terraneo, *CrystEngComm*, 2011, **13**, 6593–6596.

165 P. Li, J. M. Maier, E. C. Vik, C. J. Yehl, B. E. Dial, A. E. Rickher, M. D. Smith, P. J. Pellechia and K. D. Shimizu, *Angew. Chem. Int. Ed.*, 2017, **56**, 7209–7212.

166 Y. Lu, M. Sun and N. Xi, *RSC Adv.*, 2022, **12**, 32082–32096.

167 S. Jiang, J. T. A. Jones, T. Hasell, C. E. Blythe, D. J. Adams, A. Trewin and A. I. Cooper, *Nat. Commun.*, 2011, **2**, 1–7.

168 E. Andrzejewska, *Polym. Int.*, 2017, **66**, 366–381.

169 M. Liu, M. A. Little, K. E. Jelfs, J. T. A. Jones, M. Schmidtmann, S. Y. Chong, T. Hasell and A. I. Cooper, *J. Am. Chem. Soc.*, 2014, **136**, 7583–7586.

170 M. Liu, L. Zhang, M. A. Little, V. Kapil, M. Ceriotti, S. Yang, L. Ding, D. L. Holden, R. Balderas-Xicohténcatl, D. He, R. Clowes, S. Y. Chong, G. Schütz, L. Chen, M. Hirscher and A. I. Cooper, *Science*, 2019, **366**, 613–620.

171 S. Bera, K. Dey, T. K. Pal, A. Halder, S. Tothadi, S. Karak, M. Addicoat and R. Banerjee, *Angew. Chem. Int. Ed.*, 2019, **58**, 4243–4247.

172 R. Pinal, *Org. Biomol. Chem.*, 2004, **2**, 2692–2699.

173 R. J. C. Brown and R. F. C. Brown, *J. Chem. Educ.*, 2000, **77**, 724–731.

174 J. R. Kearsey, PhD thesis, University of Liverpool, 2020.

175 M. Liu, L. Chen, S. Lewis, S. Y. Chong, M. A. Little, T. Hasell, I. M. Aldous, C. M. Brown, M. W. Smith, C. A. Morrison, L. J. Hardwick and A. I. Cooper, *Nat. Commun.*, 2016, **7**, 1–9.

176 M. K. Muthayala and A. Kumar, *ACS Comb. Sci.*, 2012, **14**, 5–9.

177 J. L. Culshaw, G. Cheng, M. Schmidtmann, T. Hasell, M. Liu, D. J. Adams and A. I. Cooper, *J. Am. Chem. Soc.*, 2013, **135**, 10007–10010.

178 D. Wang, Y. Xin, X. Li, F. Wang, Y. Wang, W. Zhang, Y. Zheng, D. Yao, Z. Yang and X. Lei, *Chem. Eng. J.*, 2020, DOI:10.1016/j.cej.2020.127625.

179 M. Liu, L. Zhang, M. A. Little, V. Kapil, M. Ceriotti, S. Yang, L. Ding, D. L. Holden, R. Balderas-Xicohténcatl, D. He, R. Clowes, S. Y. Chong, G. Schütz, L. Chen, M. Hirscher and A. I. Cooper, *Science*, 2019, **366**, 613–620.

180 H. Chen, Z. Yang, C. L. Do-Thanh and S. Dai, *ChemSusChem*, 2020, **13**, 6182–6200.

181 S. Jiang, Y. Du, M. Marcello, E. W. Corcoran, D. C. Calabro, S. Y. Chong, L. Chen, R. Clowes, T. Hasell and A. I. Cooper, *Angew. Chem. Int. Ed.*, 2018, **57**, 11228–11232.

182 H. Li, E. A. Homan, A. J. Lampkins, I. Ghiviriga and R. K. Castellano, *Org. Lett.*, 2005, **7**, 443–446.

183 A. Halder, S. Karak, M. Addicoat, S. Bera, A. Chakraborty, S. H. Kunjattu, P. Pachfule, T. Heine and R. Banerjee, *Angew. Chem. Int. Ed.*, 2018, **57**, 5797–

5802.

184 S. I. Swamy, J. Bacsa, J. T. A. Jones, K. C. Stylianou, A. Steiner, L. K. Ritchie, T. Hasell, J. A. Gould, A. Laybourn, Y. Z. Khimyak, D. J. Adams, M. J. Rosseinsky and A. I. Cooper, *J. Am. Chem. Soc.*, 2010, **132**, 12773–12775.